Unraveling host-derived molecular mechanisms for interacting with a bacterial endosymbiont in the trypanosomatid *Angomonas deanei* with a particular focus on endosymbiont division

Inaugural dissertation

for the attainment of the title of doctor
in the Faculty of Mathematics and Natural Sciences
at the Heinrich Heine University Düsseldorf

presented by

Anay Kumar Maurya

from India

Düsseldorf, May 2025

From the Institute for Microbial Cell Biology
at the Heinrich Heine University Düsseldorf

Published by permission of the
Faculty of Mathematics and Natural Sciences at
Heinrich Heine University Düsseldorf

Supervisor: Prof. Dr. Eva C. M. Nowack
Co-supervisor: Prof. Dr. Johannes H. Hegemann

Date of the oral examination: 11.07.2025

Declaration on oath:

I declare in lieu of an oath that the dissertation has been prepared by me independently and without unauthorized external assistance in compliance with the "Principles for Safeguarding Good Scientific Practice at Heinrich Heine University Düsseldorf". The dissertation has not been submitted in its current or similar form to any other university. I have not previously made any unsuccessful doctoral attempts.

Place, Date **Anay Kumar Maurya**

The studies for this thesis were carried out from December 2020 to March 2025 at the Institute for Microbial Cell Biology, Heinrich Heine University in Düsseldorf (Germany) under the supervision of Prof. Dr. Eva C. M. Nowack.

This thesis includes the following publications and manuscripts:

1. Morales, J.*, Ehret, G.*, Poschmann, G., Reinicke, T., **Maurya, A.K.,** Kröninger, L., Zanini, D., Wolters, R., Kalyanaraman, D., Krakovka, M., Bäumers, M., Stuhler, K., and Nowack, E.C.M. (2023). Host-symbiont interactions in *Angomonas deanei* include the evolution of a host-derived dynamin ring around the endosymbiont division site. *Current Biology*, 33(1), 28-40. DOI: 10.1016/j.cub.2022.11.020.

2. **Maurya, A.K.,** Kröninger, L., Ehret, G., Bäumers, M., Marson, M., Scheu, S., Nowack, E.C.M. (2025). A nucleus-encoded dynamin-like protein controls endosymbiont division in the trypanosomatid *Angomonas deanei*. *Science Advances*, 11(12), eadp8518. DOI: 10.1126/sciadv.adp8518.

3. Kröninger, L., **Maurya, A.K.,** Stiebeling C., Stirba F.P., Kim, Z., and Nowack, E.C.M. (2025). T7 RNA polymerase-based gene expression from a transcriptionally silent rDNA spacer in the endosymbiont-harboring trypanosomatid *Angomonas deanei*. *PloS One* (Accepted). Preprint on BioRxiv. DOI: 10.1101/2025.01.30.635516.

4. **Maurya, A.K.,** Cadena, L.R., Ehret, G., Nowack, E.C.M. (2025). A novel host-encoded protein, ETP2, plays an important role in endosymbiont division in the trypanosomatid *Angomonas deanei*. (Under review in mBio). Preprint on BioRxiv. DOI: 10.1101/2025.04.22.649992.

Summary

Endosymbiosis has been a key process in the evolution of eukaryotic cells, as mitochondria and plastids, the organelles responsible for energy supply in most eukaryotic cells, were acquired via endosymbiotic events. Both events occurred more than 1.5 billion years ago, which makes it difficult to study the early steps of endosymbiosis and organelle evolution.

During my doctoral research, I used a recent endosymbiotic system, the trypanosomatid *Angomonas deanei* with a single bacterial endosymbiont (ES). To understand the level of integration of the ES in *A. deanei*, the lab had previously characterized the proteome of isolated endosymbionts by protein mass spectrometry and found seven host-encoded proteins targeted to the ES, which were termed 'endosymbiont-targeted proteins' (ETPs). It was postulated that these proteins provide the host with control over its ES.

Overexpression of fluorescent protein fusions of ETPs showed differential subcellular localization of various ETPs. Recombinant ETP9, ETP2, and ETP7 formed a ring-like structure around the ES division site (ESDS). ETP5 was detected at the periphery of the ES. Additionally, it showed a fluorescence signal at the upper flagellar pocket of the host cell as well as associated with the nucleus, kinetoplast, and possibly cytoskeletal structures. ETP1 showed a fluorescence signal at the ES envelope. Lastly, ETP3 and ETP8 appeared to localize in the ES cytosol and the Golgi apparatus, based on confocal microscopy data. This observation led to the hypothesis that their import is mediated by vesicular transport. Vesicle fusions with specific target membranes are usually mediated by specific SNARE proteins, and interestingly, three nucleus-encoded SNARE proteins were identified in the ES fractions.

The overarching goal of this thesis was to elucidate molecular mechanisms underlying the host-symbiont interaction and the role of ETPs in *A. deanei*. To this end, I specifically aimed at (I) studying the localization of ETP9, ETP2, and ETP7 throughout cell cycle stages, (II) investigating cellular functions of ETP9, ETP2, ETP7, ETP1, and ETP5, and (III) exploring the question if SNARE proteins may mediate vesicle fusion to the ES and likely the import of ETP3 and ETP8.

To study the localization of ETP9, ETP2, and ETP7 over the cell cycle stages, I performed IFA and found that all three ETPs showed a cell cycle-dependent localization where ETP7 appeared to be always detectable over the ES, however, it enriched at the ESDS during bacterial elongation. This is followed by the arrival at the ESDS of ETP2, the ES-encoded FtsZ, and finally ETP9.

To investigate the cellular functions of ETP9 and ETP2, I performed a complementation analysis and found that ETP9 and ETP2 fused to the green fluorescent protein eGFP expressed from their respective endogenous loci, showed the same fluorescence pattern as the overexpressed versions. However, the function of the recombinant ETP9, but not ETP2, appeared to be partially impaired as cells showed division phenotypes, for example, with the ES forming long tubular chains. This problem was largely solved by using the smaller V5 tag instead of eGFP. Further, we found by comparative genomics that the ES has lost most of the essential division components and the autonomy to divide. ETP9, ETP2, and ETP7 compensate for the loss of bacterial division proteins. The generation of heterozygous deletion mutants revealed that *etp9* mutants showed

weak division phenotypes, but not *etp2* mutants. Importantly, homozygous mutants could not be generated for *etp9* but was possible for *etp2* which interestingly showed severe division phenotypes such as long filamentous endosymbionts. Since the generation of homozygous mutants of *etp9* was not possible, I developed a protocol for specific gene knockdowns using morpholino antisense oligos (MAOs) and used it to knockdown protein synthesis from *etp9* as well as *etp2* and *etp7* mRNA. This resulted in similar division phenotypes as described above suggesting their roles in ES division.

To find the cellular function of ETP1, a heterozygous *etp1* mutant was previously generated. Further, I observed by microscopy that endosymbionts in this mutant appeared roundish compared to the regular peanut-shape of the ES in Wt cells, suggesting a role in structural maintenance of the ES.

To explore the cellular function(s) of ETP5, I performed knockout studies and found that reduced gene dosage of *etp5* resulted in a slower growth rate with division phenotypes, for instance, the elongated ES. Based on all observations, it appears that ETP5 mainly plays a role in segregation of the ES and other cellular structures to the daughter cells and contributes to ES division.

To explore the question if ETP3 and ETP8 could be imported into the ES via vesicle fusion mediated by SNARE proteins, I studied the subcellular localization of SNARE proteins. I observed that two of the SNAREs showed a fluorescence signal mainly at the flagellar pocket. Additionally, a weak dot-like fluorescence signal in close vicinity of the ES was detected in many cells. To test if these signals close to the ES result from ETP-carrying vesicles that eventually fuse with the ES outer membrane (OM), further analyses by transmission electron microscopy (TEM) of SNARE-containing vesicles and their possible co-localization with ETP3 and ETP8 by double labelling is planned.

In conclusion, the studies of this thesis show that the ES co-evolved with its host and both partners show coordinated cell cycle stages, protein import from the host, and importantly the evolution of a host-derived ES division and segregation machineries controlling the ES has occurred. The data suggests that the bacterium has evolved far beyond an ES and already fulfils some of the criteria of being an early-stage organelle that provides essential metabolites to its host. This work lays the basis for further studies to understand key events involved in the organelle evolution.

Zusammenfassung

Die Endosymbiose war ein Schlüsselprozess in der Evolution eukaryontischer Zellen, da Mitochondrien und Plastiden, die Organellen, die in den meisten eukaryontischen Zellen für die Bereitstellung von Energie verantwortlich sind, durch endosymbiontische Ereignisse erworben wurden. Beide Ereignisse fanden vor mehr als 1,5 Milliarden Jahren statt, was es schwierig macht, die frühen Schritte der Endosymbiose und der Organellenentwicklung zu untersuchen.

Während meiner Doktorarbeit habe ich ein verhältnismäßig junges Endosymbiosesystem verwendet, den Trypanosomatiden *Angomonas deanei* mit einem einzelnen bakteriellen Endosymbiont (ES). Um den Grad der Integration des ES in *A. deanei* zu verstehen, hatte das Labor zuvor das Proteom isolierter Endosymbionten mit Hilfe der Protein-Massenspektrometrie charakterisiert und sieben vom Wirt kodierte Proteine gefunden, die am ES lokalisieren und als „endosymbiont-targeted proteins“ (ETPs) bezeichnet werden. Es wurde postuliert, dass diese Proteine dem Wirt Kontrolle über seinen ES ermöglichen.

Die Überexpression von Fluoreszenzproteinfusionen der ETPs zeigte eine unterschiedliche subzelluläre Lokalisierung der verschiedenen ETPs am ES. Die rekombinanten Proteine ETP9, ETP2 und ETP7 bildeten eine ringförmige Struktur um die ES-Teilungsstelle (ESDS). ETP5 wurde an der Peripherie des ES nachgewiesen. Außerdem zeigte es ein Fluoreszenzsignal in der Flagellentasche der Wirtszelle sowie eine Verbindung mit dem Zellkern, dem Kinetoplasten und möglicherweise mit Zytoskelettstrukturen. ETP1 zeigte ein Fluoreszenzsignal an der ES-Hülle. ETP3 und ETP8 schließlich scheinen im Cytosol des ES und im Golgi-Apparat zu lokalisieren, wie konfokale Mikroskopiedaten zeigen. Ihr Import wird möglicherweise durch vesikulären Transport bewerkstelligt. Vesikelfusionen mit spezifischen Zielmembranen werden üblicherweise durch spezifische SNARE-Proteine vermittelt, und interessanterweise wurden in den ES-Fraktionen per Massenspektrometrie drei im Nucleus kodierte SNARE Proteine identifiziert.

Das übergeordnete Ziel dieser Arbeit war die Aufklärung der molekularen Mechanismen, die der Wirt-Symbionten-Interaktion und der Rolle der ETPs in *A. deanei* zugrunde liegen. Zu diesem Zweck wollte ich insbesondere (I) die Lokalisierung von ETP9, ETP2 und ETP7 während der verschiedenen Stadien des Zellzyklus untersuchen, (II) die zellulären Funktionen von ETP9, ETP2, ETP7, ETP1, und ETP5 analysieren und (III) erste Hinweise darauf finden, ob SNARE-Proteine möglicherweise die Vesikelfusion mit dem ES und wahrscheinlich den Import von ETP3 und ETP8 vermitteln.

Um die Lokalisierung von ETP9, ETP2 und ETP7 während der Stadien des Zellzyklus zu untersuchen, führte ich IFA durch und stellte fest, dass alle drei ETPs eine zellzyklusabhängige Lokalisierung aufwiesen, wobei ETP7 immer am gesamten ES nachweisbar zu sein schien, sich jedoch während der bakteriellen Elongation an der ESDS anreicherte. Im Anschluss an diesen Prozess folgt die schrittweise Anreicherung von ETP2, dem vom Bakterium kodierten FtsZ und schließlich ETP9 an der ESDS.

Um die zellulären Funktionen von ETP9 und ETP2 zu untersuchen, führte ich zunächst eine Komplementationsanalyse durch und stellte fest, dass ETP9 und ETP2 fusioniert mit eGFP, die von ihren endogenen Loci exprimiert wurden, das gleiche Fluoreszenzmuster zeigten wie die

überexprimierten Versionen. Allerdings schien die Funktion von ETP9, nicht aber von ETP2, teilweise beeinträchtigt zu sein, da die Zellen Teilungsphänotypen zeigten, bei denen die ES beispielsweise lange röhrenförmige Ketten bildeten. Dieses Problem konnte durch die Verwendung eines kleineren V5-Tags anstelle von eGFP weitgehend gelöst werden.

Durch vergleichende Genomik haben wir festgestellt, dass der ES die meisten wesentlichen Teilungskomponenten und die Autonomie zur Teilung verloren hat. Interessanterweise stellten wir fest, dass ETP9, ETP2 und ETP7 den Verlust der bakteriellen Teilungsproteine kompensieren. Die Erzeugung heterozygoter Deletionsmutanten zeigte, dass *etp9*-Mutanten einen schwachen Teilungsphänotyp aufwiesen, nicht aber *etp2*-Mutanten. Wichtig ist, dass homozygote Mutanten für *etp9* nicht erzeugt werden konnten, wohl aber für *etp2*, die interessanterweise schwere Teilungsphänotypen wie lange filamentöse Endosymbionten zeigten. Da die Erzeugung homozygoter Mutanten von *etp9* nicht möglich war, verwendete ich Morpholino-Antisense-Oligos (MAOs), um die Proteinsynthese ausgehend von *etp9*- sowie von *etp2*- und *etp7*-mRNA spezifisch auszuschalten. Dies führte zu ähnlichen Teilungsphänotypen wie oben beschrieben, was auf ihre Rolle bei der ES-Teilung schließen lässt.

Um die zelluläre Funktion von ETP1 zu ermitteln, wurde zuvor eine heterozygote *etp1*-Mutante erzeugt. Außerdem beobachtete ich mit Hilfe von Mikroskopie, dass die Endosymbionten im Vergleich zur Erdnussform in Wt-Zellen rundlich erschienen, was auf eine Rolle bei der strukturellen Aufrechterhaltung des ES hindeutet.

Um die zelluläre(n) Funktion(en) von ETP5 zu erforschen, habe ich Knockout-Studien durchgeführt und festgestellt, dass eine reduzierte Gendosierung von *etp5* zu einer langsameren Wachstumsrate mit Teilungsphänotypen, z. B. verlängerten ES, führt. Aus allen Beobachtungen geht hervor, dass ETP5 hauptsächlich eine Rolle bei der Verteilung der ES und anderer zellulärer Strukturen auf die Tochterzellen spielt und zur Teilung der ES beiträgt.

Um zu verstehen, ob ETP3 und ETP8 in den ES importiert werden, wahrscheinlich durch die von SNARE-Proteinen vermittelte Fusion von Wirtsvesikeln mit dem ES, habe ich zunächst die subzelluläre Lokalisierung der SNARE-Proteine untersucht. Ich beobachtete, dass zwei der SNAREs ein Fluoreszenzsignal hauptsächlich in der Flagellentasche zeigten. Zusätzlich wurde in vielen Zellen ein schwaches, punktförmiges Signal in unmittelbarer Nähe zum ES entdeckt. Eine weitere Untersuchung, ob diese SNARE-positiven Vesikel tatsächlich ETPs durch Fusion mit der äußeren ES-Membran in den ES transportieren, soll später durch Transmissionselektronenmikroskopie (TEM) und Ko-Lokalisationsanalysen von ETP3 und ETP8 und den SNAREs durch Doppelmarkierung durchgeführt werden.

Zusammenfassend zeigen die Studien dieser Arbeit, dass sich der ES gemeinsam mit seinem Wirt entwickelt hat und dass beide Partner koordinierte Zellzyklusphasen und den Import von Proteinen aus dem Wirt aufweisen, und, was besonders wichtig ist, dass sich eine vom Wirt abgeleitete ES-Teilungs- und -Segregationsmaschinerie entwickelt hat, die den ES kontrolliert. Die Daten deuten darauf hin, dass sich das Bakterium weit über einen ES hinaus entwickelt hat und bereits einige der Kriterien eines Organells im Frühstadium erfüllt, das seinen Wirt mit wichtigen Stoffwechselprodukten versorgt. Diese Arbeit bildet die Grundlage für weitere Studien zum Verständnis der Schlüsselereignisse, die an der Organellevolution beteiligt sind.

List of abbreviations

ARC, Accumulation and replication of chloroplast

ATCC, American type culture collection

BB, Basal body

BSE, Bundle signaling element

Caf4, CCR4-associated factor 4

DRP/DLP, Dynamin-related/like protein

DS, Division site

DSP, Dynamin superfamily protein

EGT, Endosymbiotic gene transfer

ETP, Endosymbiont-targeted protein

F, Flagellum

Fis, Fission 1 (mitochondrial)

FISH, Fluorescence *in situ* hybridization

FR, Flanking region

G domain, GTPase domain

HB, Helical bundle

Hyg^{r}, *Hygromycin* resistance

IEM/IM, Inner (envelope) membrane

IFA, Immunofluorescence assay

InsB, Insert B

IR, Intergenic region

K, Kinetoplast

KMP, Kinetoplastid membrane protein

L, Linker

LOPIT, Localization of organelle proteins by isotope tagging

MAO, Morpholino antisense oligo

MD/MDR, Mitochondria dividing (ring)

Mdv1, Mitochondrial division 1

MiD, Mitochondrial dynamics

MIEF, Mitochondrial elongation factor

N, Nucleus

Neo^{r}, *Neomycin*/G418 resistance

OEM/OM, Outer (envelope) membrane

Ox, Overexpression

PARC6, Paralog of ARC6

PBP, Penicillin-binding protein

PD/PDR, Plastid dividing (ring)

PG, Peptidoglycan

PH(D), Pleckstrin homology (domain)

POI, Protein of interest

PRD, Proline-rich domain

S/ES, Symbiont/endosymbiont

SNARE, Soluble N-ethylmaleimide-sensitive factor attachment protein receptor

TEM, Transmission electron microscopy

TM(H), Transmembrane (helix)

UCYN-A, Endosymbiont, *Candidatus* Atelocynobacterium thalassa

VD, Variable domain

Here are other common abbreviations: https://rupress.org/jcb/pages/standard-abbreviations.

Table of contents

1. Introduction

1.1. General introduction to symbiosis

Bacteria are genetically and physiologically highly diverse and they are found in nearly every habitat of this planet. Their ubiquitous nature and diverse physiology has led to interesting associations with other phylogenetically unrelated organisms (Moya et al., 2008). Such interactions have been referred to as symbiosis. It is defined as a close association between two or more organisms from different species (Moya et al., 2008). This interaction can either be of an obligative or facultative nature based on the level of dependence.

In addition, based on the fitness effects on the interacting organisms, symbiosis can generally be categorized into three groups- parasitism, commensalism, and mutualism. In parasitism, one organism benefits while the other is harmed during the interaction, for example, *Mycobacterium tuberculosis* and *Salmonella* spp., are well-known human pathogens causing tuberculosis and salmonellosis, respectively. In commensalism, one organism benefits while the other remains unaffected, for example, *Nitromonas* spp. and *Nitrobacter* spp., the latter obtains energy for its growth from oxidation of nitrite that is produced by the former one. In mutualism, both interacting partners provide benefits to each other, for example, *Candidatus* Kinetoplastibacterial endosymbionts in members of the trypanosomatid subfamily Strigomonadinae (e.g., *Angomonas*).

Symbiosis can further be classified into ectosymbiosis and endosymbiosis depending on the location of one organism (the symbiont) with respect to the other (the host). Ectosymbiosis is when one organism lives on the external and or internal body surfaces of another organism, for example, the movement of the protozoan flagellate *Mixotricha paradoxa* is supported by its bacterial ectosymbiont *Spirochetae* (Rosati, 2004). Endosymbiosis is defined as an association where the symbiont lives inside the host cell, for example, nitrogen-fixing bacteria that reside in the plant root nodules (Maróti & Kondorosi, 2014). Another interesting example of endosymbiosis is the trypanosomatid *A. deanei* which harbors a single β-proteobacterial ES that lives inside the host cytosol (Fig. 1.2 and Morales et al., 2023).

Endosymbioses can be further categorized as primary, secondary, and tertiary, see below.

1.2. Primary, secondary, and tertiary endosymbiosis

Initially, the eukaryotic cells were simple and less diverse in their metabolic capacity, though some researchers believe that eukaryotic cells did not exist until the acquisition of mitochondria. In contrast, bacteria are genetically and metabolically very diverse. Likely, to increase the complexity of cellular structures and functional diversity, archaeal cells acquired bacteria via primary endosymbiosis (Margulis, 1993). Over time, this led to the generation of modern eukaryotic cells with additional organelles adding several metabolic functions such as energy supply and metabolite synthesis (Margulis, 1993 and Moya et al., 2008).

The endosymbiotic origin of organelles such as mitochondria and plastids and the evolution of eukaryotes have been proposed previously by many scientists during the end of 19th and the beginning of 20th century; however, these theories were rejected until the discovery of DNA in these organelles in 1960s (Bodył & Mackiewicz, 2013). Later, Lynn Margulis, in 1967, proposed not only models for the endosymbiotic origin of eukaryotes, but also mitochondria and plastids. It has been suggested that mitochondria and plastids independently evolved from Gram-negative bacteria, an α-proteobacterium and a cyanobacterium, respectively, more than 1.5 billion years ago (via two independent primary endosymbiosis events) where the acquisition of the former organelle occurred first (Bodył & Mackiewicz, 2013).

Once the ES entered from free-living to intracellular phase, many genes became unnecessary or redundant, and were later lost (Moya et al., 2008). In the endosymbionts and pathogenic intracellular bacteria, the smaller genome became AT-rich likely due to the loss of DNA repair genes allowing to increase GC to AT mutations as compared to free-living bacteria (Wernegreen, 2002). The level of genome reduction and higher AT contents help figuring out the age of an endosymbiotic associations. Once the ES was established, there as an accumulation of mobile genetic elements that were also later found deleterious and removed (Moran & Plague, 2004; Moya et al., 2008 and Plague et al., 2008). The genes that were retained in the ES involve mainly DNA replication, transcription, translation, and other accessory components (Pérez-Brocal et al., 2006). In contrast, gene losses mainly involved genes from metabolism (Moya et al., 2008).

One of the most peculiar features of establishment of an organelle is protein import from the host to the ES/organelle, which have been considered the strongest evidence of organellogenesis (Jarvis, 2008; Carrie et al., 2009; Chacinska et al., 2009; Nowack & Grossman, 2012; Zimorski et al., 2014; Singer et al., 2017; Coale et al., 2024 and Sørensen et al., 2024). Secondly, there was an involvement of gene transfers from the ES to the host nucleus, termed endosymbiotic gene transfer (EGT) resulting in the expansion of the host genome and reduction of the ES genome (Timmis et al., 2004; Zimorski et al., 2014; Nowack et al., 2016; Lhee et al., 2021 and Suzuki et al., 2021). Lastly, the ES/organelle cell cycle is synchronized with that of its host cells (Hoogenraad, 1927; Pyke, 1999; Melkonian & Mollenhauer, 2005; Arakaki et al., 2006 and Coale et al., 2024). Importantly, the order and timing of events in which an ES was transformed into a genetically integrated organelle yet remains to be fully understood.

Secondary endosymbiosis occurred when a unicellular protist cell engulfed a eukaryotic cell with an existing primary plastid (Gibbs, 1993 and Bhattacharya et al., 2004), for example, the alga *Euglena,* belonging to the phylum Euglenozoa, harbors a green plastid originated from secondary endosymbiosis (Bhattacharya et al., 2004).

Tertiary endosymbiosis occurred when a protist cell acquired an algal cell with a secondary plastid and can be observed in most dinoflagellates. In dinoflagellates, even quaternary endosymbiosis has been observed (Bhattacharya et al., 2004).

1.3. Recent organellogenesis events

1.3.1. *Paulinella chromatophora*

The third independent primary endosymbiosis and second plastid primary endosymbiosis occurred very recently when a heterotrophic ancestor of *P. chromatophora* (a cercozoan amoeba belonging to the supergroup Rhizaria) engulfed an α-cyanobacterium around 90-140 million years ago (Delaye et al., 2016). The cyanobacterial ES evolved over time into a photosynthetic organelle named as the 'chromatophore' (Lauterborn, 1895; Melkonian & Mollenhauer, 2005 and Lhee et al., 2021). The chromatophore has a reduced genome size of ~1 Mb compared to its free-living close relative *Synechococcus* sp. (~3 Mb) (Lhee et al., 2019). Only approximately 50 genes out of two-third missing from the chromatophore genome have been identified that are transferred from the chromatophore to the host nucleus by EGT (Nowack et al., 2016 and Lhee et al., 2021). Moreover, the chromatophore shows synchronized cell division with its host cell (Hoogenraad, 1927 and Melkonian & Mollenhauer, 2005) and massive protein import from the host cytosol (Nowack & Grossman, 2012 and Singer et al., 2017). This recently evolved system is currently being used to better understand early stages in the integration of a photosynthetic organelle by primary endosymbiosis; however, it poses a couple of major challenges. First, it has an around one week of doubling time in culture and secondly, it cannot be genetically modified.

1.3.2. *Braarudosphaera bigelowii*

A marine unicellular alga *B. bigelowii*, initially known to harbor a single ES *Candidatus* Atelocynobacterium thalassa (UCYN-A) derived from a nitrogen-fixing cyanobacterium (Zehr et al., 2016), is another example of recently evolved organelle. In a recent study, it was found that UCYN-A evolved beyond an endosymbiont and shows many features of an early-stage N_2-fixing organelle termed as 'nitroplast' (Coale et al., 2024). Using soft X-ray tomography and proteomic approaches, it has been shown that the UCYN-A is tightly integrated into the host cell and divides synchronously. Additionally, protein import from the host to the UCYN-A but no gene transfer from the UCYN-A to the host nucleus has been reported (Suzuki et al., 2021). Genome reduction of UCYN-A has been previously reported (Tripp et a., 2010), however, it has a complete set of *nif* genes required for N_2-fixation (Zehr et al., 2008). *B. bigelowii* is a good model system to study organelle evolution, however, also for this symbiotic system genetic tools are yet to be established for better understanding its biology.

Lastly, some trypanosomatids are also currently being used to study endosymbiosis and organellogenesis events as described below.

1.4. Trypanosomatids

Trypanosomatids are uniflagellate protists and include clinically relevant human pathogens such as *Leishmania* spp. and *Trypanosoma* spp. as well as the plant pathogen *Phytomonas* spp. *Trypanosoma brucei*, *Trypanosoma cruzi*, and *Leishmania* spp. are the causative agents of sleeping sickness, Chagas disease, and leishmaniasis, respectively (Barrett et al., 2003 and Ivens et al., 2005). These pathogens have a dixenous lifestyle and complete their life cycle in two distinct

host species, for example, in humans and insects. The pathogen *Phytomonas* infects plant species worldwide (Dollet, 1984).

The family Trypanosomatidae (aka Trypanosomatids) belongs to the order Trypanosomatida (Fig. 1.1 B, Maslov et al., 2019), class Kinetoplastea (Fig. 1.1 A, Faktorová et al., 2016), and phylum Euglenozoa. The members of Kinetoplastea (aka Kinetoplastids) are flagellated protists with a specialized structure, the 'kinetoplast', that contains all the mitochondrial DNA in these organisms.

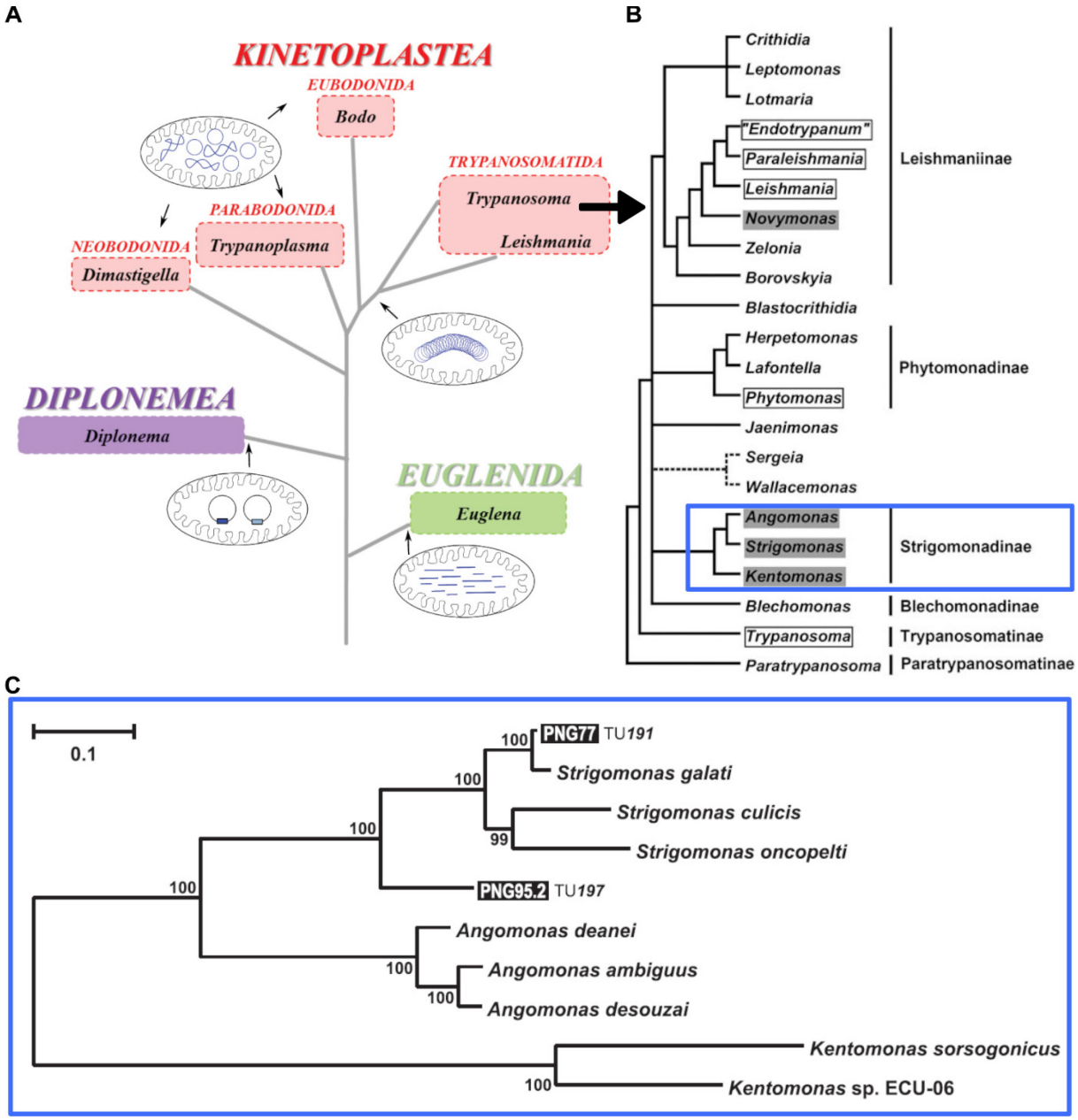

Figure 1.1: Phylogenetic mapping of symbiont-harboring trypanosomatids under Kinetoplastea.

A: The tree shows members of three classes- Euglenida, Diplonemea, and Kinetoplastea of the phylum Euglenozoa (taken from Faktorová et al., 2016). **B:** Members of the order Trypanosomatida (taken from Maslov et al., 2019). **C:** Members of the subfamily Strigomonadinae (taken from Králová et al., 2019). Highlighted in the blue rectangles are members of Strigomonadinae.

Trypanosomatids have another unique organelle, a specialized peroxisome, called glycosome where glycolysis partially occurs (Parsons, 2004). Some more peculiar biological features found in Trypanosomatids involve: the lack of introns in the majority of genes, arrangements of genes as polycistronic gene clusters which are functionally unrelated and transcribed as long pre-mRNAs, trans-splicing resulting in individual mRNA, post-transcriptional gene regulation, presence of a capped 39 nucleotides long spliced leader sequence at the 5' end of mRNAs, presence of spliced leader acceptor site upstream that allows trans-splicing and a polyadenylation site downstream of a gene (De Gaudenzi et al., 2011).

Interestingly, the family Trypanosomatidae also includes symbiont-harboring trypanosomatids, belonging to the subfamily Strigomonadinae (Fig. 1.1 B and C, Králová et al., 2019 and Maslov et al., 2019). This subfamily contains the genera *Angomonas*, *Strigomonas*, and *Kentomonas*. These organisms are non-pathogenic and monoxenous, meaning that they have a single host, which are insects. All members harbor a single β-proteobacterial ES named *Candidatus* Kinetoplastibacterium belonging to the family Alcaligenaceae that originated in the common ancestor of Strigomonadinae (Borghesan et al., 2018).

Another symbiont-harboring trypanosomatid is *Novymonas esmeraldas*. It belongs to the subfamily Leishmaniinae and harbors a different β-proteobacterial ES *Candidatus* Pandorea novymonadis from the family Burkholderiaceae and originated from a different endosymbiotic event (Kostygov et al., 2016). The host harbors many endosymbionts suggesting that the cell cycle is not synchronized. Additionally, the ES has undergone less genome reduction, indicating more recent association between the host and the ES (Zakharova et al., 2021).

1.4.1. *Angomonas deanei*

In my thesis, I used *A. deanei* strain ATCC PRA-265 (Strigomonadinae) as a model to study the molecular mechanisms underlying the cellular integration of its ES *Candidatus* Kinetoplastibacterium crithidii (Fig. 1.2). *A. deanei*, previously known as *Crithidia deanei*, was first isolated in Brazil from a bug *Zelus leucogrammus* (Carvalho & Deane, 1974). Interestingly, the ES genome is highly reduced (0.8 Mb) compared to its free-living counterparts. The genome of the ES as well as the host has been sequenced (Alves et al., 2013b; Motta et al., 2013; Morales et al., 2016 and Davey et al., 2021). The ES maintains a peanut shape in the host cytosol and is located at the posterior end of the cell. The ES possesses one inner membrane (IM) and one OM with a reduced peptidoglycan (PG) layer in the middle (Motta et al., 1997). It has previously been shown that the host and the ES have a tightly synchronized cell cycle where the ES divides first followed by the basal body (BB), kinetoplast, nucleus, and finally the host cell (Motta et al., 2010). Lastly, it has been shown that the ES provides essential nutrients to the host such as aromatic amino acids, heme, and riboflavin, and in return obtains energy and other metabolites from the host such as proline, cysteine, and biotin (Mundim & Roitman, 1977; Alves et al., 2013a; Alves et al., 2013b and Klein et al., 2013).

Previously, several efforts were made to generate an aposymbiotic strain (without the ES) from *A. deanei* ATCC PRA-265 (Kokkori, 2018, PhD thesis and Morales et al, 2023), however, all attempts remaind without success suggesting the essentiality of the ES in the host. However, *A. deanei* ATCC 30969, an aposymbiotic strain, has previously been generated from another parental *A. deanei* strain by chloramphenicol treatment (Mundim & Roitman, 1977) and was obtained from the American Type Culture Collection. This aposymbiotic strain could be maintained in our laboratory by providing horse serum (10% v/v) in addition to BHI supplemented with hemin.

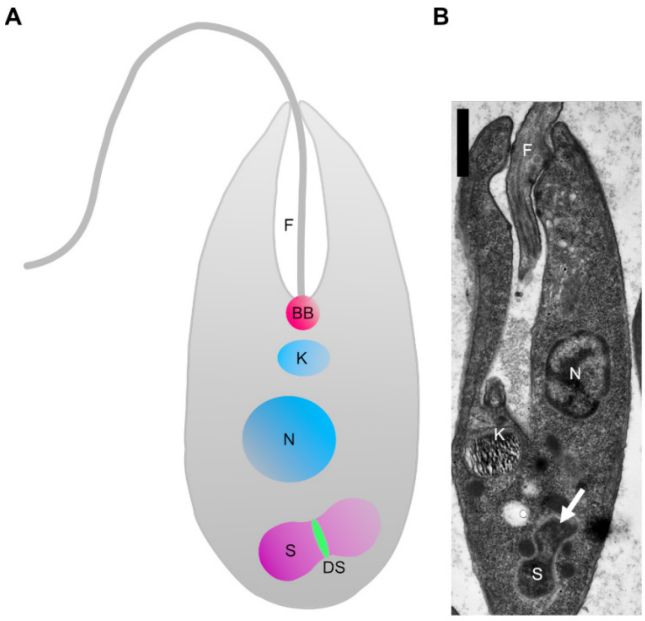

Figure 1.2: Structure of *A. deanei* highlighted with its ES and other host cellular organelles.

A: Schematic representation of an *A. deanei* cell. **B:** Transmission electron micrograph of *A. deanei* (Maurya et al., 2025). Scale bar: 1 µm. Abbreviations: F, flagellum; BB, basal body; K, kinetoplast; N, nucleus; S, symbiont and DS, division site.

The fast growth rate, sequenced nuclear and endosymbiont genomes, availability of genetic tools (Morales et al., 2016), and synchronized cell cycles make *A. deanei* a suitable model system for the study of endosymbiosis and organelle evolution.

The elongasome and divisome, two complex machineries responsible for the bacterial cell elongation and division, respectively are described later together with the bacterial ES of *A. deanei* (Maurya et al., 2025). Therefore, both machineries are briefly discussed below.

1.5. Elongasome: the bacterial cell elongation machinery

Bacterial cells proliferate by repetitive cell elongation and division. The bacterial elongation in rod-shaped bacteria is regulated by a Rod complex or elongasome. The Rod complex mainly consists of MreB, RodZ, penicillin-binding protein 2 (PBP2), MreC, MreD, RodA, and PBP1a.

MreB, conserved in rod-shaped bacteria, is an actin homolog in prokaryotes and scaffold protein of elongasome. It is assembled into helical polymers at cytoplasmic side of the inner/cytoplasmic membrane (Van den Ent et al., 2001) and mainly localized to areas with curved geometries (Bratton et al., 2018). It is an essential cell shape determinant (Bendezú & de Boer, 2008).

RodZ is a morphogenic protein, conserved in most bacteria (Daniel & Errington, 2003). In rod-shaped bacteria, it has been shown to contribute to cell shape, for example, in *Escherichia coli*,

Caulobacter crescentus, *Bacillus subtilis*, and *Deinococcus grandis* (Shiomi et al., 2008; Alyahya et al., 2009; Bendezú et al., 2009; Muchová et al., 2013 and Morita et al., 2019). In cocci-shaped bacteria such as *Staphylococcus* spp. and *Streptococcus* spp., which lack MreB, have conserved RodZ suggesting its universal role in cell morphogenesis, for example, in regulation of PG synthesis (Alyahya et al., 2009 and Philippe et al., 2014). In sum, MreB and RodZ are necessary for each other's assembly and localization (Ago & Shiomi, 2019).

RodA is a glycosyltransferase and synthesizes the glucan backbone whereas PBP2 is a transpeptidase that cross-links the peptide chains. MreC and MreD have been shown to regulate the function of RodA and PBP2 complex during PG synthesis (Liu et al., 2020). Lastly, class A PBP1a has been shown to regulate elongasome and is likely involved in peripheral PG synthesis in *S. pneumoniae* (Lamanna et al., 2022).

1.6. Divisome: the bacterial cell division machinery

Divisome, a supramolecular protein complex, is responsible for bacterial cell division. Elongasome and divisome are two independent protein complexes. However, in the recent years, it has been shown that components of the Rod complex and divisome interact with each other, for example, elongation-specific protein MreB has been shown to directly interact with divisome-specific protein FtsZ (Fenton & Gerdes, 2013). In addition, an elongasome-specific PG synthesis enzyme PBP2 co-localizes and directly interacts at the division site (DS) with a divisome-specific PG synthesis enzyme PBP3 (Van der Ploeg et al., 2013).

The bacterial division machinery mainly consists of FtsZ, a tubulin homolog in prokaryotes, FtsA, ZipA, FtsE, FtsX, FtsK, FtsQ, FtsL, FtsB, FtsW, FtsI, FtsN, and other accessary proteins, for instance, amidases and regulatory proteins (Cameron & Margolin, 2024).

FtsZ, a conserved self-assembling polymer-forming GTPase, forms a 'Z-ring' at the inner phase of the IM (Bi & Lutkenhaus, 1991) by interacting with membrane-associated proteins such as FtsA and ZipA (Van den Ent & Löwe, 2000). FtsA (a conserved actin homolog) and ZipA (a less conserved protein), both form a so called 'proto-ring' together with FtsZ (Hale & de Boer, 1997; Pichoff & Lutkenhaus, 2002; Pichoff & Lutkenhaus, 2005 and Rico et al., 2013). FtsE and FtsX interact with FtsA to arrive at the DS playing a dispensable role in cell division (Du et al., 2019). FtsK, FtsQ, FtsL, FtsB, FtsW, FtsI, FtsN reach the DS in the same order (Margolin, 2005 and Attaibi & den Blaauwen, 2022). FtsK (DNA translocase) contributes to the nucleoid segregation and cell division (Liu et al., 1998 and Aussel et al., 2002). FtsQ, FtsL and FtsB form a conserved subcomplex and act as a positive regulator of the subcomplex FtsWI (Marmont & Bernhardt, 2020). FtsW and FtsI (aka PBP3) are cell division-specific glycosyltransferase and transpeptidase, respectively that play an indispensable role in septal wall synthesis (Taguchi et al., 2019). Furthermore, FtsA and other divisome proteins such as FtsI recruit FtsN at the DS (Wissel & Weiss, 2004; Busiek et al., 2012 and Pichoff et al., 2015). Once recruited, FtsN stimulates septal wall synthesis by FtsWI (Gerding et al., 2009). Additionally, FtsN-like proteins, homologs of FtsN, are conserved among proteobacteria such as *C. crescentus* and play an essential role in division (Möll & Thanbichler, 2009). Lastly, murein hydrolases, for instance, amidases AmiA, AmiB, and AmiC cleave the cell septum (Heidrich et al., 2002).

1.7. Role of host-encoded effectors in division of endosymbionts/organelles

In the evolution of endosymbiosis, formerly free-living bacteria capable of autonomous cell division co-evolve with eukaryotic host cells, become tightly integrated and live as vertically transmitted endosymbionts. Depending on the level of integration, host-encoded effector proteins play a crucial role in controlling division of endosymbionts/organelles. The most extensively studied host-encoded proteins are dynamin superfamily proteins (DSPs) such as dynamins and dynamin-related proteins (DRPs).

1.7.1. *Dynamins and DRPs*

Dynamins and DRPs are self-assembling, polymer-forming GTPases, distributed from bacteria to humans, and play diverse roles. They mainly function in membrane remodeling events (endocytosis, exocytosis, organelle fission, and cytokinesis) and regulation of actin and microtubule organization (Chiang et al., 2014 and Jimah & Hinshaw, 2019). For organelle division, DRPs such as DRP1 (aka DLP1) in mammals, Dnm1 in yeast, CmDnm1 in the red alga *Cyanidioschyzon merolae*, and DRP3A/3B/5B in *Arabidopsis thaliana* play an indispensable role in mitochondria as well as peroxisome fission (Otsuga et al., 1998; Smirnova et al., 1998; Bleazard et al., 1999; Koch et al., 2003; Li & Gould, 2003; Miyagishima et al., 2003; Kuravi et al., 2006; Twig et al., 2008; Pan & Hu, 2011; Imoto et al., 2013 and Ramachandran & Schmid, 2018). Similarly, plastid dynamins Dnm2/DRP5B/ARC5 are involved in plastid division in different eukaryotes (Gao et al., 2003; Ramachandran & Schmid, 2018 and Yoshida, 2018).

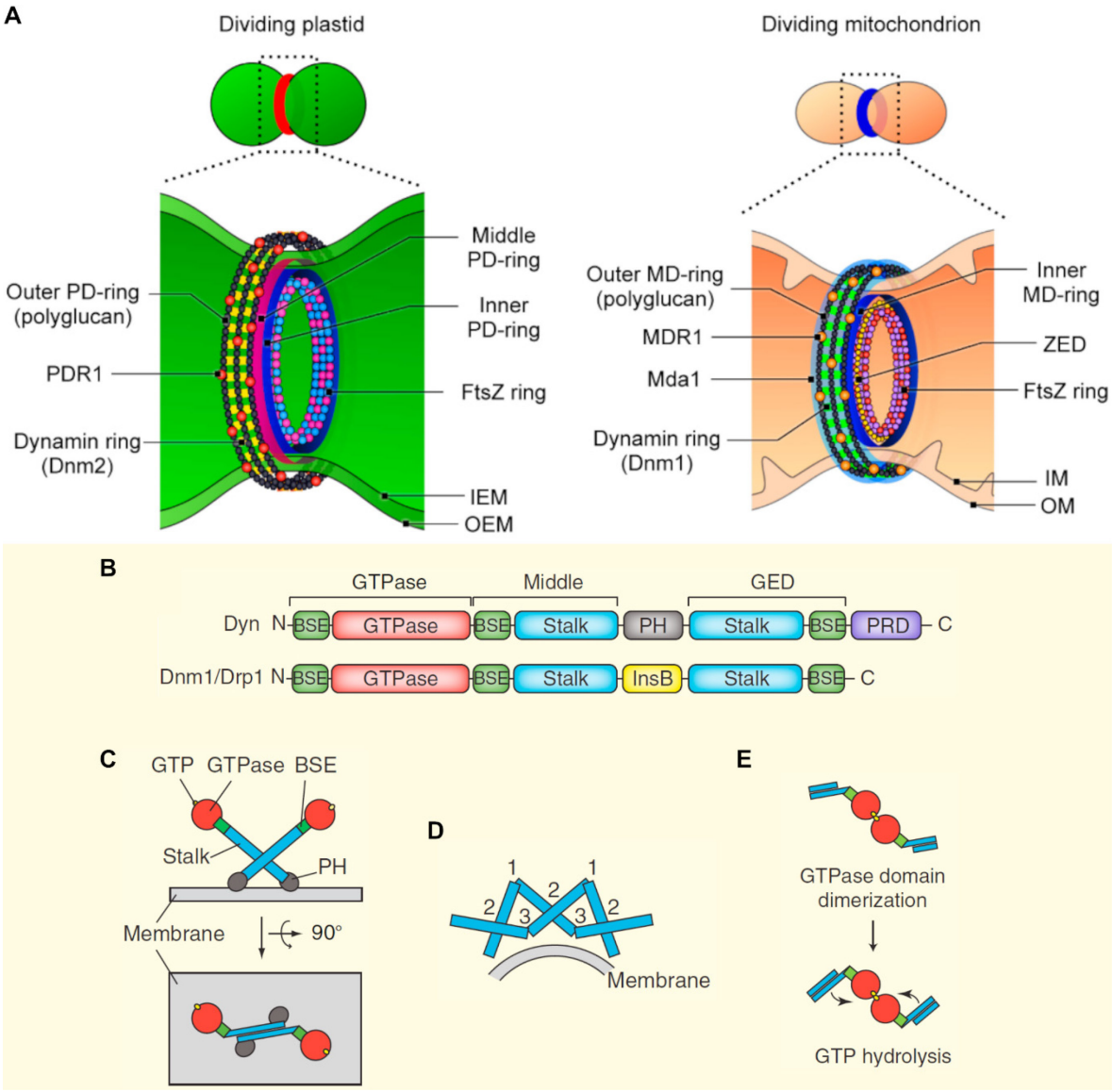

Figure 1.3: Organelle division rings, domain architecture, and mechanism of action of fission DSPs.

A: Various division rings in plastids and mitochondria involved in fission (taken from Yoshida, 2018). **B:** Linear domain organization of classical dynamins and mitochondrial DRP1/Dnm1 involved in fission. **C:** Arrangement of dynamin proteins in dimers. **D:** Arrangement of dynamin proteins in tetramers and oligomers. **E:** Mechanism of GTPase domain dimerization and GTP hydrolysis (B-E, modified from Bui & Shaw, 2013). Abbreviations: DSP, dynamin superfamily protein; IEM, inner envelope membrane; OEM, outer envelope membrane; IM, inner membrane; OM, outer membrane; PD, plastid dividing; PDR, plastid dividing ring; MD, mitochondria dividing; MDR, mitochondria dividing ring; Mda1, mitochondrial division apparatus 1 in outer MD, Drp, dynamin-related protein; Dyn, dynamin; BSE, bundle signaling element; InsB, insert B; PH, pleckstrin homology domain; GED, GTPase effector domain and PRD, proline-rich domain.

1.7.2. *Structure of dynamins and DRPs*

Both dynamins and DRPs interact reversibly with membranes by their respective membrane-interacting domains, exceptionally, Dyn2 and DRP1 can perform membrane-independent functions such as actin bundling (Ramachandran & Schmid, 2018).

They have a highly conserved GTPase domain (G domain) at the N-terminus (Fig. 1.3 B), the most conserved domain in DSPs (Jimah & Hinshaw, 2019). The G domain is responsible for GTP binding and hydrolysis. For this, four conserved motifs have been identified. First, a P-loop or G1 motif, important for nucleotide binding. Second, a G2 motif, interacts with Mg^{2+} and supports GTP hydrolysis. Third, a G3 motif, interacts with Mg^{2+}. Fourth, a G4 motif that binds the base of the nucleotide (Niemann et al., 2001; Ramachandran & Schmid, 2018 and Jimah & Hinshaw, 2019). Lastly, a fifth motif (G5) has been found conserved in dynamin and DRP1, that binds to the nucleotide base or sugar and regulates binding affinity (Ramachandran & Schmid, 2018).

The second most conserved structure in DSPs is the elongated α-helical bundle (HB) domain. In dynamin and DRP1, there are two HBs referred as bundle signaling elements (BSEs) and stalk domain (Fig. 1.3 B). In addition, there are three to four conserved hydrophobic interfaces identified in HBs that play an indispensable role in polymerization. First, interface 2 (Fig. 3 D) is present in the middle of the stalk domain and used for dimerization of two dynamin monomers (Fig. 1.3 C). Second, interface 1 and interface 3 are present at the membrane-distal and proximal ends of the stalk domain, respectively and used for dimer-dimer interaction and self-assembly (Fig. 1.3 D) (Jimah & Hinshaw, 2019 and Kraus et al., 2021). Lastly, a fourth interface has also been reported in DRP1 that plays a role in dimer-dimer interaction (Ramachandran & Schmid, 2018).

Finally, the most divergent region in DSPs is a membrane-interacting domain. It has been termed pleckstrin homology (PH) domain in dynamins (Fig. 1.3 B) and variable domain (VD) or insert B (InsB) in DRPs (Ferguson et al., 1994; Timm et al., 1994; Clinton et al., 2016 and Jimah & Hinshaw, 2019). The PH domain is a ~ 100 amino acid residues long structured region and the best characterized lipid-binding domain in DSPs whereas the VD/InsB domain is unstructured (Mears et al., 2011). Both domains PH and VD interact with negatively charged lipids, for example, cardiolipin and phosphatidic acid, and can inhibit premature self-assembly likely by interacting with interface 3 in the stalk (Bustillo-Zabalbeitia et al., 2014; Adachi et al., 2016; Francy et al., 2017; Lu et al., 2018; Ramachandran & Schmid, 2018 and Kraus et al., 2021).

Moreover, in dynamins, an additional domain is present at the C-terminal end of the protein named proline-rich domain (PRD) (Fig. 1.3 B). This unstructured domain is important for the interaction with SH3 and BAR domain-containing proteins in the membranes (for example, endophilin, intersectin, and amphiphysin), helping dynamin recruitment to the target membrane (Evergren et al., 2007; Cowling et al., 2017 and Hohendahl, et al., 2017).

1.7.3. *Mechanism of action of dynamins and DRPs*

In fission DSPs, the polypeptide chain folds on itself and gives rise to a monomer. It has been suggested based on structural studies and *in vitro* assays that dynamins adopt three conformations. In conformation 1, the protein is not bound to GTP and remains in the solution

(Faelber et al., 2011 and Ford et al., 2011). In conformation 2, it binds GTP and assembles on the membrane (Fig. 1.3 C and Zhang & Hinshaw, 2001). Lastly, conformation 3 represents the oligomerized protein in the transition state during GTP hydrolysis (Fig. 1.3 D and Chappie et al., 2010). The final constriction involves dimerization of G domains from two adjacent strands on the membrane via interface 4 followed by GTP hydrolysis (Fig. 1.3 E) resulting in conformational changes, like in DRP1 (Chappie et al., 2010; Bui & Shaw, 2013 and Fröhlich et al., 2013).

In mitochondria, there is an FtsZ ring (in some organisms), an inner mitochondrial dividing (MD) ring, an outer MD ring, and a dynamin ring (Fig. 1.3 A, on the right). The outer MD ring is composed of mitochondrial dividing ring 1 (MDR1, a glycosyltransferase) (Kuroiwa et al., 2006; Yoshida et al., 2017 and Yoshida, 2018). For the recruitment on the membrane, dynamins use their PH domain and directly interact with the membrane. In contrast, Dnm1 and likely DRP1 need additional proteins for membrane interaction (Mears et al., 2011). One of these is a mitochondrial fission 1 (Fis1), a conserved OM-associated protein in yeast and mammals. Fis1 plays an indispensable role in yeast for the recruitment of Dnm1 by interacting with two adaptor proteins, mitochondrial division 1 (Mdv1) and CCR4-associated factor 4 (Caf4) (Mozdy et al., 2000; Tieu et al., 2002 and Griffin et al., 2005). In mammals, there are no orthologs of Mdv1 or Caf4, however, Fis1 and three OM-associated adaptors mitochondrial dynamics 49 (aka mitochondrial elongation factor 2 (MIEF2)), MiD51 (MIEF1), and a mitochondrial fission factor fulfil this requirement, even in yeast when heterologously expressed (Gandre-Babbe & van der Bliek, 2008; Palmer et al., 2011; Zhao et al., 2011; Koirala et al., 2013 and Losón et al., 2013).

In plastids, the division machinery involves two inner rings (Fig. 1.3 A, on the left) at the stromal side of the IM, an FtsZ ring and the inner plastid-dividing (PD) ring (Kuroiwa et al., 1998 and Yoshida et al., 2012). It also involves two outer rings at the cytosolic side of the OM, an outer plastid-dividing (PD) ring that is composed of a glycosyltransferase plastid-dividing ring 1 (PDR1) (a homolog of MDR1) (Yoshida et al., 2010), and a plastid dynamin ring (Gao et al., 2003 and Miyagishima et al., 2003). Moreover, a third (middle) PD ring has also been observed in the intermembrane space of plastids of *C. merolae* (Miyagishima et al., 1998). For co-ordination, FtsZ interacts with two IM proteins, accumulation and replication of chloroplast 6 (ARC6) and a paralog of ARC6 (PARC6) (Glynn et al., 2009; Zhang et al., 2016 and Sun et al., 2023). Further, ARC6 and PARC6 interact with the OM proteins PDV2 and PDV1, respectively (Glynn et al., 2008; Zhang et al., 2016 and Wang et al., 2017). Lastly, plastid dynamins ARC5/Dnm2/DRP5B interact with both OM proteins PDV2 and PDV1 (Yoshida, 2018 and Sun et al., 2023).

1.7.4. *Additional factors contributing to the organelle division*

Interestingly, a host-encoded PG hydrolase DipM has been reported to play an essential role in chloroplast fission in Glaucophyte algae and some Viridiplantae (Miyagishima et al., 2014).

In addition, the actin cytoskeleton together with the ER has been shown to contribute to mitochondrial fission (Li et al., 2015a). Lastly, contacts of mitochondria with lysosomes and the Golgi have also been reported to be crucial for ultimate fission (Wong et al., 2018 and Nagashima et al., 2020).

1.8. Organelle/ES segregation components

In eukaryotes such as *Saccharomyces cerevisiae*, *Chlamydomonas reinhardtii*, and mammals, Centrin (a calcium-binding protein associated with microtubules) is involved in spindle pole body, BB, and centrosome duplication and segregation, respectively as well as in cell division (Salisbury et al., 1988; Spang et al., 1993; Errabolu et al., 1994; Satisbury, 1995 and Wolfrum & Salisbury,1998).

In the trypanosomatid *T. brucei*, five Centrins (*Tb*Cen1-5) have been identified (Berriman et al., 2005 and He et al., 2005). The knockdown of *Tb*Cen1, *Tb*Cen2, and *Tb*Cen3 using RNAi showed their role in segregation of the duplicated organelles such as the kinetoplast, BB, nucleus, and/or the Golgi as well as in cytokinesis (Selvapandiyan et al., 2007 and Selvapandiyan et al., 2012). Interestingly, the BB movement in *T. brucei* has also been shown to organize organelle division and cell morphogenesis (Lacomble et al., 2010).

In kinetoplastids, the kinetoplastid membrane protein 11 (KMP11) is a small (11 kDa), abundant, and conserved membrane-associated surface protein with no homologs in mammals (Stebeck et al., 1995 and Lim et al., 2017). It has been shown to mainly localize in the flagellum and flagellar pocket in *L. infantum*; however, it has been found as a microtubule-associated protein localizing in the flagellum and BB in *T. brucei* (Berberich et al., 1998 and Li et al., 2008). Furthermore, depletion of KMP11 using RNAi has been shown to inhibit segregation of the BB and cytokinesis (Li and Wang, 2008). Interestingly, it has been previously shown that polarity and dynamics of microtubules in trypanosomes control the positioning, segregation, and cytokinesis of organelles (Robinson et al., 1995).

1.9. Vesicle trafficking and protein imports

In eukaryotic cells, most of the proteins are secreted via a conventional pathway in which proteins enter the ER lumen first, then the Golgi apparatus, and finally cross the plasma membrane. Consequently, a huge amount of vesicle transport happens constantly across the cell carrying proteins to be delivered to their target sites. For this, vesicle budding from the donor membrane and subsequent vesicle fusion to the target membrane occur (Rothman, 2013). There are several proteins involved in these processes. One of the key proteins involved in the membrane fusion is a soluble N-ethylmaleimide-sensitive factor attachment protein receptor (SNARE) (Söllner et al., 1993a and Hanson et al., 1997). There are two types of SNAREs: t-SNARE, associated with the target membrane and v-SNARE, on the vesicle membrane (Söllner et al., 1993a and Söllner et al., 1993b). Further, depending on which amino acid residue is involved in interaction, they have been named as R-SNARE (for arginine) and Q-SNARE (for glutamine) (Bas et al., 2018 and Bruinsma et al., 2018). For a membrane fusion to occur, two membranes come close and form a zip-like structure. For this, one R-SNARE interacts with three Q-SNAREs via their α-helical structures bringing two membranes in close contact, forming a trans-SNARE complex named ‘SNAREpin’. This is followed by hemifusion and fusion, and finally the membrane relaxes (Söllner et al., 1993a; Söllner et al., 1993b; Chen & Scheller, 2001; Jahn & Scheller, 2006 and Jahn et al., 2024). In eukaryotes, Sec22 is an important example of R-SNARE present on vesicles (acts here as a v-SNARE) during anterograde transport (vesicle movement from the ER to the Golgi) and

retrograde transport (from the Golgi to the ER) (Flanagan et al., 2015; Li et al., 2015b and Zhao et al., 2015).

In trypanosomatids, a plethora of SNARE proteins have also been identified by phylogenetic analysis, for example, in *Trypanosoma* spp. and *Leishmania* sp. For some trypanosome SNAREs such as *Tb*Syn5, *Tb*Syn16B, and *Tb*VAMP7C differential subcellular localizations have been shown. Overall, trypanosomatid SNAREs show a high level of conservation in their number and identity and some show conservation across the whole eukaryotic lineage (Murungi et al., 2014 and Venkatesh et al., 2017).

Moreover, some SNARE-like proteins have also been identified in intravacuolar bacterial pathogens (Chatterjee et al., 2024), for example, SipA in *Salmonella* (Singh et al., 2018), LegCs and IcmG/DotF in *Legionella* (Paumet et a., 2009 and Shi et al., 2016), and IncA in *Chlamydia* (Delevoye et al., 2008). These proteins are localized on the membrane of the bacterial pathogen-containing host vacuoles. These proteins have SNARE inhibitory function and thus hijack the host intracellular trafficking and promote their own survival in the vacuole.

1.10. Aims of this thesis

As described above, *A. deanei* has recently been established as a model system for studying endosymbiosis, aided by its fast-doubling time in culture, sequenced host and ES genomes, and available genetic tools. The highly reduced ES genome size and synchronization of the host and the ES cell cycles suggested an unusually advanced level of the ES integration. To gain first insights into the molecular mechanisms that may guide host-symbiont interactions, initially, I participated in a team effort aiming at determining the extent of protein targeting from the host to the ES. In this study, seven host-encoded ETPs were identified (see publication I, result section).

The primary goal of my thesis was next to illuminate the role of ETPs in the molecular mechanisms of host-symbiont interaction. To this end, I specifically aimed at the following objectives:

Aim I: to study the subcellular localization of the host-encoded ETP9, ETP2, and ETP7 throughout cell cycle stages together with the ES-encoded FtsZ.

Aim II: to investigate cellular functions of ETP9, ETP2, ETP7, ETP1, and ETP5 in *A. deanei* using different approaches such as knockout and knockdown studies.

Aim III: to gain first insights into the question if SNARE proteins may be involved in mediating vesicle fusions to the ES in the context of ETP3 and ETP8 import.

2. Results

2.1. Results: Publications and manuscripts

2.1.1. Publication I

Morales, J.*, Ehret, G.*, Poschmann, G., Reinicke, T., **Maurya, A.K.,** Kröninger, L., Zanini, D., Wolters, R., Kalyanaraman, D., Krakovka, M., Bäumers, M., Stühler, K., and Nowack, E.C.M. (2023). Host-symbiont interactions in *Angomonas deanei* include the evolution of a host-derived dynamin ring around the endosymbiont division site. *Current Biology*, 33(1), 28-40.

To explore the intricate molecular interactions between *A. deanei* and its ES, the level of integration of the ES in the host, and the extent of protein import from the host to the ES, Morales et al. performed proteome analyses of whole cell lysates and isolated ES fractions using protein mass spectrometry. Nucleus-encoded proteins that appeared enriched in ES fractions were considered as ETP candidates. Candidates were fused to fluorescent marker proteins and their subcellular localization established by microscopy. Using this approach, the team found seven ETPs that are transported to the ES and are likely involved in the host-endosymbiont interaction.

My contribution to Morales* and Ehret* et al., 2023, Current Biology. [* Equal authorship]

- To show more representative confocal images of ETP5 subcellular localization, Georg Ehret and I performed confocal microscopy leading to Fig. S2 B. The resulting data showed that ETP5 exhibited a similar localization pattern in all images.
- To show if the dot-like fluorescent signal of ETP5 next to the kinetoplast is the BB, I performed an immunofluorescence assay (IFA) for co-localization studies of eGFP-ETP5 and alpha tubulin of the BB resulting in Fig. S2 C. The outcome suggested a clear co-localization of ETP5 (dot-like signal next to the kinetoplast) and the BB.
- To investigate that an additional fluorescence signal of ETP8 as a dot-like structure positioned next to the nucleus is a Golgi structure, I together with Georg Ehret supervised Lucie Hansen's B.Sc. project (2022) for a co-localization study of ETP8-eGFP and a trans-Golgi marker ARL1 tagged with V5 at the C-terminus of the protein (detected with an α-V5 antibody) yielding Fig. S2 D. The data confirmed a partial co-localization of ETP8 and ARL1 suggesting that ETP8 is also localized in the Golgi apparatus and likely transported to the ES via the Golgi network.
- To verify the correct genomic insertion of pAdea303 (generated by me) leading to the generation of heterozygous *etp9* mutant in the symbiotic *A. deanei* strain (Adea341, generated by me), I performed a Southern blot analysis resulting in Fig. S3 D. The data showed a correct insertion and successful generation of the mutant.

Article

Current Biology

Host-symbiont interactions in *Angomonas deanei* include the evolution of a host-derived dynamin ring around the endosymbiont division site

Highlights

- The proteome of *Angomonas deanei* was characterized by mass spectrometry
- Seven host proteins targeted to its bacterial endosymbiont were identified
- Three host proteins apparently form part of the endosymbiont division machinery
- Modifications of the glycosome metabolism seem to support symbiont integration

Authors

Jorge Morales, Georg Ehret, Gereon Poschmann, ..., Miriam Bäumers, Kai Stühler, Eva C.M. Nowack

Correspondence

e.nowack@hhu.de

In brief

Morales et al. characterize the proteome of the symbiont-bearing trypanosomatid *Angomonas deanei* by mass spectrometry. Expressing fluorescent fusion proteins, they demonstrate the recruitment of various host proteins to distinct sites in the bacterial symbiont. These proteins include three proteins that form a putative symbiont division machinery.

Morales et al., 2023, Current Biology *33*, 28–40
January 9, 2023
https://doi.org/10.1016/j.cub.2022.11.020

CellPress

CellPress

Current Biology

Article

Host-symbiont interactions in *Angomonas deanei* include the evolution of a host-derived dynamin ring around the endosymbiont division site

Jorge Morales,[1,8,10] Georg Ehret,[1,9,10] Gereon Poschmann,[2] Tobias Reinicke,[1] Anay K. Maurya,[1] Lena Kröninger,[1] Davide Zanini,[1] Rebecca Wolters,[1,5] Dhevi Kalyanaraman,[1,6] Michael Krakovka,[1,7] Miriam Bäumers,[3] Kai Stühler,[2,4] and Eva C.M. Nowack[1,11,12,*]

[1]Institute of Microbial Cell Biology, Department of Biology, Heinrich Heine University Düsseldorf, Universitätsstr. 1, 40225 Düsseldorf, Germany

[2]Institute of Molecular Medicine, Proteome Research, Medical Faculty and University Hospital, Heinrich Heine University Düsseldorf, Universitätsstr. 1, 40225 Düsseldorf, Germany

[3]Center for Advanced Imaging, Heinrich Heine University Düsseldorf, Universitätsstr. 1, 40225 Düsseldorf, Germany

[4]Molecular Proteomics Laboratory, Biological and Medical Research Centre (BMFZ), Heinrich Heine University Düsseldorf, Universitätsstr 1, 40225 Düsseldorf, Germany

[5]Present address: School of Molecular Science, The University of Western Australia, 35 Stirling Hwy, Perth, WA 6009, Australia

[6]Present address: Institute for Evolution and Biodiversity, Faculty of Biology, University of Münster, Hüfferstr. 1, 48149 Münster, Germany

[7]Present address: Institute of Cell Dynamics and Imaging, Faculty of Medicine, University of Münster, Von-Esmarch-Str. 56, 48149 Münster, Germany

[8]Present address: Envigo RMS GmbH, Grafenberger Allee 337 b, 40235 Düsseldorf, Germany

[9]Present address: Biotrend Chemikalien GmbH, Wilhelm-Mauser-Str. 41-43, 50827 Köln, Germany

[10]These authors contributed equally

[11]Twitter: @eva_nowack

[12]Lead contact

*Correspondence: e.nowack@hhu.de

https://doi.org/10.1016/j.cub.2022.11.020

SUMMARY

The trypanosomatid *Angomonas deanei* is a model to study endosymbiosis. Each cell contains a single β-proteobacterial endosymbiont that divides at a defined point in the host cell cycle and contributes essential metabolites to the host metabolism. Additionally, one endosymbiont gene, encoding an ornithine cyclodeaminase (OCD), was transferred by endosymbiotic gene transfer (EGT) to the nucleus. However, the molecular mechanisms mediating the intricate host/symbiont interactions are largely unexplored. Here, we used protein mass spectrometry to identify nucleus-encoded proteins that co-purify with the endosymbiont. Expression of fluorescent fusion constructs of these proteins in *A. deanei* confirmed seven host proteins to be recruited to specific sites within the endosymbiont. These endosymbiont-targeted proteins (ETPs) include two proteins annotated as dynamin-like protein and peptidoglycan hydrolase that form a ring-shaped structure around the endosymbiont division site that remarkably resembles organellar division machineries. The EGT-derived OCD was not among the ETPs, but instead localizes to the glycosome, likely enabling proline production in the glycosome. We hypothesize that recalibration of the metabolic capacity of the glycosomes that are closely associated with the endosymbiont helps to supply the endosymbiont with metabolites it is auxotrophic for and thus supports the integration of host and endosymbiont metabolic networks. Hence, scrutiny of endosymbiosis-induced protein re-localization patterns in *A. deanei* yielded profound insights into how an endosymbiotic relationship can stabilize and deepen over time far beyond the level of metabolite exchange.

INTRODUCTION

The transformation of endosymbiotic bacteria into genetically integrated organelles was central to eukaryote evolution. During organellogenesis, control over endosymbiont (ES) division, proteome composition, and physiology largely shifted from the ES to the host cell nucleus. To understand the order and timing of events underpinning organellogenesis, novel model systems are required. Besides the ancient endosymbiotic events that initiated the evolution of mitochondria and plastids more than one billion years ago, diverse bacterial lineages have evolved intimate endosymbiotic associations with eukaryotic hosts, often involving vertical ES transmission from one host generation to the next.[1–3] Similar to how eukaryotes control organelle abundance, some protist hosts have additionally evolved the ability to strictly control the number of ESs per host cell.[4–6] Over time,

Current Biology
Article

CellPress

permanent host association results in gene losses and size reduction of ES genomes.[7,8] In these cases, the holobiont appears to rely on chimeric metabolic pathways involving enzymes encoded in both the ES and host genomes.[9–16] However, the molecular mechanisms enabling cross-compartment linkage of metabolic pathways, synchronization of host and ES cell cycles, and controlled ES segregation are largely unknown.

The most critical step in ES-to-organelle conversion supposedly is the evolution of a dedicated protein translocation system enabling import of nucleus-encoded proteins into the ES.[17,18] The cases of the cercozoan amoeba *Paulinella* where hundreds of nucleus-encoded proteins are imported into the cyanobacterial ES[19] and mealybug insects where peptidoglycan (PG) biosynthesis in the innermost of two nested bacterial ESs depends on the import of a nucleus-encoded D-Ala-D-Ala ligase[20] suggest that organellogenesis events are not restricted to mitochondria and plastids but can occur in more recently established endosymbiotic associations too. Also, in a few other endosymbiotic associations, there are scattered reports on single host proteins that translocate into the ES cytoplasm.[21,22] Deciphering the rules underpinning the evolution of host control over a bacterial ES and ES-to-organelle transition would depend on the proteomic characterization of further endosymbiotic associations and the development of efficient genetically tractable model systems for endosymbiosis.

The trypanosomatid *A. deanei* (subfamily Strigomonadinae) is an emerging endosymbiosis model.[23,24] All members of the Strigomonadinae are monoxenous flagellates that live as parasites or commensals in the digestive tracts of heteropteran and dipteran insects.[24,25] A distinctive feature of the Strigomonadinae is that all members carry a β-proteobacterial ES (family Alcaligenaceae).[24,25] This common ES was likely acquired in a single initiating endosymbiotic event, but within the genus *Angomonas*, interspecific ES transfers have been documented.[26,27] *Candidatus* Kinetoplastibacterium crithidii, the ES of *A. deanei*, lies surrounded by the bacterial inner and outer membranes and a reduced PG layer free in the host cytosol.[28] The cell cycle of host and ES are strictly synchronized, starting with the division of the ES, followed by the subsequent division of host cell basal body, kinetoplast, and nucleus.[5] The segregation of one copy of each genetic compartment to the daughter cell results in strictly one ES per host cell when cytokinesis is completed.

In accord with the obligately endosymbiotic lifestyle of *Ca.* K. crithidii, its genome (0.8 Mbp) is highly streamlined. It lost most genes for the core energy metabolism and the biosynthetic capacity for amino acids and cofactors such as proline, cysteine, and biotin; other biosynthetic pathways (e.g., for aromatic amino acids, riboflavin, and heme) were retained and apparently contributed to the host metabolism.[9,29–31] Whether gaps in metabolic pathways in the ES can be filled by the import of nucleus-encoded proteins (e.g., import of the endosymbiotic gene transfer [EGT]-derived ornithine cyclodeaminase [OCD] that converts ornithine into proline[9]) is unknown.

To enable scrutiny of host/ES interactions, we previously developed genetic tools for *A. deanei* that allow for transgene expression and targeted gene knockouts (KOs).[32] Furthermore, we identified one nucleus-encoded protein of unknown function, termed ES-targeted protein 1 (ETP1), that specifically localizes to the ES,[32] suggesting that protein targeting to the ES plays a role in host/ES interaction. However, the extent of protein targeting to the ES, the underlying targeting mechanism, and its functional relevance are unclear.

Using a combination of proteomics and expression analysis of fluorescent marker protein fusions, here, we identified six new ETPs in *A. deanei*. These host proteins localize to distinct sites within the ES including a ring-shaped structure surrounding the ES division site that remarkably resembles organellar division machineries. The EGT-derived OCD acquired a new localization in the ES-associated glycosomes likely supporting the linkage of host and ES metabolic networks.

RESULTS

Identification of candidate ETPs by protein mass spectrometry

To determine the extent of protein import into *Ca.* K. crithidii, we analyzed proteins extracted from isolated ESs (ES samples) (Figures 1A and 1B) and whole-cell lysates (WC samples) by liquid chromatography coupled to tandem mass spectrometry (LC-MS/MS). Two independent proteomic analyses totaling 9 biological replicates detected with high confidence 573 and 638 ES-encoded proteins overall (i.e., 78% and 87% of the 730 predicted ES-encoded proteins[29]) and 2,646 and 2,175 host-encoded proteins (i.e., 26% and 21% of the 10,365 predicted nucleus-encoded proteins[33]), respectively (Table S1; search data are provided in the PRIDE archive: PXD017908). Proteins identified exclusively or appearing enriched in ES samples comprised not only ES-encoded but also several host-encoded proteins (Figures 1C and 1D).

Host-encoded proteins that either showed significant enrichment in ES samples in both experiments (red crosses in Figures 1C and 1D) or showed significant enrichment in one experiment but were not detected at all or showed only nonsignificant enrichment in ES samples in the other experiment (orange crosses in Figures 1C and 1D) were considered putative ETPs. This group of 14 putative ETPs (for details, see Table S2) also contained the previously identified ETP1.[32] Host-encoded proteins that appeared as ES-enriched in one experiment but as ES-depleted in the other experiment (yellow crosses in Figures 1C and 1D) contained several predicted glycosomal or mitochondrial proteins. Thus, this group of proteins was regarded putative contaminants and was not further analyzed.

Localization studies of fluorescent reporter protein fusions establish seven ETPs

Next, we aimed to determine the subcellular localization of each of the 13 newly identified candidate ETPs in *A. deanei* using recombinant reporter protein fusions. We have previously demonstrated by a combination of fluorescence *in situ* hybridization (FISH) using a bacterium-specific probe and immunofluorescence analysis (IFA) that ETP1 N- or C-terminally fused to the green fluorescent protein eGFP localized specifically to *Ca.* K. crithidii.[32] The same localization was observed by IFA of *A. deanei* cell lines expressing ETP1 N- or C-terminally fused to the simian virus 5-derived small epitope V5 tag (V5-ETP1 and ETP1-V5, respectively) (Figure 2A). Immunogold transmission electron microscopic (TEM) analysis demonstrates V5-ETP1 to be restricted to the envelope of *Ca.* K. crithidii, making

CellPress

Current Biology
Article

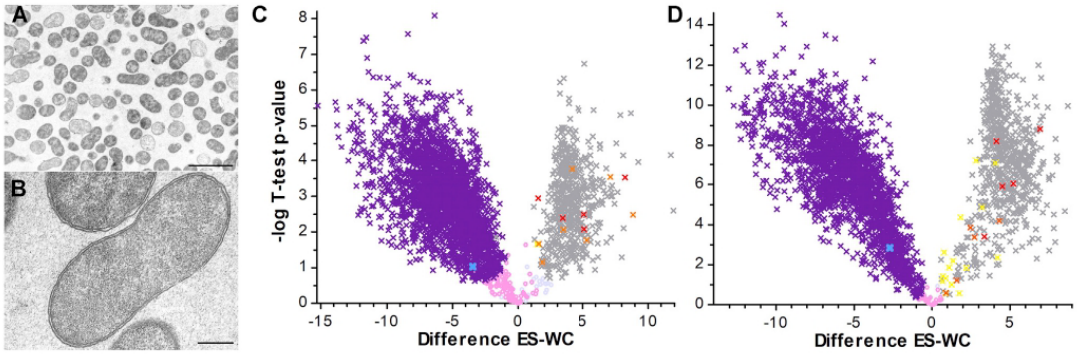

**Figure 1. Proteome analysis of *A. deanei* whole-cell lysates (WC) and purified endosymbionts (ESs)
(A and B) TEM of *Ca.* K. crithidii.**
(A) Overview of the collected endosymbiont fraction. Most of the structures observed in this fraction are peanut-shaped or round and surrounded by a double membrane consistent with the endosymbiont. Scale bar, 2.5 μm.
(B) Outer and inner endosymbiont membranes remained intact in most cells during isolation. Scale bar, 250 nm.
(C and D) Volcano plots of proteins identified by LC-MS/MS in experiment 1 (C) and experiment 2 (D). The difference of intensities of individual proteins between WC and ES samples ($(\overline{log2(norm\ Int_{ES})} - \overline{log2(norm\ Int_{WC})})$) is plotted against significance ($-\log_{10}$ p value in Student's t test). Gray, endosymbiont-encoded proteins; colorful, nucleus-encoded proteins (for details of the color code, see the main text). Crosses in bright colors, significant; circles in pale colors, nonsignificant values.
See also Tables S1 and S2.

ETP1 a marker that precisely outlines the shape of the ES (Figure 2B). Therefore, a cell line expressing ETP1 fused to the C terminus of the red fluorescent protein mScarlet (mS-ETP1) was used as background for co-expression of the remaining 13 proteins of interest (POIs) fused to the C or Nterminus of eGFP (eGFP-POI and POI-eGFP, respectively). Western blot analyses of whole-cell lysates and purified ESs (up to the percoll step) obtained from the 13 cell lines co-expressing mS-ETP1 and each one of the eGFP-POI constructs showed that recombinant ETP1, ETP2, ETP3, ETP5, and ETP7 are enriched in the ES fraction, whereas recombinant ETP8 and ETP9 co-purify to a certain extent with the ES (Figure 2C). Apparent sizes of these proteins roughly correspond to their estimated molecular weights, only mS-ETP1 appears at ~80 kDa slightly higher than expected (69 kDa; Table S2). For the remaining candidate ETPs, neither N-terminal nor C-terminal fusion constructs showed a signal in the ES fraction or (for one protein) no signal in the western blot at all (Figure S1). Hence, these proteins were excluded from further analyses.

Localization of ETP2, ETP3, ETP5, ETP7, ETP8, and ETP9 at the ES was further confirmed by epifluorescence microscopy (Figure 2D). Interestingly, the various ETPs localize to specific sites within the ES. Recombinant ETP2, ETP7, and ETP9 localize specifically at the constriction site of the peanut-shaped ES; ETP5 localizes to the ES and structures toward the anterior end of the host cell; ETP3 and ETP8 show a diffuse eGFP signal over the ES and additionally in a defined dot-like structure near the host cell nucleus (Figure 2D). Shifting the eGFP-tag to the C terminus did not affect the localization of ETP2, ETP5, ETP7, ETP8, and ETP9; only ETP3-eGFP did not yield any fluorescence signal (Figure S2A).

3D reconstruction of the fluorescence signal of each recombinant ETP obtained from focal planes of confocal fluorescence microscopy (Figure 2E; Video S1) revealed that ETP2, ETP7, and ETP9 form a ring-shaped structure around the constriction site of the ES (i.e., the site where ES division occurs); ETP5 localizes at the anterior end of the host cell flagellar pocket (approximately around the flagellar exit point) from where thin fiber-like projections surround the periphery of the ES and seem to associate with the host cell kinetoplast and nucleus; IFA with anti α-tubulin primary antibody co-localizes ETP5 in particular with the kinetoplast-attached basal body (Figures S2B and S2C). ETP3 and ETP8 show a fluorescence pattern that suggests their localization inside the ES. Interestingly, ETP3 and ETP8 are additionally found in a dot or barbell-shaped structure that sits on the anterior side of the nucleus. This structure is similar in shape and positioning to the Golgi apparatus of *Trypanosoma brucei* and *Leishmania donovani*[34,35] and co-localization analysis of ETP8-eGFP with the *trans* Golgi network (TGN) marker ARL1-V5[35] shows the extra endosymbiotic recombinant ETP8 strictly next and partially overlapping with recombinant ARL1 (Figure S2D). However, neither ETP3 nor ETP8 (or any of the other ETPs) contain a predicted targeting signal for the secretory pathway (nor the mitochondrion), all are soluble, and contain no obvious common characteristics such as similar sequence extensions or motifs (as analyzed by MEME 5.0.5[36]; cut-off: e value < 0.05) that could serve as targeting signals.

Subcellular localization and homology-based annotations suggest ETPs to be involved in distinct cellular processes

To explore the cellular functions of the ETPs, we aimed to generate null mutants of ETP1, ETP2, ETP7, and ETP9. However, although heterozygous KO mutants could be obtained (for southern blot results, see Figure S3), deletion of both alleles of the corresponding genes did not yield any viable clones after several attempts suggesting an essential function of these proteins. Since no inducible gene expression systems are available

Current Biology
Article

CellPress

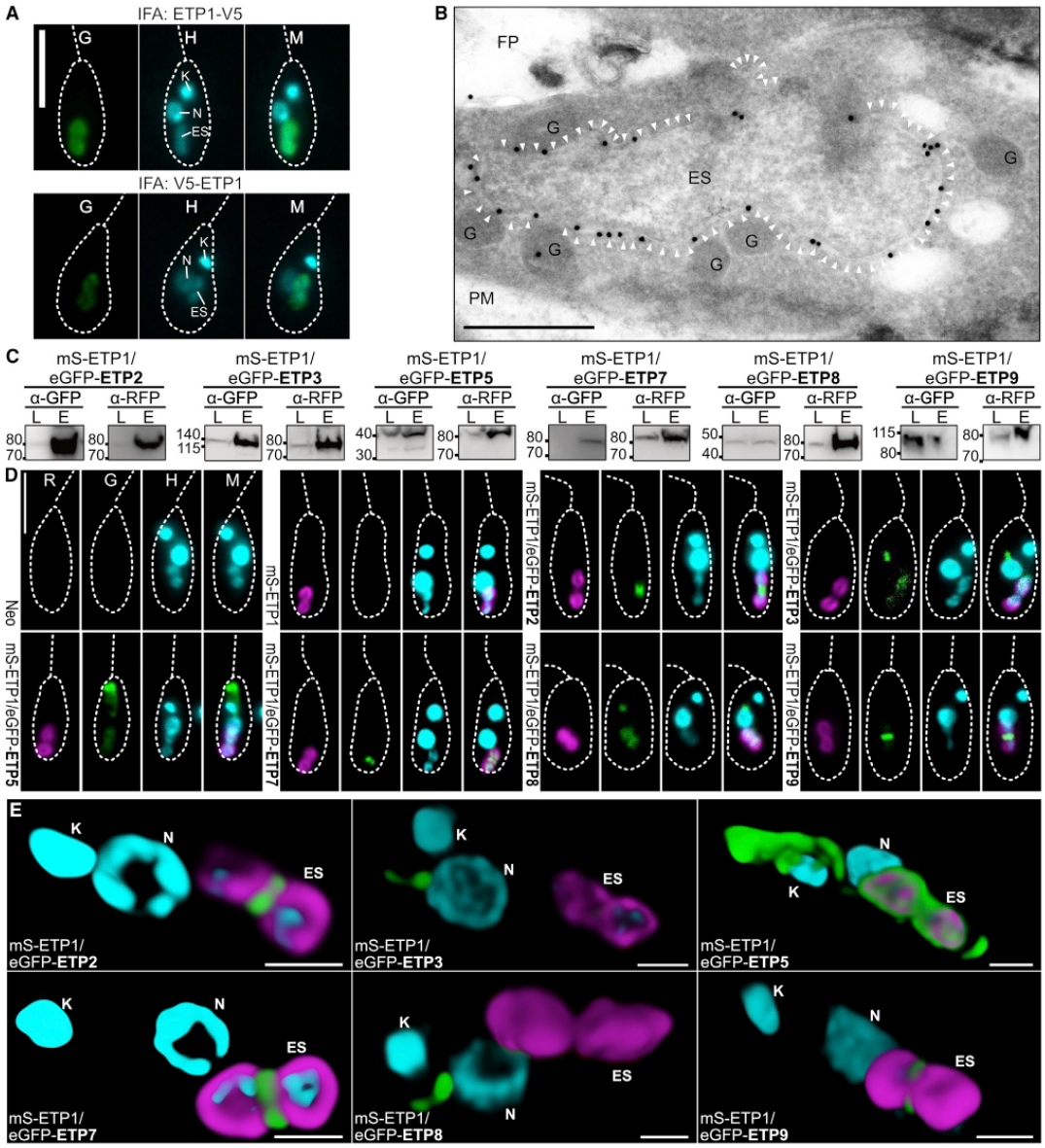

Figure 2. ETPs show distinct subcellular localizations

(A) ETP1-V5 and V5-ETP1-expressing cells were analyzed by IFA using anti-V5 (α-V5) primary antibody with a secondary antibody conjugated to Alexa Fluor 488 (green channel). Scale bar, 5 μm.

(B) Immunogold electron micrograph of a cross-sectioned endosymbiont in the context of a V5-ETP1-expressing *A. deanei* cell labeled with α-V5 (mouse), α-mouse-IgG (rabbit), and protein A conjugated to 15 nm gold particles. White arrowheads highlight the endosymbiont outer membrane. Crisp black dots correspond to 15 nm gold particles. Scale bar, 500 nm.

(C) Recombinant proteins in whole-cell lysate (L) or purified endosymbionts (E) were analyzed by western blot using anti-GFP or anti-RFP antibodies.

(D) Epifluorescence microscopic analysis of cell lines expressing the neomycin phosphotransferase (Neo) alone, mS-ETP1, or mS-ETP1 in combination with eGFP-POIs. Cell shape is indicated by white dashed lines. R, red channel (visualizing mS); G, green channel (visualizing eGFP); H, blue channel (visualizing Hoechst 33342); M, merge of the fluorescence channels. Scale bar, 5 μm.

(legend continued on next page)

yet for *A. deanei*, a detailed functional characterization of these genes is yet to come.

Nevertheless, for several ETPs, observed subcellular localizations and functional annotations (Table 1) imply their involvement in distinct cellular processes. The ring-shaped arrangement of ETP2, ETP7, and ETP9 around the ES division site is suggestive of a function in ES division. For all three recombinant proteins, this ring structure is seen in nearly half of the cells in a mid-log phase culture (Figure 3A). The function of ETP2, which shows neither amino acid sequence nor structural similarity to known proteins and is predicted to be mainly unstructured, remains unclear. ETP7, however, is annotated as "phage tale lysozyme." Although sequence identity between both proteins is only 24%, Phyre2[37] predicts with 92.6% confidence structural homology of the C-terminal part of ETP7 (aa 358–518) to the PG-hydrolyzing N-terminal domain (NTD) of the bacteriophage φ29 protein gp13.[38] Importantly, the structural comparison of the two proteins revealed that the catalytically active glutamic acid that is invariably found in the catalytic center of lysozymes is conserved in ETP7 (i.e., E369 in ETP7, corresponding to E45 of gp13) as is a conserved loop in close proximity of the catalytic site (Figures 3B and 3C; Data S2).

ETP9 is annotated as "dynamin family protein." Members of the dynamin family are self-assembling, polymer-forming GTPases that are involved in diverse cellular membrane remodeling events. Although many organisms contain multiple, functionally specialized dynamin family proteins,[42] trypanosomatids outside the Strigomonadinae typically encode only one dynamin-like protein (DLP).[43] Only *Trypanosoma brucei* contains two tandemly duplicated DLPs, *Tb*DLP1 and *Tb*DLP2, which are almost identical except a few amino acid substitutions.[41,44] These proteins are involved in both, mitochondrion division and endocytosis,[41,43,44] and seem to play complementary roles at least in the insect procyclic form.[41] In *A. deanei*, we find besides ETP9 (CAD2212698.1), which is highly divergent in sequence compared with other trypanosomatid DLPs (34% identity to *Tb*DLPs), the typical trypanosomatid DLP ortholog, *Ad*DLP (CAD2218610.1; 68% identity to *Tb*DLPs) (Figures 3D–3F). Importantly, although trypanosomatids outside the ES-harboring Strigomonadinae lack a copy of ETP9, in *Strigomonas culicis*,[45] another member of the Strigomonadinae, proteins similar to both *Ad*DLP and *Ad*ETP9 were identified in the draft genome. We refer to these proteins as *Stc*DLP and *Stc*ETP9, respectively.

Phylogenetic analysis of Euglenozoan DLPs recovers *Ad*ETP9 and *Stc*ETP9 as well as *Ad*DLP and *Stc*DLP as sisters with 100% and 98% UFBoot2 support, respectively (Figure 3D). Both ortholog pairs fall within the kinetoplastid DLPs that form a monophyletic group within the Euglenozoan DLPs. However, although *Ad*DLP is positioned in a well-supported clade containing other trypanosomatid DLPs, the ETP9 orthologs form a very long branch that is grouped (without UFBoot2 support) together with the bodonid *B. saltans*, a free-living close relative of the trypanosomatids.

Also, in a eukaryote-wide phylogenetic analysis including members of the dynamin family of Alveolates, Amoebozoa, Archaeplastida, Excavata, Opisthokonta, and Stramenopiles, the kinetoplastid DLPs including *Ad*ETP9 and *Stc*ETP9 form a monophyletic group. This group is closest to the *Dictyostelium discoideum* protein DymB (which has been reported to affect events at the plasma membrane, peroxisomes, contractile vacuole system, cytoskeleton, and cell adhesion sites[46]) and close to further DLPs involved in vesicle trafficking (Vps1p proteins) as well as mitochondrial and peroxisomal division (including the well-studied yeast Dnm1p and human DRP1) (Figure 3E). This placement is in congruence with previous phylogenetic analyses.[43] However, neither positioning of the kinetoplastid DLP clade nor its monophyly received a robust UFBoot2 support (i.e., values at these branches are <95%).

Despite low sequence conservation, *Ad*ETP9 and *Stc*ETP9 show the same domain organization as DRP1 and Dnm1p (human/yeast) and *T. brucei* DLPs.[41,43] The highly conserved N-terminal GTPase domain, which mediates GTP binding and hydrolysis, is followed by a middle domain, a variable region (that is in DRP1/Dnm1p referred to as insert B), and a C-terminal GTPase effector domain (GED) (Figure 3F). Middle domain and GED of DLPs together form a "stalk," which contains several interfaces important for protein oligomerization.[47]

ETP5 shows high sequence identity (94%) to the "kinetoplastid membrane protein 11" (KMP-11) of *T. cruzi*, which is highly conserved across trypanosomatids.[48] As in other trypanosomatids, ETP5 is encoded by a multicopy gene and occurs in four tandemly arranged identical gene copies. In *T. brucei*, *T. cruzi*, and *Leishmania infantum*, KMP-11 localizes to the basal body, flagellar pocket, and flagellum[49,50] and associates with microtubules.[51] Although its exact cellular function is unknown, its depletion blocks cytokinesis in *T. brucei*.[52]

ETP1, ETP3, and ETP8 are annotated as hypothetical proteins. Blastp searches against the NCBI non-redundant (nr) database returned either no similar proteins from other organisms (for ETP1) or exclusively proteins of unknown function for ETP3 and ETP8 (Table 1). 3D structure prediction using Phyre2 revealed either no significant similarities to any known protein structures (for ETP1 and ETP8) or, with confidence levels >96%, similarity to several long stretched α-helical proteins with diverse functions such as muscle contraction, PG hydrolysis, or chromosome maintenance. Hence, predicting the cellular function of these proteins is impossible based on the data at hand.

The EGT-derived OCD re-localized to the glycosome

Finally, the EGT-derived OCD (blue cross in Figures 1C and 1D) was not among the candidate ETPs. Examination of the OCD amino acid sequence revealed that following EGT, the protein acquired a peroxisomal targeting sequence type 1 (PTS1) in all members of the Strigomonadinae (Figure 4A), suggesting localization to the glycosome, a specialized peroxisome in trypanosomatids characterized by the presence of the first six or seven steps of glycolysis. Interestingly, glycosomes closely associate with the ES in the Strigomonadinae[23,53] (Figures 2B and 4B). To visualize glycosomes by epifluorescence microscopy, we

(E) Three-dimensional reconstruction of the localization of the recombinant ETPs from the superposition of 12–32 confocal images of z stacks after deconvolution. Scale bars, 1 μm. ES, endosymbiont; K, kinetoplast; N, nucleus.
See also Figures S1–S4, Table S2, Video S1, and Data S1.

Current Biology
Article

CellPress

Table 1. Endosymbiont-targeted proteins in *A. deanei*

ETP	Annotation	Best BLASTp hit[a]	e value	%Id[b]	BBH[c]
ETP1	hypothetical protein, cons.	–	–	–	–
ETP2	hypothetical protein, cons.	–	–	–	–
ETP3	hypothetical protein, cons.	hypothetical protein JIQ42_00906 (*Leishmania* sp. Namibia)	2e−19	26	no
ETP5	kinetoplastid membrane protein 11, put.	kinetoplastid membrane protein KMP-11 (*Trypanosoma cruzi* strain CL Brener)	7e−52	94	yes
ETP7	phage tail lysozyme, put.	–	–	–	–
ETP8	hypothetical protein, cons.	unnamed protein product (*Phytomonas* sp. isolate EM1)	3e−12	28	yes
ETP9	dynamin family/dynamin central region/ dynamin GTPase effector domain containing protein, putative	unnamed protein product (*Trypanosoma congolense* IL3000)	1e−114	34	no

See also Tables S1 and S2 and Data S1.
[a]Protein with the lowest e value (outside *A. deanei*) returned by BLASTp against the NCBI nr database as of July 14, 2021 (e value cut-off of 1e−6)
[b]Percentage of identity between both proteins
[c]Best bidirectional blast hits between nr database and an in-house database containing the previously generated *A. deanei* transcriptome

expressed the red fluorescent protein mCherry fused to a PTS1 signal (mCherry-SKL) in *A. deanei*, resulting in the dotted fluorescence pattern typical for glycosomal proteins (Figure 4D). Similar fluorescence patterns are observed in cells expressing the known glycosomal surface protein GIM5A fused to eGFP (GIM5A-eGFP, Figure 4E[54]). Co-expression of both markers results in co-localization of the recombinant proteins at the glycosome (Figure 4F). Finally, co-expression of a recombinant protein in which the EGT-derived OCD was fused to the C terminus of eGFP (eGFP-OCD) with the glycosome marker mCherry-SKL resulted in clear co-localization of eGFP-OCD with mCherry-SKL, confirming a glycosomal localization of the recombinant OCD (Figure 4G).

DISCUSSION

Extent of protein targeting to the endosymbiont in *A. deanei*

Ca. K. crithidii reached an astonishing level of cellular integration that is reminiscent of the multilayered integration of an organelle into the biological networks of the surrounding cell. Although aposymbiotic strains of *A. deanei* (and other species within the Strigomonadinae) have been generated by chloramphenicol treatment ~45 years ago,[31,55] we have tried repeatedly without success to obtain aposymbiotic strains from *A. deanei* ATCC PRA-265 growing in brain heart infusion (BHI) medium supplemented with hemin and horse serum using chloramphenicol or diverse other antibiotics cocktails. Although FISH with ES-specific probes initially revealed many cells without ES in antibiotics-treated cultures, after prolonged cultivation periods or after generation of clonal cell lines by limiting dilution, only cells with ES were obtained. The failure to generate aposymbionts suggests that at least in this strain and under the culture conditions used, the presence of the symbiont is obligate.

Despite its organelle-like cellular integration, our proteomic analyses demonstrated that large-scale import of host-encoded proteins into *Ca.* K. crithidii does not occur. However, the establishment and stabilization of the endosymbiotic association was accompanied by the recruitment of specific nucleus-encoded proteins to the ES. Since our MS study applied a relatively strict quality cutoff (STAR Methods), we captured only ~25% of the nucleus-encoded proteins. Furthermore, the identification of ETPs relied on their specific enrichment in the ES fraction discouraging the identification of dually localized proteins. Thus, the actual number of ETPs is likely higher.

Evolution of a putative host-controlled endosymbiont division machinery in *A. deanei*

Arguably, the most remarkable finding concerning the ETPs is the arrangement of three ETPs, ETP2, ETP7, and ETP9, around the ES constriction site (Figures 2D and 2E). The *etp9* gene likely evolved by an ancient duplication and divergence of the typical trypanosomatid *dlp* gene in a common ancestor of *Angomonas* and *Strigomonas* (Figures 3D and 3E). However, *etp9* and *Addlp* localize on different chromosomes and maximum likelihood (ML) analyses failed to establish a sister group relationship likely owing to the high level of sequence divergence, which might cause a long branch attraction artifact.

In the Archaeplastida, a plant-specific dynamin (DRP5B or ARC5) evolved—likely by the duplication and divergence of DRP5A, which is involved in cytokinesis.[40] Upon plastid division, DRP5B is recruited to the plastid division site. This site is defined by the formation of the FtsZ ring on the stromal site of the inner membrane aided by ARC6, an inner envelope membrane-spanning protein of cyanobacterial origin.[56] Through protein-protein interaction in the intermembrane space, ARC6 recruits the eukaryotic protein PDV2 to the plastid which spans the outer membrane; PDV2, finally, recruits DRP5B to the cytosolic side of the outer membrane.[56,57] Reciprocal interactions between the FtsZ-containing constriction ring inside and DRP5B-containing constriction ring outside result in the formation of a functional plastid division machinery.[58]

Also for mitochondria, assembly of Dnm1p/DRP1 (in yeast/human) into helical oligomers on the outer membrane and constriction upon GTP hydrolysis is involved in organelle fission.[59,60] Recruitment of these DLPs to the mitochondrial surface involves the conserved membrane anchor protein, Fis1, as well as several adaptor proteins that are not conserved between yeast and

CellPress

Current Biology
Article

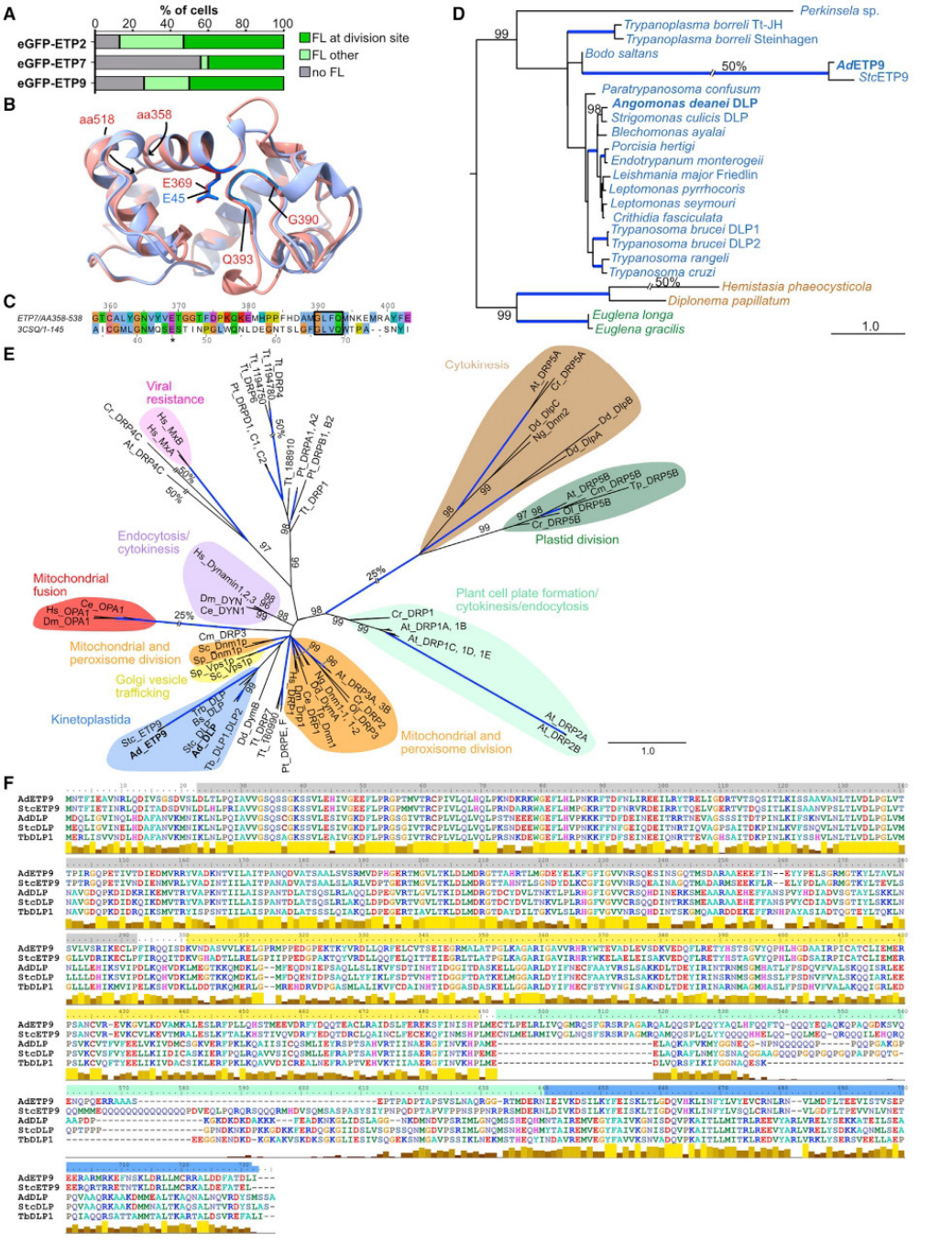

(legend on next page)

Current Biology
Article

CellPress

mammals.[47] The variable insert B domain is predicted to reside at the base of the DLP oligomers, closest to the mitochondrial membrane,[47] and in Dnm1p, a motif in this domain has been identified, which is essential for binding to the mitochondrial Mdv1 adaptor protein.[61] In the light of these data, the high sequence divergence of the variable region of ETP9 from those in the typical trypanosomatid DLPs (Figure 3F) would be congruent with the hypothesis that this region in ETP9 is involved in recognizing the new target membrane possibly via interaction with a so far unknown receptor in the ES outer membrane and/or suitable adaptor proteins.

The predicted function of ETP7 is PG hydrolysis, which is supported by its structural similarity to the phage tail lysozyme pg13. Intriguingly, PG hydrolysis by a nucleus-encoded enzyme that localizes at the plastid division site is also essential for plastid division in the Glaucophyte algae that possess a PG layer between the two envelope membranes and at least in some basally branching Viridiplantae.[62] The lack of amino acid sequence or structural homology of ETP2 to any other known proteins prevents the assignment of a putative function. However, its apparent localization in the putative ES division machinery suggests its involvement in symbiont division.

Ca. K. crithidii encodes FtsZ, a GTPase that typically self-assembles into a ring structure at the inner side of the cytoplasmic membrane at bacterial division sites initiating cytokinesis, and the Min system, which is typically involved in positioning the FtsZ ring.[63] However, antibodies specific against FtsZ distribute evenly throughout *Ca.* K. crithidii,[64] suggesting that its own division machinery might not be fully functional. Furthermore, exposure of *A. deanei* to the eukaryotic translation inhibitor cycloheximide not only results in cessation of host cell growth but also blocks ES division,[65] suggesting the involvement of host-derived factors in ES division.

ETP5 might orchestrate segregation of organelles and the endosymbiont during cytokinesis

The localization of ETP5 suggests that in *A. deanei*, there is a host-derived structure that connects the three DNA-containing compartments (nucleus, mitochondrion, and ES) with the basal body. ETP5 likely interacts with these compartments by direct interaction with their membrane lipids.[66] Importantly, in trypanosomes, division of the basal body marks the transition from G to S phase of the cell cycle.[67] The basal body is physically linked to the kinetoplast through the tripartite attachment complex facilitating positioning and segregation of the replicated mitochondrial genome.[68] Thus, the observed localization of recombinant ETP5 in *A. deanei*, in combination with the cytokinesis defects following the silencing of the ETP5 ortholog KMP-11 in *T. brucei*,[52] suggests that ETP5 plays a role in orchestrating segregation of organelles and cellular structures during cytokinesis.

Protein targeting to the endosymbiont

Most ETPs (ETP1, ETP2, ETP5, ETP7, and ETP9) seem to localize to the ES envelope. Whether these proteins associate with the outer membrane, reside in the ES periplasm, or translocate across the inner membrane is not entirely clear. The observed fluorescence pattern suggests that at least ETP5 resides in a layer outside of the localization of ETP1 (Figure 2E; Video S1). Thus, ETP5 is likely associated with the ES's outer membrane, whereas ETP1 localizes to the periplasm or associates with the inner membrane. The predicted function of ETP7 as PG hydrolase implies a periplasmic localization. The mechanism that potentially enables ETP1 and ETP7 to cross the outer ES membrane is currently unclear.

Fluorescence signals observed for recombinant ETP3 and ETP8 suggest that these proteins localize inside the ES (Video S1). However, more advanced imaging and/or biochemical techniques will be required to unambiguously establish that these two proteins translocate across both ES membranes and reach the ES cytoplasm. Interestingly, ETP3 and ETP8 were additionally observed in a structure sandwiched between nucleus and TGN, indicative of the Golgi. The Golgi is the main hub of vesicular trafficking in eukaryotic cells and in different endosymbiotic associations, nucleus-encoded, ETPs traffic through the Golgi.[22,69–71] However, an important difference in these

Figure 3. ETP2, ETP7, and ETP9 form a putative host-derived endosymbiont division machinery

(A) Subcellular localization of eGFP-ETP2, eGFP-ETP7, and eGFP-ETP9 in cells from a mid-log phase culture. For each cell line, 100 Hoechst 33342-stained cells were analyzed. No FL, no eGFP fluorescence; FL at division site, eGFP fluorescence at endosymbiont division site; FL other, eGFP fluorescence distributed equally over the endosymbiont or restricted to one or both endosymbiont poles.

(B) Superposition of the predicted structure of ETP7 aa 358–518 (red shades) and the pg13 NTD (PDB: 3CSQ[38]; blue shades). The predicted catalytically active glutamic acid (E369) and a conserved loop in close proximity of the active site (G390-Q393) are highlighted. The Phyre2-predicted structure of ETP7 aa 358–518 is provided as a PDB file (Data S2).

(C) Amino acid conservation around E369 in the structure-based sequence alignment of ETP7 and gp13. E369 is marked by an asterisk, and the conserved loop by a black box.

(D and E) ML analyses of dynamin family proteins. Values at branches are ultra-fast bootstrap (UFboot2[39]) support ≥95%; bold branches in blue have 100% support. Indicated branches were reduced to 25% or 50% of their length.

(D) Euglenozoa-wide analysis. Outgroup are the DLPs of Diplonemids (brown) and Euglenids (green). Kinetoplastid DLPs are in blue.

(E) Eukaryote-wide analysis including DLPs of the kinetoplastids *A. deanei* (Ad), *S. culicis* (Stc), *T. brucei* (Tb), *Bodo saltans* (Bs), and *Trypanoplasma borreli* (Trb); the Archaeplastida *Arabidopsis thaliana* (At), *Chlamydomonas reinhardtii* (Cr), *Ostreococcus lucimarinus* (Ot), and *Cyanidioschyzon merolae* (Cm); the Stramenopile *Thalassiosira pseudonana* (Tp); the Amoebozoan *Dictyostelium discoideum* (Dd); the Excavate *Naegleria gruberi* (Ng); the Alveolates *Tetrahymena thermophila* (Tt) and *Paramecium tetraurelia* (Pt); and the Opisthokonts *Saccharomyces cerevisiae* (Sc), *Schizosaccharomyces pombe* (Sp), *Homo sapiens* (Hs), *Drosophila melanogaster* (Dm), and *Caenorhabditis elegans* (Ce). Annotated functions are as provided in Miyagishima et al.[40] and references therein.

(F) Sequence alignment of DLPs from *A. deanei* (*Ad*DLP and *Ad*ETP9), *S. culicis* (*Stc*DLP and *Stc*ETP9), and *T. brucei* (*Tb*DLP1). Colored boxes indicate domain organization: gray, dynamin-type guanine nucleotide-binding domain; blue, GED domain (both as identified by Expasy Prosite scan); yellow, middle (or stalk domain) as defined for *T. brucei* in Benz et al.;[41] green, variable region. The histogram underneath the alignment provides conservation scores reflecting conservation of physico-chemical properties per column.

See also Data S2.

CellPress

Current Biology
Article

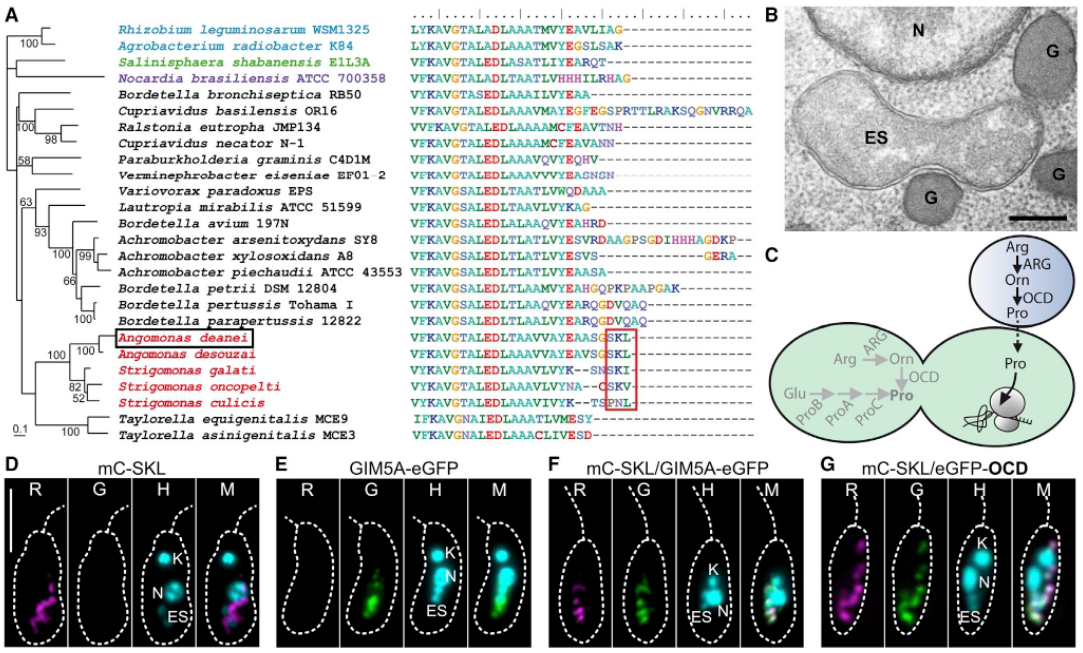

Figure 4. The EGT-derived OCD localizes to the glycosome

(A) Left: ML phylogeny of the OCD. Species names in red, Strigomonadinae; black, β-proteobacteria; green, γ-proteobacteria; blue, α-proteobacteria; violet, actinobacteria (taxon sampling as in Alves et al.[8]). Values at branches are bootstrap support >50%. Right: alignment of the C termini of the corresponding proteins. Red box, PTS1.

(B) TEM of *A. deanei* shows *Ca.* K. crithidii surrounded by glycosomes. Scale bar, 250 nm.

(C) Scheme of proline metabolism in *A. deanei*. Endosymbiont, green; glycosome, blue. Arrows in gray, enzymes missing from the endosymbiont genome; arrows in black, enzymes encoded in the nuclear genome. Dashed arrow, metabolite transport. ARG, arginase (EC:3.5.3.1); OCD, ornithine cyclodeaminase (EC:4.3.1.12); ProB, glutamate 5-kinase (EC:2.7.2.11); ProA, glutamate-5-semialdehyde dehydrogenase (EC:1.2.1.41); ProC, pyrroline-5-carboxylate reductase (EC:1.5.1.2).

(D–G) Epifluorescence microscopic analysis of *A. deanei* cell lines expressing mCherry-SKL (mC-SKL) (D), GIM5A-eGFP (E), mC-SKL and GIM5A-eGFP (F), or eGFP-OCD and mC-SKL (G). Fluorescence channels and cell outlines are as in Figure 2D. Scale bar, 5 μm. ES, endosymbiont; G, glycosome; N, nucleus; K, kinetoplast.

See also Figure S4.

associations is that the outermost membrane surrounding the ES is host derived. Nevertheless, vesicles that appear to fuse with the outer ES membrane have been observed before in electron micrographs of members of the Strigomonadinae.[55] These observations raise the possibility that Golgi-derived vesicles can target *Ca.* K. crithidii in *A. deanei* and confer protein translocation across the ES's outer membrane.

Modification of the glycosome metabolic capacity following endosymbiosis

Finally, the gene product of the only EGT-derived nuclear gene, the OCD, does not localize to the ES but acquired a glycosomal localization (Figure 4). OCD catalyzes the generation of proline from ornithine, which can be formed by the activity of a glycosomal arginase (ARG). Since *Ca.* K. crithidii lost the ability to generate proline[29] (Figure 4C), which is required for protein biosynthesis, a speculative hypothesis is that the proximity of the ES to proline-generating glycosomes supports the metabolic integration of the ES (e.g., by increasing the local proline concentration around the ES to a level at which it can be efficiently taken up by a low-affinity transporter in the ES). Close association of ESs with specific host cell compartments generating metabolites consumed by the ES has been observed also in other systems (e.g., the archaeal and bacterial ESs tightly associated with hydrogenosomes in anerobic ciliates[72–74]). Dynamic interactions of plastids and mitochondria with other cell compartments such as the ER, nucleus, or peroxisomes play a role for the regulation of biogenesis, division, or functioning of these organelles.[75,76]

In sum, we identified seven ETPs in *A. deanei*, representing a combination of typical trypanosomatid proteins and proteins that evolved newly in *A. deanei* or the Strigomonadinae (probably by divergence beyond recognition of pre-existing proteins, proteins acquired by horizontal gene transfer or proteins resulting from gene duplications). Their discrete subcellular localizations within the ES, as well as their functional annotations, suggests their involvement in distinct biological processes. We postulate that convergent to the evolution of the plastid division machinery, a dynamin and PG hydrolase-based host-derived part of the ES

division machinery evolved, which provides *A. deanei* with control over the division of its ES. Despite the capacity of specific nucleus-encoded proteins to associate with the ES, cross-compartment linkage of metabolic pathways seems to rely rather on metabolite shuttling than protein import. Metabolic integration of the ES might be facilitated by the tight association of glycosomes that produce metabolites required by the ES. In conclusion, our work demonstrates that in addition to studying gene presence/absence patterns by genomics, analysis of symbiosis-induced protein re-localization is key to understand the molecular mechanisms guiding endosymbiotic interactions. The results obtained strongly support the emerging pattern that protein targeting to a bacterial ES (possibly including translocation across both bacterial membranes) evolves early during endosymbiosis providing the host with control over the ES.[2]

STAR★METHODS

Detailed methods are provided in the online version of this paper and include the following:

- KEY RESOURCES TABLE
- RESOURCE AVAILABILITY
  - Lead contact
  - Materials availability
  - Data and code availability
- EXPERIMENTAL MODEL AND SUBJECT DETAILS
- METHOD DETAILS
  - Generation of transgenic cell lines
  - Analysis of homologous recombination
  - Endosymbiont isolation
  - TEM
  - Immunogold TEM
  - Proteome analysis and identification of ETPs
  - Rapid amplification of cDNA ends (RACE)
  - Construction of plasmids
  - Bioinformatic analyses of the ETPs
  - Fluorescence microscopy
  - IFA
  - Western blot analyses
- QUANTIFICATION AND STATISTICAL ANALYSIS

SUPPLEMENTAL INFORMATION

Supplemental information can be found online at https://doi.org/10.1016/j.cub.2022.11.020.

ACKNOWLEDGMENTS

This study was supported by Deutsche Forschungsgemeinschaft grant NO 1090/1-1 and NO 1090/1-2 (to E.C.M.N.) and fellowships of the Jürgen Manchot Graduate School "Molecules of Infection" p8, MOI III (to G.E.), and p9, MOI IV (to A.K.M.). The authors acknowledge the Center for Advance Imaging (CAi) at Heinrich Heine University Düsseldorf for providing access to the Leica TCS SP8 (INST 208/805-1 FUGG) and especially Sebastian Hänsch for technical assistance with image deconvolution and 3D reconstructions.

AUTHOR CONTRIBUTIONS

E.C.M.N., J.M., and G.E. designed the research. J.M., G.E., G.P., T.R., A.K.M., L.K., D.Z., R.W., D.K., M.K., and M.B. performed the research. G.E., A.K.M., J.M., G.P., and E.C.M.N. analyzed the data. E.C.M.N. and K.S. supervised the research. J.M., G.E., and E.C.M.N. wrote the manuscript.

DECLARATION OF INTERESTS

The authors declare no competing interests.

Received: June 30, 2022
Revised: September 9, 2022
Accepted: November 9, 2022
Published: December 7, 2022

REFERENCES

1. Dubilier, N., Bergin, C., and Lott, C. (2008). Symbiotic diversity in marine animals: the art of harnessing chemosynthesis. Nat. Rev. Microbiol. *6*, 725–740.
2. Husnik, F., Tashyreva, D., Boscaro, V., George, E.E., Lukeš, J., and Keeling, P.J. (2021). Bacterial and archaeal symbioses with protists. Curr. Biol. *31*, R862–R877.
3. Moya, A., Peretó, J., Gil, R., and Latorre, A. (2008). Learning how to live together: genomic insights into prokaryote-animal symbioses. Nat. Rev. Genet. *9*, 218–229.
4. Brum, F.L., Catta-Preta, C.M., de Souza, W., Schenkman, S., Elias, M.C., and Motta, M.C. (2014). Structural characterization of the cell division cycle in *Strigomonas culicis*, an endosymbiont-bearing trypanosomatid. Microsc. Microanal. *20*, 228–237.
5. Motta, M.C.M., Catta-Preta, C.M.C., Schenkman, S., Martins, A.C.A., Miranda, K., de Souza, W., et al. (2010). The bacterium endosymbiont of *Crithidia deanei* undergoes coordinated division with the host cell nucleus. PLoS One *5*, e12415.
6. Nowack, E.C.M., and Melkonian, M. (2010). Endosymbiotic associations within protists. Philos. Trans. R. Soc. Lond. B Biol. Sci. *365*, 699–712.
7. McCutcheon, J.P. (2010). The bacterial essence of tiny symbiont genomes. Curr. Opin. Microbiol. *13*, 73–78.
8. Nowack, E.C.M., and Weber, A.P.M. (2018). Genomics-informed insights into endosymbiotic organelle evolution in photosynthetic eukaryotes. Annu. Rev. Plant Biol. *69*, 51–84.
9. Alves, J.M.P., Klein, C.C., Da Silva, F.M., Costa-Martins, A.G., Serrano, M.G., Buck, G.A., Vasconcelos, A.T.R., Sagot, M.F., Teixeira, M.M.G., Motta, M.C.M., and Camargo, E.P. (2013). Endosymbiosis in trypanosomatids: the genomic cooperation between bacterium and host in the synthesis of essential amino acids is heavily influenced by multiple horizontal gene transfers. BMC Evol. Biol. *13*, 190.
10. Husnik, F., Nikoh, N., Koga, R., Ross, L., Duncan, R.P., Fujie, M., Tanaka, M., Satoh, N., Bachtrog, D., Wilson, A.C.C., et al. (2013). Horizontal gene transfer from diverse bacteria to an insect genome enables a tripartite nested mealybug symbiosis. Cell *153*, 1567–1578.
11. Luan, J.B., Chen, W.B., Hasegawa, D.K., Simmons, A.M., Wintermantel, W.M., Ling, K.S., Fei, Z.J., Liu, S.S., and Douglas, A.E. (2015). Metabolic coevolution in the bacterial symbiosis of whiteflies and related plant sap-feeding insects. Genome Biol. Evol. *7*, 2635–2647.
12. Nowack, E.C.M., Price, D.C., Bhattacharya, D., Singer, A., Melkonian, M., and Grossman, A.R. (2016). Gene transfers from diverse bacteria compensate for reductive genome evolution in the chromatophore of *Paulinella chromatophora*. Proc. Natl. Acad. Sci. USA *113*, 12214–12219.
13. Sloan, D.B., Warren, J.M., Williams, A.M., Wu, Z.Q., Abdel-Ghany, S.E., Chicco, A.J., and Havird, J.C. (2018). Cytonuclear integration and co-evolution. Nat. Rev. Genet. *19*, 635–648.
14. Zakharova, A., Saura, A., Butenko, A., Podešvová, L., Warmusová, S., Kostygov, A.Y., Nenarokova, A., Lukeš, J., Opperdoes, F.R., and Yurchenko, V. (2021). A new model trypanosomatid, novymonas esmeraldas: genomic perception of its "*Candidatus* Pandoraea novymonadis" endosymbiont. mBio *12*. e0160621.

15. Kostygov, A.Y., Butenko, A., Nenarokova, A., Tashyreva, D., Flegontov, P., Lukeš, J., and Yurchenko, V. (2017). Genome of *Ca*. Pandoraea novymonadis, an endosymbiotic bacterium of the trypanosomatid *Novymonas esmeraldas*. Front. Microbiol. *8*, 1940.

16. Sloan, D.B., Nakabachi, A., Richards, S., Qu, J., Murali, S.C., Gibbs, R.A., and Moran, N.A. (2014). Parallel histories of horizontal gene transfer facilitated extreme reduction of endosymbiont genomes in sap-feeding insects. Mol. Biol. Evol. *31*, 857–871.

17. Cavalier-Smith, T., and Lee, J.J. (1985). Protozoa as hosts for endosymbioses and the conversion of symbionts into organelles. J. Protozool. *32*, 376–379.

18. Nowack, E.C.M. (2014). *Paulinella chromatophora* - rethinking the transition from endosymbiont to organelle. Acta Soc. Bot. Pol. *83*, 387–397.

19. Singer, A., Poschmann, G., Mühlich, C., Valadez-Cano, C., Hänsch, S., Hüren, V., Rensing, S.A., Stühler, K., and Nowack, E.C.M. (2017). Massive protein import into the early evolutionary stage photosynthetic organelle of the amoeba *Paulinella chromatophora*. Curr. Biol. *27*, 2763–2773.e5.

20. Bublitz, D.C., Chadwick, G.L., Magyar, J.S., Sandoz, K.M., Brooks, D.M., Mesnage, S., Ladinsky, M.S., Garber, A.I., Bjorkman, P.J., Orphan, V.J., and McCutcheon, J.P. (2019). Peptidoglycan production by an insect-bacterial mosaic. Cell *179*, 703–712.e7.

21. Login, F.H., Balmand, S., Vallier, A., Vincent-Monégat, C., Vigneron, A., Weiss-Gayet, M., Rochat, D., and Heddi, A. (2011). Antimicrobial peptides keep insect endosymbionts under control. Science *334*, 362–365.

22. Nakabachi, A., Ishida, K., Hongoh, Y., Ohkuma, M., and Miyagishima, S.Y. (2014). Aphid gene of bacterial origin encodes a protein transported to an obligate endosymbiont. Curr. Biol. *24*, R640–R641.

23. Motta, M.C.M. (2010). Endosymbiosis in trypanosomatids as a model to study cell evolution. Open Parasitol. J. *4*, 139–147.

24. Votýpka, J., Kostygov, A.Y., Kraeva, N., Grybchuk-Ieremenko, A., Tesařová, M., Grybchuk, D., Lukeš, J., and Yurchenko, V. (2014). *Kentomonas* gen. n., a new genus of endosymbiont-containing trypanosomatids of Strigomonadinae subfam. Protist *165*, 825–838.

25. Teixeira, M.M.G., Borghesan, T.C., Ferreira, R.C., Santos, M.A., Takata, C.S.A., Campaner, M., Nunes, V.L.B., Milder, R.V., de Souza, W., and Camargo, E.P. (2011). Phylogenetic validation of the genera *Angomonas* and *Strigomonas* of trypanosomatids harboring bacterial endosymbionts with the description of new species of trypanosomatids and of proteobacterial symbionts. Protist *162*, 503–524.

26. Skalický, T., Alves, J.M.P., Morais, A.C., Režnarová, J., Butenko, A., Lukeš, J., Serrano, M.G., Buck, G.A., Teixeira, M.M.G., Camargo, E.P., et al. (2021). Endosymbiont capture, a repeated process of endosymbiont transfer with replacement in trypanosomatids *Angomonas* spp. Pathogens *10*, 702.

27. Borghesan, T.C., Campaner, M., Matsumoto, T.E., Espinosa, O.A., Razafindranaivo, V., Paiva, F., Carranza, J.C., Añez, N., Neves, L., Teixeira, M.M.G., and Camargo, E.P. (2018). Genetic diversity and phylogenetic relationships of coevolving symbiont-harboring insect trypanosomatids, and their Neotropical dispersal by invader african blowflies (Calliphoridae). Front. Microbiol. *9*, 131.

28. Motta, M.C.M., Leal, L.H.M., Souza, W.D., De Almeida, D.F., and Ferreira, L.C.S. (1997). Detection of penicillin-binding proteins in the endosymbiont of the trypanosomatid *Crithidia deanei*. J. Eukaryotic Microbiology *44*, 492–496.

29. Alves, J.M.P., Serrano, M.G., Maia da Silva, F., Voegtly, L.J., Matveyev, A.V., Teixeira, M.M.G., Camargo, E.P., and Buck, G.A. (2013). Genome evolution and phylogenomic analysis of *Candidatus* Kinetoplastibacterium, the betaproteobacterial endosymbionts of *Strigomonas* and *Angomonas*. Genome Biol. Evol. *5*, 338–350.

30. Klein, C.C., Alves, J.M.P., Serrano, M.G., Buck, G.A., Vasconcelos, A.T.R., Sagot, M.-F., Teixeira, M.M.G., Camargo, E.P., and Motta, M.C.M. (2013). Biosynthesis of vitamins and cofactors in bacterium-harbouring trypanosomatids depends on the symbiotic association as revealed by genomic analyses. PLoS One *8*, e79786.

31. Mundim, M.H., and Roitman, I. (1977). Extra nutritional requirements of artificially aposymbiotic *Crithidia deanei*. J. Protozool. *24*, 329–331.

32. Morales, J., Kokkori, S., Weidauer, D., Chapman, J., Goltsman, E., Rokhsar, D., Grossman, A.R., and Nowack, E.C.M. (2016). Development of a toolbox to dissect host-endosymbiont interactions and protein trafficking in the trypanosomatid *Angomonas deanei*. BMC Evol. Biol. *16*, 247.

33. Davey, J.W., Catta-Preta, C.M.C., James, S., Forrester, S., Motta, M.C.M., Ashton, P.D., and Mottram, J.C. (2021). Chromosomal assembly of the nuclear genome of the endosymbiont-bearing trypanosomatid *Angomonas deanei*. G3 (Bethesda) *11*, jkaa018.

34. He, C.Y., Ho, H.H., Malsam, J., Chalouni, C., West, C.M., Ullu, E., Toomre, D., and Warren, G. (2004). Golgi duplication in *Trypanosoma brucei*. J. Cell Biol. *165*, 313–321.

35. Sahin, A., Espiau, B., Tetaud, E., Cuvillier, A., Lartigue, L., Ambit, A., Robinson, D.R., and Merlin, G. (2008). The *Leishmania* ARL-1 and Golgi traffic. PLoS One *3*, e1620.

36. Bailey, T.L., and Elkan, C. (1994). Fitting a mixture model by expectation maximization to discover motifs in biopolymers. Proc. Int. Conf. Intell. Syst. Mol. Biol. *2*, 28–36.

37. Kelley, L.A., Mezulis, S., Yates, C.M., Wass, M.N., and Sternberg, M.J.E. (2015). The Phyre2 web portal for protein modeling, prediction and analysis. Nat. Protoc. *10*, 845–858.

38. Xiang, Y., Morais, M.C., Cohen, D.N., Bowman, V.D., Anderson, D.L., and Rossmann, M.G. (2008). Crystal and cryoEM structural studies of a cell wall degrading enzyme in the bacteriophage phi 29 tail. Proc. Natl. Acad. Sci. USA *105*, 9552–9557.

39. Hoang, D.T., Chernomor, O., Von Haeseler, A., Minh, B.Q., and Vinh, L.S. (2018). UFBoot2: improving the ultrafast bootstrap approximation. Mol. Biol. Evol. *35*, 518–522.

40. Miyagishima, S.Y., Kuwayama, H., Urushihara, H., and Nakanishi, H. (2008). Evolutionary linkage between eukaryotic cytokinesis and chloroplast division by dynamin proteins. Proc. Natl. Acad. Sci. USA *105*, 15202–15207.

41. Benz, C., Stříbrná, E., Hashimi, H., and Lukeš, J. (2017). Dynamin-like proteins in *Trypanosoma brucei*: a division of labour between two paralogs? PLoS One *12*. e0177200.

42. Jimah, J.R., and Hinshaw, J.E. (2019). Structural insights into the mechanism of dynamin superfamily proteins. Trends Cell Biol. *29*, 257–273.

43. Morgan, G.W., Goulding, D., and Field, M.C. (2004). The single dynamin-like protein of *Trypanosoma brucei* regulates mitochondrial division and is not required for endocytosis. J. Biol. Chem. *279*, 10692–10701.

44. Chanez, A.L., Hehl, A.B., Engstler, M., and Schneider, A. (2006). Ablation of the single dynamin of *T. brucei* blocks mitochondrial fission and endocytosis and leads to aprecise cytokinesis arrest. J. Cell Sci. *119*, 2968–2974.

45. Motta, M.C.M., Martins, A.C.d.A., de Souza, S.S.A., Catta-Preta, C.M.C., Silva, R., Klein, C.C., et al. (2013). Predicting the proteins of *Angomonas deanei*, *Strigomonas culicis* and their respective endosymbionts reveals new aspects of the trypanosomatidae family. PLoS One *8*. e60209–e60209.

46. Rai, A., Nöthe, H., Tzvetkov, N., Korenbaum, E., and Manstein, D.J. (2011). *Dictyostelium* dynamin B modulates cytoskeletal structures and membranous organelles. Cell. Mol. Life Sci. *68*, 2751–2767.

47. Bui, H.T., and Shaw, J.M. (2013). Dynamin assembly strategies and adaptor review proteins in mitochondrial fission. Curr. Biol. *23*, R891–R899.

48. Stebeck, C.E., Beecroft, R.P., Singh, B.N., Jardim, A., Olafson, R.W., Tuckey, C., Prenevost, K.D., and Pearson, T.W. (1995). Kinetoplastid membrane protein-11 (KMP-11) is differentially expressed during the life-cycle of african trypanosomes and is found in a wide variety of kinetoplastid parasites. Mol. Biochem. Parasitol. *71*, 1–13.

49. Berberich, C., Machado, G., Morales, G., Carrillo, G., Jiménez-Ruiz, A., and Alonso, C. (1998). The expression of the *Leishmania infantum*

KMP-11 protein is developmentally regulated and stage specific. Biochim. Biophys. Acta *1442*, 230–237.

50. Finkelsztein, E.J., Diaz-Soto, J.C., Vargas-Zambrano, J.C., Suesca, E., Guzmán, F., López, M.C., Thomas, M.C., Forero-Shelton, M., Cuellar, A., Puerta, C.J., et al. (2015). Altering the motility of *Trypanosoma cruzi* with rabbit polyclonal anti-peptide antibodies reduces infection to susceptible mammalian cells. Exp. Parasitol. *150*, 36–43.
51. Li, Z.Y., Lee, J.H., Chu, F.X., Burlingame, A.L., Günzl, A., and Wang, C.C. (2008). Identification of a novel chromosomal passenger complex and its unique localization during cytokinesis in *Trypanosoma brucei*. PLoS One *3*, e2354.
52. Li, Z., and Wang, C.C. (2008). KMP-11, a basal body and flagellar protein, is required for cell division in *Trypanosoma brucei*. Eukaryot. Cell *7*, 1941–1950.
53. Loyola-Machado, A.C., Azevedo-Martins, A.C., Catta-Preta, C.M.C., de Souza, W., Galina, A., and Motta, M.C.M. (2017). The symbiotic bacterium fuels the energy metabolism of the host trypanosomatid *Strigomonas culicis*. Protist *168*, 253–269.
54. Maier, A., Lorenz, P., Voncken, F., and Clayton, C. (2001). An essential dimeric membrane protein of trypanosome glycosomes. Mol. Microbiol. *39*, 1443–1451.
55. Chang, K.P. (1974). Ultrastructure of symbiotic bacteria in normal and antibiotic treated *Blastocrithidia culicis* and *Crithidia oncopelti*. J. Protozool. *21*, 699–707.
56. Osteryoung, K.W., and Pyke, K.A. (2014). Division and dynamic morphology of plastids. Annu. Rev. Plant Biol. *65*, 443–472.
57. Miyagishima, S.Y. (2017). Chloroplast division: a handshake across membranes. Nat. Plants *3*, 17025.
58. Wang, W., Li, J., Sun, Q., Yu, X., Zhang, W., Jia, N., An, C., Li, Y., Dong, Y., Han, F., et al. (2017). Structural insights into the coordination of plastid division by the ARC6-PDV2 complex. Nat. Plants *3*, 17011.
59. Ingerman, E., Perkins, E.M., Marino, M., Mears, J.A., McCaffery, J.M., Hinshaw, J.E., and Nunnari, J. (2005). Dnm1 forms spirals that are structurally tailored to fit mitochondria. J. Cell Biol. *170*, 1021–1027.
60. Kalia, R., Wang, R.Y.R., Yusuf, A., Thomas, P.V., Agard, D.A., Shaw, J.M., and Frost, A. (2018). Structural basis of mitochondrial receptor binding and constriction by DRP1. Nature *558*, 401–405.
61. Bui, H.T., Karren, M.A., Bhar, D., and Shaw, J.M. (2012). A novel motif in the yeast mitochondrial dynamin Dnm1 is essential for adaptor binding and membrane recruitment. J. Cell Biol. *199*, 613–622.
62. Miyagishima, S.Y., Kabeya, Y., Sugita, C., Sugita, M., and Fujiwara, T. (2014). DipM is required for peptidoglycan hydrolysis during chloroplast division. BMC Plant Biol. *14*. 57, 57.
63. Adams, D.W., and Errington, J. (2009). Bacterial cell division: assembly, maintenance and disassembly of the Z ring. Nat. Rev. Microbiol. *7*, 642–653.
64. Motta, M.C.M., Picchi, G.F.A., Palmié-Peixoto, I.V., Rocha, M.R., De Carvalho, T.M.U., Morgado-Diaz, J., De Souza, W., Goldenberg, S., and Fragoso, S.P. (2004). The microtubule analog protein, FtsZ, in the endosymbiont of trypanosomatid protozoa. J. Eukaryot. Microbiol. *51*, 394–401.
65. Catta-Preta, C.M.C., Brum, F.L., da Silva, C.C., Zuma, A.A., Elias, M.C., de Souza, W., Schenkman, S., and Motta, M.C.M. (2015). Endosymbiosis in trypanosomatid protozoa: the bacterium division is controlled during the host cell cycle. Front. Microbiol. *6*, 520.
66. Lim, L.Z., Ee, S., Fu, J., Tan, Y.M., He, C.Y., and Song, J.X. (2017). Kinetoplastid membrane protein-11 adopts a four-helix bundle fold in DPC micelle. FEBS Lett. *591*, 3793–3804.
67. Lacomble, S., Vaughan, S., Gadelha, C., Morphew, M.K., Shaw, M.K., McIntosh, J.R., and Gull, K. (2010). Basal body movements orchestrate membrane organelle division and cell morphogenesis in *Trypanosoma brucei*. J. Cell Sci. *123*, 2884–2891.
68. Schneider, A., and Ochsenreiter, T. (2018). Failure is not an option - mitochondrial genome segregation in trypanosomes. J. Cell Sci. *131*, jcs221820.
69. Nowack, E.C.M., and Grossman, A.R. (2012). Trafficking of protein into the recently established photosynthetic organelles of *Paulinella chromatophora*. Proc. Natl. Acad. Sci. USA *109*, 5340–5345.
70. Shigenobu, S., and Stern, D.L. (2012). Aphids evolved novel secreted proteins for symbiosis with bacterial endosymbiont. Proc. R. Soc. Lond. B *280*. 20121952.
71. van de Velde, W., Zehirov, G., Szatmari, A., Debreczeny, M., Ishihara, H., Kevei, Z., Farkas, A., Mikulass, K., Nagy, A., Tiricz, H., et al. (2010). Plant peptides govern terminal differentiation of bacteria in symbiosis. Science *327*, 1122–1126.
72. Embley, T.M., and Finlay, B.J. (1993). Systematic and morphological diversity of endosymbiotic methanogens in anaerobic ciliates. Antonie Leeuwnhoek Internatl. J. Mol. Microbiol. *64*, 261–271.
73. Clarke, K.J., Finlay, B.J., Esteban, G., Guhl, B.E., and Embley, T.M. (1993). *Cyclidium porcatum* n. sp.: a free-living anaerobic scuticociliate containing a stable complex of hydrogenosomes, eubacteria and Archaeobacteria. Eur. J. Protistol. *29*, 262–270.
74. Takeshita, K., Yamada, T., Kawahara, Y., Narihiro, T., Ito, M., Kamagata, Y., et al. (2019). Tripartite symbiosis of an anaerobic scuticociliate with two hydrogenosome-associated endosymbionts, a Holospora-related alphaproteobacterium and a methanogenic archaeon. Appl. Environ. Microbiol. *85*. e00854–e00819.
75. Friedman, J.R., Lackner, L.L., West, M., DiBenedetto, J.R., Nunnari, J., and Voeltz, G.K. (2011). ER tubules mark sites of mitochondrial division. Science *334*, 358–362.
76. Mueller-Schuessele, S.J., and Michaud, M. (2018). Plastid transient and stable interactions with other cell compartments. Methods Mol. Biol. *1829*, 87–109.
77. Sievers, F., Wilm, A., Dineen, D., Gibson, T.J., Karplus, K., Li, W., Lopez, R., McWilliam, H., Remmert, M., Söding, J., et al. (2011). Fast, scalable generation of high-quality protein multiple sequence alignments using Clustal Omega. Mol. Syst. Biol. *7*, 539.
78. Larkin, M.A., Blackshields, G., Brown, N.P., Chenna, R., McGettigan, P.A., McWilliam, H., Valentin, F., Wallace, I.M., Wilm, A., Lopez, R., et al. (2007). Clustal W and clustal X version 2.0. Bioinformatics *23*, 2947–2948.
79. Nguyen, L.T., Schmidt, H.A., Von Haeseler, A., and Minh, B.Q. (2015). IQ-TREE: a fast and effective stochastic algorithm for estimating maximum-likelihood phylogenies. Mol. Biol. Evol. *32*, 268–274.
80. Erdős, G., and Dosztányi, Z. (2020). Analyzing protein disorder with IUPred2A. Curr. Protoc. Bioinformatics *70*, e99.
81. Waterhouse, A.M., Procter, J.B., Martin, D.M.A., Clamp, M., and Barton, G.J. (2009). Jalview Version 2–a multiple sequence alignment editor and analysis workbench. Bioinformatics *25*, 1189–1191.
82. Guindon, S., and Gascuel, O. (2003). A simple, fast, and accurate algorithm to estimate large phylogenies by maximum likelihood. Syst. Biol. *52*, 696–704.
83. Abascal, F., Zardoya, R., and Posada, D. (2005). ProtTest: selection of best-fit models of protein evolution. Bioinformatics *21*, 2104–2105.
84. Almagro Armenteros, J.J.A., Tsirigos, K.D., Sønderby, C.K., Petersen, T.N., Winther, O., Brunak, S., von Heijne, G., and Nielsen, H. (2019). SignalP 5.0 improves signal peptide predictions using deep neural networks. Nat. Biotechnol. *37*, 420–423.
85. Tokuyasu, K.T. (1973). A technique for ultracryotomy of cell suspensions and tissues. J. Cell Biol. *57*, 551–565.
86. Grube, L., Dellen, R., Kruse, F., Schwender, H., Stühler, K., and Poschmann, G. (2018). Mining the secretome of C2C12 muscle cells: data dependent experimental approach to analyze protein secretion using label free quantification and peptide based analysis. J. Proteome Res. *17*, 879–890.
87. Preisner, H., Karin, E.L., Poschmann, G., Stühler, K., Pupko, T., and Gould, S.B. (2016). The cytoskeleton of parabasalian parasites comprises proteins that share properties common to intermediate filament proteins. Protist *167*, 526–543.

88. Terfrüchte, M., Joehnk, B., Fajardo-Somera, R., Braus, G.H., Riquelme, M., Schipper, K., and Feldbrügge, M. (2014). Establishing a versatile Golden Gate cloning system for genetic engineering in fungi. Fungal Genet. Biol. *62*, 1–10.

89. Engler, C., Kandzia, R., and Marillonnet, S. (2008). A one pot, one step, precision cloning method with high throughput capability. PLoS One *3*, e3647.

90. Altschul, S.F., Wootton, J.C., Gertz, E.M., Agarwala, R., Morgulis, A., Schäffer, A.A., and Yu, Y.K. (2005). Protein database searches using compositionally adjusted substitution matrices. FEBS Journal *272*, 5101–5109.

91. Hall, T.A. (1999). BioEdit: a user-friendly biological sequence alignment editor and analysis program for Windows 95/98/NT. Nucleic Acids Symp. *41*, 95–98.

92. Krogh, A., Larsson, B., von Heijne, G., and Sonnhammer, E.L.L. (2001). Predicting transmembrane protein topology with a hidden Markov model: application to complete genomes. J. Mol. Biol. *305*, 567–580.

93. Almagro Armenteros, J.J., Salvatore, M., Emanuelsson, O., Winther, O., von Heijne, G., Elofsson, A., and Nielsen, H. (2019). Detecting sequence signals in targeting peptides using deep learning. Life Sci. Alliance *2*. e201900429.

94. Lartillot, N., and Philippe, H. (2004). A Bayesian mixture model for across-site heterogeneities in the amino-acid replacement process. Mol. Biol. Evol. *21*, 1095–1109.

95. Schwanhäusser, B., Busse, D., Li, N., Dittmar, G., Schuchhardt, J., Wolf, J., Chen, W., and Selbach, M. (2011). Global quantification of mammalian gene expression control. Nature *473*, 337–342.

96. Perez-Riverol, Y., Csordas, A., Bai, J., Bernal-Llinares, M., Hewapathirana, S., Kundu, D.J., Inuganti, A., Griss, J., Mayer, G., Eisenacher, M., et al. (2019). The PRIDE database and related tools and resources in 2019: improving support for quantification data. Nucleic Acids Res. *47*, D442–D450.

97. Cox, J., Hein, M.Y., Luber, C.A., Paron, I., Nagaraj, N., and Mann, M. (2014). Accurate proteome-wide label-free quantification by delayed normalization and maximal peptide ratio extraction, termed MaxLFQ. Mol. Cell. Proteomics *13*, 2513–2526.

98. Tusher, V.G., Tibshirani, R., and Chu, G. (2001). Significance analysis of microarrays applied to the ionizing radiation response. Proc. Natl. Acad. Sci. USA *98*, 5116–5121.

STAR★METHODS

KEY RESOURCES TABLE

REAGENT or RESOURCE	SOURCE	IDENTIFIER
Antibodies		
Anti-GFP (mouse)	Santa Cruz Biotechnology	Cat#Sc-9996; RRID: AB_627695
Anti-mouse IgG antibodies (rabbit)	Dianova	Cat#315-005-048
Anti-mouse IgG HRP conjugate	Cell Signaling Technology	Cat#7076; RRID: AB_330924
Anti-mouse IgG Alexa Fluor 488 (goat)	Thermo Fisher Scientific	Cat#B40941
Anti-rat IgG Alexa Fluor 594 (goat)	Abcam	Cat#Ab150160; RRID: AB_2756445
Anti-rat IgG HRP conjugate	Thermo Fisher Scientific	Cat#PA1-28573; RRID: AB_10980086
Anti-RFP (rat)	Chromotek	Cat#5f8-100; RRID: AB_2336064
Anti-V5 primary antibodies (mouse)	Abcam	Cat#ab27671; RRID: AB_471093
m-IgGκ BP-CFL 594	Santa Cruz Biotechnology	Cat#sc-516178
Anti-α-tubulin (YL1/2) (rat)	Thermo Fisher Scientific	Cat#MA1-80017; RRID: AB_2210201
Bacterial and virus strains		
Escherichia coli Top10	Thermo Fisher Scientific	Cat#C404010
Chemicals, peptides, and recombinant proteins		
Brain heart infusion	Sigma-Aldrich	Cat#53286
Blocking solution for goat gold conjugates	Aurion	Cat#905.002
BSA-c additive	Aurion	Cat#900.099
Cacodylate	Plano-em	Cat#R1105
Epon-Araldite (Epoxy Embedding Medium Kit)	Sigma-Aldrich	Cat#45359-1EA-F
G418	Sigma-Aldrich	Cat#A1720
Glutaraldehyde	Sigma-Aldrich	Cat#G5882
Hoechst 33342	Thermo Fisher Scientific	Cat#H1399
Horse serum	Sigma-Aldrich	Cat#H1270
Hygromycin B gold	Invivogen	Cat#ant-hg-5
Iodixanol	Progen	Cat#1114542
Osmium tetroxid	Science Services	Cat#E19180
Phleomycin	Invivogen	Cat#ant-ph-1
Percoll PLUS	VWR	Cat#17-5445-01
Pierce 660 nm Protein Assay Reagent	Thermo Fisher Scientific	Cat#22662
Polylysine	Merck Millipore	Cat#A-005-C
Prolong Diamond	Thermo Fisher Scientific	Cat#P36961
Protein A conjugated to 15 nm gold particles	Cell Biology UMC Utrecht	Cat#PAG 15 nm (https://www.cellbiology-utrecht.nl/products.html)
SlowFade Diamond Antifade Mountant	Thermo Fisher Scientific	Cat#S36967
TRI Reagent	Sigma-Aldrich	Cat#93289
Uranyl acetate	TED PELLA	Cat#19481
Critical commercial assays		
Bolt 4-12% Bis-Tris Plus precast gels	Thermo Fisher Scientific	Cat#NW04122BOX
DNAeasy Blood & Tissue Kit	Qiagen	Cat#69504
DIG-High Prime DNA Labeling and Detection Starter Kit II	Sigma-Aldrich	Cat#11585614910
P3 primary cells solution from 4D Nucleofector Kit S	Lonza	Cat#V4XP-3032
5' RACE System for Rapid Amplification of cDNA Ends	Thermo Fisher Scientific	Cat#18374058

(*Continued on next page*)

Continued

REAGENT or RESOURCE	SOURCE	IDENTIFIER
RNeasy MinElute Kit	Qiagen	Cat#74204
SuperSignal West Pico PLUS chemiluminescent substrate	Thermo Fisher Scientific	Cat#34579
Deposited data		
Proteome data	This study	PRIDE Archive: PXD017908
Experimental models: Organisms/strains		
Angomonas deanei (*Crithidia deanei* Cavalho)	American Type Culture Collection	PRA-265
Oligonucleotides		
See Table S3	This study	N/A
Recombinant DNA		
pJET 1.2 cloning vector (CloneJET Kit)	Thermo Fisher Scientific	Cat#K1231
pGEM-T	Promega	Cat#A1360
See Figure S4	This study	N/A
Software and algorithms		
Basic Logarithmic Alignment Tool (BLAST)	National Center for Biotechnology Information	https://blast.ncbi.nlm.nih.gov/Blast.cgi
ChimeraX v1.4	Resource for Biocomputing, Visualization, and Informatics, University of California	https://www.cgl.ucsf.edu/chimerax/
Clustal Omega	Sievers et al.[77]	https://www.ebi.ac.uk/Tools/msa/clustalo/
ClustalW2 (now: Clustal Omega)	Larkin et al.[78]	https://www.ebi.ac.uk/Tools/msa/clustalo/
ClustalX 2.1	European Molecular Biology Laboratory	http://www.clustal.org/clustal2/
Huygens Professional v 16.10	Scientific Volume Imaging	https://svi.nl/Huygens-Professional
IQ-TREE software package v 2.2.0	Nguyen et al.[79]	http://www.iqtree.org/
IUPred2A	Erdős and Dosztányi[80]	https://iupred2a.elte.hu/
Jalview v 2.11.2.4	Waterhouse et al.[81]	https://www.jalview.org/
Leica Application Suite X software v 3.5.2.18963	Leica Microsystems	https://www.leica-microsystems.com/de/produkte/mikroskop-software/p/leica-las-x-ls/
MaxQuant v 1.6.12.0	Max Planck Institute of Biochemistry	https://www.maxquant.org/
Metamorph software package v 7.74.0	Molecular Devices	https://de.moleculardevices.com/products/cellular-imaging-systems/acquisition-and-analysis-software/metamorph-microscopy#gref
NCBI nr data base	National Center for Biotechnology Information	https://www.ncbi.nlm.nih.gov/refseq/about/nonredundantproteins/
NCBI Transcriptome Shotgun Assembly Sequence Database	National Center for Biotechnology Information	https://www.ncbi.nlm.nih.gov/genbank/tsa/
PhyML v 2.4.5	Guindon and Gascuel[82]	http://www.atgc-montpellier.fr/phyml/versions.php
Phyre2	Kelley et al.[37]	http://www.sbg.bio.ic.ac.uk/~phyre2/html/page.cgi?id=index
ProtTest v 1.4	Abascal et al.[83]	https://github.com/ddarriba/prottest3
SignalP 5.0	Almagro Armenteros et al.[84]	https://services.healthtech.dtu.dk/service.php?SignalP-5.0
TargetP 2.0	Almagro Armenteros et al.[84]	https://services.healthtech.dtu.dk/service.php?TargetP-2.0
UniProtKB	European Molecular Biology Laboratory	https://www.uniprot.org/help/uniprotkb
TriTryp Data Base	Eukaryotic Pathogen, Vector and Host Bioinformatics Resource Center	https://tritrypdb.org/
Zen Blue v 2.5	Zeiss	https://www.zeiss.com/microscopy/en/products/software.html

(*Continued on next page*)

Continued

REAGENT or RESOURCE	SOURCE	IDENTIFIER
Other		
Axio Imager M.1 with fluorescence unit (for details see main text)	Zeiss	N/A
ChemiDoc MP	Biorad	N/A
Formvar-coated nickel grids	Plano	Cat#S162N
ImageQuant LAS 4000	Cytiva	N/A
Infinite 200 Pro plate reader	Tecan Lifesciences	N/A
Leica TCS SP8 STED 3x	Leica Microsystems	N/A
NanoDrop Spectrophotometer	Thermo Fisher Scientific	Cat#ND-2000
Nucleofector 4D	Lonza	N/A
Orbitrap Elite	Thermo Fisher Scientific	N/A
QExactive Plus Mass Spectrometer	Thermo Fisher Scientific	Cat#IQLAAEGAAPFALGMBDK
SNAP i.d. 2.0 Protein Detection System	Merck Millipore	Cat#SNAP2MM
TEM Zeiss 902	Zeiss	N/A
UltiMate 3000 Rapid Separation System	Thermo Fisher Scientific	Cat#IQLAAAGABHFAPBMBFE

RESOURCE AVAILABILITY

Lead contact

Further information and requests for resources and reagents should be directed to and will be fulfilled by the lead contact, Eva C.M. Nowack (e.nowack@hhu.de)

Materials availability

Plasmids and strains generated in this study are available upon request from the lead contact.

Data and code availability

- Proteome data reported in this study have been deposited at the Cell-Press-recommended PRIDE Archive (https://www.ebi.ac.uk/pride/archive/) and are publicly available as of the date of publication. The accession number is listed in the key resources table.
- This study did not generate any unique code.
- Any additional information required to reanalyze the data reported in this paper is available from the lead contact upon request.

EXPERIMENTAL MODEL AND SUBJECT DETAILS

Angomonas deanei (ATCC: PRA-265) has been obtained from the American Type Culture Collection (https://www.atcc.org/).

METHOD DETAILS

Generation of transgenic cell lines

A. deanei was grown in brain heart infusion (BHI, Sigma Aldrich) medium supplemented with 10% v/v horse serum (Sigma Aldrich) and 10 μg/ml of hemin at 28° C as described before.[32] For transfection, between 1 x 10^6 and 1 x 10^7 cells were resuspended in 18 μl of P3 primary cells solution (Lonza), 2 μl of the restricted cassette (2-4 μg total) were added, and cells were pulsed with the program FP-158 using the Nucleofector 4D (Lonza). After transfection, cells were transferred to 5 ml of fresh medium, incubated at 28 °C for 6 h, and then diluted 10-fold in the same media containing the selection drug(s) (i.e., G418 at 500 μg/ml, hygromycin B at 500 μg/ml, and/or phleomycin at 100 μg/ml final concentration). Aliquots of 200 μl were distributed onto 96-well plates and incubated at 28 °C until clonal cell lines were recovered, typically between 5-7 days. Correct insertion of the cassette was verified by PCR using sets of primers that anneal to genomic regions upstream and downstream of the 5′- and 3′-FRs of the target genes, which were part of the plasmids used for transfection.

Analysis of homologous recombination

For Southern blots, the isolated gDNA from 2 ml culture of the selected clones was isolated with the DNAeasy Blood & Tissue kit (Qiagen) and 7.5 μg was restricted with a combination of suitable restriction enzymes (New England Biolabs), separated on 1%

w/v agarose gels, and transferred to nylon membranes (Nytran N Nylon Blotting Membrane, 0.45 μm; GE Healthcare Life Sciences). Labeling of the probe and DNA hybridization were performed according to the protocol supplied with the DIG-High Prime DNA Labeling and Detection Starter Kit II (Roche Applied Science) at a hybridization temperature of 53 °C. Detection of the chemiluminescence on the developed membranes was performed in a Chemidoc MP (Bio-Rad).

Endosymbiont isolation

Endosymbionts were isolated from *A. deanei* cells lysed by sonication on consecutive sucrose, percoll, and iodixanol gradient as described previously.[32] Finally, endosymbionts were resuspended in 200 μl of buffer B (25 mM Tris-HCl, pH 7.5, 20 mM KCl, 2 mM EDTA, and 250 mM sucrose). The resulting endosymbiont fractions mainly consisted of intact endosymbionts as judged by the presence of a double membrane surrounding the endosymbionts viewed by TEM (Figures 1A and 1B) and were thus considered suitable for proteomic analyses. Proteins from isolated endosymbionts were either precipitated by addition of trichloroacetic acid (TCA) to a final concentration of 10% v/v, washed 2x in cold acetone, and resuspended in 200 μl 0.1 N NaOH (Experiment 1) or the isolated endosymbionts were directly frozen in liquid nitrogen and stored at -80 °C until use (Experiment 2).

TEM

Isolated endosymbionts obtained from the iodixanol gradient were fixed overnight in 2.5% v/v glutaraldehyde in 0.1 M cacodylate buffer, pH 7.4 at 4 °C. Fixed endosymbionts were pelleted at 7,600 x *g* for 5 min and resuspended in buffer containing 25 mM Tris-HCl, pH 7.5, 0.4 M sucrose, 20 mM potassium chloride, 2 mM ethylenediaminetetraacetic acid (EDTA), and 20% w/v bovine serum albumin (BSA), incubated for 10 min on ice, and pelleted again. The resulting pellet was covered with 2.5% v/v glutaraldehyde in 0.1 M cacodylate buffer taking care not to disrupt its integrity and fixed overnight at 4 °C. *A. deanei* cells grown to late exponential phase were washed twice with phosphate-buffered saline (PBS), fixed as described for isolated endosymbionts, and pelleted at 2,000 x *g* for 5 min. Pellets of fixed *A. deanei* cells and endosymbionts were washed once with 0.1 M cacodylate buffer, post-fixed with 2% w/v osmium tetroxide plus 0.8% w/v tetrasodium hexacyanoferrate, washed once more in 0.1 M cacodylate buffer, and embedded in 3.5% w/v agar. Agar blocks containing the pellets were dehydrated by a graded series of ethanol from 60% v/v to 100% and infiltrated with Epon-Araldite using propylenoxide as an intermediate solvent. The resin was polymerized for 24 h at 40 °C and then 24 h at 60 °C. Thin sections of 70 nm were stained with lead citrate and uranyl acetate and examined with a transmission electron microscope (Zeiss 902) at 80 kV.

Immunogold TEM

To visualize subcellular localization of ETP1 with high resolution, cells from an *A. deanei* cell line expressing V5-ETP1 from the δ−amastin locus were fixed at 4°C in 4% w/v PFA in 0.1 M phosphate buffer (pH 7.4), embedded in 10% w/v gelatin, and sectioned according to Tokuyasu.[85] 70 nm sections were loaded onto Formvar-coated nickel grids. Then, sections were consecutively blocked in blocking solution for goat gold conjugates (Aurion, Wageningen, Netherlands) for 30 min; incubated with a 1:20 dilution of α-V5 primary antibodies (mouse, ab27671, Abcam, Cambridge, UK) for 90 min; incubated with a 1:10 dilution of α-mouse IgG antibodies (rabbit, 315-005-048, Dianova, Hamburg, Germany) for 30 min; and finally, incubated with a 1:50 dilution of Protein A conjugated to 15 nm gold particles (Cellbiology Utrecht, Netherlands) for 30 min. All dilutions were prepared in TBP [PBS pH 7.4 + 0.1% v/v BSA-c additive (Aurion, Wageningen, Netherlands)]. Between incubation steps, grids were washed six times with TBP. Finally, antibody complexes were fixed with 1% v/v glutaraldehyde in PBS for 5 min. Cells were visualized by TEM (as above).

Proteome analysis and identification of ETPs

Sample separation and LC-MS/MS analyses of WC and ES samples were essentially done as described before.[32] In total, the results from 9 biological replicates were analyzed. The first three biological replicates (Experiment 1) were run together in a preliminary analysis to check the quality of the endosymbiont preparation and differed from the later six biological replicates (Experiment 2) only by a TCA precipitation step of both the WC and ES samples. In brief, peptides of tryptic digested samples were separated over 2h on C18 material using an Ultimate3000 rapid separation system (Thermo Fisher Scientific) as described[86] and subsequently analyzed with an online coupled mass spectrometer in data dependent mode. Samples of Experiment 1 were analyzed using a QExactive plus mass spectrometer (Thermo Fisher Scientific) as described[86] and samples of Experiment 2 analyzed on an Orbitrap Elite (Thermo Fisher Scientific) as described.[87] Database searches and quantification of proteins was carried out as described in section quantification and statistical analysis.

To verify correct prediction of translation start sites of POIs in the newly released, annotated *A. deanei* genome assembly (GCA_903995115.1)[33] that was used as a database for mass spectrometric protein identification, the gene model of each POI was compared to the corresponding transcript in a previously generated *A. deanei* transcriptome dataset.[32] The longest possible N-terminal extension of the open reading frame (ORF) in 5′ full-length transcripts (as indicated by the presence of a 5′ splice leader sequence (SL)) was regarded as full-length ORF and used for further analyses (Table S2; Data S1). Except for the hypothetical protein CAD2216283.1, all candidate ETPs were represented by transcripts with a full-length 5′ end. For this candidate, 5′ RACE allowed for extension of the transcript sequence up to the SL.

Current Biology
Article

CellPress

Rapid amplification of cDNA ends (RACE)

Cells from 0.5 ml *A. deanei* cultures grown to late-logarithmic phase were collected by centrifugation, the pellet was frozen in liquid nitrogen and immediately resuspended in 1 ml of TRI Reagent (Sigma Aldrich). RNA was extracted according to the manufacturer's instructions. RNA concentration was estimated by measuring the absorbance at 260 nm in a NanoDrop spectrophotometer (Thermo). 5 U of DNAase (Thermo) were added to 5 μg RNA, incubated for 10 min at room temperature to degrade residual DNA contamination, and DNase-treated RNA was purified using the RNAse MinElute Kit (Qiagen) according to the manufacturer's instructions. 3 μg of DNase-treated RNA were used per RACE reaction using the 5' RACE System for Rapid Amplification of cDNA Ends, version 2.0 (Thermo) with internal primers described in Table S3. The obtained PCR fragments were cloned into the pJET 1.2 cloning vector (Invitrogen) and sequenced using the pJet Fw/Rv primer set provided by the manufacturer.

Construction of plasmids

To efficiently generate eGFP-POI and POI-eGFP expression vectors for *A. deanei*, the pAdea043 and pAdea235 eGFP-tagging vectors, respectively, were constructed (Figure S4). These plasmids target the insertion of the respective expression cassettes into the δ-amastin locus of *A. deanei*.[32] To this end, the *lacZα* expression cassette encoding the alpha-fragment of the β-galactosidase under control of the lac promotor and operator was amplified from the circularized plasmid pGEM-T (Promega) using the forward primer 596 that includes a 5' *Xho*I restriction site and the reverse primer 597 which includes a 3' *Kpn*I restriction site. In parallel, large fragments containing the 3' flanking region (FR) of δ-amastin, the pUMA1467 backbone,[88] the 5' FR of δ-amastin, the neomycin resistance gene (*neo*), the glyceraldehyde 3-phosphate dehydrogenase intergenic region of *A. deanei* (GAPDH-IR), and eGFP were amplified from the plasmid pAEX-eGFP[32] using forward primers containing a 5' *Kpn*I-*Bsa*I extension and reverse primers containing a 3' *Xho*I-*Bsa*I extension (598/599 for pAdea043 and 763/764 for pAdea235). After restriction of the fragments with *Xho*I and *Kpn*I, a total of 20-60 fmol of each of the gel-purified *lacZα* expression cassette and the 598/599 fragment or 763/764 fragment were mixed and ligated with T4 DNA ligase to generate pAdea043 and pAdea235, respectively.

Then, each of the POI-encoding sequences were amplified from *A. deanei* gDNA with primers containing a *Bsa*I recognition site followed by 4 nucleotides complementary to the pAdea043 insertion site for the N-terminal tagging or the pAdea235 insertion site for the C-terminal tagging with eGFP (Table S3). The resulting PCR fragments were extracted from agarose gels and cloned into the tagging vectors by Golden Gate ligation[89] using equimolar or a 3:1 ratio (insert:tagging vector). In a few cases, the cloning strategy was modified, and vectors assembled by multi-fragment Golden Gate or Gibson assembly as indicated in Figure S4. *Escherichia coli* Top10 cells were transformed with the resulting vectors, transformants selected on lysogeny broth agar plates containing 100 μg/ml ampicillin, and 80 μg/ml X-Gal and 0.5 mM IPTG for blue-white selection of successful ligation events if needed.

The plasmid pAdea119 containing a cassette to express ETP1 N-terminally tagged with mScarlet from the γ-amastin locus[32] was generated from three fragments: the mScarlet was amplified from vector p3615 (kindly provided by Michael Feldbrügge), *etp1* was amplified from *A. deanei* gDNA using the primer set 1087/1088, and a large fragment containing the pUMA1467 backbone, 1,000 bp of the 5'- and 3'-FR of the γ-amastin gene, the hygromycin resistance gene (*hyg*), and the GAPDH-IR was amplified from the plasmid pAdea021 which targets the γ-amastin locus for insertion and expression of mCherry, using the primer set 1083/348 (Table S3).

The plasmids pAdea058 and pAdea059 were generated by two fragment Golden Gate ligation. The V5 tag was added by extension of the reverse primer binding to *etp1* for pAdea058 and the forward primer binding to *etp1* for pAdea059. As a template for the amplification of the fragments the plasmids pAEX ETP1-eGFP (=pAdea012) and pAEX eGFP-ETP1 (=pAdea013),[32] respectively, were used.

For generation of homozygous ETP1, ETP2, ETP7, and ETP9 KO mutants, the plasmids pAdea148 and pAdea156 (containing replacement cassettes for ETP1), pAdea092, pAdea093, and pAdea094 (containing replacement cassettes for ETP2), pAdea102 and pAdea103 (containing replacement cassettes for ETP7), and pAdea303 (containing replacement cassettes for ETP9) were constructed (Figure S4). To this end, around 1-kbp 5' and 3'-FRs of the respective genes were amplified from *A. deanei* gDNA, *neo* was amplified from pAdea036, and *hyg* from pAdea004 (=pAdea γ-ama/Hyg[32]) using primers described in Table S3. The phleomycin resistance gene (*phleo*) was synthesized by a commercial service (Integrate DNA Technologies, IDT). Vectors, carrying in the pUMA1467 backbone a replacement cassette, in which the ORF of the POI is replaced by a resistance gene, were assembled by Golden Gate or Gibson assembly. The correct nucleotide sequence of expression cassettes of all plasmids generated was verified by sequencing.

Bioinformatic analyses of the ETPs

Similarity searches of the *A. deanei* ETPs against the NCBI nr protein sequence database were performed using Blastp.[90] Best bidirectional blast hits were obtained by blasting the best NCBI hit back against the *A. deanei* transcriptome dataset using TBlastn built-in Bioedit v. 7.0.5.3.[91] Predictions of transmembrane regions were obtained using TMHMM v. 2.0,[92] targeting signals using TargetP 2.0[93] and SignalP 5.0.[84] 3D structure similarity was analyzed with Phyre2[37] and disordered protein regions predicted with IUPred2A.[80] The multiple sequence alignment of the OCD amino acid sequences was generated using ClustalX 2.1 and refined manually. Unambiguously alignable sequence blocks were extracted and used for phylogenetic analysis. Phylogenies were inferred by ML analysis using PhyML v2.4.5[82] with the WAG+I+G+F model of amino acid sequence evolution (determined as most suitable with ProtTest v1.4 software[83]). The robustness of branches was tested by ML bootstrap analysis using 100 replicates. The predicted 3D structure of the C-terminus of ETP7 was superimposed on the 3csq crystal structure (chain D) using the matchmaker function in ChimeraX v1.4.

For phylogenetic analysis of Euglenozoan DLPs, a multiple sequence alignment of the amino acid sequences of 24 DLPs from 22 Euglenozoan taxa was generated using Clustal Omega.[77] Sequences were obtained from the TriTryp Data Base (https://tritrypdb.org/): *Endotrypanum monterogeii* LV88 (EMOLV88_360052200), *Blechomonas ayalai* B08-376 (Baya_068_0150), *Porcisia hertigi* MCOE/PA/1965/C119 (JKF63_00455), *Crithidia fasciculata* Cf-Cl (CFAC1_200029900), *Paratrypanosoma confusum* CUL13 (PCON_0039990); from the NCBI nr database: *Bodo saltans* Lake Konstanz (CUF06659.1), *Trypanosoma rangeli* SC58 (ESL10883.1), *Leptomonas seymouri* ATCC 30220 (KPI86780.1), *Leishmania major* Friedlin (XP_003722303.1), *Leptomonas pyrrhocoris* (XP_015659056.1), *Trypanosoma cruzi* CL Brener (XP_822034.1), *Trypanosoma brucei brucei* TREU927 (XP_844064.1), *Trypanosoma brucei brucei* TREU927 (XP_844068.1), *Porcisia hertigi* (KAG5490335.1), *Perkinsela* sp. CCAP 1560/4 (XU18_2422); or from the NCBI Transcriptome Shotgun Assembly Sequence Database (https://www.ncbi.nlm.nih.gov/genbank/tsa/): *Trypanoplasma borreli* Tt-JH (GHOB01002299.1), *Euglena longa* CCAP 1204-17a (GGOE01025898.1), *Trypanoplasma borreli* (GFCF01011340.1), *Euglena gracilis* (GDJR01033598.1), *Diplonema papillatum* ATCC 50162 (GJNJ01015936.1), *Hemistasia phaeocysticola* YPF1303 (GHOA01017147.1).

For the Eukaryote-wide phylogenetic analysis of DLPs, a multiple sequence alignment of the amino acid sequences of 73 DLPs from 19 taxa was generated using ClustalW2.[78] The dataset largely overlaps with the dataset used in Miyagishima et al.[40] where accession numbers are provided but omits DLPs from *Oryza sativa* and includes kinetoplastida DLPs. DLPs from *Chlamydomonas reinhardtii* were replaced by updated protein models Cr_DRP1 (XP_042924642.1), Cr_DRP2 (XP_042914770.1), Cr_DRP5A (XP_042918632.1), Cr_DRP5B (XP_042920073.1), Cr_DRP4C (XP_042923301.1).

For both, the Euglenozoa-wide as well as the Eukaryote-wide phylogenetic analysis, well aligned sequence blocks were extracted, resulting in 421 and 349 aligned amino acid positions, respectively. Phylogenies were inferred by ML analysis using the IQ-TREE software package v2.2.0[79] with the LG+C60+G model of sequence evolution to account for site heterogeneity.[94] Branch support was estimated from 1000 replicates using UFBoot2 implemented in IQ-TREE.[39]

Conservation scores for columns in the DLP multiple sequence alignment shown in Figure 3F were determined by Jalview v 2.11.2.4.[81]

Fluorescence microscopy

50 μl of *A. deanei* cultures grown to densities between 1–8 x 10^7 cells/ml were mixed 1:1 with PBS containing 8% w/v paraformaldehyde (PFA), incubated for 20 min at room temperature, washed twice with PBS and then, 20 μl of the mixture was spotted on poly-L-lysine-coated glass slides. After 30 min, slides were washed 3 times with PBS followed by incubation with 10 μg/ml Hoechst 33342 in PBS for 5 min. Slides were washed two more times, and finally samples were mounted in 9 μl of Prolong Diamond (Thermo). Epifluorescence microscopy was carried out on an Axio Imager M.1 (Zeiss, Oberkochen, Germany) coupled to a Pursuit 1.4 MP Monochrome CCD camera (Diagnostic Instruments, Sterling Heights, MI, USA) and a halide lamp LQ-HXP 120 (LEj, Jena, Germany) equipped with a custom set of filters for GFP (ET470/40x, T495LPXR, ET525/50m) and Rfp/mCherry (ET560/40x, T585lp, ET630/75m) (both: Chroma, Bellow Falls, VT, USA); and DAPI (447/60 BrightLine HC, HC BS 409, 387/11 BrightLine HC) (AHF Analysentechnik, Tuebingen, Germany). Images were acquired using a 100x Plan Neofluar NA 1.3 oil M27 objective (Zeiss) and processed using the Metamorph software package v. 7.7.4.0. or an Axio Imager.A2 (Zeiss) coupled to an AxioCam MRm (Zeiss) and an Illuminator HXP 120 V (Zeiss) equipped with Filter Set 38 HE: ET470/40, BS495, ET525/50; 43 HE: ET550/25, BS570, ET605/70; 49: ET365, BS395, ET445/50. Images were acquired using an EC Plan-Neofluar 100x/1.30 Oil Ph3 M27 objective (Zeiss) and processed with Zen Blue v2.5 software. Confocal fluorescence microscopic analyses were performed on a Leica TCS SP8 STED 3X (Leica Microsystems, Wetzlar Germany) using 93x/1.3 glycerol objective equipped with a filter NF 488/561/633 with the following settings: unidirectional scan direction X, scan speed 400-1000 Hz, frame average 2, line accumulation 2 without gain. The lasers used were a diode at 405 nm and WLL at 70%. The laser line was set for Hoechst 33342 at 8.6% (405 nm), eGFP at 10% (488 nm), and mScarlet at 7.5% (561 nm). Emission was captured by PMT between 424 and 477 nm for the Hoechst 33342 signal; and hybrid detectors were set to capture emissions between 505 and 548 nm for eGFP and 589 and 621 nm for mScarlet. Images of both 2D and 3D representations were processed in the Leica X software v.3.5.2.18963 and deconvoluted on the Huygens Professional v. 16.10 on default confocal settings setting, except the manual mode threshold for background extraction was set based on the cytosolic background signal.

IFA

For IFA 1x10^7 cells from a mid-log phase culture were mixed 1:1 with 8% w/v PFA in PBS and incubated for 15 min at RT. Cells were washed 3x with PBS, spotted on poly-L-lysine covered glass slides, and incubated for 15 min. Unbound cells were removed and cells permeabilized in PBS containing 0.1% v/v Triton X-100 (PBST) for 20 min. After blocking in 1:10 diluted blocking solution (BS) (Aurion, Wageningen, Netherlands) in PBS, primary antibody (AB) [anti V5 AB (1:100 diluted for ARL1-V5 and 1:1000 for ETP1-V5 constructs, AB27671, Abcam, Cambridge) or anti α-tubulin AB (diluted 1:100, rat, MA1-80017, Thermo Fisher Scientific)] in BS was applied to the slides and incubated for 30 min (or 45 min incubation for visualization of α-tubulin). Unbound primary AB was washed off 3x in PBST, followed by an additional 30 min incubation with the secondary AB [goat anti mouse IgG conjugated to Alexafluor 488 (Thermo Fisher Scientific) or m-IgGκ BP-CFL 594 (sc-516178, Santa Cruz Biotechnology, Heidelberg) or goat anti rat IgG conjugated to Alexa Fluor 594 (Ab150160, Abcam), as indicated, all diluted 1:100 in BS]. Finally, unbound secondary AB was washed off, DNA was stained, slides were mounted in Prolong Diamond or SlowFade DiamondTM Antifade Mountants (both: Thermo), and analyzed by epifluorescence microscopy as described before.

Western blot analyses

Protein concentrations in the samples were determined using the Pierce 660 nm Protein Assay Reagent (Thermo Fisher Scientific) in 96-well plates by the absorbance in an Infinite M200 plate reader (TECAN, Austria GmbH). For SDS-PAGE, protein samples were mixed with 4X sample buffer (final concentration 63 mM Tris-HCl, pH 6.8, 10 mM dithiothreitol, 10% v/v glycerol, 2% SDS w/v, and 0.0025% w/v bromophenol blue), incubated for 5 min at 95 °C and 30 μg of protein loaded onto Bolt 4-12% w/v Bis-Tris Plus precast gels (Thermo Fisher Scientific). Electrophoresis was performed at 180 V constant in 2-morpholin-4-ylethanesulfonic acid (MES)-SDS running buffer (50 mM MES, 50 mM Tris-HCl, pH 7.3, 0.1% w/v SDS, and 1 mM ethylenediaminetetraacetic acid (EDTA). After electrophoresis, the gels were blotted onto polyvinylidene difluoride (PVDF) membranes (Amersham Hybond, 0.45 nm, GE HealthCare Life Science) at 60 mA for 1 h. Membranes were blocked, incubated with a 1:1,000 dilution of mouse anti-GFP [[B-2] (SantaCruz Biotechnology) or a rat anti-RFP [[5F8] (Chromotek) followed by a 1:5,000 dilution of the horseradish peroxidase-conjugated secondary antibody against mouse IgG (7076, Cell Signaling Technology) or rat IgG (PA128573, Thermo Fisher Scientific), respectively, in a SNAP i.d. 2.0 (Merck-Millipore) according to the manufacturer's instructions. Finally, membranes were covered in SuperSignal West Pico PLUS chemiluminescent substrate (Thermo Fisher Life Science) and chemiluminescence was detected using an ImageQuant LAS 4000 (GE Healthcare Life Science) or a ChemiDoc MP Imaging System (Bio-Rad).

QUANTIFICATION AND STATISTICAL ANALYSIS

For the proteome analysis, database searches were carried out with MaxQuant version 1.6.12.0 (MPI for Biochemistry, Planegg, Germany) using label-free quantification separately for the two analyzed groups (WC and ES) and standard parameters if not indicated otherwise. The 'match between runs' function was enabled, as well as LFQ and iBAQ[95] quantification; LFQ quantification was carried out separately for WC and ES samples. Protein sequences as basis for searches were retrieved from UniProtKB (750 sequence entries from *Ca.* K. crithidii, downloaded on 9th April 2019) and NCBI (10365 entries from GCA_903995115.1, *A. deanei*, downloaded on 1st December 2020). The mass spectrometry proteomics data have been deposited to the ProteomeXchange Consortium via the PRIDE[96] partner repository with the dataset identifier PXD017908.

Only proteins identified with at least 3 (Experiment 1) or 5 (Experiment 2) valid iBAQ intensities,[97] two different peptides, and at least 5% sequence coverage were considered as identified with high confidence and used in downstream analyses. Next, iBAQ intensities were normalized by dividing through the median iBAQ intensity of all proteins from the respective sample. For determination of endosymbiont-encoded proteins enriched in the host cell, missing values were imputed with values drawn from a downshifted normal distribution (downshift of 1.8 standard deviations, width 0.3. standard deviations) and two-sided Student's t-test were calculated between normalized iBAQ values from WC and ES samples using the significance analysis of microarrays method[98] to control for multiple testing (S0=0.6, false discovery rate 5%).

Current Biology, Volume *33*

Supplemental Information

Host-symbiont interactions in *Angomonas deanei* include the evolution of a host-derived dynamin ring around the endosymbiont division site

Jorge Morales, Georg Ehret, Gereon Poschmann, Tobias Reinicke, Anay K. Maurya, Lena Kröninger, Davide Zanini, Rebecca Wolters, Dhevi Kalyanaraman, Michael Krakovka, Miriam Bäumers, Kai Stühler, and Eva C.M. Nowack

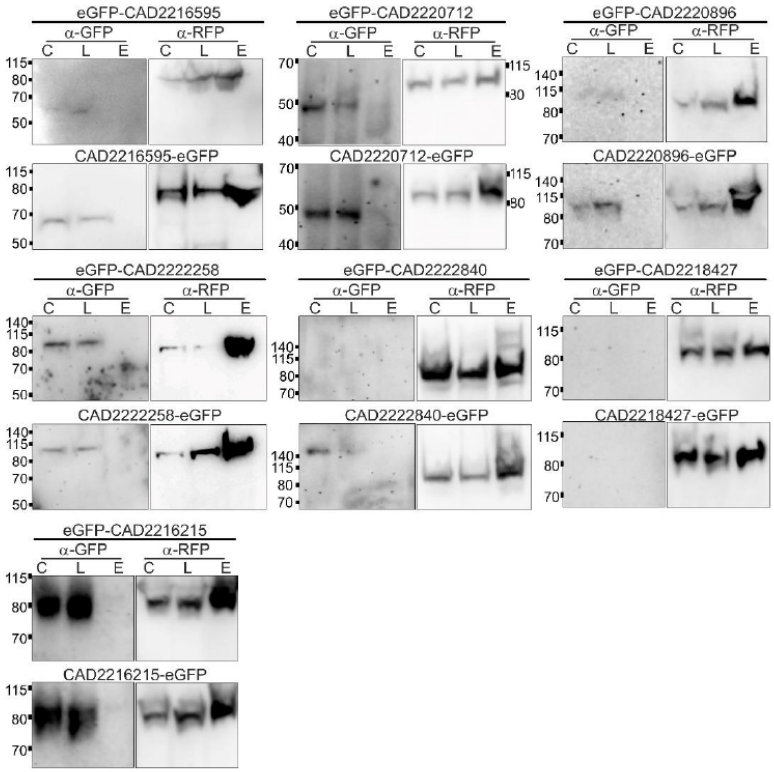

Figure S1: Candidate ETPs for which localization at the endosymbiont was not confirmed by Western blot. Related to Figure 2. 30 μg of protein from intact cells (C), whole cell lysate (L) or up to the Percoll step purified endosymbionts (E) were resolved by SDS-PAGE on 4-12% acrylamide gels, transferred onto PVDF-membranes, and recombinant proteins visualized using anti-GFP (α-GFP) or anti-RFP (α-RFP) antibodies with secondary antibodies conjugated to horseradish peroxidase. Note that these candidate ETPs for which localization at the endosymbiont was not confirmed did not receive an 'ETP annotation'.

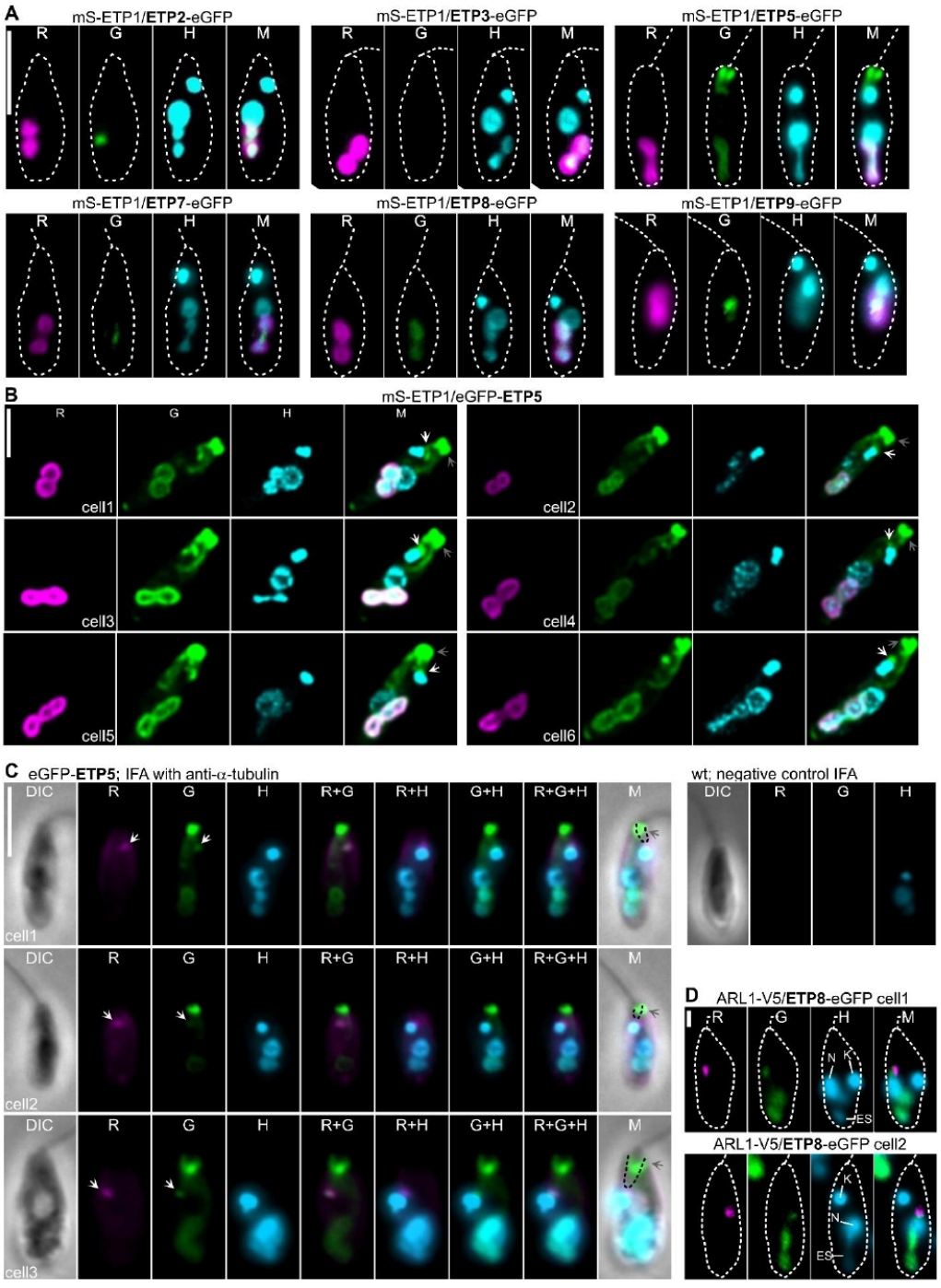
A
mS-ETP1/ETP2-eGFP
mS-ETP1/ETP3-eGFP
mS-ETP1/ETP5-eGFP
mS-ETP1/ETP7-eGFP
mS-ETP1/ETP8-eGFP
mS-ETP1/ETP9-eGFP
R
G
H
M
B
mS-ETP1/eGFP-ETP5
cell1
cell2
cell3
cell4
cell5
cell6
C
eGFP-ETP5; IFA with anti-α-tubulin
DIC
R+G
R+H
G+H
R+G+H
wt; negative control IFA
D
ARL1-V5/ETP8-eGFP cell1
ARL1-V5/ETP8-eGFP cell2
N
K
ES

Figure S2: Subcellular location of the various ETPs. Related to Figure 2. (A) The recombinant ETPs with C-terminal eGFP tags show a green fluorescence signal corresponding to the subcellular localization observed when the eGFP tag was placed at their N-terminus. Only for ETP3-eGFP no fluorescence signal was detected. Scale bar is 5 μm. **(B)** Maximum projection of all focal planes of a Z-stack obtained by confocal fluorescence microscopy of cells co-expressing mS-ETP1 and eGFP-ETP5 (same cell line as in Figure 2c-e). The fluorescence pattern of six representative cells is displayed. The scale bar is 2.5 μm. Note that all cells show a similar subcellular localization of the recombinant ETP5 at the endosymbiont envelope, the anterior end of the cell (grey arrows), and in thin fibers that seem to connect kinetoplast (white arrows), nucleus, and endosymbiont. **(C)** IFA shows eGFP-ETP5 to co-localize with the basal body and at the anterior end of the flagellar pocket. eGFP-ETP5-expressing *A. deanei* cells were fixed, permeabilized, and stained with a primary antibody against α-tubulin (Y1/2, rat) and a secondary antibody (goat anti rat IgG conjugated to Alexa Fluor 594). Red channel, α-tubulin; green channel, eGFP-ETP5 autofluorescence. Note that the eGFP signal close to the kinetoplast (white arrows) co-localizes with the kinetoplast-attached basal body that is intensely stained by IFA with the α-tubulin-specific antibody. The most intense eGFP signal at the anterior end of the cell (grey arrows) localizes to the region around the opening of the flagellar pocket. The flagellar pocket (approximate position indicated by the dotted line in M) spans between the flagellum exit point and basal body. Scale bar is 5 μm. Three cells of the same cell line representing the typical fluorescence pattern are displayed. Wt cells that were processed as the eGFP-ETP5-expressing cells but for which the primary antibody was omitted served as a negative control. **(D)** IFA shows partial overlap of the subcellular localization of the trans Golgi network (TGN) marker ARL1-V5 with ETP8-eGFP in *A. deanei.* Primary antibody: Ab27671 (Abcam) α–V5 1:100, secondary antibody sc-516178 CFL-594 (Santa Cruz Biotechnology) 1:100. Red channel, ARL1-V5; green channel, ETP8-eGFP autofluorescence. Note that ETP8-eGFP fluorescence is found throughout the endosymbiont cytosol as well as a spot between nucleus and TGN, indicative of the Golgi. Scale bar is 1 μm. Two cells of the same cell line representing the typical fluorescence pattern are displayed. Abbreviations for all panels: R, red channel; G, green channel; H, blue channel visualizing Hoechst 33342 staining; M, merge between all shown fluorescence channels. ES, endosymbiont; FP, flagellar pocket; G, glycosome; K, kinetoplast; PM, host cell plasma membrane.

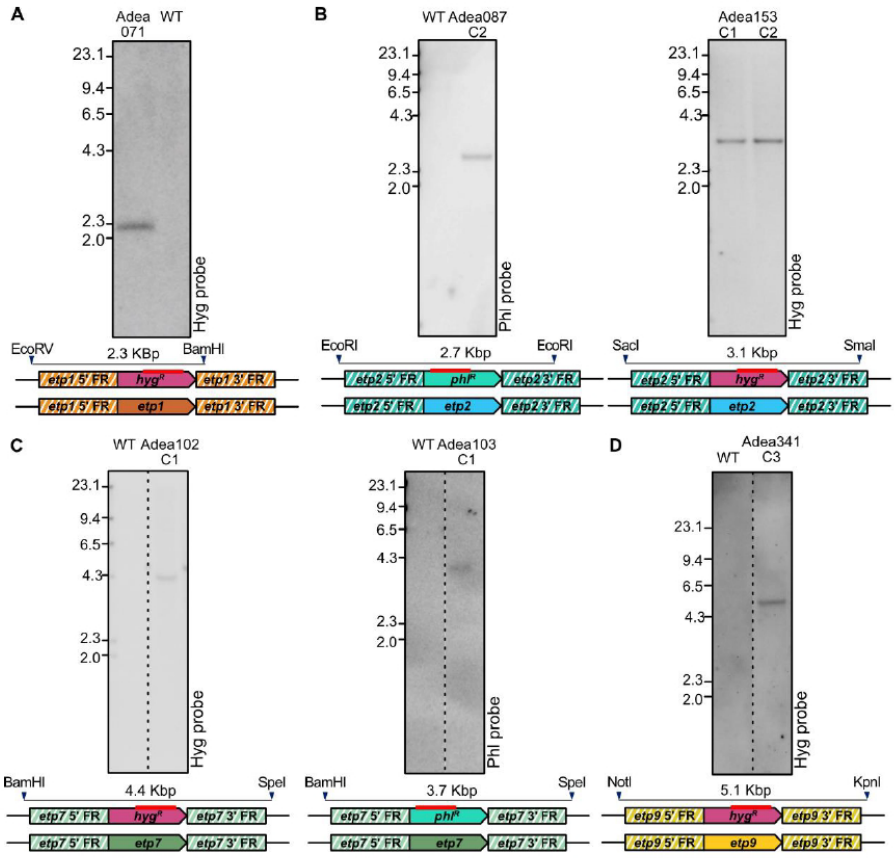

Figure S3: Heterozygous KO mutant cell lines of *etp1*, *etp2*, *etp7*, and *etp9* were generated by homologous recombination and confirmed by Southern blot analyses. Related to Figure 2. Genomic DNA was extracted from at least one PCR-verified *A. deanei* cell line in which one allele of *etp1* **(A)**, *etp2* **(B)**, *etp7* **(C)**, or *etp9* **(D)** was replaced by a cassette containing a resistance gene against the antibiotics hygromycin (*hyg*) or phleomycin (*phl*). The DNA was restricted by the specified enzymes and analyzed by Southern blot hybridizations using probes against *hyg* or *phl*, as indicated. Wild type (WT) cells were used as negative controls. C1 to C3 indicates internal names of clones from the same cell line. Dotted black lines indicate that different lanes cut from the same blotting membrane are displayed next to each other. Underneath each blot, restriction maps are provided that indicate the expected band sizes. The 5′- and 3′-flanking regions (FR) of a gene that were used for homologous recombination are represented by striped rectangles, genomic regions up and downstream of the insertion sites for the cassettes are represented by a black line. The *hyg* and *phl* genes are represented by arrows in magenta and cyan, respectively; the *etp1*, *etp2*, *etp7*, and *etp9* genes by arrows in brown, blue, green, and yellow, respectively. The red bar indicates the binding region of the probe.

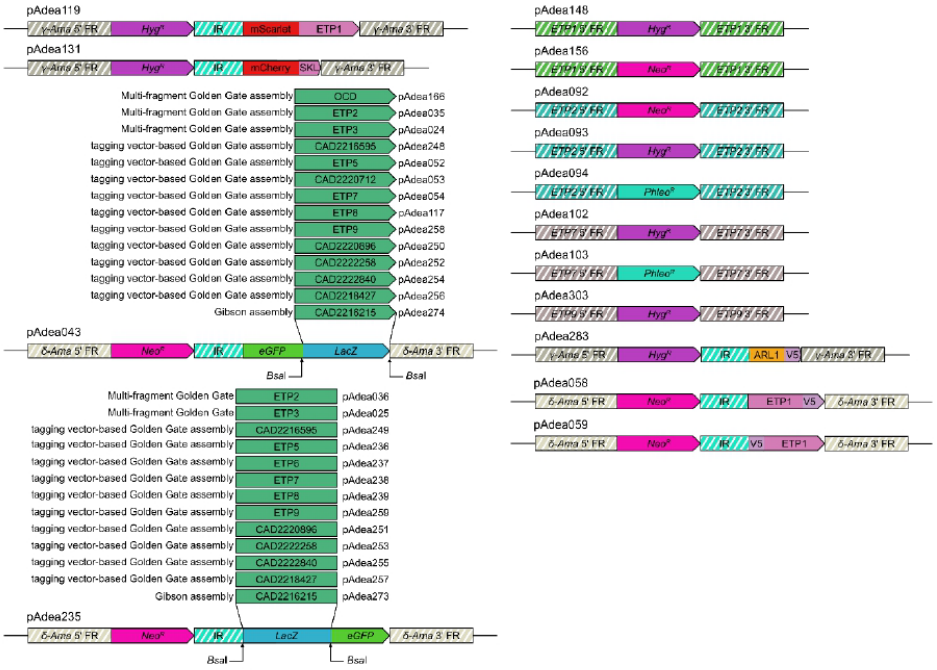

Figure S4: Cassettes used for the expression of recombinant proteins and targeted gene KOs in *A. deanei*. Related to Figures 2 and 4. The plasmid pAdea119 contains a cassette for the expression of ETP1 (pink arrow) fused to the C-terminus of mScarlet (red rectangle) from the γ-amastin locus; the γ-amastin flanking regions (FRs) used for homologous recombination (HR) are represented by hatched grey bars. The plasmids pAdea043 and pAdea235 contain cassettes for expression from the δ-amastin locus; FRs used for HR are represented by hatched brown bars. By replacement of the *lacZα* expression cassette with the POI (dark green rectangles) at the *Bsa*I sites, the POI is scarlessly fused to the C-terminus (pAdea043) or N-terminus (pAdea235) of eGFP (green rectangle/arrow). The absence/presence of the *lacZα* cassette allows for blue/white selection of the resulting plasmids. Hygromycin resistance gene (*hyg*, violet arrow); neomycin resistance gene (*neo*, fuchsia arrow); the intergenic region between the glyceraldehyde 3-phosphate dehydrogenase I and II from *A. deanei* (IR, hatched cyan bar); *lacZα* expression cassette (*lacZ*, blue-green rectangle). The plasmids pAdea148, pAdea156, pAdea092, pAdea093, pAdea094, pAdea102, and pAdea303 contain the resistance marker genes *hyg, neo* or *phleo* flanked by ~1,000 bp of the 5' and 3' FR of ETP1, ETP2, ETP7, and ETP9 as indicated. These cassettes were used to target both alleles of the respective genes for deletion by HR. Plasmid pAdea283 contains a cassette for the expression of the TGN marker ARL1 (orange rectangle) fused to the N-terminus of the V5 short epitope tag (lilac arrow) from the γ-amastin locus. Plasmids pAdea058 and pAdea059 contain cassettes for the expression of ETP1 (pink) fused to the N-terminus or C-terminus, respectively, of the V5 tag (lilac arrow) from the δ-amastin locus.

Accession[a]	Annotation	Exp. 1[b]	Exp. 2[c]	Chr [d]	N-ext [aa][e]	M.W. [kDa][f]	Fluorescent fusions [kDa][g]	ETP[h]
CAD2220707.1	Hypothetical protein, cons.	3.4/2.4	4.1/8.2	18	98	42.7	69.0 (mScarlet)	ETP1
CAD2221027.1	Hypothetical protein, cons.	8.2/3.5	6.9/8.8	19	-	53.4	80.2 (eGFP)	ETP2
CAD2213480.1	Hypothetical protein, cons.	1.5/2.9	5.2/6.0	02	-	105.1	131.9 (eGFP)	ETP3
CAD2216595.1	Nodulation protein S (NodS)/Methyltransferase domain/Ribosomal protein L11 methyltransferase (PrmA), put.	5.3/1.8	0.1/0.0	07	-	32.9	59.9 (eGFP)	
CAD2216818.1; CAD2216819.1; CAD2216820.1; CAD2216821.1	Kinetoplastid membrane protein 11, put.	0.4/0.3	2.7/3.4	07 07 07 07	-	11.0	37.8 (eGFP)	ETP5
CAD2220712.1	Hypothetical protein, cons.	4.1/3.8	nd	18	-	22.5	49.4 (eGFP)	
CAD2217314.1	Phage tail lysozyme, put.	5.1/2.1	3.4/3.4	08	-	61.0	87.8 (eGFP)	ETP7
CAD2216283.1	Hypothetical protein, cons.	5.1/2.5	4.5/5.9	06	122	22.6	49.4 (eGFP)	ETP8
CAD2212698.1	Dynamin family/Dynamin central region/Dynamin GTPase effector domain containing protein, putative	1.6/1.7	0.5/0.4	01	-	77.4	104.4 (eGFP)	ETP9
CAD2220896.1	Hypothetical protein, cons.	8.8/2.5	nd	19	263	73.9	100.8 (eGFP)	-
CAD2222258.1	WD domain, G-beta repeat, put.	3.5/2.1	nd	25	185	66.2	93.1 (eGFP)	-
CAD2222840.1	Hypothetical protein, cons.	nd	2.5/3.9	28	-	123.8	150.7 (eGFP)	-
CAD2218427.1	Sugar (and other) transporter/Major Facilitator Superfamily/Uncharacterised MFS-type transporter YbfB/Organic Anion Transporter Polypeptide (OATP) family, putative	7.1/3.5	nd	11	-	74.8	101.7 (eGFP)	-
CAD2216215.1	ABC transporter transmembrane region/ABC transporter, putative	nd	4.3/4.2	06	153	67.6	94.5 (eGFP)	-

Table S2: Mass spectrometric identification of candidate ETPs. Related to Figure 2 and Table 1.

[a] GenBank accession number.

[b,c] Enrichment of protein in ES fractions in LC-MS/MS Experiment 1 and 2, indicated by (difference ES-WC/-log T-test p-value) as in **Figure 1c-d**. Nd, not detected.

[d] Chromosomal localization in *A. deanei* nuclear genome assembly GCA_903995115.1.

[e] N-terminal extension of the ORF as predicted by full-length transcript by indicated number of amino acids (see **Data S1**).

[f] Estimated molecular weight of the protein encoded by the full length ORF (Expasy Protparam).

[g] Estimated molecular weight of the fluorescent fusion protein mScarlet-ETP1 and eGFP-POI.

[h] Newly assigned name.

2.1.2. Publication II

Maurya, A.K., Kröninger, L., Ehret, G., Bäumers, M., Marson, M., Scheu, S., Nowack, E.C.M. (2025). A nucleus-encoded dynamin-like protein controls endosymbiont division in the trypanosomatid *Angomonas deanei*. *Science Advances*, 11(12), eadp8518.

To explore the subcellular localization throughout the cell cycle stages (aim I) and cellular function of ETP9 (aim II), We performed IFA, comparative genomic analysis, gene knockouts as well as knockdown of ETP9 using MAOs. Subsequently, we observed that the ES lost most of the essential division genes and thus the autonomy to divide. Interestingly, nucleus-encoded ETP9 that showed a cell cycle-dependent localization together with the bacterium-encoded division protein FtsZ at the ESDS, was found to compensate for the lost ES division genes. Importantly, ETP9 showed an indispensable role in ES division in *A. deanei*. In sum, the data revealed that a host-derived ES division machinery which is of dual genetic nature evolved in *A. deanei* (and in other members of Strigomonadinae) to gain a tight control by the host over its bacterial ES.

My contribution to Maurya et al., 2025, Science Advances.

Most of the research (~ 90%) presented in this publication was performed by me (see author contributions in the publication II below). The contributions of others were the following. Eva Nowack performed the comparative genomic analysis leading to Fig. 1 and Table S1, and also generated Fig. S3 A. Lena Kröninger performed the Western blot analysis leading to Fig. S1 A-B and Fig. S2 A-B. She also generated plasmid pAdea301. Georg Ehret performed confocal microscopy leading to Fig. 2B and generated Adea363 (Δ*etp9*^{hyg}*/etp9*, in aposymbiotic *A. deanei* strain). Miriam Bäumers helped with TEM analysis leading to Fig. 4D and Fig. S4. Marcel Marson and Stefanie Scheu designed the RT-qPCR strategy and helped performing the experiments leading to Fig. 4E.

SCIENCE ADVANCES | RESEARCH ARTICLE

EVOLUTIONARY BIOLOGY

A nucleus-encoded dynamin-like protein controls endosymbiont division in the trypanosomatid *Angomonas deanei*

Anay K. Maurya[1], Lena Kröninger[1], Georg Ehret[1]†, Miriam Bäumers[2], Marcel Marson[3], Stefanie Scheu[3]‡, Eva C. M. Nowack[1]*

***Angomonas deanei* is a trypanosomatid of the Strigomonadinae. All members of this subfamily contain a single β-proteobacterial endosymbiont. Intriguingly, cell cycles of host and endosymbiont are synchronized. The molecular mechanisms underlying this notable level of integration are unknown. Previously, we identified a nucleus-encoded dynamin-like protein, called ETP9, that localizes at the endosymbiont division site of *A. deanei*. Here, we found by comparative genomics that endosymbionts throughout the Strigomonadinae lost the capacity to autonomously form a division septum. We describe the cell cycle–dependent subcellular localization of ETP9 that follows accumulation of the bacterium-encoded division protein FtsZ at the endosymbiont division site. Furthermore, we found that ETP9 is essential in symbiotic but dispensable in aposymbiotic *A. deanei* that lost the endosymbiont. In the symbiotic strain, ETP9 knockdowns resulted in filamentous, division-impaired endosymbionts. Our work unveiled that in *A. deanei* an endosymbiont division machinery of dual genetic origin evolved in which a neo-functionalized host protein compensates for losses of endosymbiont division genes.**

INTRODUCTION

Endosymbiotic associations with phylogenetically and physiologically diverse bacteria are widespread among eukaryotes (*1*–*4*). Long-term coevolution between hosts and endosymbionts can result in pronounced genome reduction in the endosymbiont (*2*, *3*). In extreme cases, bacterial endosymbionts can lose their genetic autonomy and transform into genetically integrated organelles that import a large proportion of their proteins, which are now synthesized by eukaryotic ribosomes. This was the case for mitochondria and primary plastids, two hallmark organelles of the eukaryotic cell that were acquired >1.5 billion years ago, as well as for the more recently acquired photosynthetic chromatophores in the cercozoan amoeba *Paulinella chromatophora* (*5*) and the nitrogen-fixing nitroplasts of the haptophyte alga *Braarudosphaera bigelowii* (*6*).

An important step in the transformation of an endosymbiotic bacterium into a eukaryotic organelle was the establishment of nuclear control over endosymbiont division. Division of mitochondria and chloroplasts is orchestrated by multiprotein machineries that drive the constriction and fission of the inner and outer organellar membranes. These machineries comprise proteins of eukaryotic origin and, to a variable extent, proteins encoded by bacterial division genes that have mostly been transferred to the nucleus (*7*–*10*). In algae with a single or few primary plastids, many nucleus-encoded plastid division proteins show a cell cycle–regulated expression, and it has been suggested that the continuity of plastids in the host cells was originally established by the synchronization of endosymbiont and host cell division (*11*, *12*). The most central bacterium-derived component of the organellar division machineries is the tubulin-like guanosine triphosphatase (GTPase) FtsZ, which forms homopolymers on the inner face of the inner membrane at the prospective division site, the so-called Z-ring (*13*–*15*). Key players in organelle division of eukaryotic origin are dynamin-like proteins (DLPs), which are polymer-forming GTPases that assemble into ring-like structures on the outer face of the outer organellar membranes and constrict upon GTP hydrolysis, leading to membrane fission (*16*, *17*). How the division of chromatophores in *Paulinella* and nitroplasts in *B. bigelowii* is controlled, which are also strictly synchronized with the cell cycle of the host cell, is unknown (*6*, *18*).

Angomonas deanei is a monoxenous trypanosomatid that lives throughout its life cycle as a commensal in the digestive tract of insects. Within the trypanosomatids, *A. deanei* belongs to the subfamily Strigomonadinae that contains besides *Angomonas*, the genera *Strigomonas* and *Kentomonas* (*19*, *20*). All members of this subfamily contain a genomically reduced, β-proteobacterial endosymbiont of the Alcaligenaceae, called *Candidatus* Kinetoplastibacterium spp. (hereafter collectively referred to as Kinetoplastibacteria), that supplies the flagellate host with several essential metabolites such as heme, purines, vitamins, and amino acids (*21*–*24*). In *A. deanei*, a single transfer of an endosymbiont gene to the nucleus has been documented (*22*). However, the gene product, an ornithine cyclodeaminase, is not imported back into the endosymbiont but has acquired glycosomal localization (*25*). Large-scale import of nucleus-encoded proteins is not observed although a few proteins might be imported into the endosymbiont (*25*).

Kinetoplastibacteria likely originated from a single endosymbiosis event around 40 to 120 million years ago (*26*). The symbiont lies free in the host cytosol surrounded by a bacterial inner and outer membrane but no additional host-derived membrane (*27*, *28*). Neither a peptidoglycan (PG) layer surrounding the cell nor a division septum is visible by transmission electron microscopy (TEM); however, treatment of different members of the Strigomonadinae,

[1]Institute of Microbial Cell Biology, Department of Biology, Heinrich Heine University Düsseldorf, Universitätsstr. 1, 40225 Düsseldorf, Germany. [2]Center for Advanced Imaging, Department of Biology, Heinrich Heine University Düsseldorf, Universitätsstr. 1, 40225 Düsseldorf, Germany. [3]Institute of Medical Microbiology and Hospital Hygiene, Medical Faculty and University Hospital Düsseldorf, Heinrich Heine University Düsseldorf, Universitätsstr. 1, 40225 Düsseldorf, Germany.
*Corresponding author. Email: e.nowack@hhu.de
†Present address: Biotrend Chemikalien GmbH, Wilhelm Mauser Str. 41-43, 50827 Köln, Germany.
‡Present address: Institute of Immunology, University Medical Center Rostock, Schillingallee 70, 18057 Rostock, Germany.

including *A. deanei*, with β-lactam antibiotics that interfere with PG cross-linking, results in heavily distorted endosymbionts (*27*, *29*). These findings suggest that a reduced PG layer can be formed. Similar to the plastid in monoplastidic algae and nitroplasts in *B. bigelowii* (*6*), there is strictly one endosymbiont per Strigomonadinae host cell that duplicates just before host cell division, indicating an advanced level of cellular integration (*28*, *30*). However, for some strains within the Strigomonadinae, artificially aposymbiotic cells can be generated by antibiotics treatment if metabolites otherwise produced by the endosymbiont are externally provided (*21*, *29*).

Strigomonadinae are not the only symbiont-harboring trypanosomatids. *Novymonas esmeraldas* (subfamily Leishmaniinae) is only distantly related to the Strigomonadinae but also harbors a β-proteobacterial endosymbiont (*Candidatus* Pandoraea novymonadis, Burkholdariaceae) (*31*). Recently, a host protein has been described that appears to be required for faithful endosymbiont segregation during cytokinesis in *N. esmeraldas* (*32*). However, the number of endosymbionts per host cell is more variable in this species and varies from 0 to 15 (*31*).

How the strict coordination of host and endosymbiont cell cycles in the Strigomonadinae is achieved is unknown. In *Ca.* K. crithidii, the endosymbiont of *A. deanei*, a number of bacterial division genes have been lost during reductive genome evolution (*33*) and FtsZ has been reported to distribute evenly throughout the endosymbiont based on immunofluorescence assay (IFA) and immunogold TEM analyses using antibodies raised against *Escherichia coli* FtsZ (*34*). The finding suggested that in *A. deanei,* FtsZ does not form the characteristic Z-ring, and instead an alternative, unknown mechanism for division is used. Recently, we identified a nucleus-encoded DLP, named ETP9 (short for endosymbiont-targeted protein 9) that localizes at the endosymbiont division site (ESDS) (*25*). ETP9 likely evolved in the Strigomonadinae via duplication of the common trypanosomatid DLP (referred to as *Ad*DLP in *A. deanei*) that is probably involved in mitochondrial fission and endocytosis as its (recently duplicated) orthologs in *Trypanosoma brucei* (*25*, *35*–*37*). However, attempts to generate ETP9 null mutants in *A. deanei* to study its function remained futile, suggesting an essential function of this protein (*25*).

To test the hypothesis that ETP9 is a nuclear effector involved in endosymbiont division, we evaluated the capacity of Kinetoplastibacteria to divide autonomously by comparative genomics. We characterized the subcellular localization of ETP9 throughout the cell cycle and re-evaluated subcellular localization of the endosymbiont-encoded FtsZ using antibodies specifically raised against epitopes from *A. deanei* FtsZ. Furthermore, we studied the phenotype induced by ETP9 knockdowns. The results obtained unambiguously demonstrate that Kinetoplastibacteria lost their capacity to divide autonomously and characterize ETP9 as a nucleus-encoded effector that directly controls endosymbiont division.

RESULTS

Kinetoplastibacteria lack most essential bacterial cell division genes

Since the ability of Kinetoplastibacteria to synthesize PG and form a division septum is uncertain, we analyzed the presence/absence of genes involved in these processes throughout the Kinetoplastibacteria and 25 other β-proteobacteria, including *Ca.* P. novymonadis, the endosymbiont of *N. esmeraldas*, plus an outgroup containing *E. coli*, *Pseudomonas aeruginosa*, *Caulobacter vibrioides*, and *Myxococcus xanthus* (Fig. 1 and table S1).

All enzymes required to (i) synthesize the soluble PG precursors, uridine 5′-diphosphate (UDP)–*N*-acetylglucosamine and UDP-*N*-acetylmuramyl pentapeptide (MurA, MurB, MurC, MurD, MurE, MurF, and DdlA), (ii) attach them to undecaprenyl phosphate at the inner leaflet of the cytoplasmic membrane resulting in the PG precursor lipid II (MraY and MurG), and (iii) flip lipid II to the periplasmic side [MurJ (*38*)], were found to be highly conserved throughout all bacteria analyzed including the Kinetoplastibacteria.

In rod-shaped bacteria, two distinct machineries exist to synthesize PG from lipid II during cell elongation and division, called the "elongasome" and the "divisome," respectively (*39*, *40*). During elongation, the dynamic filaments of the actin-like MreB serve as guides for PG synthesis at the sidewalls, locally guiding a complex of the glycosyltransferase RodA and the transpeptidase peptidoglycan-binding protein 2 (PBP2), that synthesize the glucan backbone and cross-link the peptide side chains of PG, respectively. MreC and MreD apparently regulate PG synthesis by affecting the activity of the RodA-PBP2 complex (*41*). RodZ helps to tether MreB filaments to the inner membrane. However, in *E. coli*, MreB also binds directly to the inner membrane and loss of RodZ is not lethal but results in adoption of a more spherical cell shape (*42*). In the Kinetoplastibacteria, all essential components of the elongasome are encoded and only RodZ is missing. The same pattern is observed for the closely related human pathogen *Bordetella parapertussis*. Together, the data suggest that Kinetoplastibacteria are autonomous for PG biosynthesis during cell elongation.

During cell division, the divisome orchestrates the coordinated invagination of the inner and outer membrane and the generation of an ingrowing annulus of septal PG that represents an integral component of the constricting septal ring. The Z-ring formed by FtsZ serves as the primary guide for divisome assembly (*13*–*15*). The position of the Z-ring is determined by the Min system, composed of the proteins MinC, MinD, and MinE (*43*). Both, the Min system and FtsZ are conserved throughout the Kinetoplastibacteria. However, FtsZ cannot attach to the membrane by itself and needs to bind to membrane-associated proteins to organize into the Z-ring. In *E. coli*, these membrane tethers include FtsA and ZipA (*44*). Although FtsA is present in all bacteria analyzed, it is missing in five of six Kinetoplastibacteria and is only present in *Ca.* K. sorsogonicusi, the endosymbiont of *Kentomonas sorsogonicus* (Fig. 1). ZipA is in general poorly conserved and missing in all bacteria analyzed outside of the γ-proteobacteria (table S1).

In *E. coli*, the divisome consists of over 30 proteins. In addition to FtsZ, FtsA, and ZipA, seven of these proteins form the core division machinery (*40*, *44*). Cells lacking any one of these core proteins form long filaments with several nucleoids before dying. These essential proteins are (i) the glycosyltransferase FtsW and the transpeptidase PBP3 that form a PG synthesizing complex (*45*); (ii) the proteins FtsQ, FtsL, and FtsB that form the FtsBLQ subcomplex, which recruits FtsW-PBP3 to the division septum and likely regulates its activity (*46*); (iii) FtsK, a multispanning transmembrane protein that coordinates chromosome segregation with cell division (*47*); and (iv), FtsN, the last core protein to arrive at the division septum, which helps to trigger cell constriction (*48*). Outside of the Kinetoplastibacteria, these essential divisome components are highly conserved throughout the β-proteobacteria with only FtsL missing in three of the analyzed free-living species. Although not well conserved in sequence, FtsN-like proteins that are structural and functional homologs of FtsN are conserved throughout proteobacteria

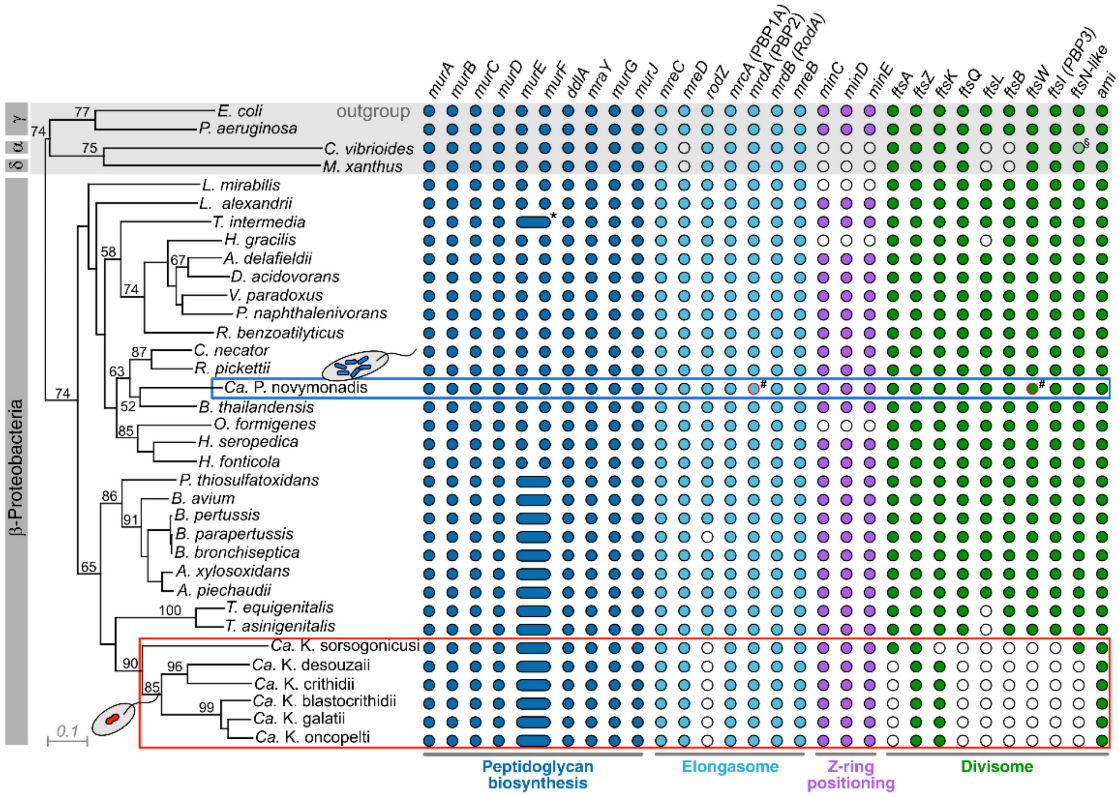

Fig. 1. Kinetoplastibacteria lack most core divisome genes. Presence/absence patterns of various components involved in the biosynthesis of peptidoglycan (PG) precursors, the elongasome, positioning of the Z-ring, and the bacterial divisome. The tree on the left side is the species tree resolved by OrthoFinder (*86*). Numbers at branches represent bootstrap values. On the right side, filled circles indicate presence, empty circles absence of a specific gene. *Elongated spheres represent gene fusions [MurE-MurF fusion proteins are widespread among bacteria (*87*)]. #Red circles: Genes are missing in the RefSeq annotation used for the OrthoFinder analysis but are present in the GenBank annotation of the same genome (accessions: FtsW, PSB92396.1; PBP2, PSB92470.1). §*C. vibrioides* contains an FtsN-like protein (YP_002517459.1) that is a structural and functional homolog of FtsN (*49*) but is in sequence quite divergent and has not been grouped into the same orthogroup as other FtsN-like proteins by OrthoFinder. Endosymbiotic bacteria are highlighted by colored frames: red, Strigomonadinae; blue, *N. esmeraldas*. For accession numbers, full species names, and strain details, see table S1.

(*49*). In the Kinetoplastibacteria, however, almost all core divisome proteins besides FtsZ are missing. FtsK is present in five of six Kinetoplastibacteria, missing only in *Ca.* K. sorsogonicusi, which, in turn, encodes copies of FtsA and an FtsN-like protein that are both missing in all other Kinetoplastibacteria. PBP1B, which is an additional PG synthase found in *E. coli* at the division septum (*40*) is missing in all bacteria analyzed outside of the γ-proteobacteria (table S1). None of the divisome genes missing in the Kinetoplastibacteria appears to be transferred into the nucleus. Blastp analyses using the *Taylorella equigenitalis* orthologs against proteins predicted from the *A. deanei* nuclear genome chromosome-level assembly (*50*) (*E* value cutoff of 1.0×10^{-6}) resulted in no hits. The endosymbiont of *N. esmeraldas*, *Ca.* P. novymonadis, that divides more autonomously, has a complete set of core divisome components (Fig. 1).

The division septum is finally split into two layers that become part of the two newly formed cell poles by the action of PG hydrolases. In *E. coli*, the most prominent proteins with this function are the *N*-acetylmuramyl-L-alanine amidases AmiA, AmiB, and AmiC (*51*). One or several amidases are conserved throughout all bacteria analyzed including the Kinetoplastibacteria.

ETP9 localization appears consistent with a contractile ring around the ESDS

The lack of core divisome genes in the Kinetoplastibacteria [(*33*) and Fig. 1] suggested that these endosymbionts lost the capacity to divide autonomously and require nucleus-encoded factors that help with division. This finding brings the DLP ETP9 into the spotlight. To confirm that the previously observed subcellular localization of the eGFP-ETP9 green fluorescent fusion protein at the ESDS when expressed from the δ-amastin locus (*25*, *52*) ($\Delta\delta\text{-}ama^{egfp\text{-}etp9}$) was not an artefact from overexpression, we generated a cell line in which eGFP-ETP9 was expressed from its endogenous locus ($\Delta etp9^{egfp\text{-}etp9/}etp9$). The endogenously expressed eGFP-ETP9 showed the same localization at the ESDS (Fig. 2A, compare micrographs 1 and 2). However, eGFP-ETP9 abundance was reduced to ~10% compared to the overexpression cell line (fig. S1), and the fluorescence signal at the ESDS

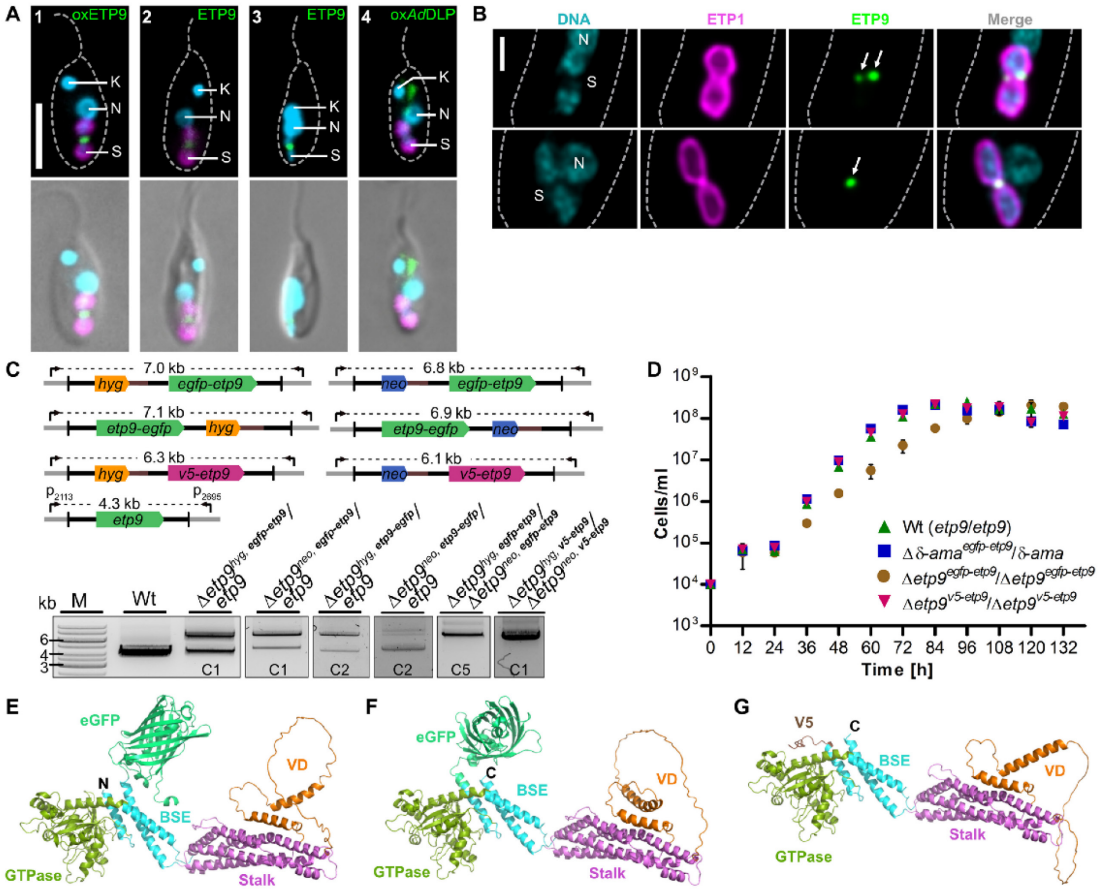

Fig. 2. Subcellular localization and functionality of ETP9 fusion proteins. (**A**) Micrographs of *A. deanei* cells coexpressing the endosymbiont marker mS-ETP1 (Δγ-*ama*$^{mS\text{-}etp1}$) with eGFP-ETP9 from the δ-amastin locus (oxETP9, Δδ-*ama*$^{egfp\text{-}etp9}$, cell 1) or eGFP-ETP9 from the endogenous locus (ETP9, Δ*etp9*$^{egfp\text{-}etp9}$/*etp9*, cell 2) or *Ad*DLP from the δ-amastin locus (ox*Ad*DLP, Δδ-*ama*$^{egfp\text{-}Addlp}$, cell 4), as well as a cell endogenously expressing eGFP-ETP9 alone (ETP9, Δ*etp9*$^{egfp\text{-}etp9}$/Δ*etp9*$^{egfp\text{-}etp9}$, cell 3). Upper row, merged micrographs of epifluorescence channels: green, eGFP; magenta, mScarlet; cyan, Hoechst 33342; lower row, epifluorescence channels merged with differential interference contrast (DIC). Cell outlines as seen by DIC are represented here and in following micrographs by broken gray lines in the fluorescence pictures. Scale bar is 5 μm. (**B**) Confocal microscopy resolves eGFP-ETP9 fluorescence at the ESDS to two dots (upper row) or a single dot (lower row) depending on the progression of the endosymbiont constriction. Cell line: Δδ-*ama*$^{egfp\text{-}etp9}$, Δγ-*ama*$^{mS\text{-}etp1}$. Scale bar is 1 μm. (**C**) Verification by touch-down PCR of *A. deanei* strains expressing *etp9* fusion constructs from the *etp9* locus. Maps provide expected PCR fragment sizes using primer pair 2113/2695. End of insertion cassettes are indicated here and in following figures by vertical black lines. (**D**) Growth of *A. deanei* Wt cells and strains expressing ETP9 fusion proteins (as indicated) in medium without antibiotics was recorded over a period of 132 hours. Plotted are mean and SD from four biological replicates. (**E** to **G**) ColabFold-predicted protein structures for ETP9-eGFP (E), eGFP-ETP9 (F), and V5-ETP9 (G). Models are colored by domain. BSE, bundle signal element; VD, variable domain. For Western blot quantification of ETP9 expression levels from different loci and Southern blot verifications of generated complementation strains, see fig. S1.

was much weaker and could only be seen in 12% of the cells of an actively growing culture, whereas in the overexpression line it is detected in ~50% of the cells (*25*). We attribute this difference in the overexpression line to a better visibility rather than an overexpression artefact. In both cell lines a weak cytosolic fluorescence signal could be observed in some cells that was however difficult to distinguish from background fluorescence, but the signal never formed specific foci other than at the ESDS. Furthermore, localization of eGFP-ETP9 at the ESDS was not dependent on coexpression of the red fluorescent endosymbiont marker mScarlet-ETP1 (*25*) (mS-ETP1, compare micrographs 1 and 2 with micrograph 3). Last, we found that *Ad*DLP, the common trypanosomatid paralog of ETP9, shows a notably different subcellular localization. In most cells, eGFP-*Ad*DLP localizes in the anterior end of the cell (Δδ-*ama*$^{egfp\text{-}Addlp}$), close to an assembly of highly concatenated mitochondrial chromosomes, termed the kinetoplast, possibly at the flagellar pocket (micrograph 4 in Fig. 2A). Sometimes, cells showed a dot-like eGFP-*Ad*DLP signal at the posterior end or in the middle part of the cell, but never at the ESDS.

Confocal microscopy of eGFP-ETP9–overexpressing cells resolved the green fluorescence signal to two dots in optical transects of the peanut-shaped endosymbiont that localize at the cell

envelope on both sides of the mid-cell constriction (Fig. 2B, upper row) and by scrolling through confocal Z-stacks the signal appears as ring-like structure around the ESDS (movies S1 and S2). When the endosymbiont appears slightly elongated and more constricted at mid-cell, apparently closer to division, the eGFP-ETP9 fluorescence becomes reduced to one dot in the center of the constriction site (Fig. 2B, lower row, and movies S3 and S4). This fluorescence pattern would be compatible with the hypothesized contractile DLP ring involved in endosymbiont division.

To test the functionality of recombinant ETP9 constructs, we generated strains in which both copies of *etp9* were replaced by recombinant versions and analyzed their growth behavior (Fig. 2, C and D). Strains in which *etp9* was either replaced by an N-terminal fusion with *egfp-etp9* ($\Delta etp9^{egfp\text{-}etp9}/\Delta etp9^{egfp\text{-}etp9}$) or the simian virus 5–derived small epitope tag *v5-etp9* ($\Delta etp9^{v5\text{-}etp9}/\Delta etp9^{v5\text{-}etp9}$) were readily obtained, indicating that both fusion proteins are generally functional. However, cells in which ETP9 was replaced by eGFP-ETP9 showed slower growth than the wild type (Wt), indicating that the function of ETP9 in this fusion construct is partially impaired. Strains in which a single *etp9* copy was replaced by the C-terminal eGFP fusion construct ($\Delta etp9^{etp9\text{-}egfp}/etp9$) grew only poorly and were not considered for further studies. Structure predictions of the ETP9 fusion proteins using ColabFold (*53*) suggest that in the C-terminal construct (ETP9-eGFP; Fig. 2E), the relatively bulky eGFP tag localizes next to the bundle signaling element (BSE) of ETP9. In other DLPs, GTP binding and hydrolysis results in conformational changes in the GTPase domain, which translates into a swing in the BSE, that may be transmitted as mechanical work (*54*). Thus, a bulky tag in this region might interfere with protein flexibility. Furthermore, polymerization behavior of the DLP could be affected by the bulky tag. To a certain extent, the problem seems to extend to the N-terminal eGFP fusion protein (eGFP-ETP9; Fig. 2F), since N and C terminus are relatively close to each other, but is largely solved when using the much smaller v5-tag (Fig. 2G). Strains in which ETP9 was replaced by v5-ETP9 ($\Delta etp9^{v5\text{-}etp9}/\Delta etp9^{v5\text{-}etp9}$) grew like Wt cells and the same was true for cells overexpressing eGFP-ETP9 from the δ-amastin locus in the *etp9* Wt background ($\Delta\delta\text{-}ama^{egfp\text{-}etp9}$) (Fig. 2D).

FtsZ and ETP9 show cell cycle–dependent localization at the ESDS

To test whether the localization of recombinant ETP9 at the ESDS depends on the cell cycle stage, we first characterized the *A. deanei* cell cycle by microscopic analysis of cells expressing the endosymbiont marker mS-ETP1 (*25*, *52*). As no methods are available yet to synchronize the culture or immobilize division-competent cells allowing for live-cell imaging, the typical cell cycle stages were reconstructed from epifluorescence microscopic analysis of >1000 fixed cells from an actively growing culture (Fig. 3, A and B).

Almost 90% of these cells showed the "normal state" containing one nucleus, one kinetoplast, and one endosymbiont (1N1K1S). Initially, the endosymbiont appears compact and peanut shaped (stage 1). Then, it becomes slightly elongated (stage 2). Next, the endosymbiont divides (1N1K2S; stage 3). Although the two endosymbionts still touch each other, this stage can be identified by a very strong apparent constriction between the two symbionts and/or a slightly tilted position of two symbionts toward each other. In stage 4, the kinetoplast divides and the nucleus increases in size. Cells with two completely separated kinetoplasts were never observed in this stage; however, its shape changes from spherical to two overlapping spheres or a rod. In stage 5, the nucleus divides. When cells reach stage 6, they take on a "heart shape" and complete separation of the two kinetoplasts starts, concomitantly moving to the posterior end of the cell through the gap between the two nuclei. In stage 7, the cells elongate again and cytokinesis proceeds from the anterior end of the cell where a second flagellum formed to the posterior end (stages 7 to 9). At the end of this process, both protist cells contain one nucleus, one kinetoplast, and one endosymbiont again.

Next, we characterized the subcellular localization of recombinant ETP9 and the conserved endosymbiont-encoded FtsZ over the cell cycle. To this end, we generated antibodies against two nonoverlapping peptides of *A. deanei* FtsZ (α-$FtsZ_{pepC}$ and α-$FtsZ_{pepInt}$) and established that they show avid and specific binding to FtsZ in Western blots on *A. deanei* lysate (fig. S2). IFA using α-$FtsZ_{pepC}$ and autofluorescence of *A. deanei* cells coexpressing eGFP-ETP9 with the endosymbiont marker mS-ETP1 (Fig. 3C) demonstrated that initially neither FtsZ nor ETP9 localizes at the ESDS (stage 1a). Then, FtsZ arrives at the ESDS (stage 1b; 13.5% of the cells). At the end of stage 1 (stage 1c), a very weak eGFP-ETP9 signal can be observed that colocalizes with FtsZ (white arrow in the magnified micrograph of the green channel). During stage 2 (4% of the cells), the eGFP-ETP9 signal becomes stronger and still colocalizes with FtsZ at the ESDS of the elongated bacterium. The same pattern is observed when using cells endogenously expressing V5-ETP9 instead of overexpressing eGFP-ETP9 (Fig. 3D).

In later stages (3 to 7), FtsZ and also eGFP-ETP9 migrate to the new constriction sites of the freshly divided endosymbionts, but largely disappear in stages 8 to 9 (fig. S2C). However, this behavior can only be detected in the eGFP-ETP9–overexpressing line, but not the endogenously v5-tagged cell line ($\Delta etp9^{v5\text{-}etp9}/\Delta etp9^{v5\text{-}etp9}$). It is not entirely clear if this difference represents an artifact from ETP9 overexpression or the eGFP tag or is owing to a reduced detectability of proteins in IFA with two different primary antibodies.

Symbiotic cells with reduced ETP9 levels show a weak division phenotype

To test the hypothesis that ETP9 is functionally involved in endosymbiont division, we tried earlier to generate ETP9 null mutants. However, although heterozygous *etp9* deletion mutants ($\Delta etp9/etp9$) could be obtained, generation of homozygous null mutants ($\Delta etp9/\Delta etp9$) failed (*25*). Also changing the strategy using the gene sequence of the remaining *etp9* copy instead of its flanking regions (fr) for homologous recombination (resulting in premature stop codons after amino acid position 372 or 357 of the 680–amino acid protein; see maps in Fig. 4A and fig. S3) did not result in homozygous null mutants. We have shown before that the endosymbiont appears essential for *A. deanei* strain ATCC PRA-265 and generation of aposymbiotic cells by antibiotics treatment failed under all growth conditions tested. Together, these data suggest that ETP9 is essential for endosymbiont maintenance and hence, for survival of the protist.

However, previously an aposymbiotic *A. deanei* strain has been generated from a parental strain apparently less dependent on the endosymbiont (*21*). We obtained this aposymbiotic strain, ATCC 30969, from the American Type Culture Collection (ATCC). Although it grows slower than the symbiotic strain, it can be maintained in brain heart infusion (BHI) medium containing hemin and horse serum (fig. S3). We argued that if loss of ETP9 is lethal because it is essential for endosymbiont maintenance, it should be dispensable in the aposymbiotic strain. Using the same transfection strategy that remained futile for the

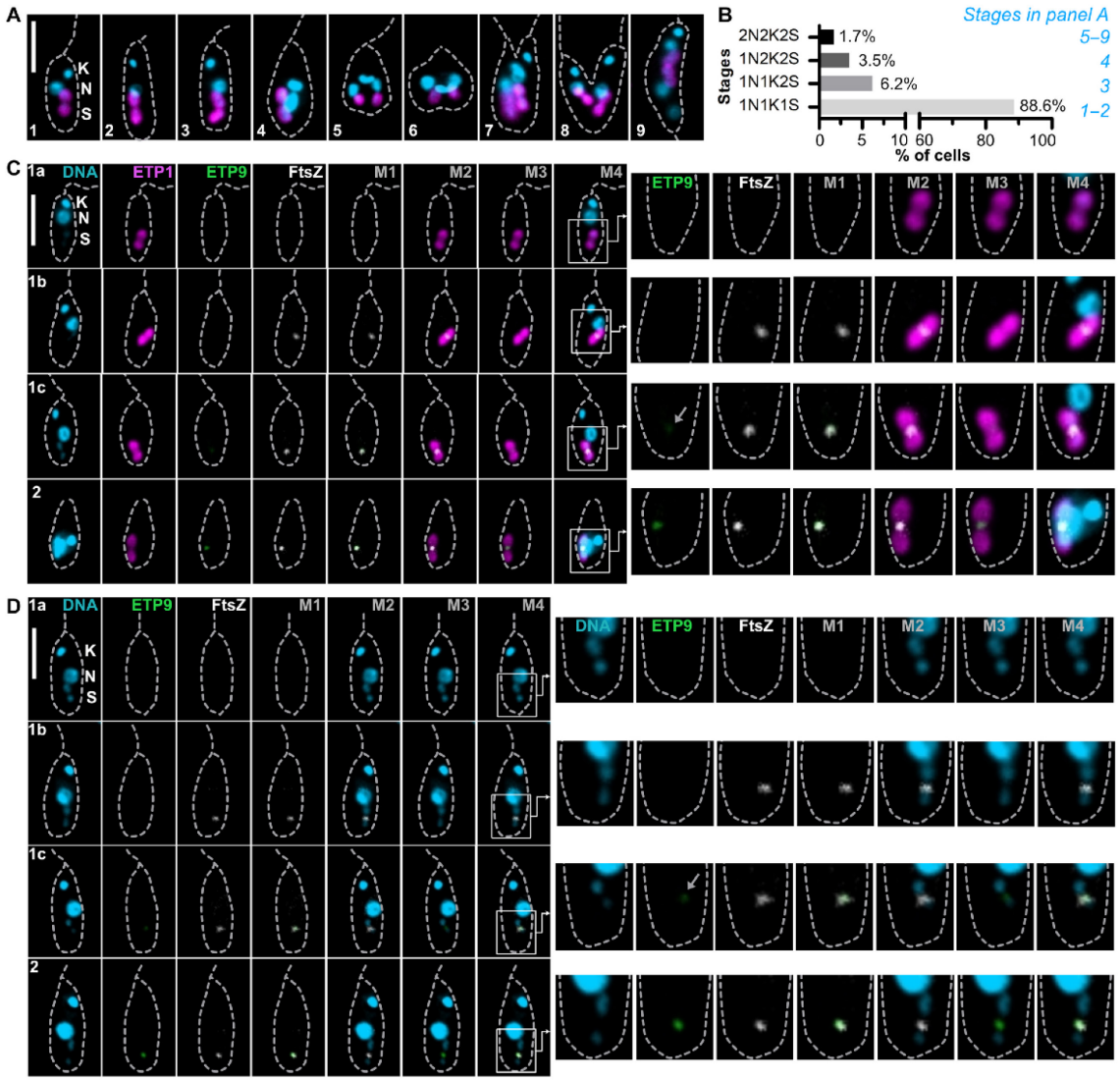

Fig. 3. ETP9 fusion proteins and FtsZ show differential subcellular localization over the cell cycle. (**A**) Reconstruction of the *A. deanei* cell cycle from epifluorescence microscopical analysis of >1000 fixed, Hoechst 33342–stained cells (at 6.5 × 10^7 cells/ml) expressing the endosymbiont marker mS-ETP1 (Δγ-*ama*$^{mS\text{-}etp1}$). (**B**) Quantification of the cell cycle stages analyzed in (A). (**C**) Subcellular localization of FtsZ and eGFP-ETP9 in cell cycle stages 1 and 2, when the endosymbiont divides, was analyzed by IFA using mid-log phase cells coexpressing mS-ETP1 and eGFP-ETP9 (Δγ-*ama*$^{mS\text{-}etp1}$, Δδ-*ama*$^{egfp\text{-}etp9}$). In all micrographs, mScarlet autofluorescence is represented in magenta, eGFP autofluorescence in green, the FtsZ IFA signal in white, and Hoechst 33342–stained DNA in cyan. M1 to M4 are merged pictures of M1, eGFP + FtsZ; M2, mScarlet + FtsZ; M3, mScarlet + eGFP; and M4, all four channels. (**D**) The same analysis was performed for cells in which both endogenous copies of *etp9* were replaced by the *v5-etp9* fusion construct (Δ*etp9*$^{v5\text{-}etp9}$/Δ*etp9*$^{v5\text{-}etp9}$). Localization of V5-ETP9 was detected by IFA here. M1 to M4 are merged pictures of M1, V5-ETP9 + FtsZ; M2, Hoechst 33342 + FtsZ; M3, V5-ETP9 + Hoechst 33342; and M4, all three channels. In all panels, scale bars are 5 μm. K, kinetoplast; N, nucleus; S, endosymbiont. For Western blot verification of the newly generated anti-FtsZ antibodies as well as FtsZ and eGFP-ETP9 localizations at later cell cycle stages, see fig. S2.

symbiotic strain readily yielded homozygous *etp9* null mutants (Δ*etp9*^{hyg}/Δ*etp9*^{neo}) for the aposymbiotic strain (Fig. 4, A and B), which appeared by light microscopy identical to the aposymbiotic Wt (fig. S3).

Microscopic quantification of cells that are in division versus the normal state (1N1K) did not show clear differences between aposymbiotic Wt and heterozygous or homozygous *etp9* deletion mutants (Fig. 4C, left graph and micrographs). We attribute the relatively high number of cells in which only one Hoechst 33342–stained structure can be seen in both, Wt and mutant cells (category "unclear"), to the smaller cell size of the aposymbiotic compared to symbiotic cells resulting in frequent overlapping of nucleus and kinetoplast and thus loss of optical resolution of the two structures.

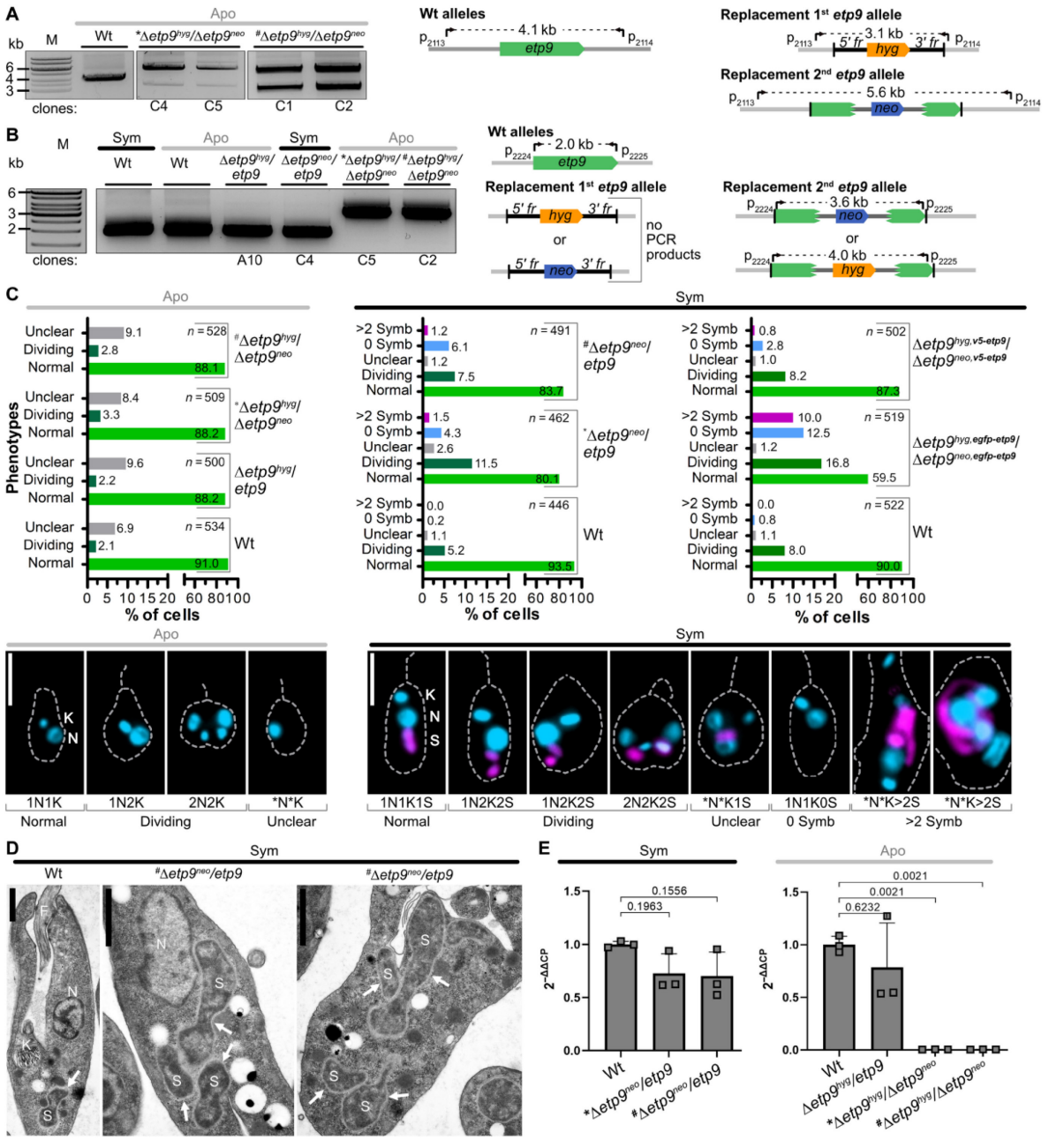

Fig. 4. Symbiotic but not aposymbiotic *etp9* mutants show a mild division phenotype. (**A**) Verification of aposymbiotic (Apo) homozygous *etp9* null mutant strains by touch-down PCR. Strains obtained from independent transfections are marked by superscript * and # symbols. The schematic maps on the right display expected PCR bands for the Wt *etp9* and recombinant alleles using primer pair 2113/2114 binding outside of the fr used for homologous recombination. (**B**) Test for absence of intact *etp9* in *etp9* deletion strains by PCR using primer pair 2224/2225 binding at the start and end of the *etp9* open reading frame. (**C**) Quantification of phenotypes observed in aposymbiotic cells by epifluorescence microscopy. In symbiotic strains, endosymbionts were stained by fluorescence in situ hybridization (FISH) with a bacterium-specific red fluorescent probe. Per strain, ~500 cells were analyzed. Characteristic images of the phenotypes observed are shown below the graphs. Scale bars are 5 μm. (**D**) TEM micrographs of a symbiotic Wt cell and two Δ*etp9*^{neo}/*etp9* mutant cells. White arrows highlight endosymbionts. Scale bars are 1 μm. For more TEM images, see fig. S4. (**E**) RT-qPCR plots show fold gene expression that was calculated by the $2^{-\Delta\Delta CP}$ method where ΔΔCP represents the difference of ΔCP values between mutants and Wt. $N = 3$. Statistics were performed using Student's *t* test. For further PCR and Southern blot confirmation of the generated mutants, see also fig. S3

When the same quantitative microscopic analysis was performed for two independently generated symbiotic heterozygous *etp9* deletion strains ($\Delta etp9^{neo}/etp9$), a slight difference was observed between Wt and mutant cells (Fig. 4C, middle graph). Although in both, Wt and *etp9* deletion strains, >90% of the cells showed either the "normal" 1N1K1S arrangement or one of the described division stages (1N1K2S, 1N2K2S, or 2N2K2S), a low percentage of mutant cells had either no symbiont (4.3 and 6.1%) or more than two endosymbionts often not properly separated or with a filamentous or distorted shape (1.5 and 1.2% in the two mutant cell lines). In the Wt, cells without endosymbiont or more than two/filamentous endosymbionts were virtually not observed [only in 0.2% of >400 cells analyzed no endosymbiont was detected by fluorescence in situ hybridization (FISH)]. The phenotype was more pronounced in the $\Delta etp9^{egfp\text{-}etp9}/\Delta etp9$egfp-etp9 cell line with 12.5 and 10% of the cells showing no endosymbiont or elevated numbers of endosymbionts, respectively, and the phenotype was almost back to Wt in the $\Delta etp9^{v5\text{-}etp9}/\Delta etp9$v5-etp9 cell line (Fig. 4C, right graph).

Also, with the help of TEM, $\Delta etp9^{neo}/etp9$ cells with aberrant shapes and possibly numbers of endosymbionts could be clearly seen, which was never observed in the Wt; however, since only a single plane was analyzed, endosymbiont number per cell cannot be clearly inferred with this method (Fig. 4D and fig. S4). Together, these results suggested that the reduced *etp9* gene dosage in the $\Delta etp9^{neo}/etp9$ mutant results in a protein level reduction that affects proper endosymbiont division in a low percentage of cells. In line with this interpretation, quantitative polymerase chain reaction (qPCR) analysis revealed a 0.7- and 0.8-fold reduction of *etp9* mRNA levels in the heterozygous *etp9* deletion mutants of the symbiotic and aposymbiotic strain, respectively, although this reduction did not reach the $P = 0.05$ significance level (Fig. 4E). As expected, complete absence of *etp9* mRNA was found for homozygous *etp9* null mutants (aposymbiotic cell line).

All attempts to isolate and cultivate heterozygous *etp9* deletion mutants that lost the endosymbiont by limiting dilutions in BHI medium supplemented with hemin and horse serum or a 1:1 mixture of the same medium with spent medium or spent medium only (produced using symbiotic Wt culture) failed, further supporting the obligate nature of the endosymbiont in *A. deanei* strain ATCC-PRA 265.

ETP9 knockdowns resulted in filamentous endosymbionts in distorted host cells

To directly observe the effect of ETP9 depletion in *A. deanei*, we transfected morpholino antisense oligonucleotides (MAOs) specific against *etp9* into the symbiotic and aposymbiotic Wt cells to block *etp9* mRNA translation. This approach has not been used before in *A. deanei* but has been used successfully to generate specific gene knockdowns in diverse protists including trypanosomes (*55*–*57*). Twenty-four hours after independent transfections with two nonoverlapping MAOs against *etp9*, $MAO_{etp9\text{-}1}$, and $MAO_{etp9\text{-}2}$ (Fig. 5A), symbiotic cells showed a clear growth inhibition accompanied by an impairment in endosymbiont division resulting in filamentous endosymbionts in strongly distorted protist cells as well as protists without endosymbionts (Fig. 5, B and C, upper rows). No effect on growth or morphology of the aposymbiotic cells was found following the same treatment (Fig. 5, B and C, lower rows).

Knockdown of α-tubulin using the same protocol with the α-tubulin–specific MAO_{tub} (Fig. 5A), which was performed as a positive control, resulted in symbiotic and aposymbiotic cells in a clear growth inhibition and enlarged, roundish protists (Fig. 5, B and C). A similar phenotype described as "FAT cells" has been observed in *T. brucei* following α-tubulin ablation by RNAi (*58*). Both, symbiotic and aposymbiotic *A. deanei* Wt cells that were mock treated with water replacing MAOs in the transfection protocol, recovered fast from transfection and showed no obvious phenotype (Fig. 5, B and C). The experiment was repeated twice with virtually the same results.

Next, we repeated the ETP9 knockdowns using $MAO_{etp9\text{-}1}$ and $MAO_{etp9\text{-}2}$ in a strain expressing the endosymbiont marker mS-ETP1 for better visualization of the endosymbiont. Twenty-four hours post-transfection, the same phenotype as in the ETP9 knockdowns in Wt background was observed. For both MAOs, the vast majority of protist cells were heavily distorted in shape and contained filamentous endosymbionts or lost the endosymbiont (Fig. 5D and fig. S5). In addition, we used IFA to investigate the subcellular localization of the endosymbiont-encoded FtsZ following ETP9 knockdown and found FtsZ localized in several distinct foci along the filamentous endosymbionts (Fig. 5D), suggesting that several Z-rings form in these cells.

DISCUSSION

Kinetoplastibacteria have the capacity for PG biosynthesis during elongation

Although no PG layer is visible in the Kinetoplastibacteria by TEM, the distorted endosymbiont morphology observed in different members of the Strigomonadinae following treatment with β-lactam antibiotics (*27*, *29*) suggested early on that a reduced PG layer can be formed by the endosymbionts. Our comparative genomic analysis confirmed that all essential components for PG biosynthesis during elongation are present throughout the Kinetoplastibacteria (Fig. 1).

Reduction of the PG layer to invisibility by regular TEM is not unusual in obligate intracellular bacteria (*59*). Failure to detect PG in Chlamydiae by TEM, despite their division being sensitive to β-lactam antibiotics, has been dubbed the "chlamydial anomaly." This conundrum was solved by the observation that complete PG sacculi can be isolated and observed by cryo–electron tomography in some environmental Chlamydia isolates (*60*). Moreover, the human pathogen *Chlamydia trachomatis* was found to transiently form a PG ring structure at the division site, which is required for cell constriction, by mass spectrometric detection of muropeptides and fluorescence microscopic studies of cells following metabolic labeling of PG using click chemistry (*61*, *62*). Also, in *Candidatus* Moranella endobia, the innermost of two nested bacterial endosymbionts in mealybugs, PG that is invisible by regular TEM could be visualized by a similar metabolic labeling approach (*63*).

Many plastids that became integrated into eukaryotic cells more than a billion years ago apparently still form a PG layer. Originally thought to be restricted to the peculiar plastids of the Glaucophytes (*64*), called cyanelles, it is clear today that also many Streptophytes and some Chlorophytes encode a complete enzymatic toolkit for PG biosynthesis on the nuclear genome (*65*, *66*). Metabolic PG labeling demonstrated that chloroplasts in the moss *Physcomitrella patens* and the charophyte *Klebsormidium nitens* are surrounded by a PG layer that is invisible by normal TEM (*67*, *68*). Deletion of genes involved in PG biosynthesis or treatment with different inhibitors of PG biosynthesis caused defects in chloroplast division here (*68*–*71*).

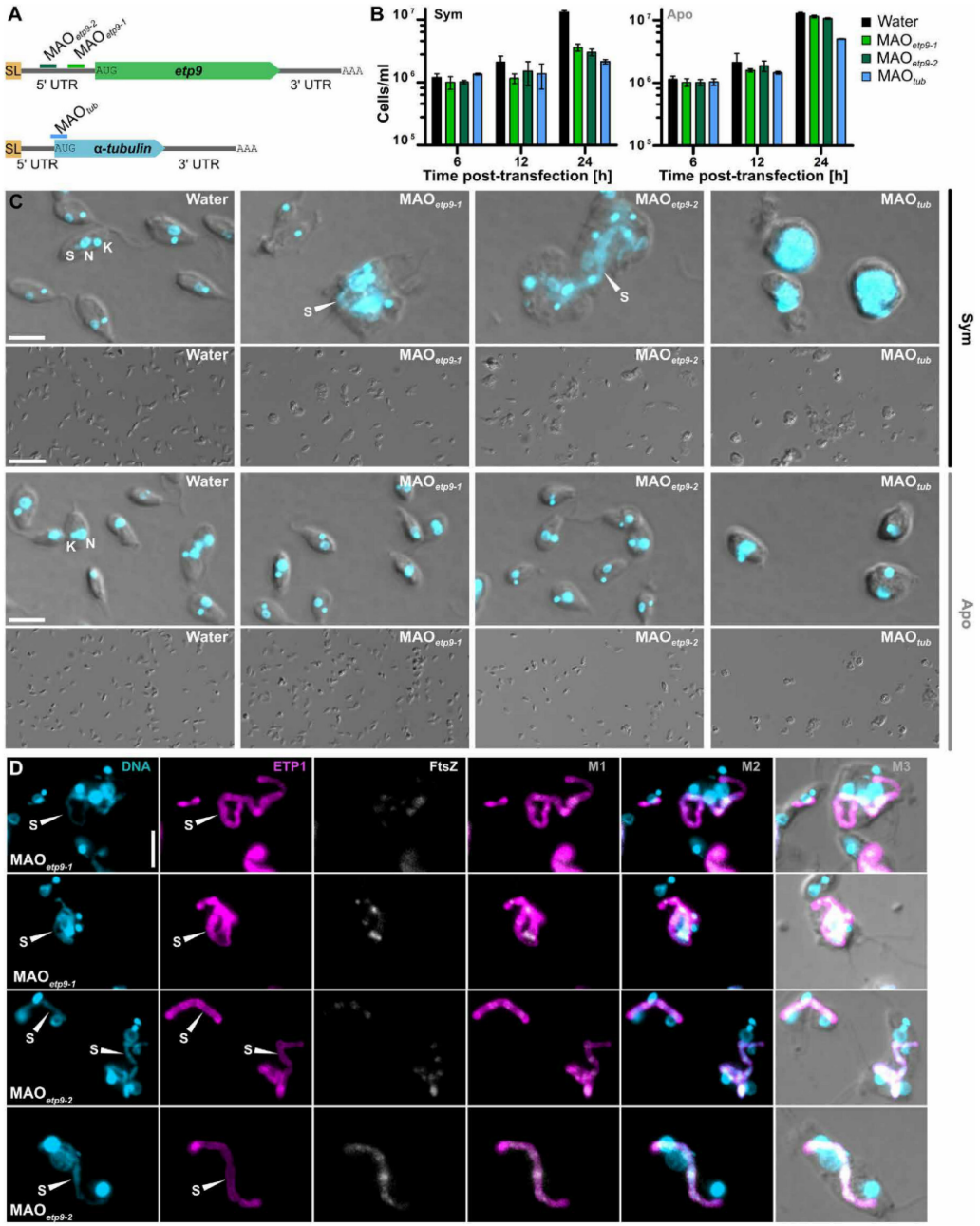

Fig. 5. Knockdown of ETP9 results in formation of filamentous endosymbionts and distorted host cells in symbiotic but not aposymbiotic *A. deanei* cells. (**A**) Schematic representation of the binding site of the three 25-mer MAOs used in this assay. SL, spliced leader; UTR, untranslated region. (**B**) Cell counts of symbiotic (Sym) and aposymbiotic (Apo) *A. deanei* cultures 6, 12, and 24 hours post-transfection with MAOs or water. (**C**) Micrographs of the same cells 24 hours post-transfection. For each treatment, an overview DIC image (lower rows) and a detail picture (overlay of Hoechst 33342 fluorescence and DIC, upper rows) are provided. Scale bars are 5 μm for the detail and 25 μm for the overview pictures. (**D**) Micrographs of *A. deanei* cells expressing the endosymbiont marker mS-ETP1 (Δδ-*ama*$^{mS\text{-}etp1}$) 24 hours post-transfection with MAO$_{etp9\text{-}1}$ or MAO$_{etp9\text{-}2}$ (as indicated), in which subcellular localization of FtsZ was analyzed by IFA before microscopy (as in Fig. 3, C and D). For each treatment, two sets of micrographs of the Hoechst 33342 fluorescence (DNA), mScarlet signal (ETP1), and IFA signal (FtsZ) are displayed. M1 to M3 are merged pictures of M1, mScarlet + IFA signal; M2, all three fluorescence channels; and M3, all three fluorescence channels + DIC. Note the long, filamentous endosymbionts highlighted by white arrowheads in the MAO$_{etp9}$-treated symbiotic cells in (C) and (D) and several FtsZ foci per filamentous endosymbiont in (D). For overview pictures of the cell populations generated for (D) without visualization of FtsZ, see fig. S5.

Gene losses in Kinetoplastibacteria imply loss of autonomous division capacity

In contrast to the elongasome, the divisome is nearly completely lost in the Kinetoplastibacteria (Fig. 1). Gene losses included *ftsW* and *ftsI*, which encode the PG synthase complex responsible for septal PG biosynthesis. Thus, a division septum cannot be formed by endosymbiont-encoded enzymes, strongly suggesting a loss of division autonomy. Similar genome reduction patterns are not observed in any of the remaining β-proteobacterial genomes analyzed including the genome of the endosymbiont *Ca.* P. novymonadis that contains a reduced, yet slightly larger genome than the Kinetoplastibacteria [~1.2 Mbp versus 0.83 to 0.74 Mbp (*24*, *72*)] and shows a more independent division behavior inside of its trypanosomatid host. Also, the closest known relatives of the Kinetoplastibacteria, bacteria of the genus *Taylorella*, encode an almost complete set of core divisome components, lacking only FtsL, which does not seem to interfere with their ability to divide. Both species in this genus are pathogens populating the urogenital tract of Equidae, at least *T. equigenitalis* has a facultative intracellular lifestyle, and both feature relatively small genomes of ~1.6 Mbp, encoding ~1.500 proteins (*73*). Thus, loss of the nearly entire core divisome appears to have occurred specifically in the Strigomonadinae-associated common ancestor of the Kinetoplastibacteria with a little variation between the species. Together, these findings suggest that the host evolved nuclear factors that compensate for the loss of bacterial division genes, restoring the ability of the endosymbiont to divide inside the host cell.

ETP9 is a nucleus-encoded effector essential for endosymbiont division

In a previous study, we identified the Strigomonadinae-specific DLP, ETP9, as a candidate protein to be involved in endosymbiont division (*25*). Here, we present several lines of evidence that unambiguously characterize ETP9 as a nuclear effector protein that is essential for endosymbiont division. This claim is based on the following findings.

(i) Recombinant ETP9 is recruited to the ESDS in a cell cycle–dependent manner (Fig. 3C) and appears to form a ring that constricts as endosymbiont division progresses (Fig. 2B). (ii) Homozygous *etp9* deletion mutants can be readily obtained in aposymbiotic, but, using the same transfection strategy, not in symbiotic *A. deanei* cell lines where ETP9 appears essential (Fig. 4, A and B). (iii) In heterozygous *etp9* deletion mutants in the symbiotic cell line, which contain reduced *etp9* mRNA levels, a low percentage of cells shows aberrant endosymbiont numbers and/or shapes (Fig. 4, C to E). (iv) MAO-induced ETP9 depletions of symbiotic *A. deanei* cells result in the majority of protists in either filamentous endosymbionts or complete loss of the endosymbiont (Fig. 5, C and D, and fig. S5).

Furthermore, we found that endosymbiont division is a precondition for proper cytokinesis of the protist cell. *A. deanei* cells in which the endosymbiont cannot divide are heavily distorted and can be several times the size of Wt cells (Fig. 5C and fig. S5). Aposymbiotic daughter cells that eventually form from a mother cell with a division-impaired endosymbiont show abnormal shapes and sizes and sometimes appear to lack genetic compartments. Nevertheless, successful endosymbiont division does not seem to represent a strict checkpoint for host cytokinesis as described for some algae with primary plastids. In the glaucophyte *Cyanophora paradoxa* and the red alga *Cyanidioschyzon merolae*, mitosis is only initiated after successful division of the plastid (*74*).

Last, our data suggest that endosymbiont division is the primary and likely only function of ETP9. ETP9 evolved in the Strigomonadinae and is not found in trypanosomatids without endosymbiont (*25*). In the aposymbiotic strain, *etp9* null mutants could be readily obtained and neither these nor MAO-induced ETP9 knockdowns showed any obvious phenotypes by light microscopy here (Figs. 4, A to C, and 5, B and C; and fig. S3). Whether *etp9* deletion is associated with any ultrastructural changes in the aposymbiotic cell has not been analyzed in detail yet. However, recombinant ETP9 shows a very specific localization at the ESDS plus dilute cytosolic signals but is never observed in secondary foci on other membranes. This localization pattern is very different from the one observed for the common trypanosomatid ETP9 paralog, *Ad*DLP. *Ad*DLP is observed mostly next to the kinetoplast (Fig. 2A, micrograph 4), resembling the strong signal in IFA studies of its ortholog, *Tb*DLP, next to the kinetoplast reported for *T. brucei* (*36*).

ETP9 might be part of a more complex endosymbiont division machinery

The observed localization patterns of FtsZ and recombinant ETP9 throughout the cell cycle (Fig. 3C) suggest that ETP9 is recruited from a predominantly cytosolic location transiently to the ESDS, following the formation of the Z-ring. Thus, as in plastids, FtsZ appears to act early and the nucleus-encoded DLP late during endosymbiont division (*8*). We assume that similar to the situation in plastids and some mitochondria, FtsZ associates with and functions on the inner face of the inner endosymbiont membrane, whereas the DLP ETP9 associates with and functions on the outer face of the outer membrane. The observed formation of several FtsZ foci along the filamentous endosymbionts following ETP9 knockdown suggests that Z-ring formation is independent of the presence of ETP9 but is not sufficient for endosymbiont division. What directs ETP9 specifically to the outer endosymbiont membrane and what defines the time point of its recruitment are unknown yet. Factors that may contribute are the inward curvature of the bacterial membrane, its unique lipid composition, or proteinaceous interaction partners. In our screening for endosymbiont-targeted host proteins, we identified two other nucleus-encoded proteins, ETP2 (of unknown function) and ETP7 (a predicted PG hydrolase), that transiently localize at the ESDS (*25*), suggesting that ETP9 might be part of a more complex endosymbiont-division machinery.

The conservation of the Min system in the reduced endosymbiont genome suggests that this system is functional and determines the position of the Z-ring. The Min system also still functions in many plastids to position the Z-ring (*12*, *75*, *76*) that lost, with a little variation between different Archaeplastida lineages, most other bacterial core divisome genes (*7*, *77*). Also, in many mitochondria, the Min system is conserved (*10*). However, most Kinetoplastibacteria lost FtsA that is required to tether FtsZ to the inner membrane in *E. coli*. This finding raises the question if the Z-ring can form autonomously or needs nucleus-encoded factors. Notably, all Kinetoplastibacteria still encode one protein known to interact with FtsZ and spanning the inner bacterial membrane (an FtsN-like protein in *Ca.* K. sorsogonicusi and FtsK in the remaining Kinetoplastibacteria). These proteins have the potential to link the Z-ring with proteins in the periplasm. Proteins spanning the outer membrane and interacting with FtsK or FtsN in the periplasm would be able to convey topological information between the inside and outside of the endosymbiont. However, such proteins have not been identified yet.

In plastids, the Z-ring forms at the inner face of the inner envelope membrane with the help of ARC6, which is an inner transmembrane protein of cyanobacterial origin. ARC6 recruits the eukaryote-derived

outer transmembrane protein PDV2 through interaction in the intermembrane space. Last, PDV2 recruits the soluble DLP DRP5B (also called ARC5) to the outer face of the outer envelope membrane. Reciprocal interactions between inside and outside localized components of the division complex result in a concerted constriction of the double ring machinery and, lastly, plastid fission (*78*, *79*).

In Glaucophytes and the moss *P. patens*, PG hydrolysis by the amidase DipM is essential for cleaving the septal PG and thus, enabling freshly duplicated plastids to separate (*80*). Since throughout the Kinetoplastibacteria an amidase gene is conserved (Fig. 1), likely nucleus-encoded proteins restore the ability to synthesize septal PG that later covers the cell poles of the freshly divided endosymbionts.

Kinetoplastibacteria are in the gray zone between endosymbiont and organelle

Together, our data characterize the Kinetoplastibacteria as an intriguing intermediate between a genetically autonomous bacterial endosymbiont and a genetically integrated organelle. Although a dedicated import system for nucleus-encoded proteins apparently has not evolved (*25*), Kinetoplastibacteria lost essential components of the bacterial cell division machinery that are vital for their ability to propagate. These losses are functionally compensated by at least one nucleus-encoded protein, ETP9, that became specialized for endosymbiont division and likely forms part of a more complex endosymbiont division machinery comprising endosymbiont-encoded and further nucleus-encoded components. Whether the nucleus-encoded components interact with the endosymbiont exclusively from the outside, as assumed for ETP9, or penetrate also into the periplasm (possibly the predicted PG hydrolase ETP7) or the bacterial cytosol is currently unknown.

The chimeric endosymbiont division machinery of dual genetic origin that evolved evinces some remarkable similarities with plastid and mitochondrial division machineries (e.g., the use of a combination of the bacterial FtsZ and a eukaryote-derived DLP). However, it also shows that no endosymbiotic gene transfer of division-related genes is required to establish nuclear control over endosymbiont division, but it suffices that functions essential for cell division are lost from the endosymbiont genome and compensated for by neofunctionalized host genes.

MATERIALS AND METHODS

Microbial strains and growth conditions

A. deanei ATCC PRA-265 (symbiotic strain) and *A. deanei* ATCC 30969 (aposymbiotic strain) were obtained from the ATCC (https://atcc.org/). Both strains were grown in BHI (Sigma-Aldrich) medium supplemented with hemin (10 μg/ml; Sigma-Aldrich) at 28°C. For aposymbiotic strains, the medium was additionally supplemented with 10% (v/v) horse serum (Sigma-Aldrich). Cultures were passaged twice a week, once they reached a cell density of 1×10^8 cells/ml for the symbiotic strain and 1×10^7 cells/ml for the aposymbiotic strain. Cell counting was performed with a Multisizer 4e cell counter (Beckman Coulter). For plasmid amplification, *E. coli* TOP10 cells were used, grown in lysogeny broth (LB) medium containing ampicillin (100 μg/ml).

Construction of plasmids

Maps of plasmids used or generated in this study are provided in Fig. 6; primers used for plasmid generation are listed in table S2. Generation of plasmids pAdea043, pAdea119, and pAdea303 has been described earlier (*25*). For pAdea308 (used for the generation of *etp9* heterozygous mutants), the pUMA 1467 backbone (*81*) was amplified from pAdea301 using the primer pair 2178/2179; around 750-bp *etp9* 5′ and 3′ fr were amplified from *A. deanei* gDNA with primer pairs 2180/2186 and 2185/2189, respectively; and *neo*^{r} was amplified from pAdea259 with primer pair 2187/2188. All fragments were assembled by the Gibson assembly method as described earlier (*25*).

pAdea340 was generated by amplifying the *Addlp* gene from *A. deanei* gDNA using primer pair 2305/2306 and cloned into pAdea043 by a Golden Gate approach as described earlier (*25*, *82*).

For pAdea368 (used for the generation of homozygous *etp9* mutants), the pUMA 1467 backbone was amplified from pAdea260 using primer pair 2555/2556. Approximately 1-kb fragments covering the first half and the second half of the *etp9* gene, respectively, were used in this plasmid as 5′ and 3′ fr for homologous recombination. Both fragments were amplified from pAdea259 with primer pairs 2557/2558 and 2561/2562, respectively. A fragment containing 422 bp of the γ-amastin 5′ fr including the spliced leader (SL)–donor sequence (γ-SL), *hyg*^{r}, and the intergenic region between glyceraldehyde-3-phosphate dehydrogenase (GAPDH) I and II (gapdh ir) was amplified from pAdea260 using primer pair 2559/2560. All fragments were assembled by the Gibson method. Similarly, pAdea369 was generated by amplifying a fragment comprising the 252-bp 5′ fr of the δ-amastin gene containing the SL-donor sequence (δ-SL), *neo*^{r}, and gapdh ir from pAdea008 (=pAEX-EGFP) (*52*) using primer pair 2560/2564, and amplifying an approximately 1-kb-long fragment covering the first half of the *etp9* gene from pAdea259 using primer pair 2557/2563. The remaining fragments were used from PCR products generated for the assembly of pAdea368. All the fragments were assembled by the Gibson assembly protocol.

For *etp9* complementation analysis with *egfp-etp9*, pAdea379 was generated by amplifying pUMA 1467 backbone from pAdea258 with primer pair 2671/2672; around 1-kb *etp9* 5′ fr and around 450-bp *etp9*-SL were amplified from *A. deanei* gDNA with primer pairs 2673/2674 and 2677/2678, respectively; a fragment containing *hyg*^{r} and gapdh ir was amplified from pAdea260 using primer pair 2675/2676; and *egfp-etp9* from pAdea258 using primer pair 2679/2680. All fragments were assembled by Gibson assembly. Similarly, for pAdea380, around 1 kb of 5′ fr of the *etp9* gene was amplified from *A. deanei* gDNA using primer pair 2673/2681 and a fragment containing *neo*^{r} and gapdh ir from pAdea258 using primer pair 2676/2682. The remaining fragments were used from PCR products generated for the assembly of pAdea379. All fragments were assembled by the Gibson assembly protocol.

For *etp9* complementation analysis with *etp9-egfp*, pAdea382 was generated by amplifying the pUMA 1467 backbone from pAdea258 using primer pair 2683/2684, *etp9-egfp* from pAdea259 with primer pair 2885/2686, around 1-kb *etp9* 3′ fr and around 550-bp *etp9* 3′ utr from *A. deanei* gDNA using primer pairs 2691/2692 and 2687/2688, respectively, and a fragment containing *hyg*^{r} and gapdh ir from pAdea260 with primer pair 2689/2690. All fragments were assembled by the Gibson assembly protocol. Similarly, for pAdea381, around 550-bp *etp9* utr 3′ was amplified from *A. deanei* gDNA with primer pair 2687/2693 and a fragment containing *neo*^{r} and gapdh ir from pAdea258 using primer pair 2690/2694. The remaining fragments were used from PCR products generated for the assembly of pAdea382. All fragments were assembled by the Gibson assembly protocol.

For *etp9* complementation analysis with *v5-etp9*, primer pair 2836/2837 including the *v5* sequence was used to generate pAdea388 and pAdea389 using pAdea379 and pAdea380 as templates, respectively.

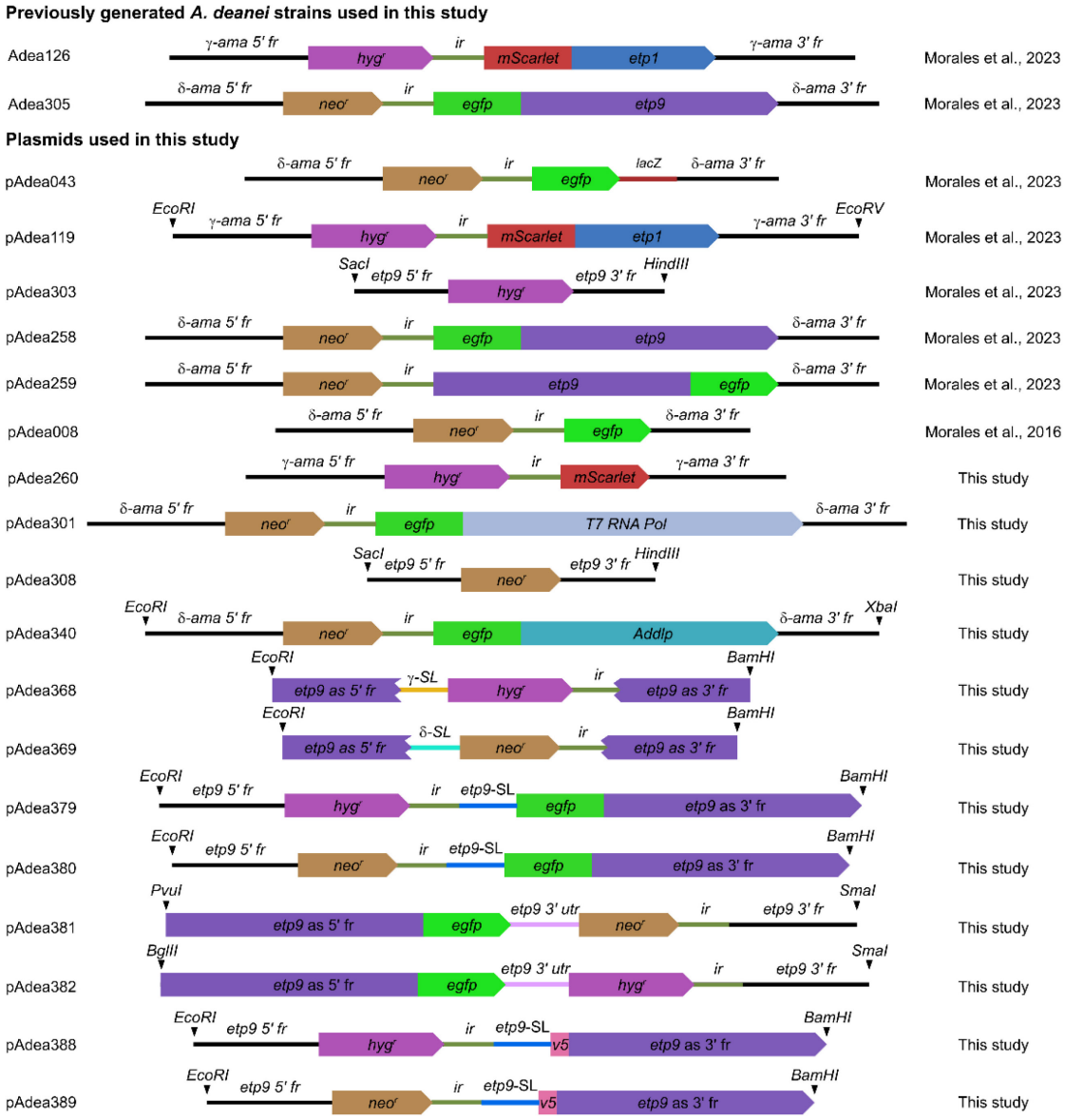

Fig. 6. *A. deanei* (Adea) strains and transfection plasmid (pAdea) generated and used in this study. The figure displays maps of the modified genetic loci in relevant Adea strains and insertion cassettes of relevant pAdea plasmids. pAdea043 was used as a backbone for inserting *Addlp* by Golden Gate cloning resulting in pAdea340. fr, 0.75 to 1 kb fr used for homologous recombination; ir, intergenic region between the genes coding for GAPDH I and GAPDH II; γ-SL, δ-SL, and *etp9*-SL 5′ fr including the SL donors of the γ- and δ-amastin, and *etp9* gene, respectively.

All plasmids were verified by colony PCR and sequencing (Microsynth AG, Balgach, Switzerland).

Generation of transgenic cell lines

A. deanei cells were transfected as described before (*25*). In brief, a total of 1×10^7 cells was harvested and resuspended in 18 µl of P3 primary cells solution (Lonza), 2 µl of the restricted cassette (2 to 4 µg of DNA; for restriction enzymes used, see Fig. 6) was added, and cells were pulsed with the program FP-158 using the Nucleofector 4D (Lonza). Cells were immediately transferred into 5 ml of fresh medium and incubated at 28°C for 6 hours. To select clonal cell lines, cells were diluted 10-fold in the same medium containing the selection drug(s) (i.e., G418 at 500 µg/ml and hygromycin B at 500 µg/ml, final concentration) and distributed in 200-µl aliquots over the

wells of a 96-well plate. Following incubation at 28°C, typically within 5 to 6 days, clonal cell lines were observed as indicated by turbidity in a few wells per plate. These cell lines were isolated and tested for the desired genetic modifications.

Verification of correct genomic insertions by PCRs, Southern blots, and sequencing

Genomic insertion of the transfected cassettes at their target locus by homologous recombination was verified by Phusion and touchdown PCRs using a combination of primers that anneal to genomic regions upstream and downstream of the fr used for homologous recombination (see table S2).

Southern blot analyses were performed as described earlier (*25*). In brief, gDNA was isolated from 5-ml *A. deanei* culture. Around 7.5 μg of gDNA was digested overnight with the restriction enzymes Not I and Kpn I (New England Biolabs) at 37°C. Digested DNA was resolved on a 0.8% (w/v) agarose gel and transferred to a nylon membrane (Nytran N Nylon Blotting Membrane, 0.45 μm; GE Healthcare Life Sciences). Digoxigenin (DIG)–labeled probes against *etp9*, *hyg*^{r}, and *neo*^{r} (G418) were generated using the primer pairs indicated in table S2, hybridized to the target DNA using a hybridization temperature of 53°C for all probes, and developed according to the protocol supplied with the DIG-High Prime DNA Labeling and Detection Starter Kit II (Roche Applied Science). Chemiluminescence was detected in a Chemidoc MP (Bio-Rad).

For further verification of correct genomic insertion in heterozygous *etp9* mutants, purified PCR products of genomic fragments were cloned in pJET 1.2 blunt vector (Thermo Fisher Scientific). For primers used, see table S2. The ligated vector was transformed into *E. coli* TOP10 and clones were selected on LB agar plates containing ampicillin (100 μg/ml). Clones were verified by colony PCR; plasmid DNA was isolated using the NucleoSpin Plasmid Kit (Macherey-Nagel). DNA sequencing was performed according to the instructions provided by Microsynth AG, Balgach, Switzerland (https://microsynth.com/home-ch.html).

Epifluorescence microscopy

Fluorescence microscopy was performed as described in Morales *et al.* (*25*). Mid-log phase cultures of *A. deanei* were mixed with final concentration of 4% (w/v) paraformaldehyde (PFA) in phosphate-buffered saline (PBS) and incubated for 15 min in the dark at room temperature (RT), washed twice with PBS, and resuspended in PBS. Fifteen microliters of the mixture was spotted on poly-L-lysine–coated glass slides and incubated with Hoechst 33342 (30 μg/ml) in PBS for 15 min. After incubation, slides were washed two to three times with PBS, and last, samples were mounted in 8 to 10 μl of Slowfade Diamond (Thermo Fisher Scientific). Images were acquired on an Axio Imager M.1 (Zeiss, Oberkochen, Germany) using an EC Plan-Neofluar 100×/1.30 Oil Ph3M27 or 40×/1.3 oil Ph3 objective (Zeiss) and processed with Zen Blue version 2.5 and ImageJ version 2.0 softwares.

For quantification of division phenotypes, precultures were inoculated in 5 ml of medium without antibiotics followed by main cultures inoculated in the same way. Cells were counted, fixed, and analyzed as described above.

Indirect IFA

All incubation steps were performed at RT in the dark. Cells from early to mid-log phase cultures were fixed with 4% (w/v) PFA (final concentration) for 15 min. Cells were washed three times in PBS, resuspended in PBS, 20 μl were spotted on poly-L-lysine–coated glass slides, and incubated for 15 min. Unbound cells were removed; then, cells were permeabilized for 20 min in 10 μl of PBS + 0.2% (v/v) Triton X-100 (PBST) and washed for 5 min in PBS. Blocking was performed with 1% blocking solution (BS; albumin bovine fraction V, pH 7.0, Serva) in PBS for 45 min. After blocking, 15 μl of a 1:80 dilutions of anti-FtsZ$_{pepC}$ (see fig. S2) or anti-V5 [immunoglobulin G1κ (IgG1κ; monoclonal antibody SV5-P-K, mouse, Chromotek, catalog no. v5ab, RRID:AB_2868500] primary antibodies in 1% BS were applied and incubated for 1.5 hours. After incubation, cells were washed three times with 1% BS. Next, 15 μl of a 1:500 dilution of secondary antibodies (IgG, polyclonal, anti-rabbit goat, Abberior STAR RED, excitation of 638 nm, abberior, catalog no. STRED-1002-500UG, RRID:AB_2833015 or m-IgGκ BP CFL 488, anti-mouse, Sc516176, Santa Cruz Biotechnology) in 1% BS were applied and incubated for 1 hour. After incubation, cells were washed three times with 1% BS. When both primary antibodies were used in combination on the same cells, anti-V5 was applied first followed by anti-FtsZ$_{pepC}$ with 1.5-hour incubation and three washes for each antibody. Then, anti-mouse followed by anti-rabbit secondary antibodies were applied with 40-min incubation and three washes for each antibody. For mS-ETP1 and eGFP-ETP9, autofluorescence was detected. After antibody staining, 15 μl of Hoechst 33342 (30 μg/ml) in PBS was applied, incubated for 10 min, and washed two times with PBS. Cells were finally mounted with 8 to 10 μl of antifade reagent, SlowFade Diamond (Thermo Fisher Scientific) and imaged with an Axio Imager M.1 as described before. Around 1000 cells were analyzed with Zen Blue version 2.5 software.

Fluorescence in situ hybridization

For quantification of division phenotypes of symbiont-harboring strains, precultures were inoculated in 5-ml BHI supplemented with hemin without antibiotics followed by main cultures inoculated in the same way. Cells were counted and fixed as described above, then washed twice with PBS, and resuspended in an appropriate volume of PBS. Twenty microliters of the suspension was spotted onto gelatin-coated glass slides. From this step onward, blind experiments were performed and identity of the samples reassigned only after microscopic analysis was completed. Cells were dehydrated with a series of 50, 80, and 100% ethanol with 3-min incubation steps in each concentration. Twenty microliters of the universal bacterial probe Eub338 (5′-GCTGCCTCCCGTAGGAGT-3′) against the 16S bacterial rRNA (*83*, *84*) coupled at its 5′-end to Cy3 diluted to 50 ng/μl in hybridization solution [900 mM NaCl, 20 mM tris-HCl (pH 7.2), 35% formamide, and 0.01% SDS] was applied and incubated for ~3 hours in the dark at 46°C in a moist chamber. Excess probe was washed off in two brief wash steps with wash buffer [80 mM NaCl, 20 mM Tris-HCl (pH 7.2), and 0.01% SDS]; then, cells were stringently washed in wash buffer for 25 min in the dark at 48°C in a moist chamber. Last, cells were washed three times in MilliQ water and stained with Hoechst 33342 (30 μg/ml), washed twice with PBS again, and mounted in 8 to 10 μl of SlowFade Diamond reagent (Thermo Fisher Scientific). Images were acquired with an Axio Imager M.1. Quantification was performed with around 500 cells on Zen Blue version 2.5. Areas of the microscopic slide with clumped or overlapping cells were excluded and only areas with properly separated cells were imaged and analyzed.

Confocal microscopy

Samples were prepared as described for epifluorescence microscopy except that poly-L-lysine was spotted on high precision microscope coverslips (L × W, 22 × 22 mm; no. 1.5H; thickness, 170 μm;

Marienfeld, VWR) and all steps were performed on the coverslips. Later, the coverslip was inverted on a glass slide. Imaging was performed at an inverted confocal microscope Leica TCS SP8 (STED 3X) with standard settings as described in reference (*25*). For movies, confocal data were deconvolved with "Huygens Professional version 23.10.0p7 64b" using default settings for confocal datasets (e.g., classic CLME, quality threshold of 0.01, 30 iterations at maximum), except the manual mode threshold for background extraction was set based on 3/4th of the cytosolic background signal. Signal-to-noise was used at the software calculated values, ranging from 6.2 to 11.20 depending on individual signal intensity and quality. Resulting deconvolved and raw data were linear contrast adjusted, annotated, and animated as movie series using "Fiji."

Growth curves

Respective *A. deanei* strains were inoculated in 5 ml of medium without antibiotics and grown until cultures reached mid-log phase. From this preculture, 1×10^4 cells/ml were inoculated in 25 ml of medium with three to four biological replicates (as indicated) and incubated at 28°C over a period of 6 days. Samples were collected every 12 hours, fixed with 4% PFA, and counted as described before.

TEM

Twenty-five milliliters of *A. deanei* cultures were grown as described for the FISH analysis. Cells were harvested at 900*g* for 3 min, washed twice in PBS. Cells were fixed with 2.5% (v/v) glutaraldehyde in 0.1 M cacodylate buffer pH 7.4 for 1 hour at RT, washed twice in the same buffer, and last, remaining glutaraldehyde was quenched by two washes with 50 mM glycine in 0.1 M cacodylate buffer. Cells were then resuspended in preheated 10% (w/v) gelatin (Dr. Oetker) in 100 mM phosphate buffer pH 7.4, pelleted at 4700*g* for 5 min, and the gelatin-enclosed pellet kept on ice for curing. The gelatin-embedded cell pellets were washed twice in 0.1 M cacodylate buffer, fixed again with 2% (w/v) osmium tetroxide in 0.1 M cacodylate buffer for 1 hour at RT, and subsequently washed four times in the same buffer. Cells were dehydrated in a series of 50, 70, 80, 90, 96, and 100% (v/v) ethanol on ice for 10 min per concentration. Dehydration was further performed twice for 10 min on ice with 100% acetone. Cells were infiltrated with a 1:1 ratio of Epon (Epon_812 substitute, Sigma-Aldrich):acetone for 1 hour, followed by a 3:1 ratio for 2 hours at 4°C. Subsequently, cells were infiltrated with freshly prepared pure Epon for 30 min at RT, then overnight at 4°C, and last, successively for 1 hour and for 2 hours at RT once more. Next, the Epon was polymerized for 72 hours at 65°C. Thin sections of 70 nm were prepared, mounted onto formvar-coated TEM grids stabilized with carbon film, and stained first with 2% (w/v) uranyl acetate for 5 min in the dark and then with lead citrate, according to the Reynolds method (*85*), for 4 min in a CO_2-free environment followed by five times washing in MilliQ water after each staining. Images were acquired with a Zeiss EM 902 operated at 80 keV using a slow-scan charge-coupled device camera (Type 7899).

RT-qPCR

Precultures were prepared in 5-ml BHI supplemented with hemin for symbiotic and hemin plus horse serum for aposymbiotic cultures of *A. deanei*. Five milliliters of main cultures in the same medium were inoculated from the precultures. Cells were harvested at 8000*g* for 5 min and washed once in PBS. Total RNA was isolated using the NucleoSpin RNA Plus, Mini Kit for RNA Isolation (Machery-Nagel, catalog number 740984) according to the manufacturer's instructions. Then, cDNA synthesis was performed according to the standard protocol using oligo(dT) 12-18 primer (ref. 18418012, Life Technologies) and superscript III reverse transcriptase (ref. 18080-044, Thermo Fisher Scientific) followed by qPCR with MESA Green qPCR master mix plus (ref. RT-SY2X-06+WOUFL, Thermo Fisher Scientific) in a 96-well plate with three independent biological and three technical replicates each. For gene expression analysis, obtained crossing point (CP) values of *etp9* were normalized and the fold change ($2^{-\Delta\Delta CP}$) was calculated using the actin gene as a housekeeping control using the following primers: actin_fw_201, 5′-CACTGGAGCTCTTCATGGAAAC-3′; actin_rev_202, GC-TAT- CTCGGACTGCACCAC; qPCR_ETP9_for_2285, 5′-TCCC-GAGAAGACAAAGTACG-3′; and qPCR_ETP9_rev_2286, 5′-AACTGATCCTCCACCTTGTC-3′.

Western blot analysis

For the preparation of raw protein extracts, cells grown in 25-ml BHI medium supplemented with hemin and horse serum were harvested at 8000*g* for 10 min at 4°C and washed twice in PBS. Protein was precipitated by mixing the cell suspension with a final concentration of 10% (w/v) ice cold trichloroacetic acid, incubation on ice for at least 10 min, and centrifugation at 21,000*g* for 20 min at 4°C. The resulting pellet was washed twice with ice cold 100% acetone. Last, the pellet was resuspended in urea buffer [8 M urea, 100 mM tris (pH 8.6), and 5.25 mM EDTA]. Protein concentration was measured using the Pierce 660-nm assay reagent (Thermo Fisher Scientific) with bovine serum albumin standards (50 to 2000 μg/ml) according to the manufacturer's instructions. Thirty micrograms of total protein per sample was solubilized in Lämmli sample buffer [final concentrations of 10% (v/v) glycerol, 2% (w/v) SDS, 0.0025% (w/v) bromophenol blue, 10 mM dithiothreitol, and 63 mM tris-HCL, pH 6.8] for 10 min at 95°C. Proteins were separated on a 10% SDS–polyacrylamide gel electrophoresis gel at 120 V with a running buffer containing 25 mM (w/v) tris, 192 mM (w/v) glycine, and 0.1% (w/v) SDS. Resolved proteins were transferred onto polyvinylidene difluoride (PVDF) membrane (Amersham Hybond, 0.45 nm, GE HealthCare Life Science) with a Turbo-Blot transfer system (Bio-Rad) using transfer buffer [final concentration, 25 mM (w/v) tris, 192 mM (w/v) glycine (pH 8.6), and 10% (v/v) isopropanol] and standard conditions (25 V, 1.0 A for 30 min). The following steps were performed in a SNAP i.d.2.0 system (Merck-Millipore). The membrane was blocked with 0.1% milk powder (Roth) in PBS + 0.05% (v/v) Tween 20 (PBST), primary antibodies [anti-GFP, mouse, Santa Cruz Biotechnology, catalog no. sc-9996, RRID:AB_627695 (1:1000 dilution) and anti-tubulin, rat, Thermo Fisher Scientific, catalog no. MA1-80017, RRID:AB_2210201 (1:1000 dilution)] were applied, and incubated for 10 min at RT, followed by four wash steps in PBST. The membrane was further incubated with secondary antibody [anti-mouse IgG conjugated to horseradish peroxidase (HRP), Thermo Fisher Scientific, catalog no. 31430, RRID:AB_228307, 1:5,000 dilution; and anti-rat IgG-HRP, Thermo Fisher Scientific, catalog no. PA1-28573, RRID:AB_10980086, 1:10,000 dilution (for detecting anti-tubulin)] for 10 min followed by four wash steps. Last, the membrane was incubated with SuperSignal West Pico chemiluminescent reagent (Thermo Fisher Scientific) and luminescence imaged in a Chemidoc MP Imaging System (Bio-Rad). Where needed, band intensities were quantified using the wand tool in ImageJ software.

Western blot test of newly generated FtsZ antibodies

Thirty micrograms of total protein from lysed *A. deanei* cells were resolved and transferred to PVDF membranes as described above. Membranes were blocked overnight in 5% milk powder (Roth) in PBST at 4°C and washed three times for 5 min in PBST. Then, blocked membranes were incubated with the primary antibodies or sera (as indicated) in PBST for 1.5 hours at RT. Membranes were washed again three times for 5 min in PBST, before they were incubated with the secondary antibody (anti-rabbit IgG-HRP, Cell Signaling Technology, catalog no. 7074S, RRID:AB_2099233; 1:5000 dilution in PBST) for 2 hours at RT. Last, membranes were washed again three times for 5 min in PBST, and HRP was detected as described above.

Generation of specific gene knockdowns

A. deanei cells (1×10^7) were harvested and transfected with 2 µl (final concentration, 100 µM) of MAOs (MAO$_{etp9\text{-}1}$: 5′-ATGTGGAATATCTATGAGGATTTGT-3′; MAO$_{etp9\text{-}2}$: 5′-GTTTTGTGCTGTTTTTCAGGCGATT-3′; and MAO$_{tub}$: 5′-TGAATGCAGATAGCCTCACGCATGG-3′ synthesized by Gene Tools, LLC, Philomath, Oregon and dissolved in autoclaved MilliQ water) or as a negative control, with 2 µl of autoclaved MilliQ water alone according to the transfection protocol described above. After transfection, cells were transferred to 5-ml BHI medium supplemented with hemin and horse serum (for all strains) and incubated at 28°C. Eight hundred microliters of samples were collected at 6, 12, and 24 hours post-transfection and fixed with 4% (w/v) PFA (final concentration). Hoechst 33342 staining and fluorescence microscopy was performed as described before. Cells were also counted at each time point using the Multisizer 4e cell counter (Beckman Coulter).

Divisome gene analysis

To analyze presence/absence patterns of genes involved in PG biosynthesis, cell elongation, and division, all six available genomes from the Kinetoplastibacteria, plus the genome sequences of further 25 β-proteobacteria along with the genomes of *E. coli*, *P. aeruginosa*, *C. vibrioides*, and *M. xanthus* (as outgroup) were downloaded from National Center for Biotechnology Information (www.ncbi.nlm.nih.gov/datasets/genome; for species names, strains, and accession numbers, see table S1). Clusters of orthologous proteins (orthogroups) were generated using the OrthoFinder software version 2.5.5 (*86*). OrthoFinder assigned 113,750 genes (91.1% of total) to 9355 orthogroups. Orthogroups were inspected manually for the annotations of the included genes and the corresponding resolved tree. When an orthogroup contained functionally divergent paralogs, affiliation of the various members to the functionally divergent subgroups was determined on the basis of the tree morphology.

3D structure prediction of ETP9 fusion proteins

Structures of ETP9 fusion proteins were predicted with default settings using ColabFold (*53*) version 1.5.5: AlphaFold2 using MMseqs2 (with Google Collaboratory) by increasing the number of recycles from 3 (default) to 6 and dpi from 200 (default) to 300. Five models were obtained with different ranks sorted by pLDDT scores for monomeric proteins. The model with the highest rank is provided in Fig. 2. These models were colored by domain using the PyMOL Molecular Graphics System, version 2.5.5, Schrödinger, LLC.

Supplementary Materials

The PDF file includes:

Figs. S1 to S5

Table S2
Legend for table S1
Legends for movies S1 to S4
References

Other Supplementary Material for this manuscript includes the following:

Table S1
Movies S1 to S4

REFERENCES AND NOTES

1. N. Dubilier, C. Bergin, C. Lott, Symbiotic diversity in marine animals: The art of harnessing chemosynthesis. *Nat. Rev. Microbiol.* **6**, 725–740 (2008).
2. F. Husnik, D. Tashyreva, V. Boscaro, E. E. George, J. Lukeš, P. J. Keeling, Bacterial and archaeal symbioses with protists. *Curr. Biol.* **31**, R862–R877 (2021).
3. A. Moya, J. Peretó, R. Gil, A. Latorre, Learning how to live together: Genomic insights into prokaryote-animal symbioses. *Nat. Rev. Genet.* **9**, 218–229 (2008).
4. E. C. M. Nowack, M. Melkonian, Endosymbiotic associations within protists. *Philos. Trans. R. Soc. Lond. B Biol. Sci.* **365**, 699–712 (2010).
5. A. Singer, G. Poschmann, C. Mühlich, C. Valadez-Cano, S. Hänsch, S. A. Rensing, K. Stühler, E. C. M. Nowack, Massive protein import into the early evolutionary stage photosynthetic organelle of the amoeba *Paulinella chromatophora*. *Curr. Biol.* **27**, 2763–2773.e5 (2017).
6. T. H. Coale, V. Loconte, K. A. Turk-Kubo, B. Vanslembrouck, W. K. E. Mak, S. Cheung, A. Ekman, J.-H. Chen, K. Hagino, Y. Takano, T. Nishimura, M. Adachi, M. Le Gros, C. Larabell, J. P. Zehr, Nitrogen-fixing organelle in a marine alga. *Science* **384**, 217–222 (2024).
7. S. Miyagishima, Mechanism of plastid division: From a bacterium to an organelle. *Plant Physiol.* **155**, 1533–1544 (2011).
8. K. W. Osteryoung, J. Nunnari, The division of endosymbiotic organelles. *Science* **302**, 1698–1704 (2003).
9. C. Chen, J. S. MacCready, D. C. Ducat, K. W. Osteryoung, The molecular machinery of chloroplast division. *Plant Physiol.* **176**, 138–151 (2018).
10. M. M. Leger, M. Petru, V. Zárský, L. Eme, C. Vlcek, T. Harding, B. F. Lang, M. Eliás, P. Dolezal, A. J. Roger, An ancestral bacterial division system is widespread in eukaryotic mitochondria. *Proc. Natl. Acad. Sci. U.S.A.* **112**, 10239–10246 (2015).
11. S. Miyagishima, K. Suzuki, K. Okazaki, Y. Kabeya, Expression of the nucleus-encoded chloroplast division genes and proteins regulated by the algal cell cycle. *Mol. Biol. Evol.* **29**, 2957–2970 (2012).
12. J. de Vries, S. B. Gould, The monoplastidic bottleneck in algae and plant evolution. *J. Cell Sci.* **131**, jcs203414 (2018).
13. W. Margolin, FtsZ and the division of prokaryotic cells and organelles. *Nat. Rev. Mol. Cell Biol.* **6**, 862–871 (2005).
14. D. W. Adams, J. Errington, Bacterial cell division: Assembly, maintenance and disassembly of the Z ring. *Nat. Rev. Microbiol.* **7**, 642–653 (2009).
15. E. Bi, J. Lutkenhaus, FtsZ ring structure associated with division in *Escherichia coli*. *Nature* **354**, 161–164 (1991).
16. R. Ramachandran, Mitochondrial dynamics: The dynamin superfamily and execution by collusion. *Semin. Cell Dev. Biol.* **76**, 201–212 (2018).
17. S. Miyagishima, K. Nishida, T. Mori, M. Matsuzaki, T. Higashiyama, H. Kuroiwa, T. Kuroiwa, A plant-specific dynamin-related protein forms a ring at the chloroplast division site. *Plant Cell* **15**, 655–665 (2003).
18. R. Lauterborn, Protozoenstudien. *Z. Wiss. Zool.* **59**, 537–544 (1895).
19. J. Votýpka, A. Y. Kostygov, N. Kraeva, A. Grybchuk-Ieremenko, M. Tesařová, D. Grybchuk, J. Lukeš, V. Yurchenko, *Kentomonas* gen. n., a new genus of endosymbiont-containing trypanosomatids of Strigomonadinae subfam. n. *Protist* **165**, 825–838 (2014).
20. M. M. G. Teixeira, T. C. Borghesan, R. C. Ferreira, M. A. Santos, C. S. A. Takata, M. Campaner, V. L. B. Nunes, R. V. Milder, W. de Souza, E. P. Camargo, Phylogenetic validation of the genera *Angomonas* and *Strigomonas* of trypanosomatids harboring bacterial endosymbionts with the description of new species of trypanosomatids and of proteobacterial symbionts. *Protist* **162**, 503–524 (2011).
21. M. H. Mundim, I. Roitman, Extra nutritional requirements of artificially aposymbiotic *Crithidia deanei*. *J. Protozool.* **24**, 329–331 (1977).
22. J. M. P. Alves, C. C. Klein, F. M. da Silva, A. G. Costa-Martins, M. G. Serrano, G. A. Buck, A. T. R. Vasconcelos, M.-F. Sagot, M. M. G. Teixeira, M. C. M. Motta, E. P. Camargo, Endosymbiosis in trypanosomatids: The genomic cooperation between bacterium and host in the synthesis of essential amino acids is heavily influenced by multiple horizontal gene transfers. *BMC Evol. Biol.* **13**, 190 (2013).
23. J. M. P. Alves, M. G. Serrano, F. M. da Silva, L. J. Voegtly, A. V. Matveyev, M. M. G. Teixeira, E. P. Camargo, G. A. Buck, Genome evolution and phylogenomic analysis of *Candidatus* Kinetoplastibacterium, the betaproteobacterial endosymbionts of *Strigomonas* and *Angomonas*. *Genome Biol. Evol.* **5**, 338–350 (2013).
24. F. M. Silva, A. Y. Kostygov, V. V. Spodareva, A. Butenko, R. Tossou, J. Lukeš, V. Yurchenko, J. M. P. Alves, The reduced genome of *Candidatus* Kinetoplastibacterium sorsogonicusi,

the endosymbiont of *Kentomonas sorsogonicus* (Trypanosomatidae): Loss of the haem-synthesis pathway. *Parasitology* **145**, 1287–1293 (2018).
25. J. Morales, G. Ehret, G. Poschmann, T. Reinicke, A. K. Maurya, L. Kroninger, D. Zanini, R. Wolters, D. Kalyanaraman, M. Krakovka, M. Bäumers, K. Stühler, E. C. M. Nowack, Host-symbiont interactions in *Angomonas deanei* include the evolution of a host-derived dynamin ring around the endosymbiont division site. *Curr. Biol.* **33**, 28–40 (2023).
26. Y. Du, D. A. Maslov, K. P. Chang, Monophyletic origin of β-division proteobacterial endosymbionts and their coevolution with insect trypanosomatid protozoa *Blastocrithidia culicis* and *Crithidia* spp. *Proc. Natl. Acad. Sci. U.S.A.* **91**, 8437–8441 (1994).
27. M. C. M. Motta, L. H. M. Leal, W. DeSouza, D. F. DeAlmeida, L. C. S. Ferreira, Detection of penicillin-binding proteins in the endosymbiont of the trypanosomatid *Crithidia deanei*. *J. Eukaryot. Microbiol.* **44**, 492–496 (1997).
28. M. H. Mundim, I. Roitman, M. A. Hermans, E. W. Kitajima, Simple nutrition of *Crithidia deanei*, a reduviid trypanosomatid with an endosymbiont. *J. Protozool.* **21**, 518–521 (1974).
29. K. P. Chang, Ultrastructure of symbiotic bacteria in normal and antibiotic treated *Blastocrithidia culicis* and *Crithidia oncopelti*. *J. Protozool.* **21**, 699–707 (1974).
30. M. C. Machado Motta, C. M. Costa Catta-Preta, S. Schenkman, A. C. de Azevedo Martins, K. Miranda, W. de Souza, M. C. Elias, The bacterium endosymbiont of *Crithidia deanei* undergoes coordinated division with the host cell nucleus. *PLOS ONE* **5**, e12415 (2010).
31. A. Kostygov, E. Dobáková, A. Grybchuk-Ieremenko, D. Váhala, D. Maslov, J. Votýpka, J. Lukeš, V. Yurchenko, Novel trypanosomatid–bacterium association: Evolution of endosymbiosis in action. *mBio* **7**, e01985 (2016).
32. A. Zakharova, D. Tashyreva, A. Butenko, J. Morales, A. Saurá, M. Svobodová, G. Poschmann, S. Nandipati, A. Zakharova, D. Noyvert, O. Gahura, J. Týč, K. Stühler, A. Y. Kostygov, E. C. M. Nowack, J. Lukeš, V. Yurchenko, A neo-functionalized homolog of host transmembrane protein controls localization of bacterial endosymbionts in the trypanosomatid *Novymonas esmeraldas*. *Curr. Biol.* **33**, 2690–2701.e5 (2023).
33. M. C. Machado Motta, A. C. de Azevedo Martins, S. S. de Souza, C. M. Costa Catta-Preta, R. Silva, C. C. Klein, L. Gonzaga Paula, de Almeida, O. de Lima Cunha, L. P. Ciapina, M. Brocchi, A. C. Colabardini, B. de Araujo Lima, C. R. Machado, C. M. de Almeida Soares, C. M. Probst, C. B. A. de Menezes, C. E. Thompson, D. C. Bartholomeu, D. F. Gradia, D. P. Pavoni, E. C. Grisard, F. Fantinatti-Garboggini, F. K. Marchini, G. Flávia Rodrigues-Luiz, G. Wagner, G. H. Goldman, J. Lopes Rangel Fietto, M. C. Elias, M. H. S. Goldman, M.-F. Sagot, M. Pereira, P. H. Stoco, R. P. de Mendonça-Neto, S. M. Ribeiro Teixeira, T. E. Ferreira Maciel, T. A. de Oliveira Mendes, T. P. Ürményi, W. de Souza, S. Schenkman, A. T. R. de Vasconcelos, Predicting the proteins of *Angomonas deanei*, *Strigomonas culicis* and their respective endosymbionts reveals new aspects of the trypanosomatidae family. *PLOS ONE* **8**, e60209 (2013).
34. M. C. M. Motta, G. F. A. Picchi, I. V. Palmie-Peixoto, M. R. Rocha, T. M. U. De Carvalho, J. Morgado-Diaz, W. De Souza, S. Goldenberg, S. P. Fragoso, The microtubule analog protein, FtsZ, in the endosymbiont of Trypanosomatid protozoa. *J. Eukaryot. Microbiol.* **51**, 394–401 (2004).
35. C. Benz, E. Stribrna, H. Hashimi, J. Lukeš, Dynamin-like proteins in *Trypanosoma brucei*: A division of labour between two paralogs? *PLOS ONE* **12**, e0177200 (2017).
36. A.-L. Chanez, A. B. Hehl, M. Engstler, A. Schneider, Ablation of the single dynamin of *T. brucei* blocks mitochondrial fission and endocytosis and leads to a precise cytokinesis arrest. *J. Cell Sci.* **119**, 2968–2974 (2006).
37. G. W. Morgan, D. Goulding, M. C. Field, The single dynamin-like protein of *Trypanosoma brucei* regulates mitochondrial division and is not required for endocytosis. *J. Biol. Chem.* **279**, 10692–10701 (2004).
38. L. T. Sham, E. K. Butler, M. D. Lebar, D. Kahne, T. G. Bernhardt, N. Ruiz, MurJ is the flippase of lipid-linked precursors for peptidoglycan biogenesis. *Science* **345**, 220–222 (2014).
39. T. den Blaauwen, M. A. de Pedro, M. Nguyen-Distèche, J. A. Ayala, Morphogenesis of rod-shaped sacculi. *FEMS Microbiol. Rev.* **32**, 321–344 (2008).
40. A. J. F. Egan, J. Errington, W. Vollmer, Regulation of peptidoglycan synthesis and remodelling. *Nat. Rev. Microbiol.* **18**, 446–460 (2020).
41. X. Liu, J. Biboy, E. Consoli, W. Vollmer, T. den Blaauwen, MreC and MreD balance the interaction between the elongasome proteins PBP2 and RodA. *PLOS Genet.* **16**, e1009276 (2020).
42. D. Shiomi, M. Sakai, H. Niki, Determination of bacterial rod shape by a novel cytoskeletal membrane protein. *EMBO J.* **27**, 3081–3091 (2008).
43. P. A. J. de Boer, R. E. Crossley, L. I. Rothfield, A division inhibitor and a topological specificity factor coded for by the minicell locus determine proper placement of the division septum in *Escherichia coli*. *Cell* **56**, 641–649 (1989).
44. T. A. Cameron, W. Margolin, Insights into the assembly and regulation of the bacterial divisome. *Nat. Rev. Microbiol.* **22**, 33–45 (2024).
45. A. Taguchi, M. A. Welsh, L. S. Marmont, W. Lee, M. Sjodt, A. C. Kruse, D. Kahne, T. G. Bernhardt, S. Walker, FtsW is a peptidoglycan polymerase that is functional only in complex with its cognate penicillin-binding protein. *Nat. Microbiol.* **4**, 587–594 (2019).
46. L. S. Marmont, T. G. Bernhardt, A conserved subcomplex within the bacterial cytokinetic ring activates cell wall synthesis by the FtsW-FtsI synthase. *Proc. Natl. Acad. Sci. U.S.A.* **117**, 23879–23885 (2020).
47. G. W. Liu, G. C. Draper, W. D. Donachie, FtsK is a bifunctional protein involved in cell division and chromosome localization in *Escherichia coli*. *Mol. Microbiol.* **29**, 893–903 (1998).
48. M. A. Gerding, B. Liu, F. O. Bendezú, C. A. Hale, T. G. Bernhardt, P. A. J. de Boer, Self-enhanced accumulation of FtsN at division sites and roles for other proteins with a spor domain (DamX, DedD, and RlpA) in *Escherichia coli* cell constriction. *J. Bacteriol.* **191**, 7383–7401 (2009).
49. A. Möll, M. Thanbichler, FtsN-like proteins are conserved components of the cell division machinery in proteobacteria. *Mol. Microbiol.* **72**, 1037–1053 (2009).
50. J. W. Davey, C. M. C. Catta-Preta, S. James, S. Forrester, M. C. M. Motta, P. D. Ashton, J. C. Mottram, Chromosomal assembly of the nuclear genome of the endosymbiont-bearing trypanosomatid *Angomonas deanei*. *G3* **11**, jkaa018 (2021).
51. C. Heidrich, A. Ursinus, J. Berger, H. Schwarz, J. V. Höltje, Effects of multiple deletions of murein hydrolases on viability, septum cleavage, and sensitivity to large toxic molecules in *Escherichia coli*. *J. Bacteriol.* **184**, 6093–6099 (2002).
52. J. Morales, S. Kokkori, D. Weidauer, J. Chapman, E. Goltsman, D. Rokhsar, A. R. Grossman, E. C. M. Nowack, Development of a toolbox to dissect host-endosymbiont interactions and protein trafficking in the trypanosomatid *Angomonas deanei*. *BMC Evol. Biol.* **16**, 247 (2016).
53. M. Mirdita, K. Schütze, Y. Moriwaki, L. Heo, S. Ovchinnikov, M. Steinegger, ColabFold: Making protein folding accessible to all. *Nat. Methods* **19**, 679–682 (2022).
54. J. R. Jimah, J. E. Hinshaw, Structural insights into the mechanism of dynamin superfamily proteins. *Trends Cell Biol.* **29**, 257–273 (2019).
55. R. D. Arroyo-Olarte, I. Martínez, E. Lujan, F. Mendlovic, T. Dinkova, B. Espinoza, Differential gene expression of virulence factors modulates infectivity of TcI *Trypanosoma cruzi* strains. *Parasitol. Res.* **119**, 3803–3815 (2020).
56. J. Budzak, R. Jones, C. Tschudi, N. G. Kolev, G. Rudenko, An assembly of nuclear bodies associates with the active VSG expression site in African trypanosomes. *Nat. Commun.* **13**, 101 (2022).
57. S. Kramer, A. Marnef, N. Standart, M. Carrington, Inhibition of mRNA maturation in trypanosomes causes the formation of novel foci at the nuclear periphery containing cytoplasmic regulators of mRNA fate. *J. Cell Sci.* **125**, 2896–2909 (2012).
58. H. Ngô, C. Tschudi, K. Gull, E. Ullu, Double-stranded RNA induces mRNA degradation in *Trypanosoma brucei*. *Proc. Natl. Acad. Sci. U.S.A.* **95**, 14687–14692 (1998).
59. C. Otten, M. Brilli, W. Vollmer, P. H. Viollier, J. Salje, Peptidoglycan in obligate intracellular bacteria. *Mol. Microbiol.* **107**, 142–163 (2018).
60. M. Pilhofer, K. Aistleitner, J. Biboy, J. Gray, E. Kuru, E. Hall, Y. V. Brun, M. S. VanNieuwenhze, W. Vollmer, M. Horn, G. J. Jensen, Discovery of chlamydial peptidoglycan reveals bacteria with murein sacculi but without FtsZ. *Nat. Commun.* **4**, 2856 (2013).
61. G. W. Liechti, E. Kuru, E. Hall, A. Kalinda, Y. V. Brun, M. VanNieuwenhze, A. T. Maurelli, A new metabolic cell-wall labelling method reveals peptidoglycan in *Chlamydia trachomatis*. *Nature* **506**, 507–510 (2014).
62. M. Packiam, B. Weinrick, W. R. Jacobs, A. T. Maurelli, Structural characterization of muropeptides from *Chlamydia trachomatis* peptidoglycan by mass spectrometry resolves "chlamydial anomaly". *Proc. Natl. Acad. Sci. U.S.A.* **112**, 11660–11665 (2015).
63. D. C. Bublitz, G. L. Chadwick, J. S. Magyar, K. M. Sandoz, D. M. Brooks, S. Mesnage, M. S. Ladinsky, A. I. Garber, P. J. Bjorkman, V. J. Orphan, J. P. McCutcheon, Peptidoglycan production by an insect-bacterial mosaic. *Cell* **179**, 703–712 (2019).
64. B. Pfanzagl, G. Allmaier, E. R. Schmid, M. A. DePedro, W. Löffelhardt, N-acetylputrescine as a characteristic constituent of cyanelle peptidoglycan in glaucocystophyte algae. *J. Bacteriol.* **178**, 6994–6997 (1996).
65. A. I. MacLeod, M. R. Knopp, S. B. Gould, A mysterious cloak: The peptidoglycan layer of algal and plant plastids. *Protoplasma* **261**, 173–178 (2024).
66. A. J. Dowson, A. J. Lloyd, A. C. Cuming, D. Roper, L. Frigerio, C. G. Dowson, Plant peptidoglycan precursor biosynthesis: Conservation between moss chloroplasts and Gram-negative bacteria. *Plant Physiol.* **190**, 165–179 (2022).
67. T. Hirano, K. Tanidokoro, Y. Shimizu, Y. Kawarabayasi, T. Ohshima, M. Sato, S. Tadano, H. Ishikawa, S. Takio, K. Takechi, H. Takano, Moss chloroplasts are surrounded by a peptidoglycan wall containing D-amino acids. *Plant Cell* **28**, 1521–1532 (2016).
68. H. Takano, T. Tsunefuka, S. Takio, H. Ishikawa, K. Takechi, Visualization of plastid peptidoglycan in the charophyte alga *Klebsormidium nitens* using a metabolic labeling method. *Cytologia* **83**, 375–380 (2018).
69. B. Kasten, R. Reski, Beta-lactam antibiotics inhibit chloroplast division in a moss (*Physcomitrella patens*) but not in tomato (*Lycopersicon esculentum*). *J. Plant Physiol.* **150**, 137–140 (1997).
70. M. Machida, K. Takechi, H. Sato, S. J. Chung, H. Kuroiwa, S. Takio, M. Seki, K. Shinozaki, T. Fujita, M. Hasebe, H. Takano, Genes for the peptidoglycan synthesis pathway are essential for chloroplast division in moss. *Proc. Natl. Acad. Sci. U.S.A.* **103**, 6753–6758 (2006).
71. N. Katayama, H. Takano, M. Sugiyama, S. Takio, A. Sakai, K. Tanaka, H. Kuroiwa, K. Ono, Effects of antibiotics that inhibit the bacterial peptidoglycan synthesis pathway on moss chloroplast division. *Plant Cell Physiol.* **44**, 776–781 (2003).

72. A. Y. Kostygov, A. Butenko, A. Nenarokova, D. Tashyreva, P. Flegontov, J. Lukes, V. Yurchenko, Genome of *Ca.* Pandoraea novymonadis, an endosymbiotic bacterium of the trypanosomatid *Novymonas esmeraldas*. *Front. Microbiol.* **8**, 1940 (2017).
73. L. Hébert, B. Moumen, N. Pons, F. Duquesne, M.-F. Breuil, D. Goux, J.-M. Batto, C. Laugier, P. Renault, S. Petry, Genomic characterization of the *Taylorella* genus. *PLOS ONE* **7**, e29953 (2012).
74. N. Sumiya, T. Fujiwara, A. Era, S. Y. Miyagishima, Chloroplast division checkpoint in eukaryotic algae. *Proc. Natl. Acad. Sci. U.S.A.* **113**, E7629–E7638 (2016).
75. K. S. Colletti, E. A. Tattersall, K. A. Pyke, J. E. Froelich, K. D. Stokes, K. W. Osteryoung, A homologue of the bacterial cell division site-determining factor MinD mediates placement of the chloroplast division apparatus. *Curr. Biol.* **10**, 507–516 (2000).
76. R. Itoh, M. Fujiwara, N. Nagata, S. Yoshida, A chloroplast protein homologous to the eubacterial topological specificity factor MinE plays a role in chloroplast division. *Plant Physiol.* **127**, 1644–1655 (2001).
77. S. Miyagishima, Y. Kabeya, Chloroplast division: Squeezing the photosynthetic captive. *Curr. Opin. Microbiol.* **13**, 738–746 (2010).
78. S. Miyagishima, A handshake across membranes. *Nat. Plants* **3**, 17025 (2017).
79. W. Wang, J. Li, Q. Sun, X. Yu, W. Zhang, N. Jia, C. An, Y. Li, Y. Dong, F. Han, N. Chang, X. Liu, Z. Zhu, Y. Yu, S. Fan, M. Yang, S. Z. Luo, H. Gao, Y. Feng, Structural insights into the coordination of plastid division by the ARC6-PDV2 complex. *Nat. Plants* **3**, 17011 (2017).
80. S. Miyagishima, Y. Kabeya, C. Sugita, M. Sugita, T. Fujiwara, DipM is required for peptidoglycan hydrolysis during chloroplast division. *BMC Plant Biol.* **14**, 57 (2014).
81. M. Terfrüchte, B. Joehnk, R. Fajardo-Somera, G. H. Braus, M. Riquelme, K. Schipper, M. Feldbrügge, Establishing a versatile Golden Gate cloning system for genetic engineering in fungi. *Fungal Genet. Biol.* **62**, 1–10 (2014).
82. C. Engler, R. Kandzia, S. Marillonnet, A one pot, one step, precision cloning method with high throughput capability. *PLOS ONE* **3**, e3647 (2008).
83. R. I. Amann, L. Krumholz, D. A. Stahl, Fluorescent-oligonucleotide probing of whole cells for determinative, phylogenetic, and environmental studies in microbiology. *J. Bacteriol.* **172**, 762–770 (1990).
84. B. M. Fuchs, J. Pernthaler, R. Amann, Single cell identification by fluorescence in situ hybridization, in *Methods for General and Molecular Microbiology*, C. A. Reddy, T. J. Beveridge, J. A. Breznak, G. Marzluf, T. M. Schmidt, L. R. Snyder, Eds. (ASM Press, Washington, D.C., ed. 3, 2007), pp. 886–896.
85. E. S. Reynolds, The use of lead citrate at high pH as an electron-opaque stain in electron microscopy. *J. Cell Biol.* **17**, 208–212 (1963).
86. D. M. Emms, S. Kelly, OrthoFinder: Phylogenetic orthology inference for comparative genomics. *Genome Biol.* **20**, 238 (2019).
87. K. T. Shirakawa, F. A. Sala, M. M. Miyachiro, V. Job, D. M. Trindade, A. Dessen, Architecture and genomic arrangement of the MurE-MurF bacterial cell wall biosynthesis complex. *Proc. Natl. Acad. Sci. U.S.A.* **120**, e2219540120 (2023).

Acknowledgments: We thank S. Hänsch from the Center for Advance Imaging (CAi) for providing secondary antibody (IgG, polyclonal, anti-rabbit goat, Abberior STAR RED, Ex: 638 nm) and for help with confocal microscopy, leading to movies S1 to S4. Furthermore, we acknowledge the CAi at Heinrich Heine University Düsseldorf for providing access to the Leica TCS SP8 STED 3X (DFG-INST 208/665-1 FUGG) and the Zeiss EM 902. **Funding:** This study was supported by the by German Research Foundation grant NO 1090/1-2 (to E.C.M.N.), PhD fellowships of the Jürgen Manchot Graduate School "Molecules of Infection", MOI IV (to A.K.M. and M.M.) and MOI III (to G.E.), and German Research Foundation (Project-ID 267205415 – SFB 1208, Z02). **Author contributions:** Conceptualization: E.C.M.N., A.K.M., and G.E. Investigation: A.K.M., E.C.M.N., L.K., G.E., M.B., and M.M. Methodology: A.K.M., G.E., S.S., L.K., and E.C.M.N. Resources: E.C.M.N., M.B., M.M., and G.E. Validation: A.K.M., M.B., M.M., and L.K. Data curation: E.C.M.N., M.M., and G.E. Formal analysis: E.C.M.N., A.K.M., M.M., and L.K. Visualization: A.K.M., E.C.M.N., G.E., and L.K. Writing–original draft: E.C.M.N., A.K.M., and S.S. Writing–review and editing: E.C.M.N., A.K.M., L.K., G.E., and M.B. Supervision: E.C.M.N. and S.S. Project administration: E.C.M.N. and A.K.M. Funding acquisition: E.C.M.N., A.K.M., and S.S. **Competing interests:** The authors declare that they have no competing interests. **Data and materials availability:** All data needed to evaluate the conclusions in the paper are present in the paper and/or the Supplementary Materials.

Submitted 16 April 2024
Accepted 13 February 2025
Published 19 March 2025
10.1126/sciadv.adp8518

Science Advances
AAAS

Supplementary Materials for

A nucleus-encoded dynamin-like protein controls endosymbiont division in the trypanosomatid Angomonas deanei

Anay K. Maurya *et al.*

Corresponding author: Eva C. M. Nowack, e.nowack@hhu.de

Sci. Adv. **11**, eadp8518 (2025)
DOI: 10.1126/sciadv.adp8518

The PDF file includes:

Other Supplementary Material for this manuscript includes the following:

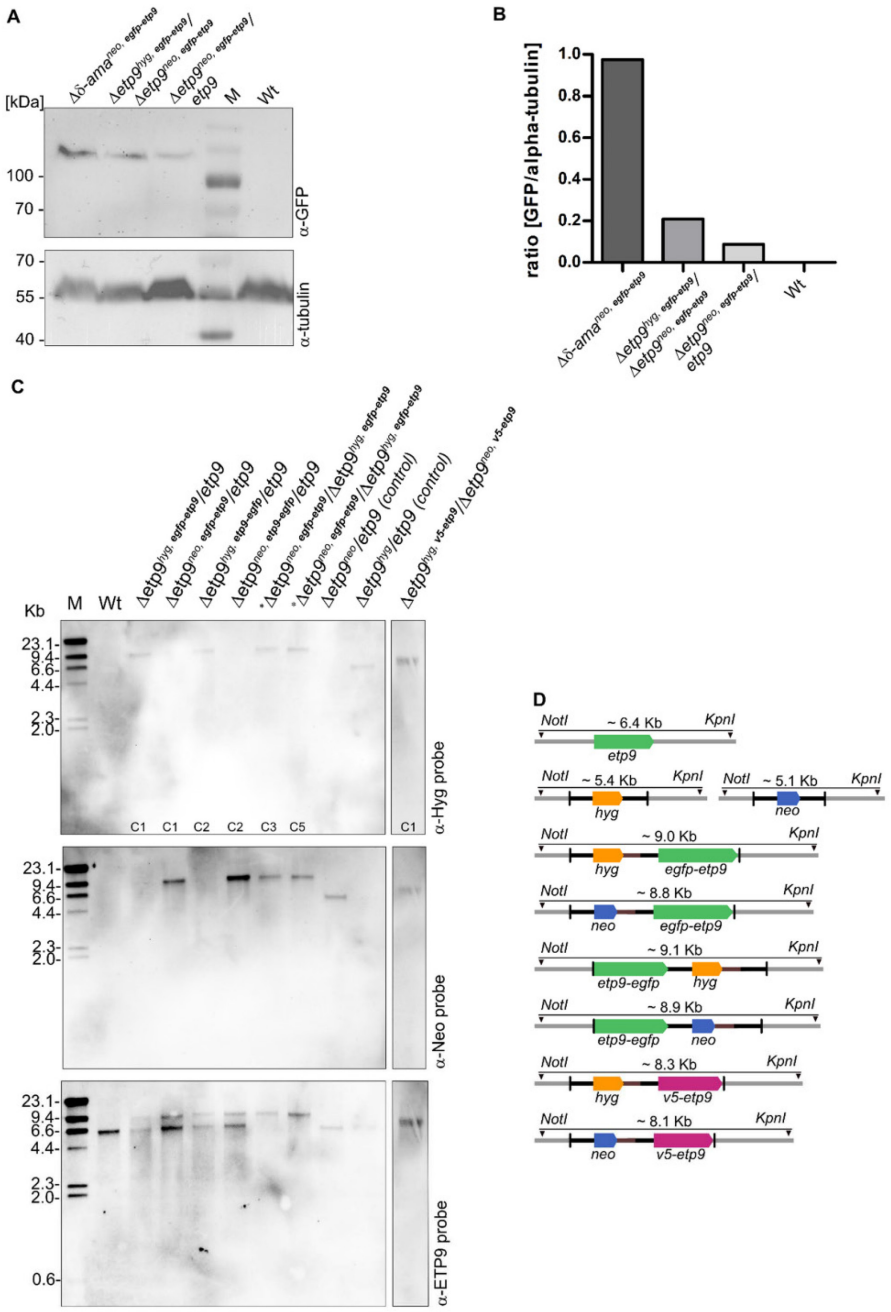

Fig. S1: Expression level analysis of recombinant ETP9 expressed from different loci and Southern blot confirmation of *etp9* complementation strains. (A) Expression levels of eGFP-ETP9 fusions were analyzed in the different *A. deanei* strains by Western blot analysis using α-GFP (1:1000, Santa Cruz, sc-9996) and α-mouse-IgG HRP (1:5000, Invitrogen, 31430) antibodies. On the stripped membrane, alpha-tubulin was detected as a loading control using α-alpha-tubulin (1:1000, Invitrogen, MA1-80017) and α-rat-IgG HRP (1:10,000, Invitrogen, PA1-28573) antibodies. **(B)** The graph shows the ratio of the GFP and alpha-tubulin signals for different strains, based on quantification of the Western blot signals. **(C)** Verification of *etp9* complementation strains by Southern blot analysis. Correct insertion of the recombinant DNA was tested by hybridizing *hyg*^{r}, *neo*^{r} and *etp9*-specific probes to KpnI and NotI-digested gDNA. Two clones from same transfection event are marked by superscript *. Wt was used as a negative control. **(D)** Expected fragment sizes are shown in the schematic maps.

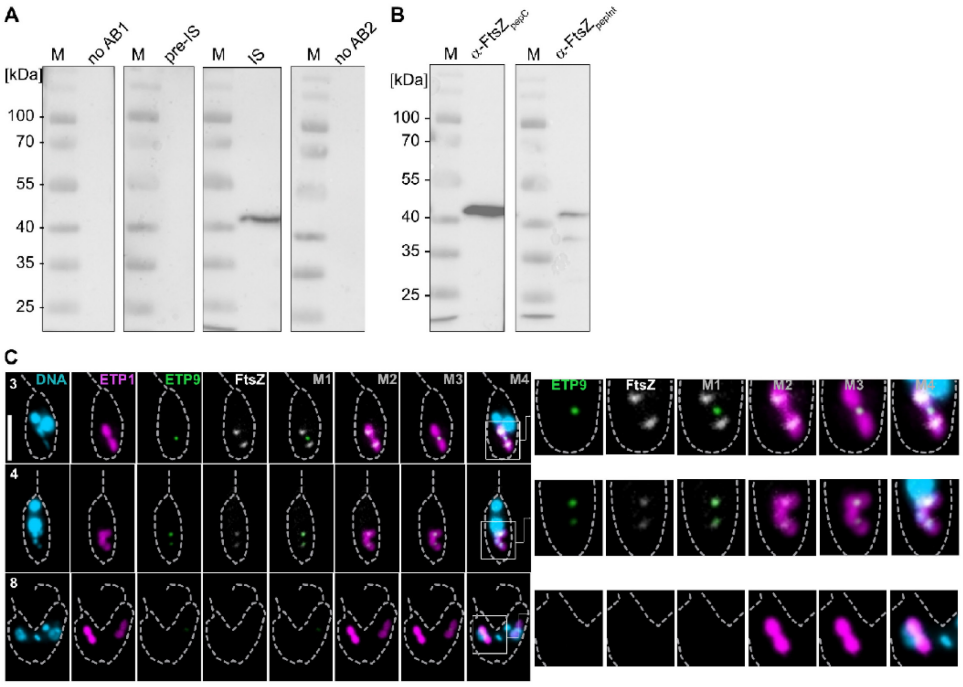

Fig. S2: Western blot test of newly generated peptide antibodies against FtsZ and subcellular localization of FtsZ and eGFP-ETP9 at later cell cycle stages. (A-B) To test the newly generated peptide antibodies raised against *A. deanei* FtsZ, Western blot analyses were performed on *A. deanei* total protein with pre-immune and immune serum **(A)**, and affinity purified antibodies **(B)**. The immune serum was raised to a mixture of two non-overlapping peptides of the endosymbiont-encoded FtsZ protein, $FtsZ_{pepC}$ (PRLKDSNIENDKSVQ) and $FtsZ_{pepInt}$ (KRSAFDSNKYQNRVS). Antibodies α-$FtsZ_{pepC}$ and α-$FtsZ_{pepInt}$ were affinity-purified from the same immune serum using the peptides $FtsZ_{pepC}$ and $FtsZ_{pepInt}$ for binding, respectively. The lanes show the results (A) without primary antibody or serum (no AB1), with pre-immune serum (pre-IS), crude immune serum (IS), and with purified α-$FtsZ_{pepC}$ antibody but without secondary antibody (no AB2), and (B) with the purified antibodies (α-$FtsZ_{pepC}$ and α-$FtsZ_{pepInt}$). Dilutions were as follows: pre-immune and immune serum, 1:10,000; α-$FtsZ_{pepC}$, 1:2,000; and α-$FtsZ_{pepInt}$, 1:1,000. Exposure time was 300 s for all blots. **(C)** Subcellular localization of FtsZ and eGFP-ETP9 in later cell cycle stages. Continuation of the analysis shown in Fig. 3C.

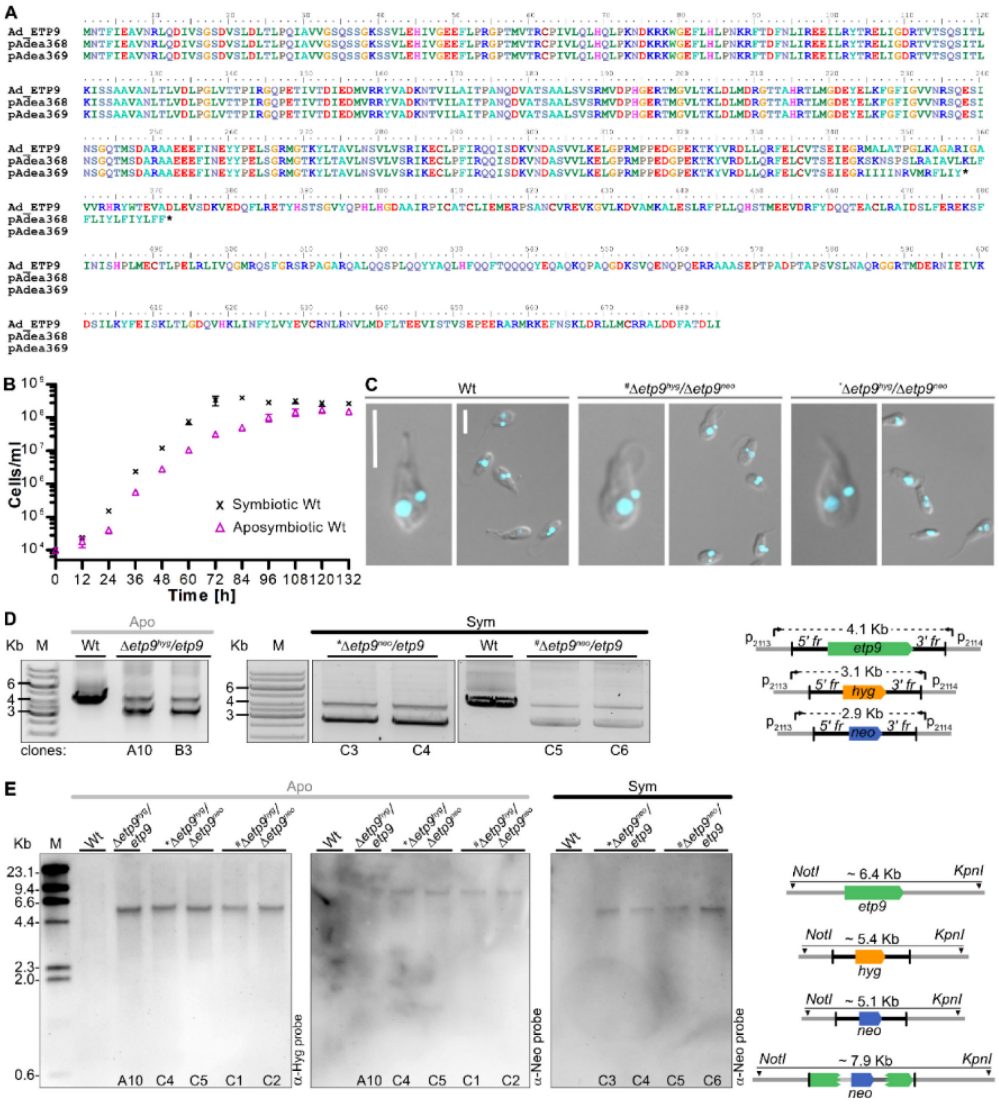

Fig. S3: Verification of ETP9 deletion strains. (A) Alignment of ETP9 and potential incomplete gene products that could be formed in the homozygous *etp9* deletion mutants resulting from transfections with plasmids pAdea368 and 369. However, note that formation of these products is unlikely as the resulting mRNA lacks a suitable stabilizing 3' UTR. **(B)** Symbiotic and aposymbiotic *A. deanei* Wt cells were used to inoculate 25 ml BHI medium supplemented with hemin and horse serum (10^4 cells per ml) and growth was recorded over a period of 132 h. Plotted are mean and standard deviation from three biological replicates. **(C)** Micrographs of a single cell and an overview of multiple cells for aposymbiotic Wt (left) and two independently generated homozygous etp9 deletion mutants in the aposymbiotic cell line (marked by superscript * and # symbols, middle and right) are shown by merging two channels (DIC and Hoechst33342 staining). Scale bars are 5 µm. **(D)** Verification of aposymbiotic (Apo) and symbiotic (Sym) heterozygous *etp9* deletion mutant strains by touch-down PCR. Strains that were obtained from independent transfections are marked by superscript * and # symbols. **(E)** Insertion of a single copy of the different resistance cassettes was verified by Southern blot hybridizations on KpnI/NotI-digested genomic DNA using probes against the *hyg*^{r} and *neo*^{r} genes as indicated. For panels D and E expected band sizes are provided in the maps on the right side. Results for the Wt are shown as a control.

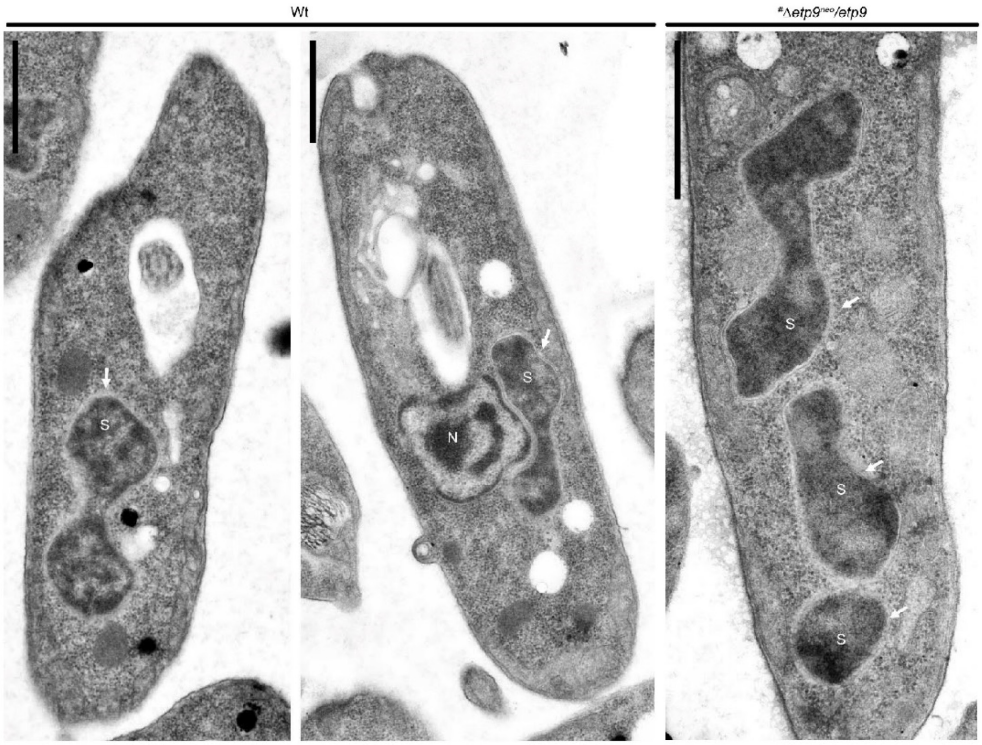

Fig. S4: The endosymbionts in some *Δetp9^{neo}/etp9* mutant cells appear to show aberrant shapes and/or numbers in TEM images. Larger TEM micrographs of further two symbiotic Wt cells and one *Δetp9^{neo}/etp9* mutant cell. White arrows highlight endosymbionts (S). Scale bars are 1 µm.

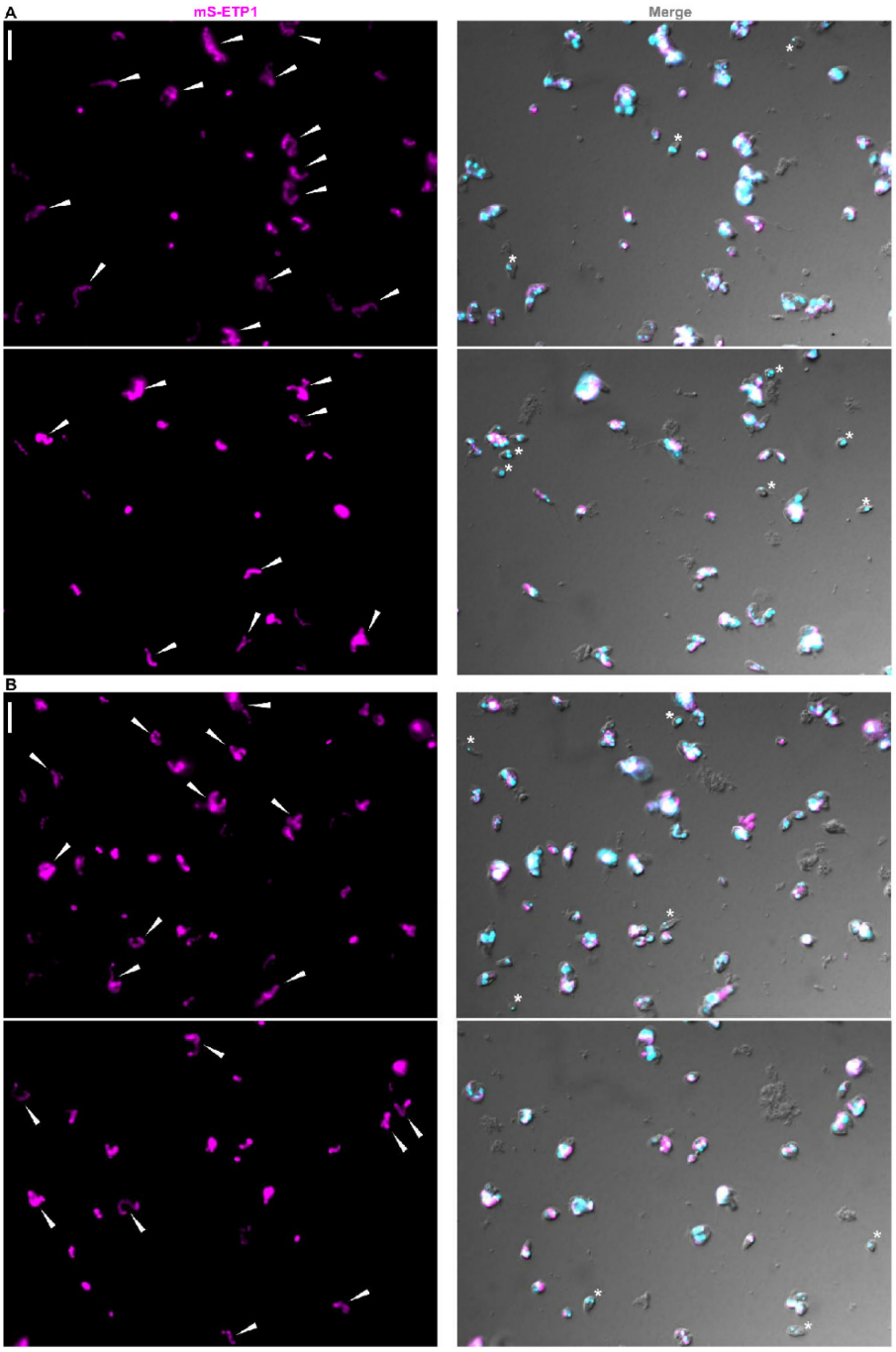

Fig. S5: ETP9 knock-downs result in the majority of the cell population in formation of distorted host cells with filamentous endosymbionts or loss of endosymbionts. Micrographs of *A. deanei* cells expressing the endosymbiont marker mS-ETP1 ($\Delta\gamma$-*ama*$^{mS\text{-}etp1}$) 24 h post-transfection with MAO$_{etp9\text{-}1}$ **(A)** or MAO$_{etp9\text{-}2}$ **(B)**. For each treatment, pictures from two representative microscopic fields of view were taken and the mScarlet signal alone (left) and the overlay of mScarlet, Hoechst 33342, and DIC picture (right) are displayed. Cells that contain multiple or filamentous endosymbionts are highlighted by white arrow heads (on the left), cells that lost the endosymbiont are highlighted by white asterisks (on the right). Scale bars are 10 µm.

2.1.3. Manuscript I

Maurya, A.K., Cadena, L.R., Ehret, G., Nowack, E.C.M. (2025). A novel host-encoded protein, ETP2, plays an important role in endosymbiont division in the trypanosomatid *Angomonas deanei*. (Under review in mBio).

To explore the subcellular localization throughout the cell cycle stages of ETP2 (aim I) and its cellular function (aim II), Maurya et al., performed IFA, and gene knockouts and knockdown using MAOs. Subsequently, they observed that ETP2 showed a cell cycle-dependent localization. Importantly, it plays an important role in division and segregation of the ES in *A. deanei*. Lastly, *in silico* data suggested that ETP2 evolved specifically in symbiont-harboring trypanosomatids. In sum, ETP2 is an important component of the ES division machinery and represents a host-derived molecular mechanism controlling ES division.

My contribution to Maurya et al., (Under review in mBio).

The majority of the research (~ 80%) presented in this manuscript was performed by me (see author contributions in the manuscript I below). The contributions of others were the following. Lawrence Rudy Cadena performed the *etp2* knockouts (in the symbiotic *A. deanei* strain) and *in silico* studies leading to Fig. 3 and Fig. 6, respectively. He helped with *etp2* knockdown studies leading to Fig. 4 and Fig. S3 as well as contributed to generate pAdea457. Georg Ehret generated plasmid pAdea115 and the symbiotic *A. deanei* cell line Adea120 (Δ*etp2*$^{egfp\text{-}etp2}$/*etp2*) and the aposymbiotic *A. deanei* cell line Adea361 (Δ*etp2*^{neo} /*etp2*).

Title: A novel host-encoded protein, ETP2, plays an important role in endosymbiont division in the trypanosomatid *Angomonas deanei*

Authors: Anay K. Maurya[1], Lawrence Rudy Cadena[1], Georg Ehret[1,†], and Eva C. M. Nowack[1,*]

Affiliation: [1]Institute of Microbial Cell Biology, Department of Biology, Heinrich Heine University Düsseldorf, Universitätsstr. 1, 40225 Düsseldorf, Germany

[†]**Present address:** Diatech Pharmacogenetics GmbH, Theresienstr.19, 80333 Munich, Germany

[*]**Corresponding author**

Key words: Endosymbiosis, organellogenesis, evolution, cell cycle synchronization, and FtsZ

Abstract

A single β-proteobacterial endosymbiont, *Candidatus* Kinetoplastibacterium crithidii, resides in the cytosol of the trypanosomatid *Angomonas deanei*, and divides at a defined stage of its host's cell cycle. This endosymbiont has a highly reduced genome of 0.8 Mb and, notably, has lost most essential genes involved in bacterial cell division, resulting in a loss of division autonomy. It has been previously demonstrated that a host-encoded dynamin-like protein, ETP9, plays an indispensable role in the division of the endosymbiont. In this study, we identified a second nucleus-encoded component of the endosymbiont division machinery, termed ETP2, currently annotated as a 'hypothetical protein'. We observed that ETP2 localizes in a cell cycle-dependent manner at the bacterial division site, alongside the bacterium-encoded FtsZ. Furthermore, we demonstrated that ETP2 plays an important role for timely endosymbiont division and segregation, as a large fraction of cells in an *etp2* deletion mutant cell line exhibited either long, filamentous endosymbionts accompanied by severely distorted host cells or host daughter cells lacking endosymbionts. *In silico* analyses revealed that ETP2 is found exclusively in endosymbiont-harboring trypanosomatids and is most likely an intrinsically disordered protein. Collectively, our data suggests that ETP2, alongside the previously described ETP9, is an integral component of the endosymbiont division machinery. This finding highlights the evolution of a complex host-derived molecular mechanism that exerts tight control over its endosymbiont without requiring gene transfers from the bacterium.

Introduction

The transformation of a free-living bacterium into a fully integrated organelle involves extensive structural, physiological, and genetic changes (Bhattacharya et al., 2007; Roger et al., 2017). Although mitochondria and plastids originated from bacteria, over a billion years of co-evolution with their host have led to a situation where the organelles and the surrounding cell can no longer be viewed as independent entities. Instead, the organelles' proteome composition, metabolic activity, division timing, positioning within the cell, and other factors are predominantly regulated by the genetic instructions of the nucleus. More recently established endosymbiotic relationships offer a unique opportunity to observe intermediate stages in the process by which a prokaryote becomes genetically integrated into a eukaryotic cell (Sørensen et al., 2024). As a result, studying the molecular mechanisms that govern these host-endosymbiont interactions holds significant potential for uncovering the scenarios and molecular processes behind organelle formation.

Interestingly, some protists that have developed vertical endosymbiont transmission from one host generation to the next, exhibit strict control over the number of endosymbionts per host cell. Examples include the cercozoan *Paulinella chromatophora*, which houses two cyanobacterium-derived photosynthetic "chromatophores" (Nowack, 2014), the haptophyte *Braarudosphaera bigelowii*, which contains a single cyanobacterium-derived nitrogen-fixing "nitroplast" (Coale et al., 2024), and the trypanosomatid *Angomonas deanei*, which contains a single β-proteobacterial endosymbiont that supplies its host with diverse metabolites and co-factors (Mundim and Roitman, 1977; Alves et al., 2011; Alves et al., 2013; Harmer et al., 2018). Intriguingly, this endosymbiont, *Ca.* Kinetoplastibacterium crithidii, consistently divides at a specific time point in the host cell cycle (Motta et al., 2010). Presence of *Ca.* K. crithidii seems to be obligate in some *A. deanei* strains including *A. deanei* ATCC-PRA 265, the strain investigated in this study (Maurya et al., 2025). However, in other *A. deanei* strains, artificially aposymbiotic cells that lost the endosymbiont can be generated through antibiotic treatment when metabolites normally provided by the endosymbiont are externally provided (Mundim and Roitman, 1977).

The *Ca.* Kinetoplastibacterium endosymbiont was apparently acquired approximately 40-120 million years ago (MYA) by a common ancestor of the trypanosomatid subfamily Strigomonadinae, to which *A. deanei* belongs (Du et al., 1994). Thus, it is also present in species of the other genera in this subfamily, *Strigomonas* and *Kentomonas* (Teixeira et al., 2011; Votýpka et al., 2014). All *Ca.* Kinetoplastibacterium endosymbionts have highly reduced genomes (~0.8 Mbp) (Alves et al., 2013; Silva et al., 2018). Notably, this reductive genome evolution included the loss of most genes encoding essential components of the bacterial division machinery (Motta et al., 2013; Maurya et al., 2025). However, the gene encoding the central cell division protein FtsZ has been retained. FtsZ is a polymer-forming GTPase that forms in free-living bacteria as well as plastids and some mitochondria the so-called Z-ring at mid cell at the inner face of the inner membrane (Margolin, 2005; Leger et al., 2015). In bacteria, the Z-ring serves as a scaffold for the assembly of the machinery that synthesizes the division septum. In plastids, the Z-ring forms a complex with proteins in the inner and outer envelope membrane that confers topological information to the outer face of the outer envelope membrane and recruits a soluble dynamin-like protein (DLP) that forms a contractile ring structure around the plastid. Reciprocal interactions

between the Z-ring inside and the DLP ring outside result in a concerted constriction of the division machinery responsible for plastid fission (Wang et al., 2017).

Trypanosomatids that thrive in their natural habitat as parasites, mostly in the digestive tract of insects, are capable of growing axenically in culture to high densities, can be cryopreserved, and are particularly well-suited for genetic manipulation (Clayton, 1999; Lukeš et al., 2018; Yagoubat et al., 2020; Kostygov et al., 2021). Hence, the Strigomonadinae represent an optimal model to investigate the molecular mechanisms establishing nuclear control over endosymbiont division. The development of genetic tools for *A. deanei* together with the mass spectrometric characterization of the endosymbiont proteome recently enabled the identification of seven endosymbiont-targeted host proteins (ETPs) (Morales et al., 2016; Morales et al., 2023). One of these proteins is the DLP ETP9 that apparently forms a contractile ring around the endosymbiont-division site (ESDS) -likely on the outer face of the endosymbiont's outer membrane- and takes part in endosymbiont division in a manner analogous to the division of mitochondria and plastids (Morales et al., 2023; Maurya et al., 2025). *A. deanei* is a diploid organism, haploid stages are not known. Attempts to generate homozygous ETP9 knockouts in which both *etp9* alleles are replaced by a resistance marker gene, proved unsuccessful, suggesting that this nucleus-encoded protein is essential for the organism's survival. ETP9 knockdown (KD) experiments demonstrated that despite the formation of Z-ring structures in ETP9-depleted cells, endosymbionts are division-impaired, forming long, filamentous structures, within significantly distorted host cells (Maurya et al., 2025). How ETP9 is recruited to the ESDS, if it acts alone or is part of a more complex division machinery, and if nucleus-encoded endosymbiont division factors are physically linked to the bacterial Z-ring is currently unknown.

Notably, ETP9 is not the sole ETP that was found to localize at the ESDS, as ETP2 (annotated as a 'hypothetical protein') and ETP7 (containing a predicted phage-tail lysozyme domain) exhibited similar localizations (Morales et al., 2023). Here, we investigated the role of ETP2 in *A. deanei*. By using a combination of microscopy and knockout/KD approaches, we observed that ETP2 shows a cell cycle-dependent localization at the ESDS and fulfills an important role in endosymbiont division and segregation into host daughter cells. *In silico* analyses found ETP2 restricted to the Strigomonadinae and is likely an intrinsically disordered protein. Together our data suggests that ETP2 evolved as a component of the endosymbiont division machinery in *A. deanei*, exhibiting a tight control of the host over its bacterial endosymbiont.

Results

Recombinant eGFP-ETP2 is functional and consistently localizes at the ESDS

Previously, we observed that ETP2 (GenBank accession CAD2221027.1) fused at its N-terminus to the green fluorescent protein eGFP, overexpressed from the δ-*amastin* locus ($\Delta\delta$-*ama*$^{egfp\text{-}etp2}$) localizes at the ESDS (**Fig. 1A** and (Morales et al., 2023)). To verify that recombinant ETP2 expressed from its endogenous locus showed the same subcellular localization, we tagged ETP2 endogenously (Δ*etp2*$^{egfp\text{-}etp2}$*/etp2)* in a parental strain expressing the endosymbiont marker mScarlet-ETP1 ($\Delta\gamma$-*ama*$^{mS\text{-}etp1}$; see (Morales et al., 2023)) or in the wildtype (Wt) background. Epifluorescence microscopy revealed that in both cell lines, the endogenously tagged ETP2

showed the same localization as when overexpressed, although the eGFP fluorescence signal was weaker (**Fig. 1B**, micrographs 1 and 2). Cells in which both alleles of *etp2* were replaced with the recombinant version ($\Delta etp2^{egfp\text{-}etp2}/\Delta etp2^{egfp\text{-}etp2}$) showed an enhanced eGFP fluorescence signal at the ESDS (**Fig. 1C**; for confirmation of the cell line by PCR and Southern blot see **Fig. S1**). Furthermore, no unusual phenotype was observed in these cells, suggesting that its N-terminal fusion to eGFP neither affects ETP2 function nor subcellular localization.

In optical transects of the ESDS by confocal microscopy, (overexpressed) eGFP-ETP2 forms two patches at both sides of the endosymbiont envelope (**Fig. 1D**, cell cycle stage 1). These patches appear to be part of a ring-shaped structure surrounding the ESDS as observed when moving through the Z-stacks (**Movie S1**). As the bacterium elongates and constricts in the middle, during bacterial division, the two eGFP-ETP2 patches seen in the optical transects meet in the middle of the ESDS, slightly cupping the newly forming bacterial cell poles, resulting in an x-like structure (**Fig. 1D**, cell cycle stage 2 and **Movie S2**).

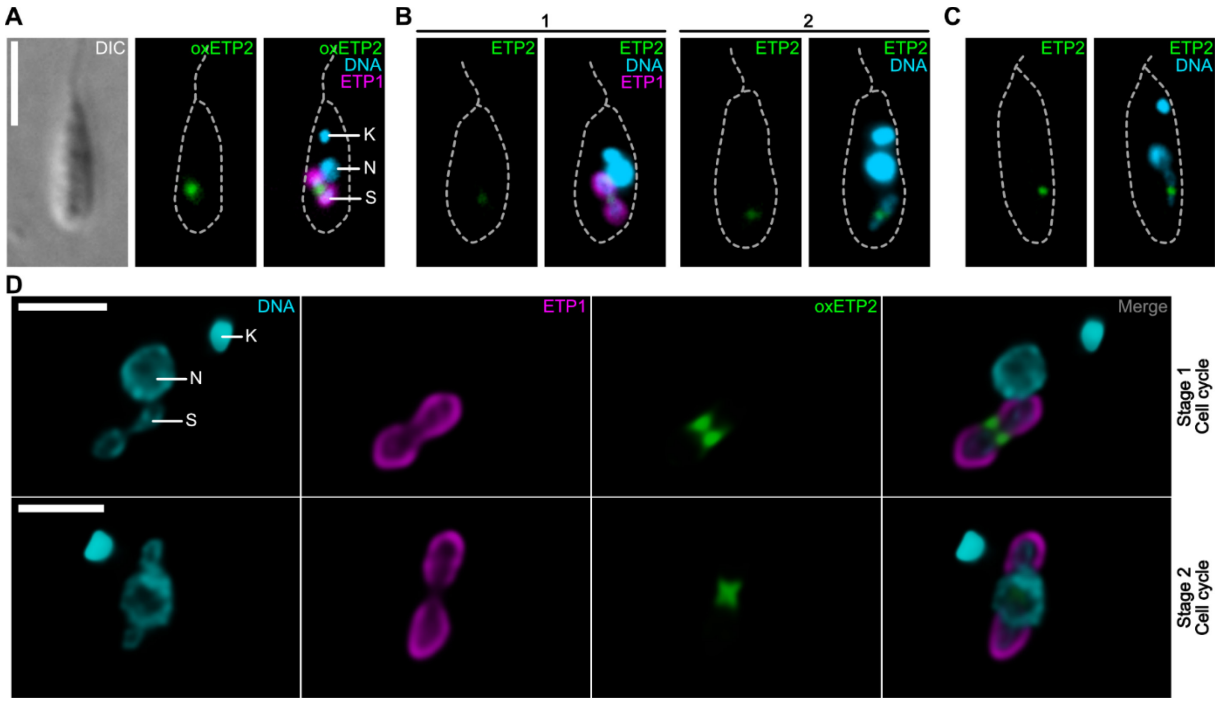

Figure 1: Subcellular localization of recombinant ETP2 in *A. deanei*. A-C: Epifluorescence microscopic analysis of subcellular localization of (A) eGFP-ETP2 overexpressed (oxETP2) from the *δ-amastin* locus in a cell co-expressing the endosymbiont marker mScarlet-ETP1; (B) eGFP-ETP2 expressed from its endogenous locus in the background of a cell expressing mScarlet-ETP1 (micrograph 1) or the Wt background (micrograph 2); and (C) eGFP-ETP2 expressed from both endogenous loci. For each image set, the eGFP channel alone (left) and the overlay of channels (right) for Hoechst 33342-stained DNA, eGFP, and (where relevant) mScarlet fluorescence are shown (A-C). As illustrated in panel A, the broken grey lines show cell outlines as seen by differential interference contrast (DIC) light microscopy. Scale bar is 5 µm. **D:** Deconvoluted fluorescence signals from confocal microscopy of eGFP-ETP2 overexpressing cells (same cell line as in A). Individual channels as well as the overlay of signals from channels for Hoechst 33342, mScarlet, and eGFP are shown. Upper row, early stage in endosymbiont division; lower row, later stage. Scale bar is 2 µm. Abbreviations: K, kinetoplast (= network of concatenated mitochondrial DNA); N, nucleus; S, endosymbiont.

Endosymbiont-encoded FtsZ and host-encoded ETP2 show a cell cycle-dependent localization at the ESDS

Previously, reconstruction of cell cycle stages of *A. deanei* had shown that the bacterium-encoded FtsZ and nucleus-encoded ETP9 exhibited a cell cycle-dependent localization at the ESDS (Maurya et al., 2025). To test whether ETP2 displayed a similar localization dynamic, we visualized FtsZ by immunofluorescence assay (IFA), and eGFP-ETP2 and the endosymbiont marker mScarlet-ETP1 by their autofluorescence. Since neither protocol for live-cell imaging nor synchronization of *A. deanei* cultures are available, we reconstructed division stages based on cell morphologies from images of >1000 fixed cells (**Fig. 2**).

For the eGFP-ETP2 overexpressing cell line (Δδ-*ama*$^{egfp\text{-}etp2}$; **Fig. 2A**), initially neither FtsZ nor eGFP-ETP2 fluorescence signals were observed (stage 0). Then, eGFP-ETP2 appears at the ESDS (stage 1a) followed by FtsZ, where they colocalize (stage 1b). During stage 2, the endosymbiont elongates with both FtsZ and ETP2 remaining co-localized at the ESDS. At later stages, the signal disappears in most cells, and only few cells show diffuse or inconsistent fluorescence signals for FtsZ and/or eGFP-ETP2. For the endogenously tagged ETP2 (Δ*etp2*$^{egfp\text{-}etp2}$/Δ*etp2*$^{egfp\text{-}etp2}$; **Fig. 2B**), the localization patterns appear similar, however, it seems that both proteins, eGFP-ETP2 and FtsZ, reach the ESDS at a similar time point. Hence, the apparently early arrival of the overexpressed eGFP-ETP2 before FtsZ (stage 1a) might rather reflect its better detectability than actual early arrival and a clear order of arrival cannot be unambiguously established.

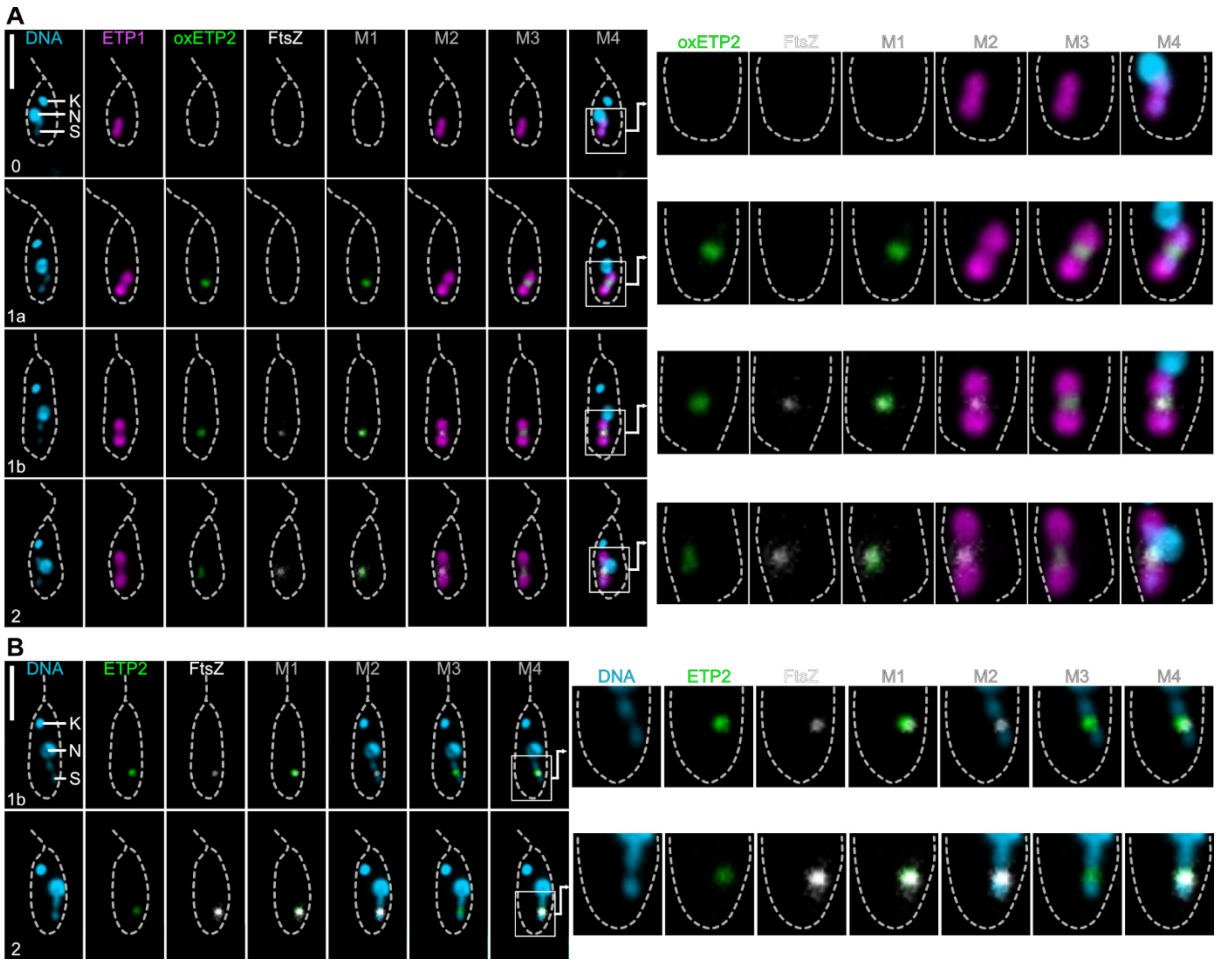

Figure 2: Subcellular localization of endosymbiont-encoded FtsZ and host-encoded recombinant ETP2 throughout early cell cycle stages. Subcellular localization of eGFP-ETP2 and FtsZ in mid-log phase cells co-expressing mScarlet-ETP1 ($\Delta\gamma$-*ama*$^{mS\text{-}etp1}$) and eGFP-ETP2 [overexpressed ($\Delta\delta$-*ama*$^{egfp\text{-}etp2}$) in **A**; and endogenously tagged (Δ*etp2*$^{egfp\text{-}etp2}$/Δ*etp2*$^{egfp\text{-}etp2}$) in **B**] throughout early cell cycle stages as analyzed by epifluorescence microscopy. eGFP-ETP2 (green) and mScarlet-ETP1 (magenta) were detected by their autofluorescence, FtsZ (white) by IFA, and DNA (cyan) by Hoechst 33342 staining. Scale bars are 5 µm. Merges in A: Merge1, overlay of eGFP and FtsZ signals; Merge2, mScarlet and FtsZ; Merge3, mScarlet and eGFP; Merge4, all four channels. Merges in B: Merge1, overlay of eGFP and FtsZ signals; Merge2, FtsZ and Hoechst33342; Merge3, eGFP and Hoechst33342; Merge4, all three channels. Abbreviations are the same as in Fig. 1. Numbers on images show cell cycle stages compared to **Maurya et al., 2025**. White boxes in the left panels indicate areas of detailed images in the right panels.

Generation of a homozygous *etp2* deletion mutant is viable and results in severe division phenotypes

To study the cellular function of ETP2, we initially generated a heterozygous *etp2* deletion mutant cell line in which one allele of *etp2* was replaced by the neomycin phosphotransferase gene, *neo*^{R}, (Δ*etp2*^{neo}/*etp2*; **Fig. 1S**). This mutant showed no noticeable phenotype. Several attempts to replace the remaining allele of *etp2* by a hygromycin phosphotransferase gene, *hyg*^{R}, failed.

However, we obtained a homozygous deletion mutant cell line, in which the second allele was disrupted by insertion of a *hyg*^{R}-containing cassette into the *etp2* open reading frame (ORF) resulting in a heavily truncated ETP2 protein (Δ*etp2*^{neo}/Δ*etp2*$_{246\text{-}491}$^{hyg}; **Fig. S1**). Both, heterozygous and homozygous *etp2* deletion mutants were generated not only in the symbiotic but also an aposymbiotic *A. deanei* strain (strains ATCC PRA-265 and ATCC 30969, respectively). All cell lines generated were verified by PCRs and Southern blot analysis (**Fig. S1**). Interestingly, in the symbiotic homozygous *etp2* deletion mutant cell line, >50% of the cells displayed either long, filamentous endosymbionts accompanied by severely distorted host cells or loss of the endosymbiont (**Fig. 3A-C**). This distortion was not witnessed in the aposymbiotic homozygous *etp2* deletion mutant cell line where cells did not differ morphologically from Wt cells (**Fig. S2**), suggesting that the function of ETP2 is confined towards the endosymbiont, with the resulting distorted host morphology caused by downstream effects of impaired endosymbiont division. This distortion of host cells was accompanied by the occurrence of multiple kinetoplasts and flagella, and notably, a singular and enlarged nucleus in most cases, suggesting that both kinetoplast and nuclear DNA replication remain active yet only segregation of the kinetoplast is fulfilled. However, ~48% of the cells appeared 'normal' retaining a singular, morphotypical endosymbiont (**Fig. 3B-C**). Upon closer examination, a number of morphologically 'normal' host cells appear in the final stages of cytokinesis, attached only by an apparently undivided endosymbiont localized at the posterior end of the cells (**Fig. 3B**, white arrowhead). Additionally, some cells lacking endosymbionts are noted in the final stages of cytokinesis (**Fig. 3B**, black arrowhead), and possibly completing it without fulfilling complete segregation of the endosymbiont, explaining the high population of aposymbiotic cells in the homozygous mutant. Hence, the disruption of the second *etp2* allele is not entirely lethal, suggesting that although now error prone, successful endosymbiont division is still possible. This is reflected also by the slower growth of the *etp2* deletion mutant compared to Wt cells (**Fig. 3D**).

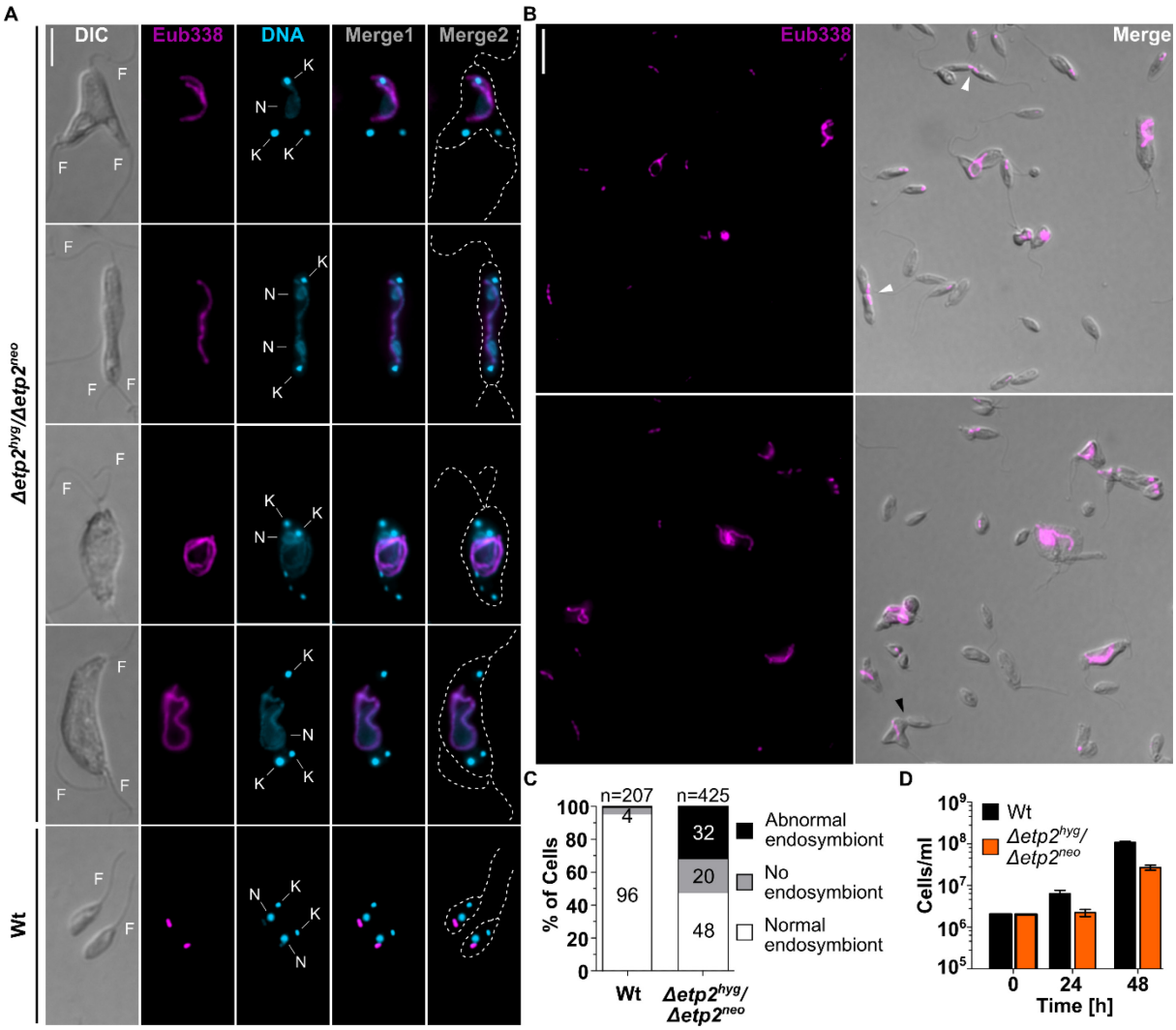

Figure 3: Characterization of homozygous *etp2* deletion mutants in symbiotic *A. deanei*. A: Fluorescence *in situ* hybridization (FISH) micrographs of homozygous *etp2* mutant cells. Wt *A. deanei* cells are shown as a control. Merge1, superposition of signals from Hoechst 33342-stained DNA (cyan) and the Cy3-Eub338 FISH probe directed against the bacterial 16S rRNA (magenta). Merge2, superposition of Hoechst 33342 and Cy3 signals on cell outlines as seen by DIC (broken grey lines). Abbreviations: K, kinetoplast; N, nucleus; F, flagellum. Scale bar is 5 µm. **B:** Overview micrographs of Cy3-Eub338 FISH-stained homozygous *etp2* mutant cells showing the occurrence of cells with abnormal, normal, or lacking endosymbionts. White arrowheads indicate host cells during the final stages of cytokinesis, however, attached by an undivided endosymbiont at the posterior end. Black arrowhead indicates a host cell in the final stage of cytokinesis lacking an endosymbiont. Scale bar is 10 µm. Note the multiple occurrences of cells lacking an endosymbiont. **C:** Quantification of division phenotypes in the *etp2* mutant compared to Wt cells. **D:** Cell counts of symbiotic Wt and *etp2* deletion mutant cells at 24 h and 48 h after inoculation (0 h). Plotted are mean and standard deviation from three biological and for each three technical replicates.

KD of ETP2 results in elongated endosymbionts in severely distorted host cells

To confirm by an independent method that the observed division phenotype in homozygous *etp2* deletion mutants is caused by the lack of ETP2, we used a KD approach based on morpholino antisense oligos (MAOs).

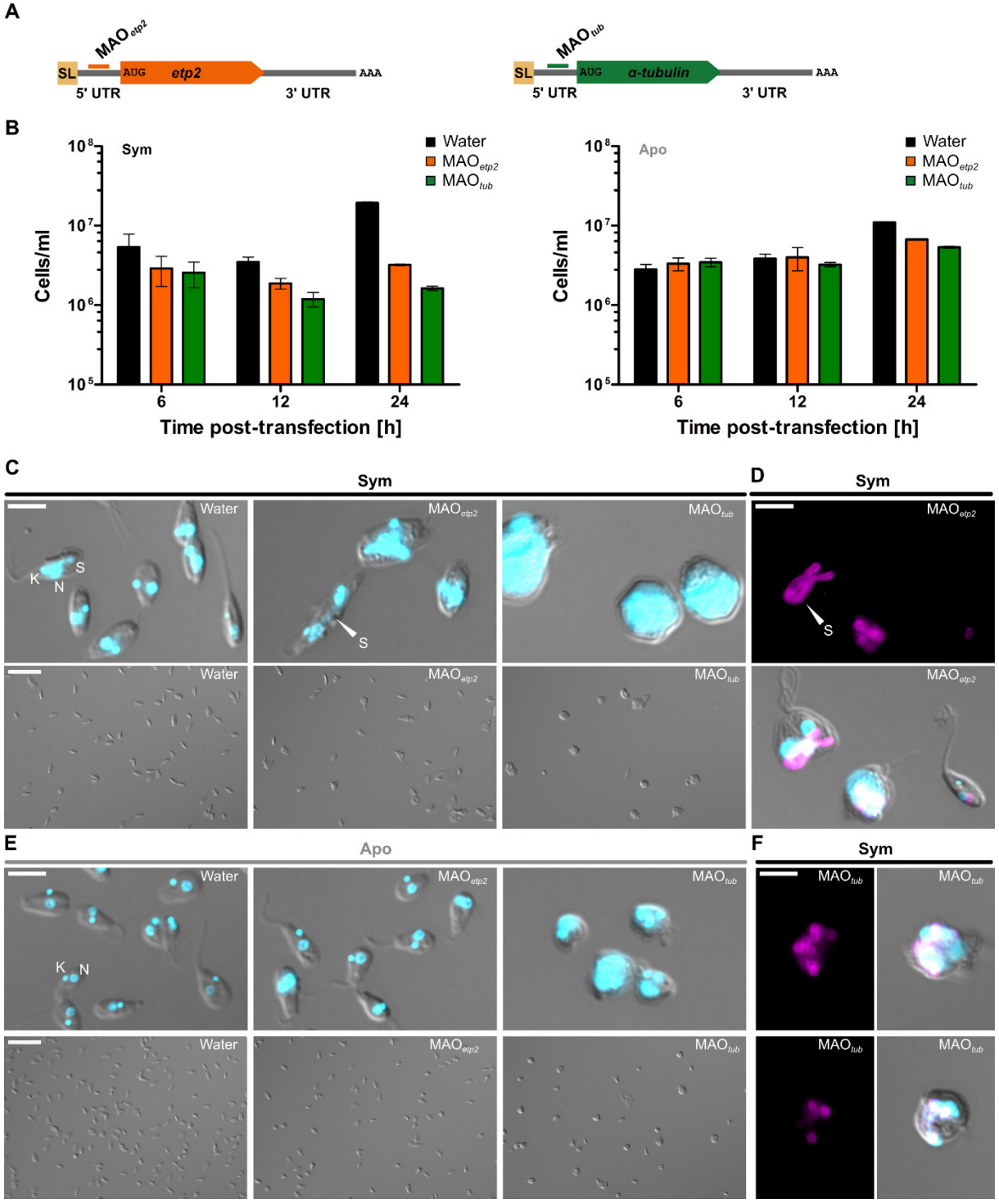

Figure 4: KD of ETP2 in symbiotic and aposymbiotic *A. deanei* strains. A: Schematic representation of MAO binding sites on the target mRNA of *etp2* and *α-tubulin*. **B:** Cell densities of cultures of the symbiotic

and aposymbiotic *A. deanei* strains 6 h, 12 h, and 24 h post-transfection with water, MAO_{etp2} or MAO_{tub}. Plotted are mean and standard deviation from three technical replicates. **C:** Micrographs of the symbiotic cells 24 h post-transfection for each treatment. A detail micrograph (merge of DIC and Hoechst 33342, upper panel) and overview micrograph (DIC, lower panel) are shown. **D:** Micrographs of symbiotic cells expressing the endosymbiont marker mScarlet-ETP1 24 h post-transfection with MAO_{etp2}. The mScarlet channel alone (upper panel) and merge of DIC, Hoechst 33342, and mScarlet channels (lower panel) are shown. (For overview images, **see Fig. S3**). **E:** Micrographs of aposymbiotic cells 24 h post-transfection for each treatment. A detail micrograph (merge of DIC and Hoechst 33342, upper panel) and overview micrograph (DIC, lower panel) are shown. **F:** Micrographs of symbiotic cells expressing the endosymbiont marker 24 h post-transfection with MAO_{tub}. The mScarlet channel alone (left panel) and merge of DIC, Hoechst 33342, and mScarlet channels (right panel) are shown. Abbreviations: K, kinetoplast; N, nucleus; S, symbiont; SL: splice leader, and UTR: untranslated region. Arrowhead highlights the symbiont. Scale bars are 5 µm (for detail) and 25 µm (for overview micrographs).

For this, we transfected symbiotic and aposymbiotic *A. deanei* Wt cells with MAOs designed against *etp2* mRNA (MAO_{etp2}) (**Fig. 4A**). Hybridization of MAOs with the 5' UTR of a specific mRNA results in the repression of its translation (Summerton and Weller, 1997). Consistent with the phenotype observed in the *etp2* deletion mutants (**Fig. 3**), 24 h post-transfection, we observed a clear reduction in growth and the formation of long, filamentous endosymbionts in distorted host cells in the symbiotic strain (**Fig. 4B-C**), whereas in the aposymbiotic strain no noticeable changes in cell morphology were observed (**Fig. 4E**). However, a slight reduction in growth was observed in the aposymbiotic strain following transfection with MAO_{etp2} compared to the water control, which might reflect off-target effects (**Fig. 4B**). For better visualization of the endosymbionts, cells expressing the endosymbiont marker mScarlet-ETP1 were also transfected with MAO_{etp2} resulting the same filamentous endosymbionts (**Fig. 4D;** for overview images see **Fig. S3**).

Importantly, symbiotic as well as aposymbiotic cells mock treated with water showed the highest cell numbers and no aberrant cell morphologies 24 h post-transfection (**Fig. 4B-C, E**); while cells transfected with MAO_{tub} against α-tubulin, as a positive control, exhibited the expected effects (**Fig. 4B-C; E**), with a markedly reduced growth and formation of roundish cell morphologies comparable to the "Fat Cells" phenotype described in *Trypanosoma brucei* following RNAi against α-tubulin (Ngô et al., 1998) and our previous results in *A. deanei* (Maurya et al., 2025). Furthermore, a massive accumulation of DNA-containing compartments was observed following α-tubulin KD. This phenomenon was more pronounced in the symbiotic strain, probably due to its generally larger cell and organelle sizes in addition to the presence of the endosymbiont (see **Fig. S4**). The red fluorescence signal of mScarlet-ETP1-expressing cells shows that although clumps of endosymbionts appear in the roundish, division-impaired host cells with reduced α-tubulin, the endosymbionts appeared to be fully divided and not filamentous, suggesting that endosymbiont division itself was not impaired **(Fig. 4F)**.

Formation of the Z-ring at the ESDS is independent of ETP2

To assess the effects of ETP2 depletion on the localization of the bacterium-encoded FtsZ, we repeated the ETP2 KD (in cells expressing mScarlet-ETP1) followed by IFA using an antibody raised against *Ca.* K. crithidii FtsZ (Maurya et al., 2025). 24 h post-transfection, FtsZ was

observed to form several foci along the filamentous endosymbionts **(Fig. 5)**, suggesting that formation of the Z-ring is independent of ETP2.

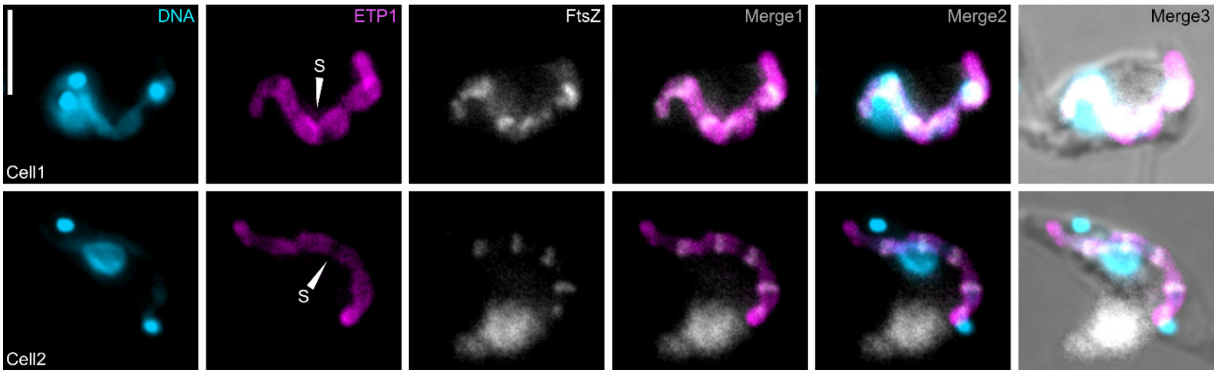

Figure 5: Localization of FtsZ in symbiotic *A. deanei* cells following *etp2* KD. Subcellular localization of the bacterium-encoded FtsZ in symbiotic cells expressing the endosymbiont marker mScarlet-ETP1 24 h post-transfection with MAO_{etp2}. Shown are the fluorescence signals of Hoechst 33342-stained DNA (cyan), mScarlet-ETP1 autofluorescence (magenta), and the IFA signal for FtsZ (white). Merge1, overlay of fluorescence signals of mScarlet-ETP1 and FtsZ; Merge2, DNA, mScarlet-ETP1, and FtsZ; Merge3, DNA, mScarlet-ETP1, FtsZ, and the DIC picture. White arrowheads show long, filamentous endosymbionts (S). Scale bar is 5 µm.

ETP2 is likely an intrinsically disordered protein and is exclusively found within the Strigomonadinae

To gain a deeper understanding of the origin and function of ETP2, we conducted BLAST searches (E-value threshold 1E-1) against both the NCBI and EukProt (Richter et al., 2022) databases. These searches yielded hits exclusively to *A. deanei* and *Strigomonas culicis* (Strigomonadinae), where the protein is annotated as 'hypothetical protein'. To gain insights into its potential cellular function, we analyzed the ETP2 sequence for the presence of specific domains using HHPred (Söding et al., 2005) and SMART domain (Letunic et al., 2021); however, no significant hits were identified. Additionally, we employed a series of secondary structure prediction tools, including JPred4 (Drozdetskiy et al., 2015) and SPIDER3 (Heffernan et al., 2017), which predicted the presence of alpha helices and beta sheets exclusively within the C-terminal region of the sequence, beyond amino acid position 343 (**Fig. 6A**). Given the absence of predicted structural motifs in the N-terminal region, we analyzed the sequence using intrinsic disorder domain (IDD) prediction software, namely IUPred (Dosztányi et al., 2005) and SPOTD (Hanson et al., 2017). These analyses indicated a high probability of intrinsic disorder throughout the entire N-terminus, up to amino acid position 341 (**Fig. 6A**).

Consistent with these sequence-based analyses, AlphaFold3 (Abramson et al., 2024) predicted for ETP2 a generally structured C-terminus and unstructured N-terminus (**Fig. 6B**). However, the predicted tertiary structure exhibited low to very low predicted local distance difference test (pLDDT) scores across the entire protein, in line with the expected confidence scores for IDDs (Ruff and Pappu, 2021). To further substantiate the prediction that the N-terminus of the protein is an IDD, we performed a more detailed analysis using AIUPred (Erdős and Dosztányi, 2024), which returned values consistent with an IDD in the N-terminal region (**Fig. 6C**).

The observed localization pattern of recombinant ETP2 suggests that the protein interacts at the ESDS with the (outer or inner) endosymbiont membrane (**Fig. 1**). Therefore, we investigated the presence of potential lipid-binding domains within the sequence by DisoLipPred (Katuwawala et al., 2022). This analysis identified a region (amino acids 333–342) with a high probability of harboring a disordered lipid-binding motif (**Fig. 6D**). The potential membrane-binding capability of this motif was further supported by PMI-Pred (van Hilten et al., 2024) analysis, which predicted a free energy of -64.453 kJ/mol for binding of this specific sequence to a negatively charged membrane, well below the required threshold of -28 kJ/mol, supporting membrane binding (van Hilten et al., 2024) (**Fig. 6D**).

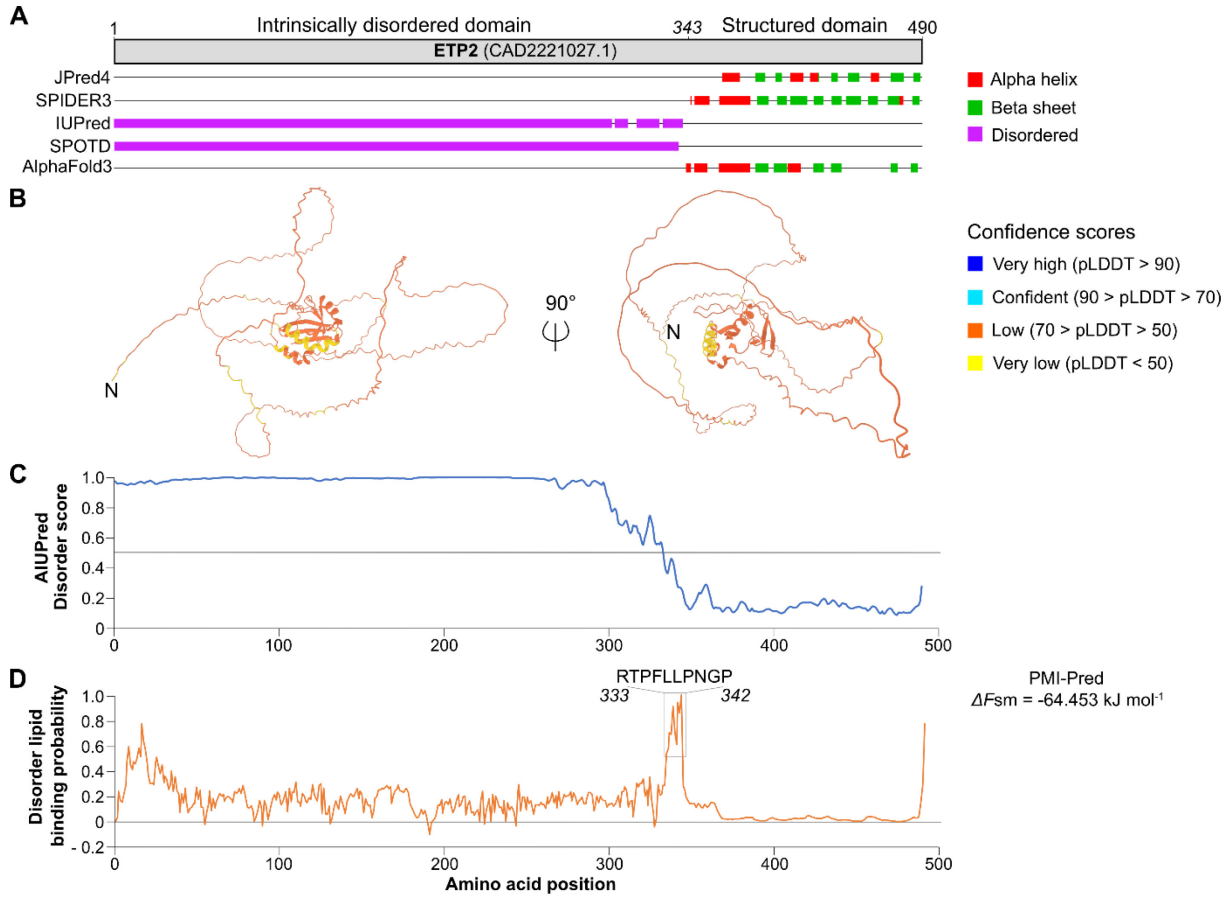

Figure 6: *In silico* analyses predict ETP2 as an intrinsically disordered protein with putative lipid binding capability. A: Overview of secondary structure elements and IDDs of ETP2 predicted by JPred4, SPIDER3, IUPred, SPOTD, and AlphaFold3 (as indicated). Consensus of the start of the structured domain of ETP2 at amino acid position 343 is indicated. **B:** AlphaFold3-predicted tertiary structure of ETP2. The N-terminus of the protein is marked with 'N'. Confidence scores are indicated on the right. **C:** Results of AIUPred analysis of ETP2 using the default options (AIUPred – only disorder, Default smoothing). Prediction scores >0.5 (above grey line) indicate disordered regions. **D:** Results of DisoLipPred analysis of ETP2. Larger scores denote higher likelihood of a disordered lipid binding region. The region containing the highest likelihood (amino acids 333–342) is highlighted. Predicted free energy for membrane-binding

of the highlighted sequence by PMI-Pred using the 'negatively charged membrane' option is shown on the right. Free energy values (ΔFsm) of <-28 kJ mol^{-1} indicate high likelihood for membrane binding.

Discussion

In some associations between protists and their bacterial endosymbionts a precise coordination between host and endosymbiont cell division has evolved, ensuring a defined number of endosymbionts per host daughter cell. The molecular mechanisms underlying this cell cycle coordination are largely unknown. *A. deanei* has been recently reported to manifest nuclear control over its endosymbiont's division by means of the DLP ETP9 that apparently forms a contractile ring structure around the ESDS and functionally compensates for the loss of essential division genes from the endosymbiont genome (Maurya et al., 2025). Here, we functionally characterized a second nucleus-encoded protein, ETP2, previously reported to localize at the ESDS in *A. deanei* (Morales et al., 2023).

Through analysis of >1000 cells expressing eGFP-tagged ETP2 (endogenously or overexpression), we found that ETP2 localizes at the ESDS specifically at cell cycle stages in which the endosymbiont divides **(Figs. 1 and 2)**. Replacement of both *etp2* alleles with the recombinant copy without a resulting phenotype **(Fig. 1C)** demonstrated that its N-terminal fusion to eGFP did not affect the localization or function of ETP2. The accumulation of ETP2 at the ESDS appears to precede the emergence of ETP9, which arrives at the ESDS after the formation of the Z-ring (compare **Fig. 2** and (Maurya et al., 2025)). The functional involvement of ETP2 in endosymbiont division is demonstrated by the striking division phenotype exhibited by homozygous *etp2* deletion mutants and by Wt cells following ETP2 KD, with filamentous endosymbionts in highly distorted host cells (**Fig. 3A-C** and **Fig. 4**). However, in both experiments numerous non-distorted host cells were also present that display Wt morphology and either harbor a single endosymbiont or lost the endosymbiont and are, hence, bound to die (**Fig. 3B-C** and **Fig. S3**). We witnessed cases where non-distorted host cells undergoing cytokinesis appeared to remain attached through their posterior ends by an undivided endosymbiont (**Fig. 3B**, white arrowhead), and apparently successfully detaching host cells not inheriting an endosymbiont (**Fig. 3B**, black arrowhead). The fact that the *etp2* deletion cell line remains alive, yet exhibits slower growth compared to the Wt (**Fig. 3D**), lends to the conclusion that despite of the disruption of the last remaining *etp2* allele, a subset of the population is still capable of undergoing cytokinesis and inheriting a morphotypical endosymbiont. Whether this outcome depends on the presence of the truncated ETP2$_{1\text{-}245}$ that remains in the homozygous deletion mutant (**Fig. S1D**) is currently unclear.

In aposymbiotic ETP2 deletion mutants and Wt cells following ETP2 KD, no division phenotype was observed (**Figs. S2** and **4E**), demonstrating that the ETP2 function is specific for endosymbiont division and the observed distorted host morphology is a secondary effect resulting from impaired endosymbiont division. The reduced growth of aposymbiotic cells following ETP2 KD (**Fig. 4B**) may represent an off-target effect. However, in the short 5' UTR of *etp2* no suitable binding site for a non-overlapping MAO was found that would help to verify this interpretation.

Intriguingly, in most symbiotic ETP2 deletion mutant cells, where the host is highly distorted, we observed the development of multiple kinetoplasts with an attached flagellum alongside a singular enlarged nucleus **(Fig. 3A)**. Hence, inhibition of endosymbiont division, which precedes kinetoplast division (Maurya et al., 2025), does not appear to affect kinetoplast and nucleus replication or kinetoplast segregation. In *T. brucei* and other trypanosomatids, the division furrow originates by the segregation of the flagella through separation of kinetoplasts via the basal bodies and tripartite attachment complex (TAC; a structure linking the kinetoplast and basal body), thus, making kinetoplast segregation a key initiator of cytokinesis (Kohl et al., 2003; Gluenz et al., 2011; Wheeler et al., 2013; Schneider and Ochsenreiter, 2018). Interestingly, while numerous proteins have been identified and functionally characterized that mediate this process in *T. brucei* (Schneider and Ochsenreiter, 2018), comparative genomics has indicated a potential loss of some of these regulatory genes in *A. deanei* (Cadena et al., 2024). Moreover, an additional nucleus-encoded protein that has been reported to associate with the endosymbiont, ETP5 (Morales et al., 2023), is orthologous to the KMP-11 protein, a known mediator in cytokinesis and localized to the basal bodies and flagella of *T. brucei* (Li and Wang, 2008). Whether the loss of proteins involved in kinetoplast, TAC, and basal body segregation is caused by the precedence of the endosymbiont dividing first in the *Strigomonadinae* cell cycle remains an open question.

Our BLAST, Hidden Markov Modeling, and SMART analysis results demonstrated that neither proteins similar to ETP2 nor potential domains therein are found in organisms outside of the Strigomonadinae. Secondary and tertiary structure predictions for ETP2 suggested an unstructured N-terminal domain (amino acid positions 1 – 346) ending in a potential membrane-binding motif and a structured C-terminus, however, with low confidence scores for tertiary structure prediction throughout the entire protein (**Fig. 6**). Collectively, these findings point to an origin of ETP2 as a result of *de novo* innovation within the Strigomonadinae (McLysaght and Guerzoni, 2015) and possibly its intrinsically disordered nature (Ruff and Pappu, 2021). The genesis of intrinsically disordered proteins resulting primarily from *de novo* gene innovation has been repeatedly suggested (Wilson et al., 2017; Bornberg-Bauer et al., 2021; Heames et al., 2023; Chen et al., 2024). Interestingly, due to their unstructured nature, intrinsically disordered proteins may transiently interact with multiple binding partners and, thus, act in form of signaling hubs or scaffolds as temporal organizers (Haynes et al., 2006; Patil and Nakamura, 2006; Cortese et al., 2008; Uversky, 2015; Cornish et al., 2020). Whether ETP2 is capable of acting as either a scaffold or signaling hub, recruiting other proteins involved in endosymbiont division to the ESDS, remains an exciting possibility to be explored. Since FtsZ localizes in distinct foci along the filamentous endosymbionts following *etp2* KD (**Fig. 5**), recruitment of FtsZ to the prospective ESDS, which is likely controlled by the endosymbiont-encoded Min system (Maurya et al., 2025), is apparently not affected by ETP2 depletion. Whether the recruitment of nucleus-encoded proteins such as ETP9 towards the ESDS is affected remains to be explored.

In sum, our work demonstrates that ETP2 plays a major role in the division of the endosymbiont. Additionally, we showed that disruption of endosymbiont division ultimately affects host cell division. With *A. deanei* cells containing a single, elongated endosymbiont displaying complete cytokinetic arrest alongside multiple kinetoplasts and flagella in a single host cell. Given the presence of ETP2 solely within Strigomonadinae, and lack of *in silico* identifiable homologous regions or domains, we hypothesize that ETP2 is a largely intrinsically disordered proteins

resulting from *de novo* origin and may function as a scaffold or signaling hub given its early recruitment to the EDSD. Although our findings lend further credence that the endosymbiont division machinery in *A. deanei* is of dual genetic origin, the full characterization of this fascinating structure remains at its infancy.

Methods

Microbial strains, media, and growth conditions. Both, symbiotic *Angomonas deanei* (ATCC PRA-265) and aposymbiotic *A. deanei* (ATCC 30969) strains were grown in brain heart infusion (BHI, Sigma Aldrich) medium supplemented with 10 µg/ml hemin (Sigma Aldrich). Medium for the aposymbiotic strain was additionally supplemented with 10% v/v horse serum (Sigma Aldrich). *A. deanei* cultures were grown at 28 °C under static conditions and sub-cultured twice a week, once they reached cell densities of ~1.0 x 10^7 cells/ml (for the aposymbiotic strain) and ~1.0 x 10^8 cells/ml (for the symbiotic strain). Cell counting was performed using a Multisizer 4e cell counter (Beckman Coulter).

Escherichia coli TOP10 cells, used for plasmid preparation, were grown in lysogeny broth (LB) medium supplemented with 100 µg/ml ampicillin at 37 °C for 16-18 h under aerobic conditions.

Plasmid generation. All primers used in this study are listed in **Table S1**, schematic maps of plasmids and strains used or generated in this study are displayed in **Fig. S5**.

For the generation of homozygous *etp2* deletion mutants, plasmid pAdea457 was generated. For this, the pUMA1467 backbone (Terfrüchte et al., 2014) was amplified from plasmid pAdea369 using the primer pair 3237/3244. The first half and second half of the *etp2* gene were used as 5' and 3' flanking region (fr) and were amplified from *A. deanei* genomic DNA (gDNA) using primer pairs 3238/3239 and 3242/3243, respectively. A fragment containing the *γ-amastin* 5' fr with its spliced leader (SL) donor sequence, *hyg*^{r}, and the intergenic region between the *gapdh1* and *gapdh2* genes, gapdh ir, was amplified from pAdea368 using primer pair 3240/3241. All the amplified fragments were assembled by Gibson cloning (Gibson et al., 2009).

For the generation of pAdea115 (used for endogenous tagging of the first *etp2* allele), the fragment *etp2* fr 3'-pUMA1467-*etp2* fr 5' was amplified from plasmid pAdea092 using primer pair 1015/1016 and the fragment *neo*^{r}-gapdh ir-*egfp-etp2* was amplified from pAdea035 using primer pair 1022/1023. Both fragments were ligated by Golden Gate cloning (Engler et al., 2008).

For the generation of pAdea477 (used for endogenous tagging of the second *etp2* allele), primer pair 3322/3323 was used for the amplification of the entire pAdea115 template except the *neo*^{r} gene and primer pair 3320/3321 was used to amplify *hyg*^{r} from pAdea260. Both fragments were ligated by Gibson cloning.

All plasmids were amplified in *E. coli* TOP10 and isolated by NucleoSpin Plasmid kit (Macherey-Nagel). Correct assembly was verified by sequencing (Microsynth AG, Balgach, Switzerland).

Transfection of *A. deanei*. For efficient integration of a prepared DNA cassette into the *A. deanei* nuclear genome, ~40 µg of plasmid DNA was digested with restriction enzyme(s) cutting at the 5'

and 3' ends of the insertion cassette (see maps in **Fig. S5**). The linearized cassette was transfected into *A. deanei* cells as described earlier (Morales et al., 2023). In brief, 1.0 x 10^7 cells were harvested and resuspended in 18 µl of P3 primary cell solution. 2 µl of the digested plasmid (2-4 µg DNA) were mixed with the cells and pulsed with the program FP158 using Nucleofector 4D (Lonza). Cells were immediately transferred to 5 ml growth medium without antibiotics. Cells were allowed to recover for 6 h at 28 °C. After this incubation, cells were diluted 10-fold in the same medium with the respective selection antibiotic(s) added at final concentrations of 500 µg/ml for both G418 (Sigma Aldrich) and hygromycin B gold (InvivoGen). Diluted cells were distributed in 200 µl aliquots on a 96-well plate and incubated at 28 ˚C until single wells showed turbidity indicating the growth of clonal cell lines (typically 5-6 days). Clones were isolated and used further for verifications by PCR.

Verification of transgenic cell lines by PCR. To verify selected clones by PCR, gDNA was isolated from cells using 200 µl of DNAzol (Thermo Fisher) according to the manufacturer's instructions and dissolved in 20 µl of sterile dH_2O. Primers that were used **(see Table S1)**, either binding in the genomic region outside of the inserted cassette or one primer binding outside and the other inside the cassette. Only verified strains were used for further analysis.

Southern blot analysis. For the replacement of the second *etp2* allele (that caused a phenotype in the context of *etp2* disruption, but not for *egfp* tagging), insertion of a single cassette was verified by Southern blot analysis as described before (Morales et al., 2023). Briefly, ~7.5 µg of gDNA was isolated by the DNeasy Blood & Tissue kit (Qiagen), digested overnight using appropriate restriction enzymes, and resolved on 0.8% w/v agarose gel. Next, DNA was transferred to a nylon membrane (Nytran N Nylon Blotting Membrane, 0.45 µm; GE Healthcare Life Sciences) overnight by capillary method and fixed on the membrane using 0.120 Joules with a UV-strato-Crosslinker (Analytik Jena). A digoxigenin (DIG)-labelled probe against *hyg*^{r} (*α-hyg*^{r}; see **Fig. S1**) was generated using the primers indicated in **Table S1** and hybridized to the DNA immobilized on the membrane at a hybridization temperature of 53 °C. Lastly, the membrane was developed as per the protocol supplied with the DIG-High Prime DNA Labeling and Detection Starter kit II (Roche Applied Science). The resulting chemiluminescence signal was detected by a Chemidoc MP (Bio-Rad).

Epifluorescence microscopy. For visualizing cells, epifluorescence microscopy was performed as described before (Morales et al., 2023). In brief, cells in the mid-log phase were mixed with formaldehyde (FA) to a final concentration of 4% w/v and incubated in dark at room temperature (RT) for 10-15 min. Next, cells were washed twice and resuspended in phosphate buffered saline (PBS). Then, cells were spotted onto a glass slide coated with 0.01% poly-L-lysine (Specialty Media), mixed with 30 µg/ml Hoechst 33342 in PBS, and incubated at RT in the dark for 10-15 min. After incubation, cells were washed three times with PBS and coated with antifade reagent SlowFade Diamond (Thermo Fisher Scientific). Images were acquired with an Axio Imager M.1 (Zeiss, Oberkochen, Germany) using an EC Plan-Neofluar 40x/1.3 oil Ph3 or 100x/1.30 Oil Ph3M27 objective (Zeiss). Images were analyzed with Zen Blue v2.5 and processed with ImageJ v2.0 software.

Immunofluorescence assay (IFA). For visualizing FtsZ, IFA was performed as described before (Maurya et al., 2025). All steps were performed at RT in the dark. In brief, cells in the mid-log

phase were mixed with FA to a final concentration of 4% w/v and incubated for 15 min. Cells were collected, washed with PBS, and resuspended in an appropriate volume of PBS. Then, 20 µl cell suspension was spotted onto 0.01% poly-L-lysine-coated glass slides and incubated for 20 min. After incubation, unbound cells were removed and attached cells permeabilized with 10 µl 0.2% v/v Triton-X100 in PBS for 20 min. Then, cells were washed in PBS and incubated with 1% w/v blocking solution (BS; albumin bovine fraction V, pH-7.0, Serva) in PBS for 45 min. Next, 15 µl of 1:80 diluted anti-$FtsZ_{pepC}$ primary antibody (raised in rabbit against *Ca.* K. crithidii FtsZ, see (Maurya et al., 2025)) in 1% BS was applied and incubated for 1.5 h followed by three washes in 1% BS. The 1:500 diluted anti-rabbit IgG (goat, polyclonal, Abberior Star-red, Ex: 638 nm) secondary antibody in 1% BS was applied and incubated for 1 h followed by three washes in 1% BS. After antibody staining, DNA was stained with Hoechst 33342. Finally, cells were coated with 7 µl antifade reagent SlowFade Diamond (Thermo Fisher Scientific) and imaged with an Axio Imager M.1 as described before. mScarlet-ETP1 and eGFP-ETP2 were detected based on their autofluorescence. For reconstruction of cell cycle stages, more than 1,000 cells were analyzed with Zen Blue v2.5 software.

Fluorescence *in situ* hybridization (FISH). For visualizing the endosymbionts by FISH, cells from mid-log phase were mixed with FA to a final concentration of 4% w/v and incubated for 30 min. Cells were harvested thereafter, washed 3 times with PBS, and resuspended in an appropriate volume of PBS. Then, 20 µl cell suspension was spotted onto 0.01% poly-L-lysine-coated glass slides and air-dried for 30 min. The slides were consecutively placed in 50%, 80%, and 100% ethanol for 3 min each to dehydrate the cells. Then, 5 µl of a 5' Cy3-labeled Eub338 probe (50 ng DNA μl^{-1}) directed against the bacterial 16S rRNA (Amann et al., 1991; Fuchs et al., 2007) was mixed with 45 µl of hybridization buffer (900 mM NaCl, 20 mM Tris-HCl pH 7.2, 35% formamide, 10% SDS in dH_2O) and spotted onto the dry slides. The slides were incubated at 46 °C for 2 h in a humid chamber. Afterwards, the slides were washed in FISH-wash buffer (80 mM NaCl, 20 mM Tris-HCl pH 7.2, 10% SDS in dH_2O) and incubated at 48 °C for 25 min. The slides were rinsed twice with dH_2O and mixed with 30 µg/ml Hoechst 33342 in PBS, and incubated at RT in the dark for 10-15 min. After incubation, cells were washed three times with PBS and coated with SlowFade Diamond (Thermo Fisher Scientific). Images were acquired and analyzed as described before.

Confocal microscopy. Slides were prepared as described earlier (Maurya et al., 2025). The protocol was the same as for epifluorescence microscopy slide preparation except that a high precision coverslip (LxW-22x22 mm, No. 1.5H, thickness-170 µm, Marienfeld, VWR) was used to spot 0.01% poly-L-lysine. All steps were performed on this coverslip. Later, the coverslip was put upside down on a glass slide. Imaging was performed at an inverted confocal microscope, Leica TCS SP8 (STED 3X), with standard settings as described before (Morales et al., 2023) except that the laser line was set at 35% for eGFP and 15% for mScarlet. For deconvolution of the raw data, Huygens Professional v.23.10.0p7 64b was used with default settings except that in manual mode a threshold for background extraction was set based on background fluorescence signals. Generation of supplementary movies was performed as described earlier (Maurya et al., 2025).

KD assays using MAOs. For KDs, *A. deanei* cells were transfected with MAOs as described earlier (Maurya et al., 2025) using MAO_{etp2} (5'-CGTAGTCCATTTTGGTGTGTATGAT-3') or

MAO_{tub} (5'- TGAATGCAGATAGCCTCACGCATGG -3', as a positive control), all synthesized by Gene Tools, LLC, Philomath, OR, USA. After transfection, cells were transferred into BHI medium supplemented with hemin and horse serum without antibiotics for all strains and incubated at 28 °C. Samples were collected at 6 h, 12 h, and 24 h post-transfection and used for Hoechst 33342 staining and epifluorescence microscopy as described before.

Growth measurements. For the homozygous *etp2* mutant cell line, growth analysis was performed as described before (Maurya et al., 2025). Briefly, 4 x 10^5 cells/ml were inoculated in triplicates in 5 ml BHI medium supplemented with hemin without antibiotics and incubated at 28 °C. Cells were counted in triplicates at 24 h and 48 h using a cell counter (Multisizer 4e, Beckman Coulter). For MAO-treated cells, counting was performed in triplicates at 6 h, 12 h, and 24 h post-transfection.

***A. deanei* cell and organelle measurements.** For measuring the width (W) and length (L) of symbiotic and aposymbiotic *A. deanei* strains, cell line Adea126 expressing mScarlet-ETP1 and Wt aposymbiotic strains were used, respectively. For W and L measurements of the cell, DIC images were used. For kinetoplast (K) and nucleus (N), Hoechst 33342 staining was used. For measuring the endosymbiont (ES), mScarlet-ETP1, localized at the bacterial envelope, was used. Measurements were performed manually with Zen v.2.5 on cells that were categorized into different cell cycle stages. Mean values were calculated and plotted using GraphPad Prism v5.0.

Acknowledgements

This study was supported by the PhD fellowships of the Jürgen Manchot Graduate School ''Molecules of Infection'', MOI III (to GE), MOI IV (to AKM), and MOI V (to LRC). Additionally, we thank Dr. Sebastian Hänsch from the Center for Advanced Imaging (Cai - Heinrich Heine University Düsseldorf) for help with confocal microscopy, leading to movies S1 and S2.

Author contributions

ECMN and AKM designed the research. AKM, LRC, and GE performed the experiments. All authors analyzed the data. ECMN supervised the research. AKM, LRC, and ECMN wrote the manuscript.

Declaration of interests

All authors declare they have no competing interests.

References

Abramson J, Adler J, Dunger J, Evans R, Green T, Pritzel A, Ronneberger O, Willmore L, Ballard AJ, Bambrick J, Bodenstein SW, Evans DA, Hung CC, O'Neill M, Reiman D, Tunyasuvunakool K, Wu Z, Zemgulyte A, Arvaniti E, Beattie C, Bertolli O, Bridgland A, Cherepanov A, Congreve M, Cowen-Rivers AI, Cowie A, Figurnov M, Fuchs FB, Gladman H, Jain R, Khan YA, Low CMR, Perlin K, Potapenko A, Savy P, Singh S, Stecula A, Thillaisundaram A, Tong C, Yakneen S, Zhong ED, Zielinski M, Zídek A, Bapst V, Kohli P, Jaderberg M, Hassabis D, Jumper JM (2024) Accurate structure prediction of biomolecular interactions with AlphaFold 3. Nature **630:** 493-500

Alves JMP, Serrano MG, Maia da Silva F, Voegtly LJ, Matveyev AV, Teixeira MMG, Camargo EP, Buck GA (2013) Genome evolution and phylogenomic analysis of *Candidatus* Kinetoplastibacterium, the betaproteobacterial endosymbionts of *Strigomonas* and *Angomonas*. Genome Biology and Evolution **5:** 338-350

Alves JMP, Voegtly L, Matveyev AV, Lara AM, da Silva FM, Serrano MG, Buck GA, Teixeira MMG, Camargo EP (2011) Identification and phylogenetic analysis of heme synthesis genes in trypanosomatids and their bacterial endosymbionts. PLoS ONE **6:** e23518

Amann R, Springer N, Ludwig W, Görtz HD, Schleifer KH (1991) Identification *in situ* and phylogeny of uncultured bacterial endosymbionts. Nature **351:** 161-164

Bhattacharya D, Archibald JM, Weber APM, Reyes-Prieto A (2007) How do endosymbionts become organelles? Understanding early events in plastid evolution. Bioessays **29:** 1239-1246

Bornberg-Bauer E, Hlouchova K, Lange A (2021) Structure and function of naturally evolved de novo proteins. Current Opinion in Structural Biology **68:** 175-183

Cadena LR, Hammond M, Tesarová M, Chmelová L, Svobodová M, Durante IM, Yurchenko V, Lukes J (2024) A novel nabelschnur protein regulates segregation of the kinetoplast DNA in *Trypanosoma brucei*. Current Biology **34:** 4803–4812

Chen JH, Li QR, Xia SQ, Arsala D, Sosa D, Wang D, Long MY (2024) The rapid evolution of de novo proteins in structure and complex. Genome Biology and Evolution **16:** evae107

Clayton CE (1999) Genetic manipulation of kinetoplastida. Parasitology Today **15:** 372-378

Coale TH, Loconte V, Turk-Kubo KA, Vanslembrouck B, Mak WKE, Cheung S, Ekman A, Chen J-H, Hagino K, Takano Y, Nishimura T, Adachi M, Le Gros M, Larabell C, Zehr JP (2024) Nitrogen-fixing organelle in a marine alga. Science **384:** 217–222

Cornish J, Chamberlain SG, Owen D, Mott HR (2020) Intrinsically disordered proteins and membranes: a marriage of convenience for cell signalling? Biochemical Society Transactions **48:** 2669-2689

Cortese MS, Uversky VN, Dunker AK (2008) Intrinsic disorder in scaffold proteins: Getting more from less. Progress in Biophysics & Molecular Biology **98:** 85-106

Dosztányi Z, Csizmók V, Tompa P, Simon I (2005) The pairwise energy content estimated from amino acid composition discriminates between folded and intrinsically unstructured proteins. Journal of Molecular Biology **347:** 827-839

Drozdetskiy A, Cole C, Procter J, Barton GJ (2015) JPred4: a protein secondary structure prediction server. Nucleic Acids Research **43:** W389-W394

Du Y, Maslov DA, Chang KP (1994) Monophyletic origin of β-division proteobacterial endosymbionts and their coevolution with insect trypanosomatid protozoa *Blastocrithidia culicis* and *Crithidia* spp. Proceedings of the National Academy of Sciences of the United States of America **91:** 8437-8441

Engler C, Kandzia R, Marillonnet S (2008) A one pot, one step, precision cloning method with high throughput capability. PLoS ONE **3:** e3647

Erdős G, Dosztányi Z (2024) AIUPred: combining energy estimation with deep learning for the enhanced prediction of protein disorder. Nucleic Acids Research **52:** W176-W181

Fuchs BM, Pernthaler J, Amann R (2007) Single cell identification by fluorescence in situ hybridization. *In* CA Reddy, TJ Beveridge, JA Breznak, G Marzluf, TM Schmidt, LR Snyder, eds, Methods for general and molecular microbiology. 3rd ed. ASM Press, Washington, D.C., pp 886–896

Gibson DG, Young L, Chuang RY, Venter JC, Hutchison CA, Smith HO (2009) Enzymatic assembly of DNA molecules up to several hundred kilobases. Nature Methods **6:** 343-345

Gluenz E, Povelones ML, Englund PT, Gull K (2011) The Kinetoplast Duplication Cycle in Trypanosoma brucei Is Orchestrated by Cytoskeleton-Mediated Cell Morphogenesis. Molecular and Cellular Biology **31:** 1012-1021

Hanson J, Yang YD, Paliwal K, Zhou YQ (2017) Improving protein disorder prediction by deep bidirectional long short-term memory recurrent neural networks. Bioinformatics **33:** 685-692

Harmer J, Yurchenko V, Nenarokova A, Lukes J, Ginger ML (2018) Farming, slaving and enslavement: histories of endosymbioses during kinetoplastid evolution. Parasitology **145:** 1311-1323

Haynes C, Oldfield CJ, Ji F, Klitgord N, Cusick ME, Radivojac P, Uversky VN, Vidal M, Iakoucheva LM (2006) Intrinsic disorder is a common feature of hub proteins from four eukaryotic interactomes. Plos Computational Biology **2:** 890-901

Heames B, Buchel F, Aubel M, Tretyachenko V, Loginov D, Novák P, Lange A, Bornberg-Bauer E, Hlouchová K (2023) Experimental characterization of de novo proteins and their unevolved random-sequence counterparts. Nature Ecology & Evolution **7:** 570-580

Heffernan R, Yang YD, Paliwal K, Zhou YQ (2017) Capturing non-local interactions by long short-term memory bidirectional recurrent neural networks for improving prediction of protein secondary structure, backbone angles, contact numbers and solvent accessibility. Bioinformatics **33:** 2842-2849

Katuwawala A, Zhao B, Kurgan L (2022) DisoLipPred: accurate prediction of disordered lipid-binding residues in protein sequences with deep recurrent networks and transfer learning. Bioinformatics **38:** 115-124

Kohl L, Robinson D, Bastin P (2003) Novel roles for the flagellum in cell morphogenesis and cytokinesis of trypanosomes. EMBO Journal **22:** 5336-5346

Kostygov AY, Karnkowska A, Votypka J, Tashyreva D, Maciszewski K, Yurchenko V, Lukes J (2021) Euglenozoa: taxonomy, diversity and ecology, symbioses and viruses. Open Biology **11:** 200407

Leger MM, Petru M, Zársky V, Eme L, Vlcek C, Harding T, Lang BF, Eliás M, Dolezal P, Roger AJ (2015) An ancestral bacterial division system is widespread in eukaryotic mitochondria. Proceedings of the National Academy of Sciences of the United States of America **112:** 10239-10246

Letunic I, Khedkar S, Bork P (2021) SMART: recent updates, new developments and status in 2020. Nucleic Acids Research **49:** D458-D460

Li Z, Wang CC (2008) KMP-11, a basal body and flagellar protein, is required for cell division in *Trypanosoma brucei*. Eukaryotic Cell **7:** 1941-1950

Lukeš J, Butenko A, Hashimi H, Maslov DA, Votýpka J, Yurchenko V (2018) Trypanosomatids are much more than just Trypanosomes: Clues from the expanded family tree. Trends in Parasitology **34:** 466-480

Margolin W (2005) FtsZ and the division of prokaryotic cells and organelles. Nature Reviews Molecular Cell Biology **6:** 862-871

Maurya AK, Kröninger L, Ehret G, Bäumers M, Marson M, Scheu S, Nowack ECM (2025) A nucleus-encoded dynamin-like protein controls endosymbiont division in the trypanosomatid *Angomonas deanei*. Science Advances **11:** eadp8518

McLysaght A, Guerzoni D (2015) New genes from non-coding sequence: the role of de novo protein-coding genes in eukaryotic evolutionary innovation. Philosophical Transactions of the Royal Society B-Biological Sciences **370:** 20140332

Morales J, Ehret G, Poschmann G, Reinicke T, Maurya AK, Kroninger L, Zanini D, Wolters R, Kalyanaraman D, Krakovka M, Baumers M, Stuhler K, Nowack ECM (2023) Host-symbiont interactions in *Angomonas deanei* include the evolution of a host-derived dynamin ring around the endosymbiont division site. Current Biology **33:** 28-40

Morales J, Kokkori S, Weidauer D, Chapman J, Goltsman E, Rokhsar D, Grossman AR, Nowack ECM (2016) Development of a toolbox to dissect host-endosymbiont interactions and protein trafficking in the trypanosomatid *Angomonas deanei*. BMC Evolutionary Biology **16:** 247

Motta MCM, Catta-Preta CMC, Schenkman S, Martins ACA, Miranda K, de Souza W, Elias MC (2010) The bacterium endosymbiont of *Crithidia deanei* undergoes coordinated division with the host cell nucleus. PLoS ONE **5:** e12415

Motta MCM, Martins ACdA, de Souza SSa, Catta-Preta CMC, Silva R, Klein CC, de Almeida LGP, de Lima Cunha O, Ciapina LP, Brocchi M, Colabardini AC, de Araujo Lima B, Machado CR, de Almeida Soares CM, Probst CM, de Menezes CBA, Thompson CE, Bartholomeu DC, Gradia DF, Pavoni DP, Grisard EC, Fantinatti-Garboggini F, Marchini FK, Rodrigues-Luiz GF, Wagner G, Goldman GH, Fietto JLR, Elias MC, Goldman MHS, Sagot M-F, Pereira M, Stoco PH, de Mendonca-Neto RP, Teixeira SMR, Maciel TEF, de Oliveira Mendes TA, Urmenyi TP, de Souza W, Schenkman S, de Vasconcelos ATR (2013) Predicting the proteins of *Angomonas deanei*, *Strigomonas culicis* and their respective endosymbionts reveals new aspects of the trypanosomatidae family. PLoS ONE **8:** e60209-e60209

Mundim MH, Roitman I (1977) Extra nutritional requirements of artificially aposymbiotic *Crithidia deanei*. Journal of Protozoology **24:** 329-331

Ngô H, Tschudi C, Gull K, Ullu E (1998) Double-stranded RNA induces mRNA degradation in trypanosoma brucei. Proceedings of the National Academy of Sciences of the United States of America **95:** 14687-14692

Nowack ECM (2014) *Paulinella chromatophora* - rethinking the transition from endosymbiont to organelle Acta Societatis Botanicorum Poloniae **83:** 387-397

Patil A, Nakamura H (2006) Disordered domains and high surface charge confer hubs with the ability to interact with multiple proteins in interaction networks. Febs Letters **580:** 2041-2045

Richter DJ, Berney C, Strassert JFH, Poh YP, Herman EK, Muñoz-Gómez SA, Wideman JG, Burki F, de Varga C (2022) EukProt: A database of genome-scale predicted proteins across the diversity of eukaryotes. Peer Community Journal **2:** e56

Roger AJ, Muñoz-Gómez SA, Kamikawa R (2017) The origin and diversification of mitochondria. Current Biology **27:** R1177-R1192

Ruff KM, Pappu RV (2021) AlphaFold and implications for intrinsically disordered proteins. Journal of Molecular Biology **433:** 167208

Schneider A, Ochsenreiter T (2018) Failure is not an option - mitochondrial genome segregation in trypanosomes. Journal of Cell Science **131:** jcs221820

Silva FM, Kostygov AY, Spodareva VV, Butenko A, Tossou R, Lukeš J, Yurchenko V, Alves JMP (2018) The reduced genome of *Candidatus* Kinetoplastibacterium sorsogonicusi, the endosymbiont of *Kentomonas sorsogonicus* (Trypanosomatidae): Loss of the haem-synthesis pathway. Parasitology **145:** 1287-1293

Söding J, Biegert A, Lupas AN (2005) The HHpred interactive server for protein homology detection and structure prediction. Nucleic Acids Research **33:** W244-W248

Sørensen MES, Stiller ML, Kröninger L, Nowack ECM (2024) Protein import into bacterial endosymbionts and evolving organelles. FEBS Journal**:** Early access: doi:10.1111/febs.17356

Summerton J, Weller D (1997) Morpholino antisense oligomers: Design, preparation, and properties. Antisense & Nucleic Acid Drug Development **7:** 187-195

Teixeira MMG, Borghesan TC, Ferreira RC, Santos MA, Takata CSA, Campaner M, Nunes VLB, Milder RV, de Souza W, Camargo EP (2011) Phylogenetic validation of the genera *Angomonas* and *Strigomonas* of trypanosomatids harboring bacterial endosymbionts with the description of new species of trypanosomatids and of proteobacterial symbionts. Protist **162:** 503-524

Terfrüchte M, Joehnk B, Fajardo-Somera R, Braus GH, Riquelme M, Schipper K, Feldbrügge M (2014) Establishing a versatile Golden Gate cloning system for genetic engineering in fungi. Fungal Genetics and Biology **62:** 1-10

Uversky VN (2015) The multifaceted roles of intrinsic disorder in protein complexes. Febs Letters **589:** 2498-2506

van Hilten N, Verwei N, Methorst J, Nase C, Bernatavicius A, Risselada HJ (2024) PMIpred: a physics-informed web server for quantitative protein-membrane interaction prediction. Bioinformatics **40:** btae069

Votýpka J, Kostygov AY, Kraeva N, Grybchuk-Ieremenko A, Tesařová M, Grybchuk D, Lukeš J, Yurchenko V (2014) *Kentomonas* gen. n., a new genus of endosymbiont-containing trypanosomatids of Strigomonadinae subfam. n. Protist **165:** 825-838

Wang W, Li J, Sun Q, Yu X, Zhang W, Jia N, An C, Li Y, Dong Y, Han F, Chang N, Liu X, Zhu Z, Yu Y, Fan S, Yang M, Luo SZ, Gao H, Feng Y (2017) Structural insights into the coordination of plastid division by the ARC6-PDV2 complex. Nature Plants **3:** 17011

Wheeler RJ, Gluenz E, Gull K (2013) The limits on trypanosomatid morphological diversity. PLoS ONE **8:** e79581

Wilson BA, Foy SG, Neme R, Masel J (2017) Young genes are highly disordered as predicted by the preadaptation hypothesis of *de novo* gene birth. Nature Ecology & Evolution **1:** 0146

Yagoubat A, Corrales RM, Bastien P, Lévêque MF, Sterkers Y (2020) Gene editing in trypanosomatids: tips and tricks in the CRISPR-Cas9 era. Trends in Parasitology **36:** 745-760

Supplementary Materials

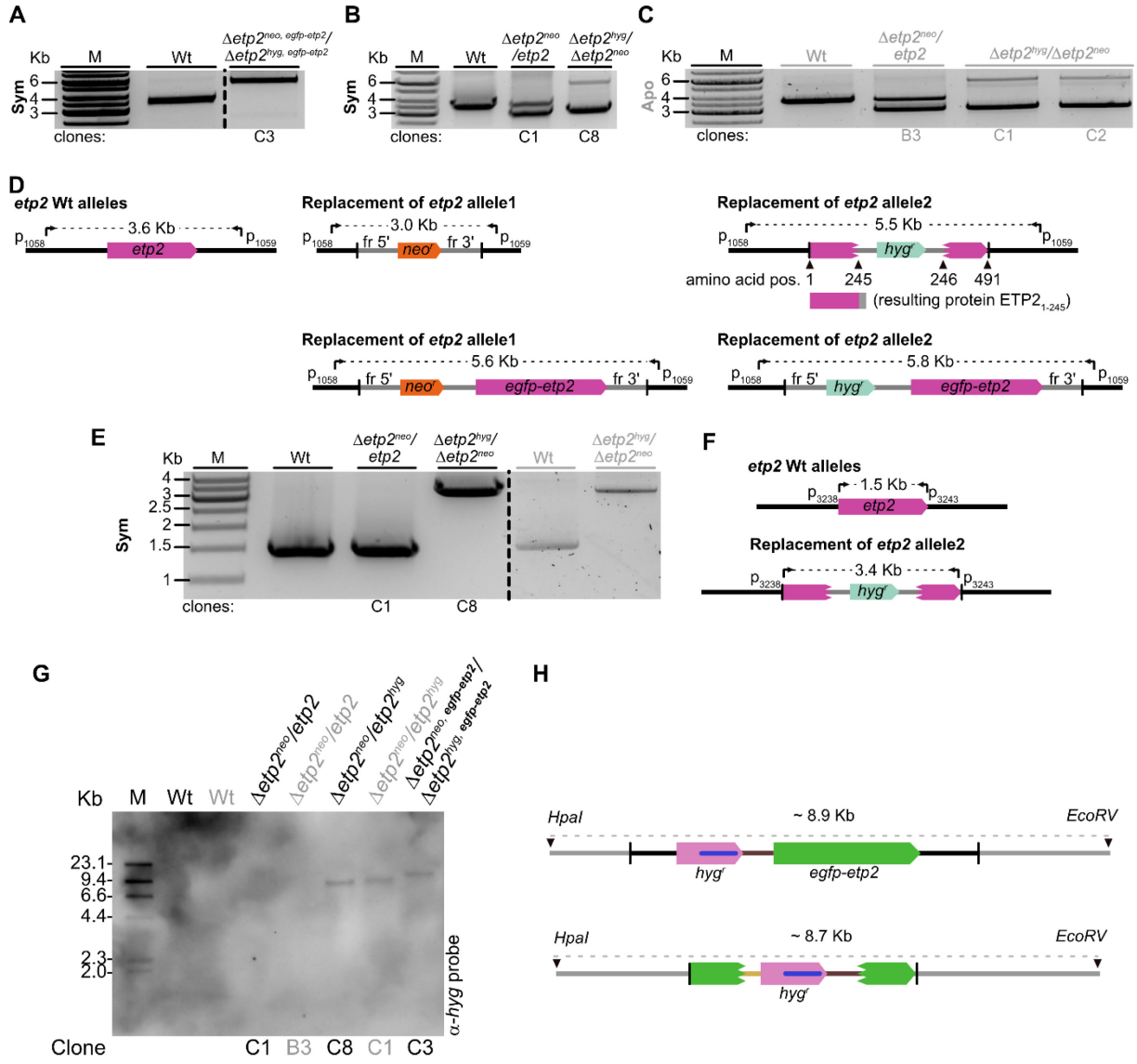

Figure S1: Verification of recombinant *A. deanei* cell lines by PCR and Southern blot analysis. A: Verification of the symbiotic strain with both alleles of *etp2* replaced by an *egfp-etp2*-containing cassette. **B:** Verification of symbiotic *etp2* heterozygous and homozygous deletion mutant cell lines. **C:** Verification of aposymbiotic heterozygous and homozygous *etp2* deletion mutant cell lines. **D:** Maps of Wt and modified *etp2* loci with expected band sizes detected by PCR (for A-C). Black arrowhead marks the amino acid position. **E:** PCR analysis of presence/absence of an intact *etp2* copy in symbiotic and aposymbiotic *A. deanei* Wt and *etp2* deletion mutant cell lines. **F:** Maps of Wt and modified *etp2* locus with expected band sizes detected by PCR in E. Black text shows symbiotic and grey aposymbiotic strains. Dotted lines show expected PCR band sizes. Curved arrows show primer binding sites. Vertical black lines on the maps show borders of inserted DNA fragments in the genome. Broken pink/green boxes on the maps show first and second halves of the *etp2* ORF used as fr 5' and fr 3' for homologous recombination, respectively (in D, F, H). **G:** Southern blot verification of *A. deanei* strains with Wt and modified *etp2* loci using a probe against *hyg*^{r}. M, DIG-labelled DNA marker. **H:** Maps of Wt and recombinant *etp2* loci analyzed by Southern blot.

Black arrowheads on the maps indicate the cutting site for the indicated restriction enzymes. The grey dotted lines indicate the expected size of the digested fragment. Binding sites of the α-*hyg* probe are marked by a blue bar. Abbreviations: fr, flanking region; *hyg*^{r}, hygromycin resistance gene, and *neo*^{r}, neomycin resistance gene.

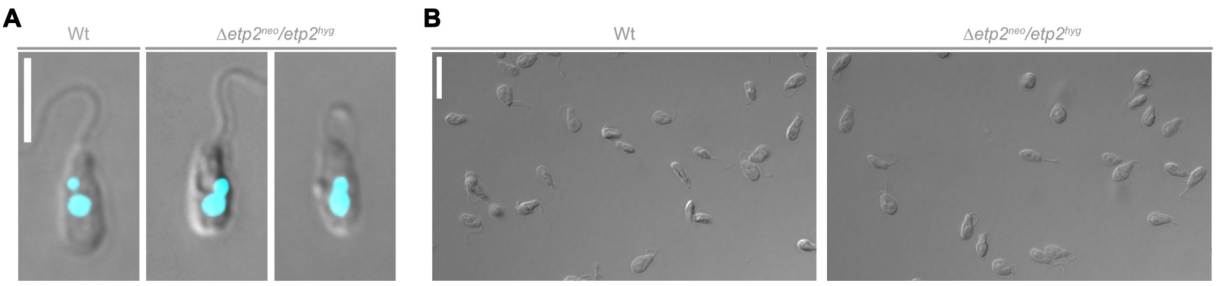

Figure S2: Effects of deletion of both alleles of *etp2* in the aposymbiotic *A. deanei* strain. A: The figure shows representative images of Wt and the homozygous *etp2* deletion mutant cell line in the aposymbiotic *A. deanei* strain. Images show an overlay of DIC and Hoechst 33342 fluorescence (cyan). Scale bar is 5 µm. **B:** Overview DIC images of cells of the same cultures. Scale bar: 10 µm. Grey text/bars indicate aposymbiotic strains.

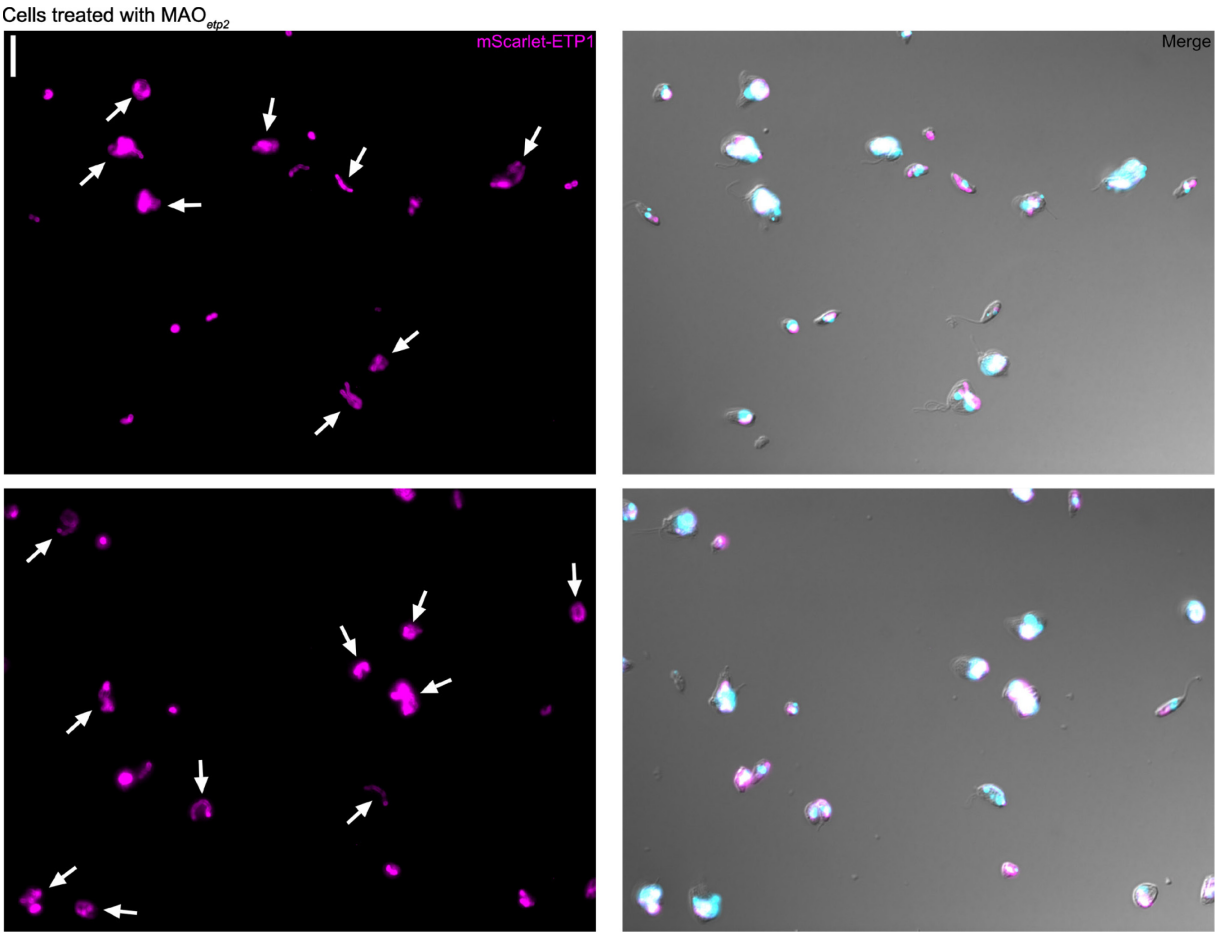

Figure S3: Effects of KD of ETP2. *A. deanei* cells expressing the endosymbiont marker mScarlet-ETP1 24 h post-transfection with MAO$_{etp2}$. Shown are the mScarlet channel alone (on the left) and a merge of the mScarlet and Hoechst 33342 channels with the DIC image (on the right). Arrows show filamentous endosymbionts. Scale bars are 10 µm.

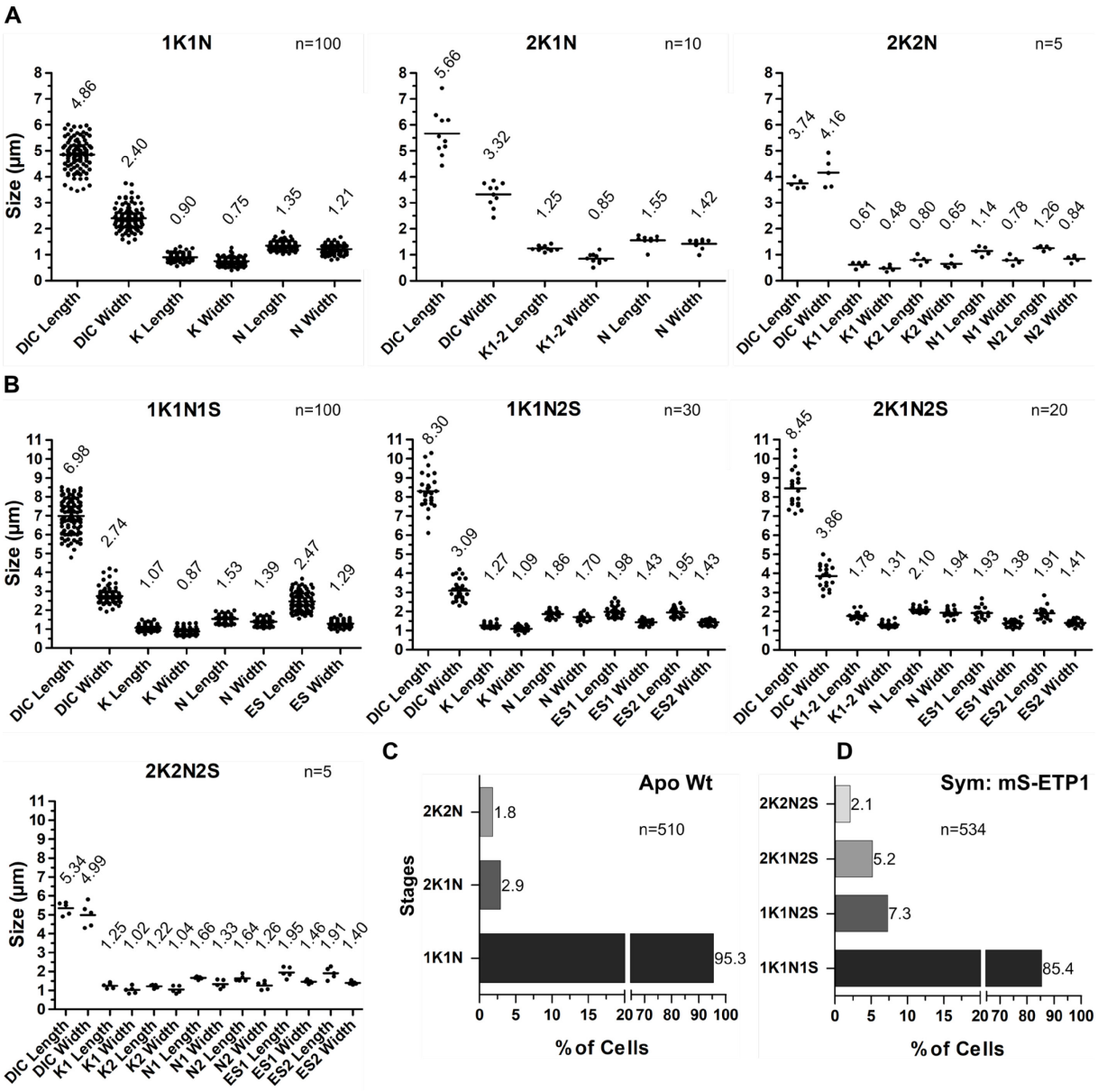

Figure S4: Measurements of cell and organelle sizes for symbiotic and aposymbiotic strains. A: Measurements for aposymbiotic Wt cells at different cell cycle stages- 1K1N, 2K1N, and 2K2N (see below). **B:** Measurements for symbiotic cells expressing the endosymbiont marker mScarlet-ETP1 at different cell cycle stages- 1K1N1S, 1K1N2S, 2K1N2S, and 2K2N2S (see below). Mean values are represented on each plot for each measurement by a horizontal line. DIC images were used to measure cell size, Hoechst 33342-stained DNA for kinetoplast (K) and nucleus (N), and mScarlet-ETP1-labelled endosymbiont (ES) for bacterium measurements, respectively. K1-2 represents two kinetoplasts that are still not completely separated. **C:** Quantification of approximately 500 aposymbiotic Wt cells categorized into different cell cycle stages. **D:** Quantification of approximately 500 symbiotic cells expressing mScarlet-ETP1 categorized into different cell cycle stages. Cell cycle stages are described by the number of kinetoplasts (K), nuclei (N), and endosymbionts (S) per cell.

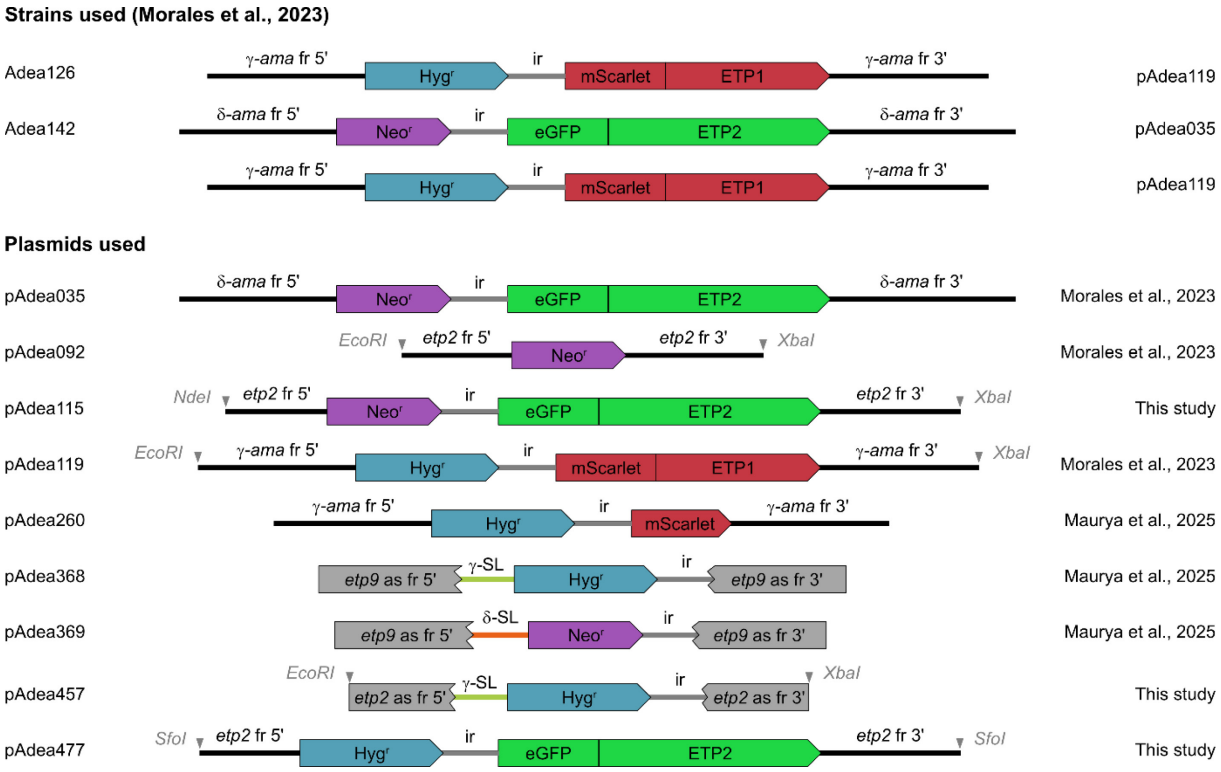

Figure S5: Schematic maps of all plasmids and *A. deanei* strains used in this study. Previously generated plasmids such as pAdea092 and pAdea119 were used in this study to generate new Adea strains or as templates to generate new plasmids in this study (pAdea260, pAdea368, and pAdea369). All other plasmids were generated in this study. Abbreviations: fr, flanking region (~0.7 - ~1.0 Kbp used for homologous recombination); ir, intergenic region between *gapdh I* and *gapdh II* genes; δ/γ-*ama*, δ- and γ-*amastin* gene (for nomenclature see Morales et al. 2016); *etp2* fr 5', upstream flanking region of *etp2* gene; *etp2* fr 3', downstream flanking region of *etp2* gene; *etp2/9* as fr 5', first half of the respective *etp* ORF used as 5' flaking region; *etp2/9* as fr 3', second half of the ORF used as 3' flaking region; δ/γ-SL, 5' flanking region of the δ/γ-*amastin* genes, respectively including the spliced leader acceptor sequence; Neo^r/Hyg^r, neomycin and hygromycin resistance markers encoded by *neo^r*/*hyg^r* genes, respectively. Arrowheads show approximate cutting sites of restriction enzymes on the plasmid used for linearization before transfection.

Table S1: All primers used in this study. Primers for the generation of plasmids, plasmid sequencing, verification of genomic insertions, and generation of Southern blot probes are described below.

Primer No.	Primer sequence (5'-3') Used for amplification of DNA fragment	Fragment amplified	Final plasmid
1015	GGTCTCCCTAATAATATATATTTATCTCGTTCGGTGTT	*etp2* fr 3'-pUMA1467-*etp2* fr 5'	pAdea115
1016	GGTCTCCTCATTTTGGTGTGTATGATTGTATTTTTC		
1022	GGTCTCCATGATTGAACAAGATGGATTGC	*neo*^{r}-gapdh ir-*egfp*-*etp2*	
1023	GGTCTCCTTAGTTCGCCGAAAGCAC		
3237	TCATCCTCGTCGTAGTCCATCAGGTGAGCTCGAATTCACT	pUMA1467	pAdea457
3244	TTGTGCTTTCGGCGAACTAAGCAGGTCTAGATATCGGATCC		
3238	AGTGAATTCGAGCTCACCTGATGGACTACGACGAGGATGAATACTTTGA	First half of *etp2* gene as fr 5'	
3239	CTAGGTGAGTTTTTACTTTTCAGTGCCTCTGGTGGGGGT		
3242	CAAAAAACACAGTTATCCAACAGGTGCATCGTACGCCGG	Second half of *etp2* gene as fr 3'	
3243	GATCCGATATCTAGACCTGCTTAGTTCGCCGAAAGCACAAAATAGGGT		
3240	CACCCCCACCAGAGGCACTGAAAAGTAAAAACTCACCTAGTTTGC	γ-*ama* SL-*hyg*^{r}-gapdh ir	
3241	ACCGGCGTACGATGCACCTGTTGGATAACTGTGTTTTTTGATGAAA		
3320	ATACAATCATACACACCAAAATGAAAAAGCCTGAACTCACC	*hyg*^{r}	pAdea477
3321	TCAAACTCTCACTAGCACTTTTATTTCTTTGCCCTCGGAC		
3322	GTCCGAGGGCAAAGAAATAAAAGTGCTAGTGAGAGTTTGACT	pAdea115 excluding *neo*^{r}	
3323	GTGAGTTCAGGCTTTTTCATTTTGGTGTGTATGATTGTATTTTTCTATATA TATAA		
Primer No.	**Primer sequence (5'-3') Used for plasmid sequencing**	**Binding position**	**-**
55	ATCTTAGCCAGACGAGCG	*hyg*^{r}	-
56	CACTATCGGCGAGTACTTCTACA		-
117	TGCCGTCTCCTTCGTGAGCAAGGGCGAGGAG	*egfp*	-
118	TGCCGTCTCCTCTTACTTGTACAGCTCGTCCA		-
131	AAGTGCTAGTGAGAGTTTGACT	gapdh ir	-
132	TTGGATAACTGTGTTTTTTGATG		-
310	CGAAACATCGCATCGAGCG	*neo*^{r}	-
311	ATCGACAAGACCGGCTTCC		-
326	ACACGGCGACGGTGCCACCCCCACC	*etp2*	-
761	TGTAAAACGACGGCCAGT	pUMA1467	-
762	CAGGAAACAGCTATGACCAT		-
1066	GCGGTCCACCGATAACGTAAAGT	*etp2*	-
1440	CGCCGAGGTGAAGTTCGAGGGC	*egfp*	-
2873	CAGATTGTACTGAGAGTGCA	pUMA1467	-
Primer No.	**Primer sequence (5'-3') Used for PCR verification of genomic insertion**	**Locus/Gene**	**-**
80	CTTTCTGCCATCTGCCTCAT	γ-*amastin* (Bind in genome, outside of insertion cassette)	-
81	CATCCTTACGATCTTCTTATTTTTTGG		-
55	ATCTTAGCCAGACGAGCG	*hyg*^{r}	-
1942	GCCCATTGTCTTCTTCTGCATT	*mscarlet*	-
1058	CTACACGTATTCCGTAGAGAG	*etp2*	-
1059	TAGAAGGAGAACACATTCCG		-
Primer No.	**Primer sequence (5'-3') Used for amplification of *etp2* gene**	**Gene**	**-**
3238	AGTGAATTCGAGCTCACCTGATGGACTACGACGAGGATGAATACTTTGA	*etp2*	-
3243	GATCCGATATCTAGACCTGCTTAGTTCGCCGAAAGCACAAAATAGGGT		-
Primer No.	**Primer sequence (5'-3') Used for Southern blot probe generation by nested PCR**	**Gene**	**-**
55	ATCTTAGCCAGACGAGCG	*hyg*^{r}	-
56	CACTATCGGCGAGTACTTCTACA		-
1302	GGTCTCAATGAAAAAGCCTGAACTCACC		-
1303	GGTCTCATTATTTCTTTGCCCTCGGACG		-

Supplementary movies

Movie S1:

Cell co-expressing eGFP-ETP2 (Δδ-*ama*$^{egfp\text{-}etp2}$) and mScarlet-ETP1 (Δγ-*ama*$^{mS\text{-}etp1}$) that is at an early stage of endosymbiont division showing a ring-shaped fluorescence signal around the ESDS when scrolling through confocal Z-stacks. Shown are individual channels for Hoechst 33342, mScarlet, and eGFP fluorescence, as well as a merge of all channels. Scale bar: 2 µm.

Movie S2:

Cell co-expressing eGFP-ETP2 and mScarlet-ETP1 that is at a later stage of endosymbiont division showing an x-like fluorescence signal at the ESDS when scrolling through confocal Z-stacks. Shown are individual channels for Hoechst 33342, mScarlet, and eGFP fluorescence, as well as a merge of all channels. Scale bar: 2 µm.

2.1.4. Manuscript II

Kröninger, L., **Maurya, A.K.,** Stiebeling C., Stirba F.P., Kim, Z., and Nowack, E.C.M. (2025). T7 RNA polymerase-based gene expression from a transcriptionally silent rDNA spacer in the endosymbiont-harboring trypanosomatid *Angomonas deanei*. *PloS One* (Accepted).

As described earlier, trypanosomatids have an unusual gene expression system that is yet not fully understood. Though genetic tools for studying protein function in some trypanosomatids, for instance, *Trypanosoma* spp. and *Leishmania* spp. are available, there are yet no conditional gene expression systems developed in *A. deanei*. The available tools often poses several challenges, for example, gene knockouts is very difficult for many genes and use of MAOs is not only very expensive but also difficult to design a suitable one. Therefore, Lena et al. aimed to establish a conditional gene expression system in *A. deanei*. For this purpose, Lena et al. established a couple of new resistance markers and importantly identified a transcriptionally silent locus in *A. deanei*. Subsequently, a method to express genes from the silent locus using T7 RNA polymerase was developed. The study certainly provides a freedom to integrate multiple recombinant fragments in the genome, functional study of essential proteins and study of artificial symbiosis.

My contribution to Lena et al., 2025, PloS One (Accepted).

- To express T7 RNA polymerase heterologously in *A. deanei*, I contributed to the cloning of pAdea302 and Adea319 ($\Delta\delta$-*ama*$^{T7\ RNAP}$/δ-*ama*).
- To compare the strength of gene expression driven by T7 RNA polymerase and RNA polymerase II, I performed epifluorescence microscopy leading to Fig. 5D and Fig. S2. The data showed comparable expression in both cases.
- To verify the correct genomic insertion of desired DNA fragments, I provided technical support during Southern blot analyses.

Title: T7 RNA polymerase-based gene expression from a transcriptionally silent rDNA spacer in the endosymbiont-harboring trypanosomatid *Angomonas deanei*

Short title: T7 RNA polymerase-based gene expression from silent locus in *Angomonas deanei*

Authors: Lena Kröninger[1], Anay K. Maurya[1], Christian Stiebeling[1], Florian P. Stirba[1], Zio Kim[1], and Eva C. M. Nowack[1,*]

Affiliations:

[1]Department of Biology, Heinrich Heine University Düsseldorf, 40225 Düsseldorf, Germany

[*]Corresponding author

E-mail: e.nowack@hhu.de

Key words:

Endosymbiosis, organellogenesis, host/symbiont interaction, ectopic expression system, T7 RNA polymerase, silent genomic locus, rDNA spacer

Abstract

Eukaryotic life has been shaped fundamentally by the integration of bacterial endosymbionts. The trypanosomatid *Angomonas deanei* that contains a β-proteobacterial endosymbiont, represents an emerging model to elucidate initial steps in symbiont integration. Although the repertoire of genetic tools for *A. deanei* is growing, no conditional gene expression system is available yet, which would be key for the functional characterization of essential or expression of toxic proteins. Development of a conditional expression system based on endogenous RNA polymerase II (POLII) is hampered by the absence of information on transcription signals in *A. deanei* as well as the unusual genetic system used in the Trypanosomatidae that relies on read-through transcription. This mode of transcription can result in polar effects when manipulating expression of genes in their endogenous loci. Finally, only a few resistance markers are available for *A. deanei* yet, restricting the number of genetic modifications that can be introduced into one strain. To increase the range of possible genetic manipulations in *A. deanei*, and in particular, build the base for a conditional expression system that does not interfere with the endogenous gene expression machinery, here we (i) implemented two new drug resistance markers, (ii) identified the spacer upstream of the rDNA array on chromosome 13 as transcriptionally silent genomic locus, and (iii) used this locus for engineering an ectopic expression system that depends on the T7 RNA polymerase expressed from the δ-amastin locus. We show that transgene expression in this system is independent of the activity of endogenous RNA polymerases, reaches expression levels similar to the previously described POLII-dependent expression from the γ-amastin locus, and can be applied for studying endosymbiosis. In sum, the new tools expand the possibilities for genetic manipulations of *A. deanei* and provide a solid base for the development of an ectopic conditional expression system.

Introduction

The trypanosomatid *Angomonas deanei* is an emerging model system for endosymbiosis [1,2]. It harbors a β-proteobacterial endosymbiont of the Alcaligenaceae, which co-evolved with its host for 40-120 million years [3]. The endosymbiont supplies its host with essential metabolites and co-factors, underwent pronounced genome reduction [4], and divides strictly synchronously with

its host cell [5], indicating an advanced level of endosymbiont integration. However, information on the exact molecular mechanisms of host-symbiont communication and control is scarce.

A few genetic tools have been developed for the asexual diploid *A. deanei*. Protocols available allow to efficiently generate heterozygous and homozygous knock-out mutants by one or two rounds of homologous recombination, respectively [6,7], or by CRISPR/Cas-based technology [8]. Furthermore, two amastin loci that have been called the δ-amastin and γ-amastin locus, coding for highly expressed surface glycoproteins (GenBank accessions CAD2222965.1 and CAD2215701.1, respectively) that are dispensable for the organism under standard growth conditions in the laboratory, were successfully hijacked for high level transgene expression [6]. Expression of fluorescent fusion proteins from these loci has been instrumental for the identification of a number of endosymbiont targeted host proteins (short ETPs) that are assumed to be involved in host/symbiont interaction [6,7]. However, inducible gene expression systems that would be important for the expression of toxic gene products and the development of conditional gene knock-outs of essential genes are not available yet, and although a protocol for RNA interference-based gene knock-downs has been published [9], it appears to be difficult to reproduce in our hands. Recently, morpholino antisense oligonucleotides (MAOs) have been successfully employed in *A. deanei* to knock-down ETP9 and characterize it as a nucleus-encoded dynamin-like protein essential for endosymbiont division [10]. However, MAO production is relatively expensive and their applicability depends on the availability of suitable binding sites in the 5' untranslated region (5' UTR) of the target gene. These limitations call for the development of further genetic tools.

Trypanosomatids use an uncommon gene expression system. They produce long polycistronic mRNA strands from unidirectional gene clusters containing dozens of genes [11–14]. During mRNA maturation, polycistronic mRNAs are processed by coupled *trans*-splicing and polyadenylation reactions resulting in mature monocistronic mRNAs that carry at their 5' ends a common spliced leader (a capped 39-nt RNA molecule) [13,15]. Regulation of gene expression occurs on the mRNA level by stabilizing elements in the 5' and 3' UTRs directly influencing gene expression [13]. Consequently, transgenes that are inserted into any expressed genomic locus are transcribed by read-through, but their expression cannot be conditionally modulated or interrupted, e.g. using operator/repressor pairs, without affecting expression of downstream genes. This makes the development of inducible gene expression systems challenging.

Due to their medical relevance, other trypanosomatids such as *Trypanosoma* spp. and *Leishmania* spp. that do not carry an endosymbiont, are far better studied and advanced genetic tools are available for them [16–20]. These tools include conditional gene expression systems, that make use of transcriptional regulators, such as the tetracycline-inducible repressor (TetR) [21] or the cumate repressor (CymR) [22]. A common strategy to prevent interference with the endogenous gene expression machinery in these systems, is ectopic expression from transcriptionally silent genomic loci. Such silent loci have been found, for example, in transcriptionally inactive mini-chromosomes in *Trypanosoma brucei* [23] (which do not exist in *A. deanei*) or upstream of the promoter for the 18S rRNA gene (hereafter referred to as the rDNA spacer) [24,25]. In the latter insertion site, the inducible gene is inserted oriented in the opposite direction to that of the 18S rDNA [26].

In *T. brucei*, some promoter sequences such as the procyclic acidic repetitive protein (PARP) promoter have been described and used to establish conditional expression systems based on the endogenous POLII [24,26]. In *A. deanei*, however, virtually nothing is known about transcription initiation. Other expression systems in trypanosomatids make use of the exogenous bacteriophage T7 RNA polymerase (T7RNAP) [21,27–31]. Advantages of the T7RNAP are not only that it is a single subunit enzyme that can be produced heterologously in a wide variety of organisms but also that promoter and terminator sequences are well-characterized and comparably short [32]. Moreover, the enzyme shows an extraordinarily high activity, beyond the activity of endogenous RNA polymerases, in some bacteria such as *Escherichia coli* [33]. In *T. brucei,* T7 RNAP-dependent gene expression exceeded POLII-dependent expression with a PARP promoter by 5-fold [27].

To increase the experimental versatility of *A. deanei* as an endosymbiosis model, here we describe a transcriptionally silent locus in its nuclear genome. We demonstrate that this locus can be used for T7RNAP-driven expression of transgenes. We compare the expression level of this newly introduced system to the previously described expression system from the amastin loci and implement blasticidin and nourseothricin resistance genes as new selectable markers in *A. deanei*. Together the new protocols contribute to the growing genetic toolbox that supports the establishment of *A. deanei* as a versatile endosymbiosis model.

Results

Identification of potentially silent genetic loci as integration site for transgenes in *A. deanei*

To identify potentially silent genomic loci in *A. deanei* that could be used for transgene expression by an exogenous transcription machinery, we searched the *A. deanei* nuclear genome for ribosomal repeats and found seven copies on different chromosomes (**Fig 1**). Putative protein-coding sequences upstream of the ribosomal arrays were identified using the auto-annotation tool of Benchling (https://www.benchling.com) and comparisons to the curated annotations in the TriTryp Database (https://tritrypdb.org) [34]. The first coding sequence upstream of the ribosomal arrays was found 3.2 kbp away from the 18S rDNA (on chromosome 25) suggesting that these intergenic spacers are indeed non-coding. All seven rDNA spacers show high sequence similarity in the first 1.5-2 kbp upstream of the ribosomal arrays, but then diverge with increasing distance from the ribosomal arrays (see alignment of the first 4000 bp upstream of the ribosomal array in **S1 Appendix**).

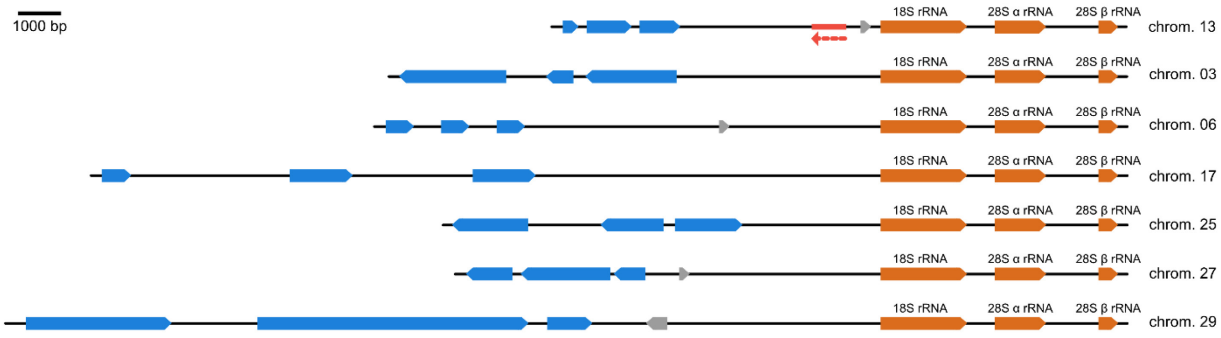

Fig 1. Potentially silent loci upstream of the ribosomal repeats in *A. deanei*.
The highly conserved ribosomal repeats were found on seven different chromosomes (chrom.) and are marked in orange. Putative protein-coding sequences upstream of the ribosomal repeats are shown in blue. Open reading frames marked in grey did not show homologs in other trypanosomatids (using BLASTp against the NCBI non-redundant database) and are unlikely to represent true protein-coding genes. The targeted insertion site on chromosome 13 is marked in red and transgene orientation is indicated by the broken red arrow.

Heterologous expression of the T7RNAP in *A. deanei*

To implement an RNA polymerase in *A. deanei* that works independently of the endogenous expression machinery, we inserted the T7RNAP coding sequence into the δ-amastin locus. For selection, the T7RNAP coding sequence was linked upstream via the intergenic region between GAPDH-I and II genes (GAPDH-IR, that contains signals for mRNA maturation and stabilization [6]) to the neomycin phosphotransferase gene (*neo*^{R}) (**Fig 2A**). Transfectants were selected on neomycin and the clonal strain obtained (Adea319) was verified by PCR with primers binding outside of the integration site (**Fig 2B**). Production of the T7RNAP was verified by Western blot analysis (**Fig 2C**).

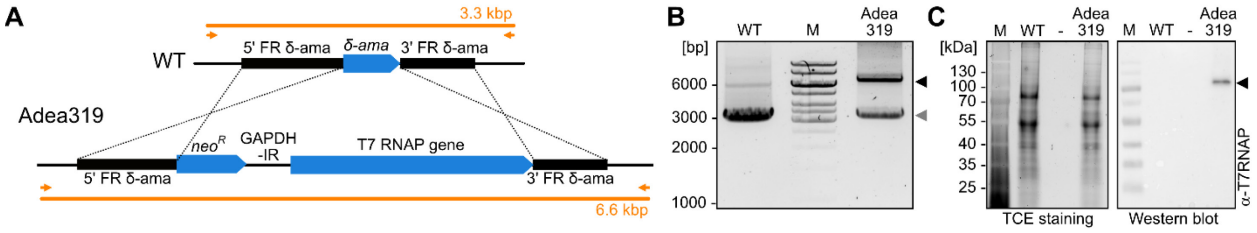

Fig 2. Construction and verification of the T7RNAP-producing strain Adea319.
(A) Genomic map of Adea319 and the *A. deanei* wildtype (WT) in the δ-amastin (δ-ama) locus. Primers 49+545, that were used for the verification of the insertion of the T7RNAP gene-containing construct, are marked in orange. **(B)** Verification of the integration of the T7RNAP expression cassette in Adea319 by PCR. The WT served as a control and showed only the δ-amastin WT locus (3.3 kbp, grey arrowhead) plus a weak unspecific band at 6.0 kbp. The recombinant locus in Adea319 additionally yielded the predicted product at 6.2 kbp (black arrowhead). **(C)** Verification of production of the ~100 kDa T7RNAP (black arrowhead) by Western blot using an α-T7RNAP primary antibody (right picture). Trichloroethanol (TCE) staining of the SDS-polyacrylamid gel electrophoresis (PAGE) before blotting confirmed equal loading of the WT and Adea319 raw extract samples (left picture).

Implementation of new antibiotic resistance markers for *A. deanei*

So far, only a limited set of antibiotic resistance markers has been established for *A. deanei* strain ATCC PRA-265 [6,7], namely *neo*^{R}, the hygromycin phosphotransferase (*hyg*^{R}), and the phleomycin-binding protein (*phleo*^{R}). To increase the number of resistance markers, we tested blasticidin and nourseothricin and their resistance genes, blasticidin deaminase (*blast*^{R}) and nourseothricin acetyltransferase (*nours*^{R}), respectively, as potential selection markers in *A. deanei*. To this end, we generated two strains, Adea373 and Adea384, expressing *blast*^{R} (alone) and *nours*^{R} (in combination with *neo*^{R}) from the δ-amastin locus and compared their

growth with the WT on various concentrations of the respective antibiotics. Whereas growth of the WT was heavily affected at blasticidin concentrations ≥75 µg/ml and nourseothricin concentrations ≥200 µg/ml, Adea373 and Adea384 were resistant to the respective antibiotics, and grew up to concentrations of 200 µg/ml blasticidin or 400 µg/ml nourseothricin, respectively, without noticeable growth defects (**Fig 3**). Subsequently, 75 µg/ml blasticidin or 200 µg/ml nourseothricin were used for mutant selection.

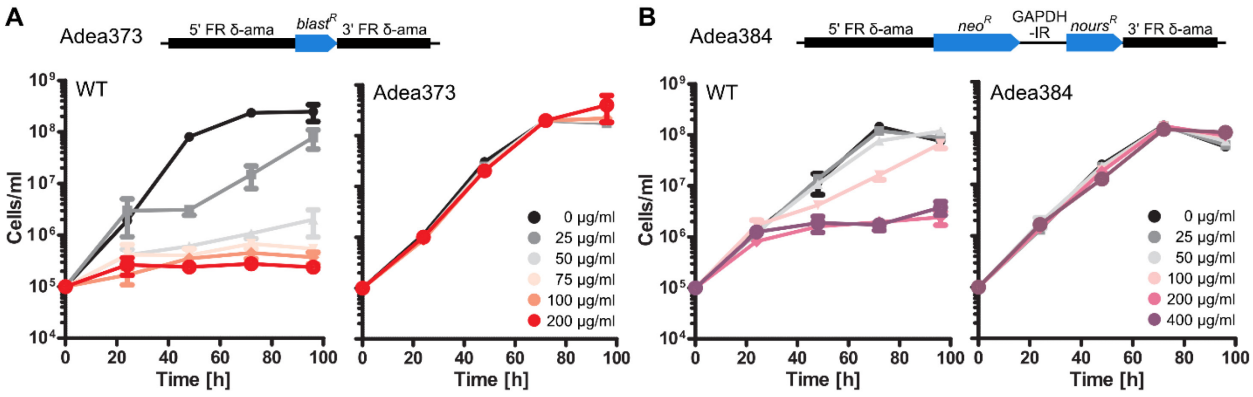

Fig 3. Susceptibility of *A. deanei* WT to blasticidin (blast) and nourseothricin (nours) compared to susceptibility of Adea373 to blasticidin and Adea384 to nourseothricin, respectively.
(A) Genomic map of Adea373 and growth of *A. deanei* WT and Adea373 on increasing blasticidin concentrations over 4 days. **(B)** Genomic map of Adea384 and growth of *A. deanei* WT and Adea384 on increasing nourseothricin concentrations over 4 days. Blasticidin (A) and nourseothricin (B) concentrations are color coded as indicated in the graphs. The graphs display mean values and standard deviations from 3 biological replicates.

T7RNAP-driven expression from the rDNA spacer

Next, we aimed for the insertion of a transgene with T7 transcription signals into the rDNA spacer on chromosome 13 (chr13 rDNA spacer, see **Fig 1**) to test functionality of the T7RNAP. As selection marker and reporter cassette we made use of *blast*^{R} flanked by sections of intergenic regions that trigger *trans*-splicing and polyadenylation during mRNA maturation, namely a 252 nt-long fragment of the intergenic region upstream of the δ-amastin gene (“spliced leader donor”, SLD) as 5’ flank and the complete GAPDH-IR as 3’ flank (**Fig 4A**). The T7 promoter and the T7 terminator were added at the 5’ and 3’ ends of this cassette, respectively. Finally, 600 bp-long sequences flanking the genomic target locus (see **S1 Appendix**) were added upstream and downstream of the T7 transcription signals for homologous recombination. Next, the T7RNAP-producing strain, Adea319, was transfected with this *blast*^{R} integration cassette and blasticidin was added to the transfectants 6 h post transfection.

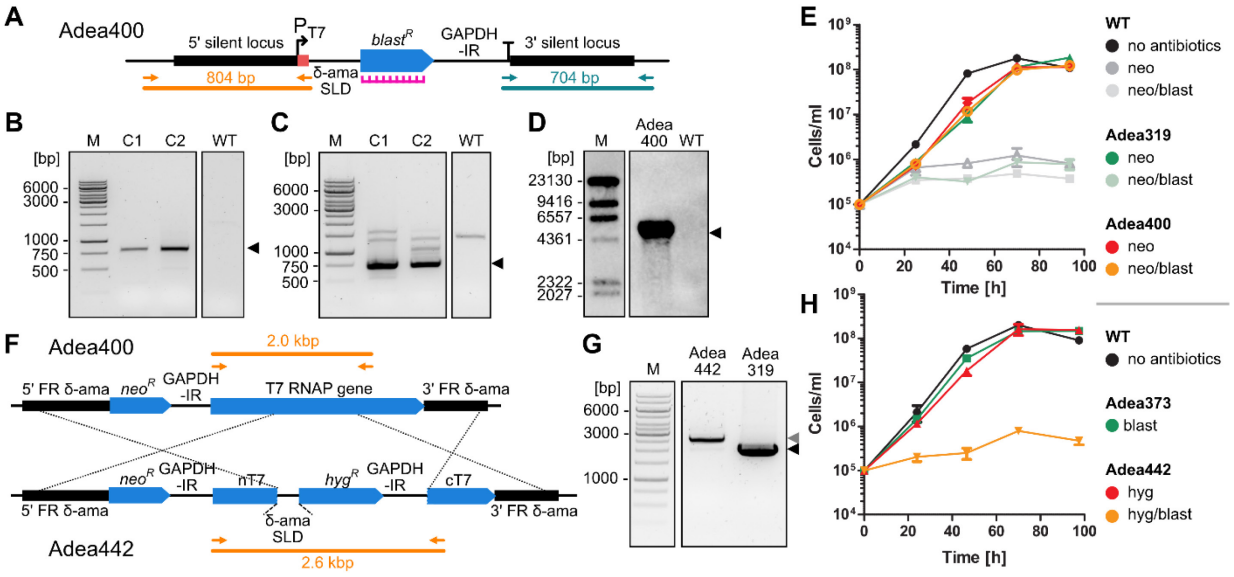

Fig 4. T7RNAP drives *blast*^{R} expression from the rDNA spacer.
(A) Genomic map of the chr13 rDNA spacer of Adea400. Primer pairs 2211+2748 and 2753+2210 that were used for the verification of the insertion of the *blast*^{R}-containing construct and expected products are shown in orange and blue-green. The annealing site of the Southern blot probe is marked with an icon in magenta. **(B, C)** Verification of integration of the *blast*^{R}-containing construct into the targeted rDNA spacer by PCR (B, orange primer pair 2211+2748 and C, blue-green primer pair 2753+2210). The WT served as a control and showed no (B) or a faint unspecific product (C), whereas samples of two individual clones (C1 and C2) yielded the expected product at ~800 bp (B) and ~700 bp (C). **(D)** Verification of insertion into the chr13 rDNA spacer in Adea400 by Southern blot. The *blast*^{R}-targeting probe yielded only a single band of the expected size at 4746 bp for Adea400 but not for the WT control (see **S1 Table** for expected sizes and **S1 Figure** for an additional Southern blot on BamHI-digested DNA). **(E)** Growth of *A. deanei* WT, Adea319, and Adea400 on neomycin (neo) and neomycin/blasticidin (neo/blast) over 4 days. **(F)** Knock-out strategy and genomic map of Adea442 depicting the interruption of the T7RNAP-encoding gene by a *hyg*^{R}-containing cassette and partial removal of the gene with only N- and C-terminal domains (nT7/cT7) remaining. **(G)** Verification of the successful T7RNAP knock-out by PCR using primers 2045+2966 (labelled in orange in the genomic map). Adea319 with functional T7RNAP gene (black arrowhead), Adea442 with successfully disrupted T7RNAP gene (grey arrowhead). **(H)** Growth of *A. deanei* WT, Adea373, and the T7RNAP knock-out strain Adea442 on hygromycin (hyg), blasticidin (blast), and hygromycin/blasticidin (hyg/blast) over 4 days. In (E) and (H) mean values and standard deviations from 3 biological replicates are displayed.

Recombinant clones recovered after 5-7 days suggesting that *blast*^{R} is expressed in sufficient amounts to render the cell resistant. As mentioned above, the rDNA spacers on different chromosomes are highly similar, so that i) insertion into a non-targeted locus and ii) multiple insertions into several rDNA spacers could not be excluded. To explore these issues, first we verified the insertion of the *blast*^{R}-containing construct into an rDNA spacer by PCR (**Fig 4B, C**). Then, we identified BclI and SpeI as restriction enzymes that allow to distinguish between insertions into the rDNA spacers on different chromosomes by Southern blot analysis due to restriction length polymorphisms (see **S1 Table**). Southern blot analysis of Adea400 with BclI and

SpeI yielded a single band of 4746 bp, indicative of an insertion specifically into the chr13 rDNA spacer (**Fig 4D**). Lastly, growth experiments (**Fig 4E**) revealed that the doubling time of Adea400 on blasticidin/neomycin (6.9 ± 0.2 h) and the T7RNAP-producing strain Adea319 on neomycin alone (6.9 ± 0.2 h) were identical. And both strains grew only slightly slower than the WT without antibiotics (doubling time of 6.6 ± 0.1 h).

To exclude that the endogenous transcription machinery of *A. deanei* is responsible for *blast*^{R} expression from the rDNA spacer, we generated a strain derived from Adea400 (named Adea442), in which the T7RNAP-encoding gene was interrupted by a *hyg*^{R} cassette as well as partially removed (**Fig 4F**). We first verified the successful insertion into the target locus by PCR (**Fig 4G**) and then tested the verified strain for blasticidin resistance. On hygromycin alone, Adea442 showed similar growth rates (doubling time 6.6 ± 0.4 h) as *A. deanei* WT without antibiotics (doubling time 6.1 ± 0.3 h) and the blasticidin resistant strain Adea373 on blasticidin (doubling time 6.4 ± 0.1 h) (**Fig 4H**). However, no growth of Adea442 was observed on blasticidin. This result clearly demonstrates that *blast*^{R} expression from the chr13 rDNA spacer is controlled by the T7RNAP system and not the endogenous transcription machinery.

Analysis of gene expression levels

To compare the expression level between the T7RNAP-dependent system and POLII-dependent expression from the amastin loci, we generated a strain that expresses the red fluorescent protein mScarlet fused to ETP1 (Adea456) from the chr13 rDNA spacer. ETP1 is one of the host-encoded ETPs and localizes at the periphery of the endosymbiont [7]. The coding sequence for the fusion protein was part of an integration cassette containing *blast*^{R} as selection marker (**Fig 5A**).

First, targeted insertion of the integration cassette into the chr13 rDNA spacer in Adea456 was verified by Southern blot (**Fig 5B** and **S1 Figure**). While the DNA load seemed to be slightly lower in Adea400 compared to Adea456 (see gel picture), the Southern blot signal was more pronounced in Adea400. Hence, it is possible that the integration cassette inserted twice (in both alleles) in Adea400 but only once in Adea456. Growth of Adea456 (doubling time of 6.6 ± 0.1 h) was only slightly slower than in the WT (6.3 ± 0.1 h) (**Fig 5C**). Next, the expression level of mScarlet-ETP1 was analyzed by an in-gel fluorescence assay and homogeneity of expression by epifluorescence microscopy. The WT and Adea126, which produces mScarlet-ETP1 from the γ-

amastin locus [7], served as references. Microscopically, Adea456 and Adea126 showed comparable mScarlet fluorescence patterns (**Fig 5D** and **S2 Figure**) with the endosymbiont being labelled in its periphery in 98 and 100 % of the cells, respectively (**Fig 5E**). Using the same microscope settings, in only ~1 % of the WT cells a weak autofluorescent signal was recorded. The in-gel mScarlet fluorescence intensity (normalized to TCE-stained total protein) for Adea456 was approximately 20 % weaker than for Adea126 but still in a similar range (**Fig 5F**).

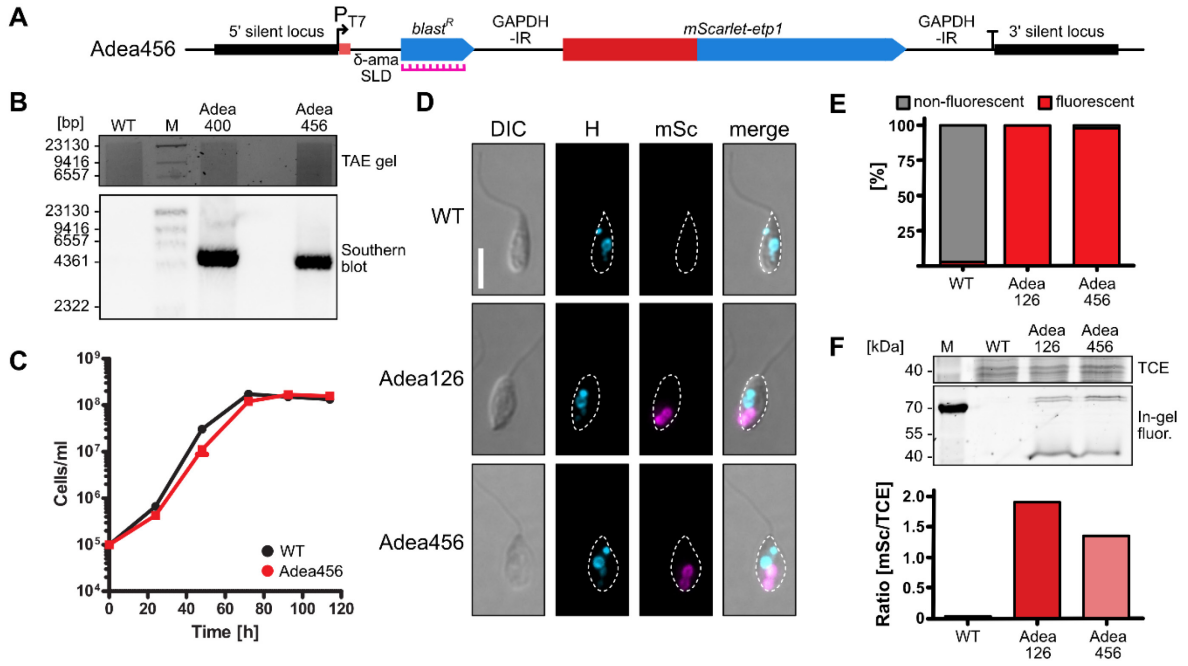

Fig 5. Quantification of T7RNAP-dependent protein expression from the rDNA spacer.
(A) Genomic map of the chr13 rDNA spacer of Adea456 containing the gene encoding mScarlet-ETP1. The annealing site of the Southern blot probe is marked with an icon in magenta. **(B)** Verification of insertion in the chr13 rDNA spacer in Adea456 by Southern blot with BclI and SpeI. The WT and blasticidin resistant strain Adea400 served as controls. The *blast*^{R}-targeting probe yielded single bands of the expected sizes for Adea400 (4746 bp) and Adea456 (4345 bp) but not for the WT (see **S1 Table** for expected sizes). **(C)** Growth of *A. deanei* WT without antibiotics and Adea456 on neomycin/blasticidin over 4 days. **(D)** Epifluorescence microscopic analysis of Adea126 and Adea456 expressing mScarlet-ETP1. Cell shape is indicated by white dashed lines. DIC, differential interference contrast; H, blue channel (visualizing Hoechst 33342); mSc, red channel (visualizing mScarlet). Scale bar represents 5 µm. **(E)** Quantification of fluorescent and non-fluorescent cells of the WT, Adea126, and Adea456 based on epifluorescence microscopy pictures. For each cell line at least 250 cells were analyzed. **(F)** In-gel fluorescence assay detecting red fluorescence in raw extracts of the WT, Adea126, and Adea456. TCE, TCE-stained total protein; In-gel fluor., in-gel fluorescence; M, marker. Note that the assay conditions result in incomplete protein denaturation resulting in several bands for mScarlet-ETP1 (69 kDa).

Discussion

Bacterial endosymbionts are widespread across eukaryotes and profoundly impact physiology and evolution of their hosts [35–37]. Although the genomes of countless bacterial endosymbionts have been sequenced and hence, metabolic complementation between host and endosymbiont are quite well understood in many systems, our understanding of the molecular mechanisms that enable metabolic complementation, signaling, and exertion of control between the symbiotic partners lacks far behind. A central problem for dissecting these questions is that endosymbiotic systems that readily grow in the laboratory and can be efficiently genetically modified are scarce. With the current work we contribute to further develop *A. deanei* into such a much sought after, versatile model for the dissection of host/endosymbiont interactions. To this end, we implemented new resistance markers, identified a transcriptionally silent genomic locus, and, most importantly, used this locus to develop an ectopic gene expression system that is independent of the endogenous transcription machinery.

As new selectable markers we introduced *nours*^{R} and *blast*^{R} and determined by titration 75 µg/ml blasticidin or 200 µg/ml nourseothricin as selective concentrations that efficiently kill the WT cells whereas resistance cassette-carrying transformants are unaffected (**Fig 3**). These selection markers are commonly used in other trypanosomatids but effective selective concentrations vary between strains. E.g. inhibitory concentrations of 0.7-10 µg/ml blasticidin [38,39] and 2-50 µg/ml nourseothricin [38,40] are reported for *Leishmania* sp.; and 2-10 µg/ml blasticidin [39,41] and 500 µg/ml nourseothricin [42] for *Trypanosoma* sp.. Together with the previously implemented *neo*^{R}, *hyg*^{R}, and *phleo*^{R}, these additional selectable markers allow to introduce up to five selectable cassettes into the same *A. deanei* strain now.

As an insertion site for ectopic gene expression, we chose the chr13 rDNA spacer into which expression cassettes were inserted in reverse orientation with respect to the rDNA array. Inactivity of endogenous RNA polymerases in this locus was evident by the sensitivity of strain Adea442, that carries a *blast*^{R} T7 expression cassette in the chr13 rDNA spacer but no functional T7RNAP gene, to selective concentrations of blasticidin (**Fig 4H**). Although the exact RNA polymerase I promoter that is needed for the production of rRNAs from the rDNA arrays, is not known in *A. deanei*, studies from *T. brucei* suggest that the promoter and the transcriptional start are ~1.2 kbp upstream of the 18S rDNA [25,43,44]. If the promoter is in the same position in *A. deanei*, it would be within the 5' flank that was used for homologous recombination, resulting in insertion of the cassette upstream of this putative promoter region (see **S1 Appendix**). Hence,

it is unlikely that integration of expression cassettes into this site interferes with transcription of the rDNA array downstream and our growth analyses demonstrate that even in strain Adea400, in which insertion of the expression cassette apparently occurred in both copies of chr13, growth is not impaired compared to its parental strain Adea319 which expresses only T7RNAP but carries no additional expression cassettes in the chr13 rDNA spacer (**Fig 4E**). Although the 5' flank that we used for homologous recombination showed a high degree of sequence similarities between the rDNA spacers of the seven different chromosomes (see **Fig 1** and **S1 Appendix**), in all clones that we obtained from transfections with insertion cassettes that carry 600 bp flanks amplified from the chr13 rDNA spacer, homologous recombination occurred into the chr13 rDNA spacer. Hence, the 3' flank that shows more sequence divergence between different chromosomes, apparently was sufficient to guide insertion of the cassette specifically into the targeted integration site.

As an exogenous RNA polymerase for the ectopic gene expression system, we relied on the T7RNAP expressed from the δ-amastin locus**.** Although the δ-amastin locus is up to this point the strongest expression locus for transgenes known in *A. deanei a*nd ranges on rank 35 of the most highly expressed genes in *A. deanei* [6], T7RNAP expression did not result in pronounced toxicity as evidenced by the only very mild growth reduction of T7RNAP-expressing cell lines compared to WT (**Fig 4E**). In *E. coli,* high T7RNAP levels can be toxic [45] and similar effects were observed in *T. brucei*. In the latter, initial attempts to generate transgenic lines that express the T7RNAP from the highly expressed PARP locus, were repeatedly unsuccessful [46]. This obstacle was solved by placing the T7RNAP-encoding gene into the weaker β-tubulin expression locus [24], suggesting that high T7RNAP concentrations are lethal.

At the same time, the T7RNAP levels obtained by expression from the δ-amastin locus resulted in high levels of T7RNAP-driven expression of transgenes that are flanked by T7 transcription signals. T7RNAP-dependant expression of *blast*^{R} (strain Adea400) rendered cells resistant to the same selective blasticidin concentration as cells with POLII-dependent expression of *blast*^{R} from the δ-amastin locus (strain Adea373) (compare **Figs 3A** and **4E**). Furthermore, T7RNAP-dependent expression of mScarlet-ETP1 (strain Adea456), resulted in protein levels that were well detectable by epifluorescence microscopy (**Fig 5D**) and only 20 % lower than those that were obtained when expressing the same fusion protein POLII-dependently from the γ-amastin locus (strain Adea126) (**Fig 5F**). These results highlight the new expression system as a suitable tool for investigating symbiosis-related proteins such as the ETPs.

Finally, the new ectopic expression system and resistance markers now provide the basis for the development of advanced gene expression systems, in which the ectopic expression of a gene of interest can be modulated by transcriptional regulators, such as TetR (in its ON or OFF variant [26,47,48]) or CymR [49] without triggering polar effects caused by interference with the endogenous gene expression machinery. Conditional expression would allow to study the effect of the expression of toxic proteins. Furthermore, conditional ectopic expression of a copy of a gene of interest in its null mutant background would enable conditional gene knock-out strategies that would leverage the dissection of cellular functions of essential gene products. Expression strength of this system can be modulated, if needed, by (i) taking advantage of known T7 promoter variants with decreased [50,51] or increased activity [52], (ii) increasing the copy number of the transgene integrated into the same or different rDNA spacers or (iii) by integrating the T7 expression cassettes into episomal elements (e.g. plasmids) which is routinely used, for example, in *L. tarentolae* [53] and *T. brucei* [46].

Materials and methods

Generation of transgenic cell lines

A. deanei (ATCC PRA-265) was grown in brain heart infusion (BHI, Sigma Aldrich) medium supplemented with 10 μg/ml of hemin (Sigma-Aldrich) at 28 °C as described before [6]. Recombinant strains were generated by transfection with specific integration cassettes that had been excised from their storage vectors prior to transfection (see **S2 Table** and **S3 Table**). For the excision of the integration cassettes EcoRI or EcoRV/EcoRI (both New England Biolabs) were used. Transfections were performed as described before [7]. After transfection and recovery, cells were mixed with specific antibiotics for selection [neomycin/G418 (Sigma-Aldrich) at 500 μg/ml, hygromycin B (Invivogen) at 500 μg/ml, blasticidin S (Invivogen) at 75 μg/ml, and nourseothricin (Carl Roth) at 200 μg/ml] before dilution and distribution over a 96-well plate [7]. Cells typically recovered after 5-9 days, and correct insertion of the transgenes was verified by PCR and/or Southern blot analysis. A list of all strains used in this study is given in **S3 Table**.

Growth analyses

For the analysis of the growth behavior of different *A. deanei* strains, precultures were grown to mid-exponential phase (approximately 1-5 x 10^7 cells/ml) with all selective drugs that would allow growth of the specific strains. Then, three replicates were prepared with 5 ml BHI plus hemin and antibiotics as indicated and inoculated to an initial cell density of 1 x 10^5 cells/ml. The tubes were incubated at 28 °C without agitation and the cell density was measured every 20-24 h using the MultiSizer 4e (Beckman Coulter).

Analysis of homologous recombination by Southern blot

Southern blot was performed as described previously [7]. Each DNA sample contained 7 µg of purified DNA. The DNA was digested using restriction enzymes BclI and SpeI or only BamHI (New England Biolabs). A 393 bp DIG-labelled probe against *blast*^{R} was generated by PCR using primers 3174 and 3175 (see **S3 Table**) and the DIG DNA Labelling Mixture (Roche) according to the manufacturer's instructions. Hybridization was conducted at a temperature of 48 °C.

Construction of plasmids

All plasmids for this study were products of Gibson [54] or Golden Gate [55] assemblies as described previously [7]. The cloning fragments, which were needed for the assemblies, were generated by PCR using the Phusion polymerase (New England Biolabs) and the primers and templates are listed in **S2 Table**. The correct sizes of cloning fragments were verified by electrophoresis. PCR products matching the expected sizes were excised from the gel and purified using the Monarch DNA Gel Extraction kit (New England Biolabs). The concentration of the DNA was determined using the NanoPhotometer NP80 (Implen). The molar concentration of the insert(s) usually exceeded the vector backbone concentration by a factor of 3. After the assembly, 1 µl of DpnI was added to each assembly mix to remove residual PCR template present in the mix. Then, *E. coli* TOP10 cells were transformed with the assembly mix and recombinant cells selected on lysogeny broth (LB) plates containing 100 µg/ml ampicillin. Recovered clones were inoculated in 5 ml LB liquid medium with ampicillin (see above) and used for plasmid purification (Monarch Plasmid Miniprep kit, New England Biolabs). Plasmids were verified by control digests and sequencing (Microsynth).

Epifluorescence microscopy

Microscopy slides were prepared from mid-exponential cultures (approximately 1-5 x 10^7 cells/ml) as described before [7]. Images were taken with the Axio Imager A.2 equipped with the AxioCam MRm and an Illuminator HXP 120 V (all instruments from Zeiss) and processed with Zen Blue v2.5 (Zeiss) as described previously [7]. *A. deanei* WT cells served as negative control and its autofluorescence was used to define a suitable fluorescence threshold. For post-processing of the pictures Fiji [56] was used.

Western blot

For the detection of specific proteins, we grew 10 ml cultures of the relevant strains to mid-exponential phase, harvested the cells by centrifugation, and precipitated the proteins using trichloroacetic acid [7]. The precipitate was resuspended in urea buffer (8 M urea, 100 mM Tris, 5.25 mM EDTA, pH 8.6) and the protein concentration was determined using Pierce 660nm Protein Assay Reagent (Thermo Fisher Scientific). For each sample, 25 µg protein were mixed with Lämmli sample buffer (final concentrations: 63 mM Tris-HCl, pH 6.8, 10 mM dithiothreitol, 10% v/v glycerol, 2% SDS w/v, and 0.0025% w/v bromophenol blue), incubated for 5 min at 95 °C, and loaded onto a 10 % SDS polyacrylamid gel containing 0.5 % TCE. PAGE and protein blot to a PVDF membrane (Amersham Hybond, 0.45 nm, Thermo Fisher Scientific) were performed as described previously [7]. After blotting, proteins were detected immunologically. In brief, the membrane was blocked with 5 % w/v milk powder for 1 h at room temperature and washed with 1x PBST (phosphate-buffered saline including 0.05 % v/v Tween-20). For the detection of the T7RNAP, α-T7RNAP antibody (29943-1-AP, Proteintech, 1:5000 dilution) was used overnight at 4 °C and α-rabbit IgG HRP conjugate (7074, CellSignaling, 1:10,000 dilution) for 1 h at room temperature. Chemiluminescence was started by addition of SuperSignal West Pico Chemiluminescent Substrate (Thermo Fisher Scientific) and recorded using the ChemiDoc MP (Biorad).

In-gel fluorescence assay

For the detection of in-gel fluorescence of mScarlet, samples were prepared as described by Sanial et al. [57] with minor modifications. First, 15 ml cultures of the relevant strains were grown to mid-exponential phase, cells were harvested by centrifugation, washed twice using 1x PBS,

and resuspended in 1 ml 1x PBS. Before cell lysis, cOmplete EDTA-free protease inhibitor tabs (Roche) and a few grains of DNase (Carl Roth) were added and the cells were lysed by sonication using the UP100H (Hielscher) with 5 x 18 pulses (cycle 0.8, amplitude ~60 %, MS1 sonotrode). Cell debris and intact cells were removed by centrifugation (3000 rpm, 4 °C, 5 min) and the protein concentration of the supernatant was determined using the Pierce 660nm Protein Assay Reagent (ThermoFisher) and the FLUOstar Omega Plate Reader (BMG Labtech). 25 µg of protein were mixed with Lämmli sample buffer (final concentrations: 50 mM Tris-HCl, pH 6.8, 10% v/v glycerol, 2% SDS w/v, 2.5 mM EDTA, and 0.005% w/v bromophenol blue, plus 12.5 mM dithiothreitol), heated to 50 °C for 5 min and applied to a 12.5 % SDS polyacrylamid gel containing 0.5 % v/v TCE. The electrophoresis ran at 40 mA until the marker bands (Prestained Ladder, Thermo Fisher Scientific) were fully resolved. Finally, mScarlet fluorescence was recorded with the ChemiDoc MP (Biorad) using the UV tray and the “Cy3” filter. Afterwards, loading of the gel was visualized using TCE fluorescence with the UV tray and the “Stain-free gel” setting of the ChemiDoc MP (Biorad). The intensities of the mScarlet and TCE bands were estimated with Fiji [56] and normalized by the TCE signals.

Data availability

The datasets generated and/or analyzed in the course of this study are included in this published article and its supplementary information files. Further data, including raw data and quantitative analyses, can be found in the Data Hub https://archive.nfdi4plants.org/records/3febm-0sd52. The data is linked to the following DOI: https://doi.org/10.60534/3febm-0sd52.

Acknowledgements

We thank Victoria Klimenko for technical support throughout the experimental work.

References

1. Motta MCM. Endosymbiosis in trypanosomatids as a model to study cell evolution. Open Parasitol J. 2010;4: 139–147. doi:10.2174/1874421401004010139
2. Harmer J, Yurchenko V, Nenarokova A, Lukeš J, Ginger ML. Farming, slaving and enslavement: histories of endosymbioses during kinetoplastid evolution. Parasitology. 2018;145: 1311–1323. doi:10.1017/S0031182018000781
3. Du Y, Maslov DA, Chang KP. Monophyletic origin of β-division proteobacterial endosymbionts and their coevolution with insect trypanosomatid protozoa *Blastocrithidia culicis* and *Crithidia* spp. Proc Natl Acad Sci U S A. 1994;91: 8437–8441. doi:10.1073/pnas.91.18.8437
4. Alves JMP, Serrano MG, Da Silva FM, Voegtly LJ, Matveyev A V., Teixeira MMG, et al. Genome evolution and phylogenomic analysis of *Candidatus* Kinetoplastibacterium, the betaproteobacterial endosymbionts of *Strigomonas* and *Angomonas*. Genome Biol Evol. 2013;5: 338–350. doi:10.1093/gbe/evt012
5. Motta MCM, Catta-Preta CMC, Schenkman S, Martins AC de A, Miranda K, de Souza W, et al. The bacterium endosymbiont of *Crithidia deanei* undergoes coordinated division with the host cell nucleus. PLoS One. 2010;5: 20–21. doi:10.1371/journal.pone.0012415
6. Morales J, Kokkori S, Weidauer D, Chapman J, Goltsman E, Rokhsar D, et al. Development of a toolbox to dissect host-endosymbiont interactions and protein trafficking in the trypanosomatid *Angomonas deanei*. BMC Evol Biol. 2016;16: 1–12. doi:10.1186/s12862-016-0820-z
7. Morales J, Ehret G, Poschmann G, Reinicke T, Maurya AK, Kröninger L, et al. Host-symbiont interactions in *Angomonas deanei* include the evolution of a host-derived dynamin ring around the endosymbiont division site. Curr Biol. 2023;33: 28-40.e7. doi:10.1016/j.cub.2022.11.020
8. Gonçalves CS, Catta-Preta CMC, Repolês B, Mottram JC, De Souza W, Machado CR, et al. Importance of *Angomonas deanei* KAP4 for kDNA arrangement, cell division and maintenance of the host-bacterium relationship. Sci Rep. 2021;11: 1–19. doi:10.1038/s41598-021-88685-8
9. Catta-Preta CMC, dos Santos Pascoalino B, de Souza W, Mottram JC, Motta MCM, Schenkman S. Reduction of tubulin expression in *Angomonas deanei* by RNAi modifies the ultrastructure of the trypanosomatid protozoan and impairs division of its endosymbiotic bacterium. J Eukaryot Microbiol. 2016;63: 794–803. doi:10.1111/jeu.12326
10. Maurya AK, Kröninger L, Ehret G, Bäumers M, Marson M, Scheu S, et al. A nucleus-encoded dynamin-like protein controls endosymbiont division in the trypanosomatid *Angomonas deanei*. Sci Adv. 2025;in press. doi:10.1126/sciadv.adp8518
11. Clayton C. Regulation of gene expression in trypanosomatids: Living with polycistronic transcription. Open Biol. 2019;9. doi:10.1098/rsob.190072
12. Maslov DA, Opperdoes FR, Kostygov AY, Hashimi H, Lukeš J, Yurchenko V. Recent advances in trypanosomatid research: genome organization, expression, metabolism, taxonomy and evolution. Parasitology. 2019;146: 1–27. doi:10.1017/S0031182018000951
13. Martínez-Calvillo S, Vizuet-De-Rueda JC, Florencio-Martínez LE, Manning-Cela RG, Figueroa-Angulo EE. Gene expression in trypanosomatid parasites. J Biomed Biotechnol. 2010;2010. doi:10.1155/2010/525241

14. Siegel TN, Hekstra DR, Kemp LE, Figueiredo LM, Lowell JE, Fenyo D, et al. Four histone variants mark the boundaries of polycistronic transcription units in *Trypanosoma brucei*. Genes Dev. 2009;23: 1063–1076. doi:10.1101/gad.1790409

15. Liang XH, Haritan A, Uliel S, Michaeli S. *trans* and *cis* splicing in trypanosomatids: mechanism, factors, and regulation. Eukaryot Cell. 2003;2: 830–840. doi:10.1128/EC.2.5.830-840.2003

16. Santos RERS, Silva GLA, Santos E V., Duncan SM, Mottram JC, Damasceno JD, et al. A DiCre recombinase-based system for inducible expression in *Leishmania major*. Mol Biochem Parasitol. 2017;216: 45–48. doi:10.1016/j.molbiopara.2017.06.006

17. Beneke T, Madden R, Makin L, Valli J, Sunter J, Gluenz E. A CRISPR Cas9 high-throughput genome editing toolkit for kinetoplastids. R Soc Open Sci. 2017;4: 1–16. doi:10.1098/rsos.170095

18. De Assis Burle-Caldas G, Grazielle-Silva V, Laibida LA, DaRocha WD, Teixeira SMR. Expanding the tool box for genetic manipulation of *Trypanosoma cruzi*. Mol Biochem Parasitol. 2015;203: 25–33. doi:10.1016/j.molbiopara.2015.10.004

19. Yagoubat A, Corrales RM, Bastien P, Lévêque MF, Sterkers Y. Gene editing in trypanosomatids: tips and tricks in the CRISPR-Cas9 era. Trends Parasitol. 2020;36: 745–760. doi:10.1016/j.pt.2020.06.005

20. Kolev NG, Tschudi C, Ullu E. RNA interference in protozoan parasites: achievements and challenges. Eukaryot Cell. 2011;10: 1156–1163. doi:10.1128/EC.05114-11

21. Kushnir S, Gase K, Breitling R, Alexandrov K. Development of an inducible protein expression system based on the protozoan host *Leishmania tarentolae*. Protein Expr Purif. 2005;42: 37–46. doi:10.1016/j.pep.2005.03.004

22. Li FJ, Xu ZS, Aye HM, Brasseur A, Lun ZR, Tan KSW, et al. An efficient cumate-inducible system for procyclic and bloodstream form *Trypanosoma brucei*. Mol Biochem Parasitol. 2017;214: 101–104. doi:10.1016/j.molbiopara.2017.04.007

23. Wickstead B, Ersfeld K, Gull K. Targeting of a tetracycline-inducible expression system to the transcriptionally silent minichromosomes of *Trypanosoma brucei*. Mol Biochem Parasitol. 2002;125: 211–216. doi:10.1016/S0166-6851(02)00238-4

24. Wirtz E, Leal S, Ochatt C, Cross GAM. A tightly regulated inducible expression system for conditional gene knock-outs and dominant-negative genetics in *Trypanosoma brucei*. Mol Biochem Parasitol. 1999;99: 89–101. doi:10.1016/S0166-6851(99)00002-X

25. White TC, Rudenko G, Borst P. Three small RNAs within the 10 kb trypanosome rRNA transcription unit are analogous to Domain VII of other eukaryotic 28S rRNAs. Nucleic Acids Res. 1986;14: 9471–9489.

26. Wirtz E, Clayton C. Inducible gene expression in trypanosomes mediated by a prokaryotic repressor. Science. 1995;268: 1179–1183. doi:10.1126/science.7761835

27. Wirtz E, Hoek M, Cross GAM. Regulated processive transcription of chromatin by T7 RNA polymerase in *Trypanosoma brucei*. Nucleic Acids Res. 1998;26: 4626–4634. doi:10.1093/nar/26.20.4626

28. Sunter J, Wickstead B, Gull K, Carrington M. A new generation of T7 RNA polymerase-independent inducible expression plasmids for *Trypanosoma brucei*. PLoS One. 2012;7. doi:10.1371/journal.pone.0035167

29. Espada CR, Quilles JC, Albuquerque-Wendt A, Cruz MC, Beneke T, Lorenzon LB, et al. Effective genome editing in *Leishmania* (*Viannia*) *braziliensis* stably expressing Cas9 and

T7 RNA polymerase. Front Cell Infect Microbiol. 2021;11: 1–13. doi:10.3389/fcimb.2021.772311

30. Yao C, Luo J, Hsiao CHC, Donelson JE, Wilson ME. *Leishmania chagasi*: a tetracycline-inducible cell line driven by T7 RNA polymerase. Exp Parasitol. 2007;116: 205–213. doi:10.1016/j.exppara.2007.01.001

31. Kraeva N, Ishemgulova A, Lukeš J, Yurchenko V. Tetracycline-inducible gene expression system in *Leishmania mexicana*. Mol Biochem Parasitol. 2014;198: 11–13. doi:10.1016/j.molbiopara.2014.11.002

32. Wang W, Li Y, Wang Y, Shi C, Li C, Li Q, et al. Bacteriophage T7 transcription system: an enabling tool in synthetic biology. Biotechnol Adv. 2018;36: 2129–2137. doi:10.1016/j.biotechadv.2018.10.001

33. Studier FW, Moffatt BA. Use of bacteriophage T7 RNA polymerase to direct selective high-level expression of cloned genes. J Mol Biol. 1986;189: 113–130. doi:10.1016/0022-2836(86)90385-2

34. Shanmugasundram A, Starns D, Böhme U, Amos B, Wilkinson PA, Harb OS, et al. TriTrypDB: an integrated functional genomics resource for kinetoplastida. PLoS Negl Trop Dis. 2023;17: 1–20. doi:10.1371/journal.pntd.0011058

35. Moya A, Peretó J, Gil R, Latorre A. Learning how to live together: genomic insights into prokaryote-animal symbioses. Nat Rev Genet. 2008;9: 218–229. doi:10.1038/nrg2319

36. Nowack ECM, Melkonian M. Endosymbiotic associations within protists. Philos Trans R Soc B Biol Sci. 2010;365: 699–712. doi:10.1098/rstb.2009.0188

37. Husnik F, Tashyreva D, Boscaro V, George EE, Lukeš J, Keeling PJ. Bacterial and archaeal symbioses with protists. Curr Biol. 2021;31: R862–R877. doi:10.1016/j.cub.2021.05.049

38. Goyard S, Beverley SM. Blasticidin resistance: a new independent marker for stable transfection of *Leishmania*. Mol Biochem Parasitol. 2000;108: 249–252. doi:10.1016/S0166-6851(00)00210-3

39. Brooks DR, McCulloch R, Coombs GH, Mottram JC. Stable transformation of trypanosomatids through targeted chromosomal integration of the selectable marker gene encoding blasticidin S deaminase. FEMS Microbiol Lett. 2000;186: 287–291. doi:10.1016/S0378-1097(00)00159-2

40. Joshi PB, Webb JR, Davies JE, McMaster WR. The gene encoding streptothricin acetyltransferase (sat) as a selectable marker for *Leishmania* expression vectors. Gene. 1995;156: 145–149. doi:10.1016/0378-1119(95)00042-5

41. Marques CA, Ridgway M, Tinti M, Cassidy A, Horn D. Genome-scale RNA interference profiling of *Trypanosoma brucei* cell cycle progression defects. Nat Commun. 2022;13. doi:10.1038/s41467-022-33109-y

42. Knüsel S, Jenni A, Benninger M, Bütikofer P, Roditi I. Persistence of *Trypanosoma brucei* as early procyclic forms and social motility are dependent on glycosylphosphatidylinositol transamidase. Mol Microbiol. 2022;117: 802–817. doi:10.1111/mmi.14873

43. Rudenko G, Chung HM, Pham VP, Van der Ploeg LH. RNA polymerase I can mediate expression of CAT and neo protein-coding genes in *Trypanosoma brucei*. EMBO J. 1991;10: 3387–3397. doi:10.1002/j.1460-2075.1991.tb04903.x

44. Janz L, Clayton C. The PARP and rRNA promoters of *Trypanosoma brucei* are composed of dissimilar sequence elements that are functionally interchangeable. Mol Cell Biol.

1994;14: 5804–5811. doi:10.1128/mcb.14.9.5804-5811.1994

45. Temme K, Hill R, Segall-Shapiro TH, Moser F, Voigt CA. Modular control of multiple pathways using engineered orthogonal T7 polymerases. Nucleic Acids Res. 2012;40: 8773–8781. doi:10.1093/nar/gks597

46. Wirtz E, Hartmann C, Clayton C. Gene expression mediated by bacteriophage T3 and 17 RNA polymerases in transgenic trypanosomes. Nucleic Acids Res. 1994;22: 3887–3894. doi:10.1093/nar/22.19.3887

47. Kamionka A, Bogdanska-Urbaniak J, Scholz O, Hillen W. Two mutations in the tetracycline repressor change the inducer anhydrotetracycline to a corepressor. Nucleic Acids Res. 2004;32: 842–847. doi:10.1093/nar/gkh200

48. Resch M, Striegl H, Henssler EM, Sevvana M, Egerer-sieber C, Schiltz E, et al. A protein functional leap: how a single mutation reverses the function of the transcription regulator TetR. Nucleic Acids Res. 2008;36: 4390–4401. doi:10.1093/nar/gkn400

49. Mullick A, Xu Y, Warren R, Koutroumanis M, Guilbault C, Broussau S, et al. The cumate gene-switch: a system for regulated expression in mammalian cells. BMC Biotechnol. 2006;6: 1–18. doi:10.1186/1472-6750-6-43

50. Lieber A, Sandig V, Strauss M. A mutant T7 phage promoter is specifically transcribed by T7-RNA polymerase in mammalian cells. Eur J Biochem. 1993;217: 387–394. doi:10.1111/j.1432-1033.1993.tb18257.x

51. Komura R, Aoki W, Motone K, Satomura A, Ueda M. High-throughput evaluation of T7 promoter variants using biased randomization and DNA barcoding. PLoS One. 2018;13: 1–16. doi:10.1371/journal.pone.0196905

52. Conrad T, Plumbom I, Alcobendas M, Vidal R, Sauer S. Maximizing transcription of nucleic acids with efficient T7 promoters. Commun Biol. 2020;3: 1–8. doi:10.1038/s42003-020-01167-x

53. Kushnir S, Cirstea IC, Basiliya L, Lupilova N, Breitling R, Alexandrov K. Artificial linear episome-based protein expression system for protozoon *Leishmania tarentolae*. Mol Biochem Parasitol. 2011;176: 69–79. doi:10.1016/j.molbiopara.2010.12.002

54. Gibson DG, Young L, Chuang RY, Venter JC, Hutchison CA, Smith HO. Enzymatic assembly of DNA molecules up to several hundred kilobases. Nat Methods. 2009;6: 343–345. doi:10.1038/nmeth.1318

55. Engler C, Kandzia R, Marillonnet S. A one pot, one step, precision cloning method with high throughput capability. PLoS One. 2008;3. doi:10.1371/journal.pone.0003647

56. Schindelin J, Arganda-Carreras I, Frise E, Kaynig V, Longair M, Pietzsch T, et al. Fiji: an open-source platform for biological-image analysis. Nat Methods. 2012;9: 676–682. doi:10.1038/nmeth.2019

57. Sanial M, Miled R, Alves M, Claret S, Joly N, Proux-Gillardeaux V, et al. Direct observation of fluorescent proteins in gels: a rapid cost-efficient, and quantitative alternative to immunoblotting. bioRxiv. 2024;33: 594679. Available: https://www.biorxiv.org/content/10.1101/2024.05.31.594679v1

Supporting information

S1 Appendix. Alignment of the 4,000 nucleotides upstream of the start of the 18S rRNA genes on different chromosomes in *A. deanei*.

Regions flanking the insertion site that were used for homologous recombination are highlighted in yellow (3' flank) and red (5' flank). rDNA sequences in *A. deanei* were identified using the rDNA sequence from *T. brucei* as query (NCBI locus tags TB927_01.rRNA.1 and onwards). The start of the rDNA arrays is marked with "Start of 18s rDNA" at the end of the alignment. For the multi-sequence alignment Clustal Omega was used (www.ebi.ac.uk/jdispatcher/msa/clustalo).

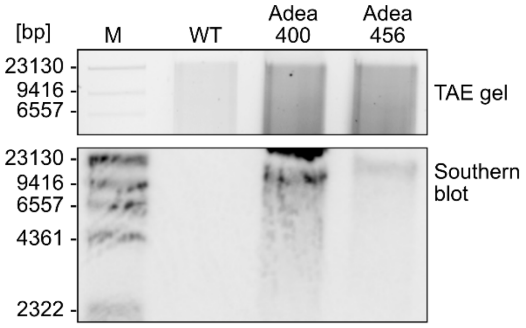

S1 Figure. Verification of insertion in the chr13 rDNA spacer in Adea400 and Adea456 by Southern blot with BamHI.

The WT served as control. The *blast*^{R}-targeting probe yielded single bands of the expected sizes for Adea400 (16252 bp) and Adea456 (18519 bp) but not for the WT (see **S1 Table** for expected sizes).

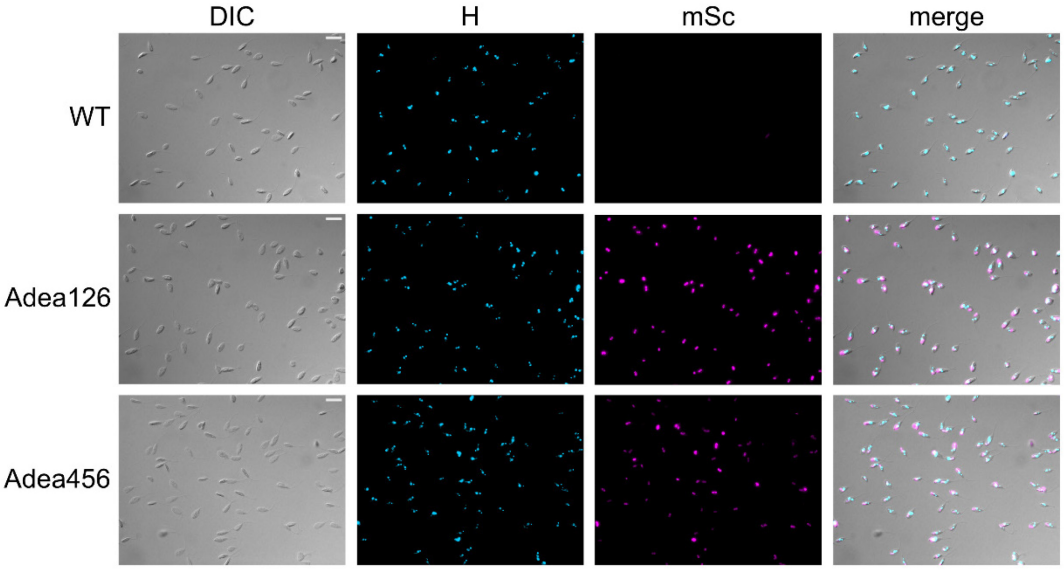

S2 Figure. Epifluorescence microscopic analysis of Adea126 and Adea456 expressing mScarlet-ETP1.

DIC, differential interference contrast; H, blue channel (visualizing Hoechst 33342-stained DNA); mSc, red channel (visualizing mScarlet). Scale bar represents 10 µm.

S1 Table. Expected Southern blot fragments for the verification of Adea400 and Adea456.
For the identification of the rDNA spacer, in which transgenes had been inserted, genomic DNA of the relevant strains was digested using a combination of BclI and SpeI or BamHI alone.

S2 Table. Generation of recombinant plasmids by Golden Gate and Gibson cloning.
Vectors were generated by inserting specific inserts into already existing backbones. For the cloning, single to multi-fragment Gibson or Golden Gate assemblies were performed as indicated. Plasmids were either generated in the course of this work ("This paper"), described previously (Morales et al. 2023), or kindly provided by external parties. gDNA from a pLEXSY strain was obtained from Jena Bioscience.

S3 Table. Overview of *A. deanei* strains used in this study.
Enzymatically excised integration cassettes, containing expressed transgenes and stabilizing elements that are not translated, were integrated into the chromosomes of recipient strains. Correct insertion was verified by PCR and/or Southern blot. Strains were either generated in the course of this work ("This paper") or described previously (Morales et al. 2023).

Author contributions

L.K. and E.C.M.N. designed the research. L.K., A.K.M, C.S., F.P.S., and Z.K. performed the research. L.K. and E.C.M.N. analyzed the data. E.C.M.N. supervised the research. L.K. and E.C.M.N. wrote the manuscript.

Competing Interests Statement

The authors declare no competing interests.

2.2. Results: Additional research outcomes

2.2.1. ETP9 shows similar level of expression in symbiotic and aposymbiotic strains

To compare the subcellular localization and expression level of ETP9 in symbiotic and aposymbiotic *A. deanei* strains, the recombinant ETP9 (mScarlet-ETP9, *γ-ama*$^{mScarlet\text{-}etp9}$) was overexpressed from the *γ-amastin* locus. I observed that the recombinant ETP9 is enriched at the ESDS (highlighted by an arrowhead in micrograph 1b) in the symbiotic strain (Fig. 2.1 A and Maurya et al., 2025), however, remained undetected in the aposymbiotic strain due to the cytosolic localization (micrograph 2b, Fig. 2.1 A). A quantitative Western blot using an anti-RFP antibody to detect the recombinant ETP9 and the level of α-tubulin for normalization, showed that both strains exhibited similar ETP9 levels (Fig. 2.1 B and C, performed by Lena Kröninger).

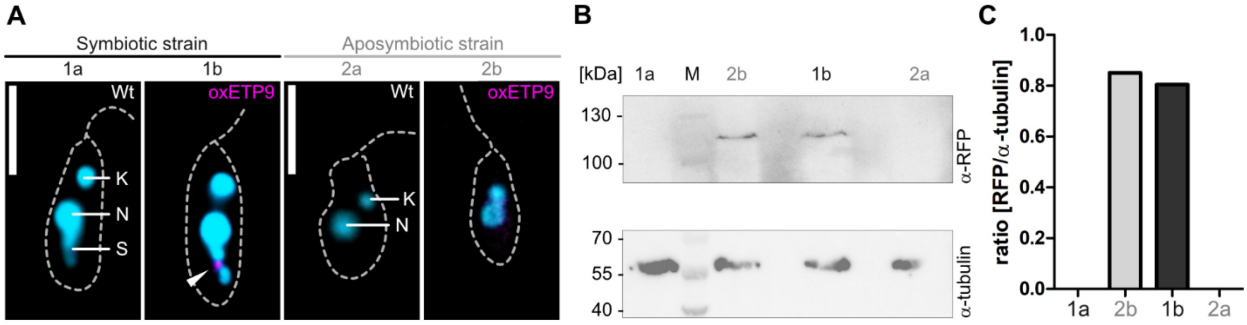

Figure 2.1: Comparison of ETP9 expression levels in symbiotic and aposymbiotic *A. deanei* strains.

A: Comparison of the subcellular localization of the mScarlet-ETP9 fusion protein overexpressed from the *γ-amastin* locus in symbiotic and aposymbiotic strains. Shown are the symbiotic Wt (micrograph 1a), the apoymbiotic Wt (micrograph 2a), overexpression of ETP9 (*γ-ama*$^{mScarlet\text{-}etp9}$) in the symbiotic strain (micrograph 1b, white arrowhead indicates ETP9 localization) and the aposymbiotic strain (micrograph 2b). Black and grey texts indicate symbiotic and aposymbiotic strains, respectively. The Hoechst 33342 staining of DNA is shown in cyan and the mScarlet autofluorescence in magenta. Abbreviations: K, kinetoplast; N, nucleus; S, symbiont and oxETP9, overexpressed ETP9. Dotted grey lines indicate cell borders. Scale bar: 5 µm. **B:** Comparison of expression levels by Western blot of the mScarlet-ETP9 in symbiotic and aposymbiotic strains. The mScarlet was detected using α-RFP (1:2000, Chromotek, 5f8, rat) and α-rat-IgG HRP (1:5000, Invitrogen, PA1-28573) antibodies. The stripped membrane was used to detect the alpha-tubulin (as a loading control) with α-alpha-tubulin (1:2000, Thermo Fisher, MA1-80017, rat) and α-rat-IgG HRP (1:10,000, Invitrogen, PA1-28573) antibodies. **C:** The graph shows the ratio of RFP and α-tubulin based on quantification from Western blot signals of different strains (from B).

2.2.2. ETP7 appears to be involved in ES division

As described earlier, we identified three ETPs, namely, ETP9, ETP2, and ETP7 at the ESDS by overexpression of fluorescent fusion proteins (Morales et al., 2023). ETP9 was found to be essential for ES division (Maurya et al., 2025). ETP2 plays an important role in ES division (Maurya et al., under review). Here, I explored the functional role of ETP7.

2.2.2.1. ETP7 shows consistent localization in a cell cycle-dependent manner

To explore the subcellular localization of ETP7 in *A. deanei*, I generated a cell line which endogenously expresses the recombinant protein, eGFP-ETP7 (Δ*etp7*$^{egfp\text{-}etp7}$/*etp7*) in the background of the ES marker mScarlet-ETP1. Here, I observed that endogenously expressed eGFP-ETP7 exhibited the same localization at the ESDS (Fig. 2.2 A, micrograph 2) as previously reported for the overexpressed version (Fig. 2.2 A, micrograph 1 and Morales et al., 2023). However, the eGFP-ETP7 expressed from the *δ-amastin* locus showed additionally a diffused fluorescence pattern over the ES with an enrichment at the ESDS especially in the elongated ES (i.e., shortly before ES division). The diffused fluorescence signal might represent an artefact of overexpression, since it was not seen in the endogenously tagged cell line (Δ*etp7*$^{egfp\text{-}etp7}$/*etp7*).

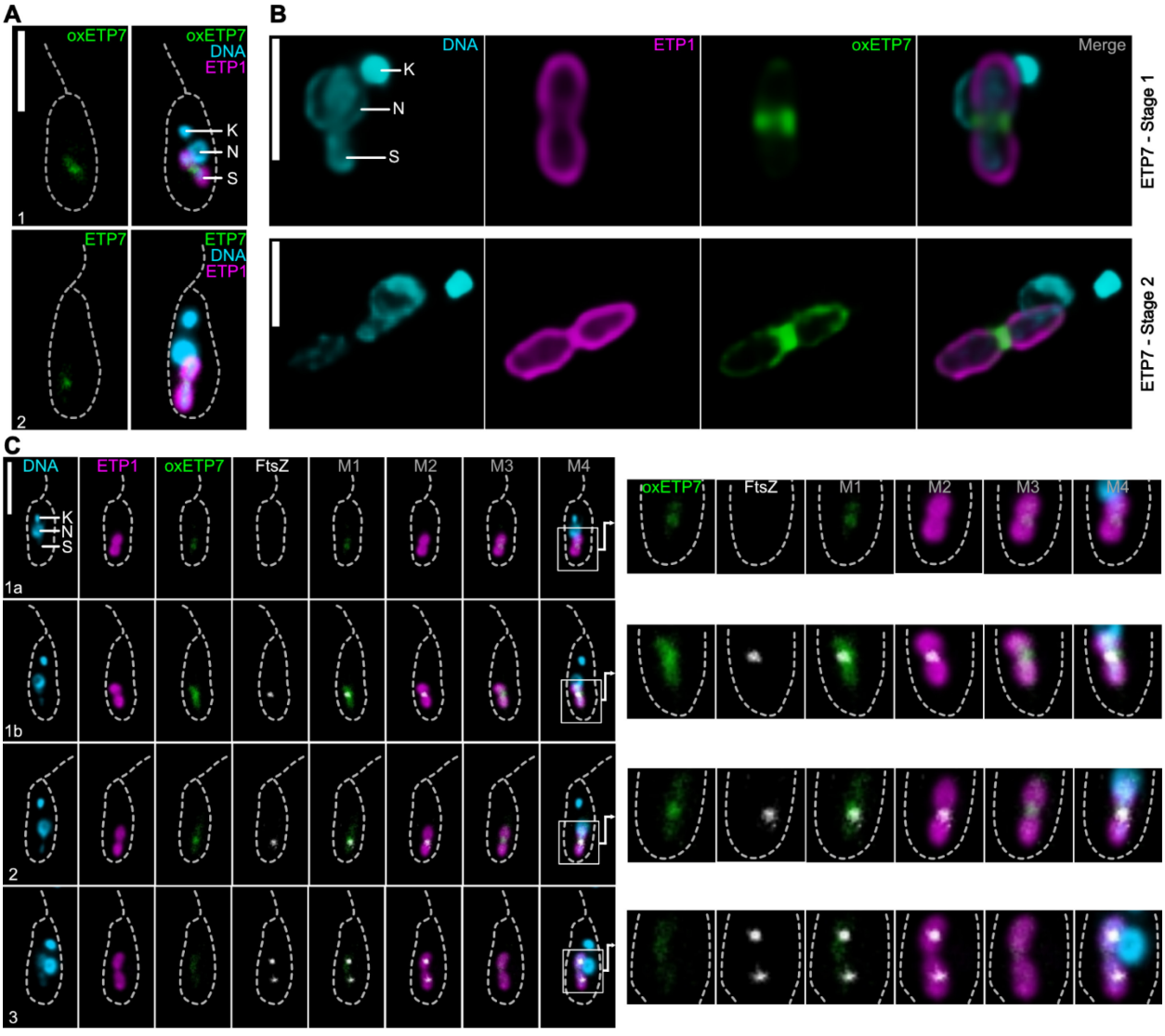

Figure 2.2: Subcellular localization of ETP7 over different cell cycle stages in *A. deanei*.

A: Subcellular localization of the recombinant ETP7 expressed from the *δ-amastin* locus (micrograph 1) and endogenous locus (micrograph 2) in the background of the ES marker mScarlet-ETP1 as analyzed by

epifluorescence microscopy is shown. Scale bar is 5 µm. **B:** Localization of the eGFP-ETP7 expressed from the *δ-amastin* locus, fluorescence signal after deconvolution as analyzed by confocal microscopy is displayed. Merge shows alignment of the Hoechst 33342, ETP1, and eGFP-ETP7. Scale bar is 2 µm. **C:** Subcellular localization of the recombinant ETP7 overexpressed from the *δ-amastin* locus is shown throughout the cell cycle stages. Shown are eGFP in green and mScarlet in magenta as detected by their autofluorescence, FtsZ in white by IFA using α-FtsZ$_{pepC}$, and DNA-containing compartments in cyan by Hoechst 33342 staining. Scale bar: 5 µm. Merge1 shows the alignment of eGFP and FtsZ; Merge2, mScarlet and FtsZ; Merge3, mScarlet and eGFP; Merge4, all four channels. Numbers on images show cell cycle stages compared to Maurya et al., 2025. The highlighted box in the left panel indicates its closeup version in the right panel. Scale bar is 5 µm. Abbreviations: S, symbiont; K, kinetoplast; N, nucleus and ox, overexpression. Cell borders are displayed by broken grey lines, drawn based on DIC image.

Next, to gain detailed insights into the localization of ETP7 at the ESDS, I performed confocal microscopy for the eGFP-ETP7 expressed from the *δ-amastin* locus. The recombinant ETP7 displayed two dot-like structures at both sides of the ES envelope at the ESDS in optical transects forming a ring-like structure (Fig. 2.2 B, ETP7 stage 1). Additionally, a weak fluorescence signal at the poles of the ES could be seen. Interestingly, during ES elongation, the eGFP-ETP7 is restricted to the ESDS and forms a plate-like structure that appears to separate two bacterial daughter cells. In addition, it is also present in the ES envelope (Fig. 2.2 B, ETP7 stage 2).

Lastly, to test if the subcellular localization of the eGFP-ETP7 depends on the cell-cycle stage (aim I), I characterized its localization by performing IFA using α-FtsZ$_{pepC}$ antibody in overexpression cell line (Δ*δ-ama*$^{egfp\text{-}etp7}$). I observed that a weak eGFP fluorescence signal was always detectable over the ES (Fig. 2.2 C, stage 1a). Next, the eGFP-ETP7 signal becomes more intense but remains distributed over the ES, though more enrichment at the ESDS compared to the remaining part of the bacterial cell can be observed (Fig. 2.2 C, stage 1b). Additionally, FtsZ appears and co-localizes with eGFP-ETP7. Next, the ES elongates and eGFP-ETP7 enriches at the ESDS where it remains co-localized with FtsZ (Fig. 2.2 C, stage 2), however, a weak signal over the ES can still be detected. Then, the ES divides and eGFP-ETP7 signal gets weaker again and remains distributed over the ES while FtsZ moves to the newly formed DS (Fig. 2.2 C, stage 3). The analysis of endogenously tagged ETP7 was excluded due to weak fluorescence intensity.

2.2.2.2. Knockdown of ETP7 results in a weak bacterial division impairment

To study the functional role of ETP7 in *A. deanei* (aim II), I performed knockdown of *etp7* in symbiotic and aposymbiotic Wt strains using two independent MAOs (Fig. 2.3 A). Here, I observed that symbiotic Wt cells treated with MAO-2$_{etp7}$ grew much slower (Fig. 2.3 B, upper graph) than the water control and resulted in weak division phenotypes 24 h post-transfection, in which some host cells were distorted, and the ES formed a filamentous chain (Fig. 2.3 C). With the same treatment, the aposymbiotic strain did not result in any phenotypes (Fig. 2.3 E), however, grew marginally slower than the water control (Fig. 2.3 B, lower graph) likely indicating off-target effects. However, the symbiotic Wt strain treated with MAO-1$_{etp7}$ grew comparable to the water treated cells (Fig. 2.3 B) and did not show any obvious phenotypes (Fig. 2.3 C). With the same treatment, the aposymbiotic Wt strain did not show any noticeable phenotypes (Fig. 2.3 E) and grew comparable to the water control (Fig. 2.3 B).

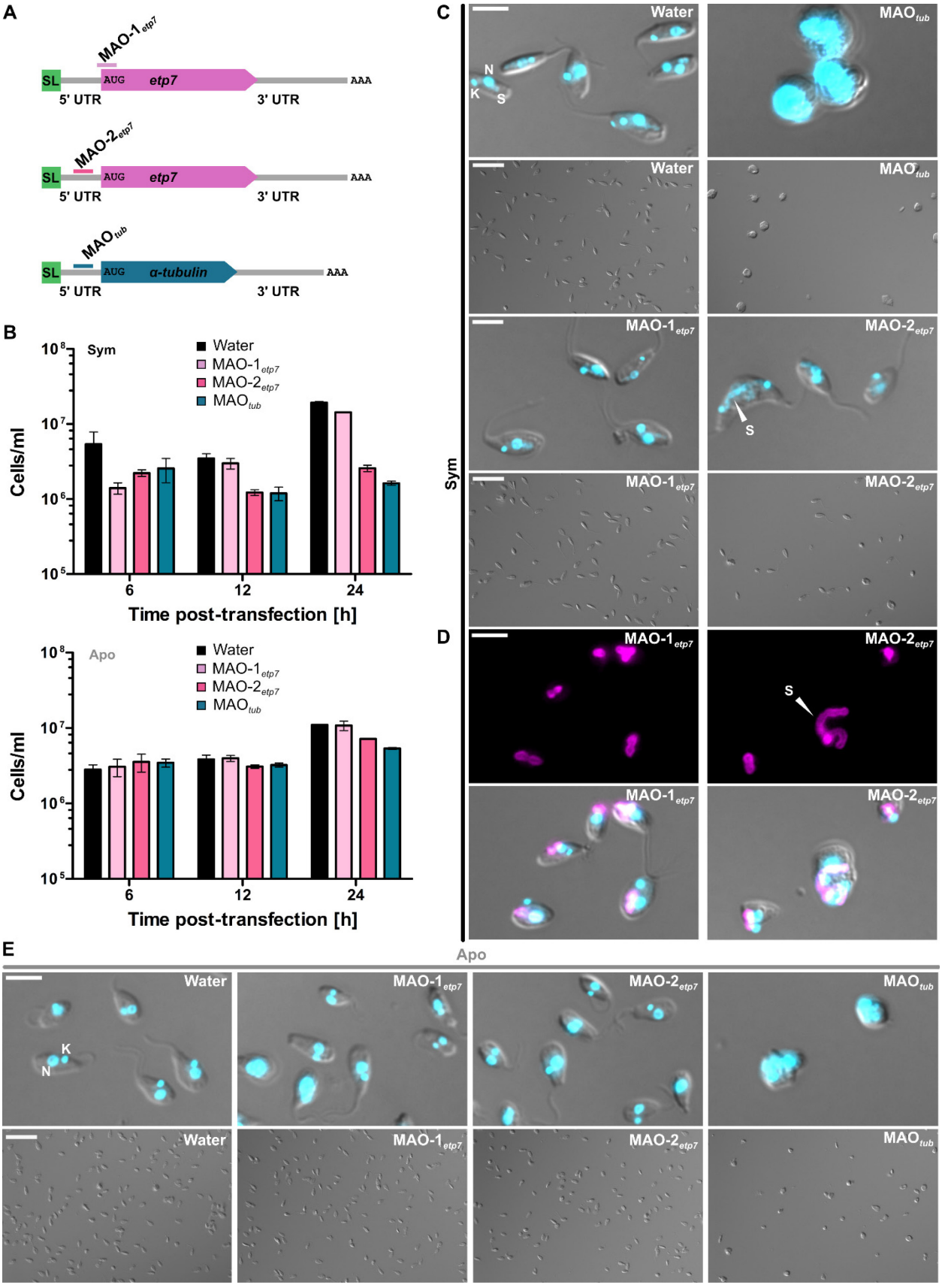
A
MAO-1etp7
SL
AUG
etp7
AAA
5' UTR
3' UTR
MAO-2etp7
SL
AUG
etp7
AAA
5' UTR
3' UTR
MAOtub
SL
AUG
α-tubulin
AAA
5' UTR
3' UTR
B
Sym
Water
MAO-1etp7
MAO-2etp7
MAOtub
Cells/ml
10^8
10^7
10^6
10^5
6
12
24
Time post-transfection [h]
Apo
Water
MAO-1etp7
MAO-2etp7
MAOtub
Cells/ml
10^8
10^7
10^6
10^5
6
12
24
Time post-transfection [h]
C
Sym
Water
MAOtub
N
K
S
Water
MAOtub
MAO-1etp7
MAO-2etp7
S
MAO-1etp7
MAO-2etp7
D
Apo
MAO-1etp7
MAO-2etp7
S
MAO-1etp7
MAO-2etp7
E
Water
MAO-1etp7
MAO-2etp7
MAOtub
K
N
Water
MAO-1etp7
MAO-2etp7
MAOtub

Figure 2.3: Effects of knockdowns of ETP7 in the symbiotic and the aposymbiotic *A. deanei*.

A: Approximate binding sites of MAOs on the mRNA of *etp7* and *α-tubulin*. **B:** Cell counts of symbiotic (upper graph) and aposymbiotic (lower graph) cells are shown at 6 h, 12 h, and 24 h post-transfection. Plotted are mean and standard deviation from three technical replicates. **C:** Detail (upper) and overview (lower) micrographs of symbiotic cells treated with water, MAO-1_{etp7}, MAO-2_{etp7} or MAO_{tub} 24 h post-transfection are shown. Merge of the Hoechst 33342 signal and DIC for detail as well as DIC for overview micrographs are displayed. **D:** The symbiotic *A. deanei* strain expressing the ES marker mScarlet-ETP1 treated with MAO-1_{etp7} and MAO-2_{etp7} 24 h post-transfection are displayed. The mScarlet channel alone (upper micrograph) and merge of mScarlet, Hoechst 33342, and DIC channels (lower micrograph) are shown. **E:** Same treatments for the aposymbiotic strain as in Fig. 2.3 C. Scale bars are 5 µm for detail and 25 µm for overview images. Abbreviations: S, symbiont; K, kinetoplast; N, nucleus; SL: splice leader and UTR: untranslated region. Arrowhead indicates the symbiont.

Next, to visualize the ES better, I used a symbiotic cell line which expresses the ES marker mScarlet-ETP1. After the knockdown with both MAOs, similar observations as in Wt cells were made. Cells treated with MAO-2_{etp7} resulted in tubular chains of the ES in distorted host cells, however, MAO-1_{etp7} did not show any phenotypes 24 h post-transfection (Fig. 2.3 D). Furthermore, the overview images of cells with both treatments can be seen (Fig. 2.4 A). Cells treated with MAO_{tub} against α-tubulin (positive control) resulted in big roundish host cells with all DNA compartments clumped together in the symbiotic Wt strain. This was observed to a similar extent in the aposymbiotic Wt strain, however, due to its smaller cell and organelle sizes as well as the lack of the ES, the phenotype appeared slightly less severe. Together the data suggests that ETP7 contributes to the ES division.

Lastly, to understand if the knockdown of ETP7 affects FtsZ localization, I repeated transfection of the symbiotic strain expressing the ES marker m-Scarlet-ETP1 with MAO-2_{etp7}. Subsequently, I observed that the localization/recruitment of FtsZ was unaffected. FtsZ still forms multiple foci at the ESDS in the background of ETP7 knockdown (Fig. 2.4 B) suggesting that the bacterium-encoded FtsZ works independent of host-encoded ETP7 in *A. deanei*.

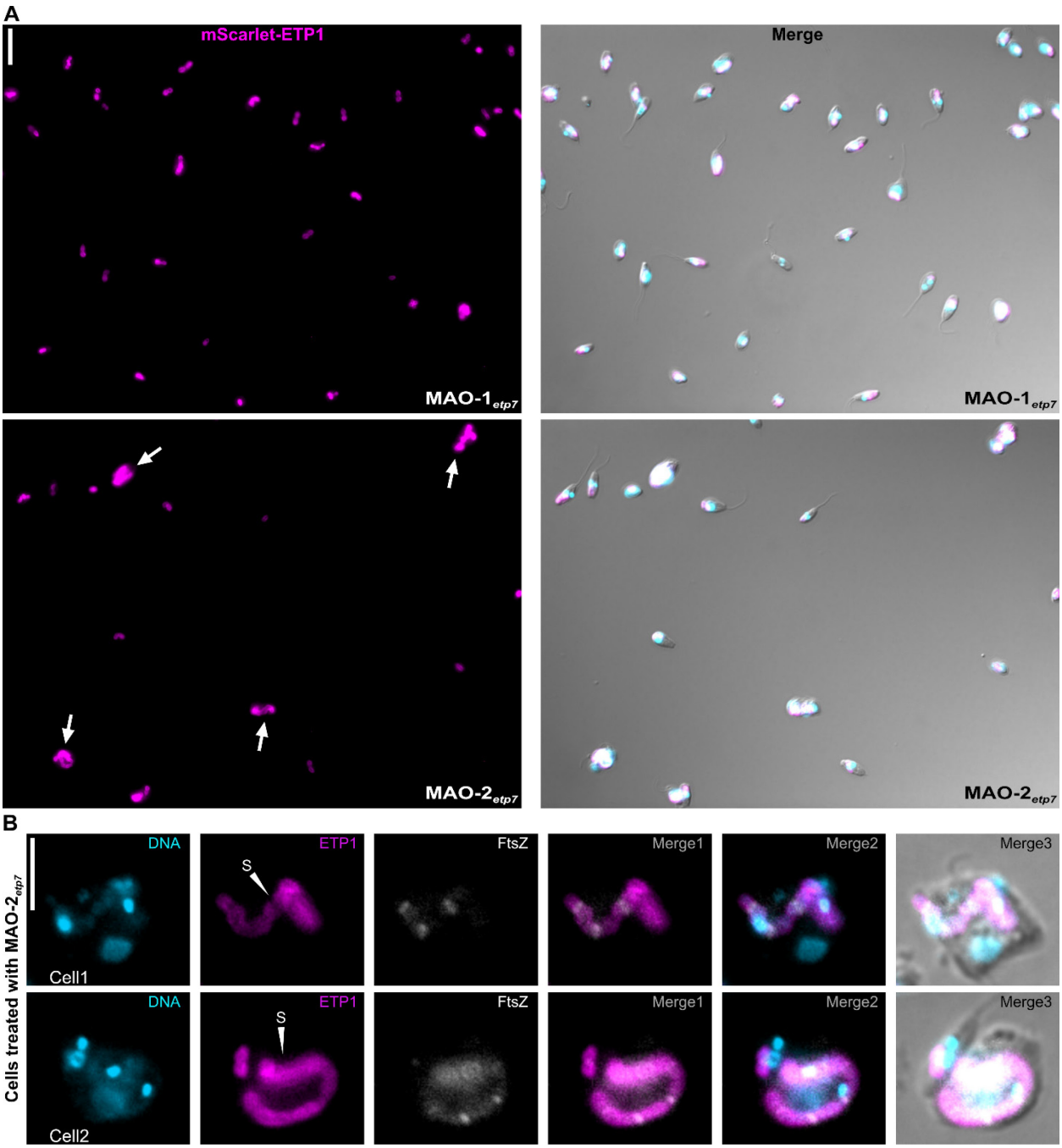

Figure 2.4: Effects of knockdowns of ETP7 in the symbiotic *A. deanei* strain.

A: *A. deanei* cells expressing the ES marker mScarlet-ETP1 treated with MAO-1_{etp7} (upper panel) and MAO-2_{etp7} (lower panel) are shown. The mScarlet channel alone (on the left) and a merge of mScarlet, Hoechst 33342 for DNA in cyan, and DIC channels (on the right) are displayed. Arrows indicate the formation of tubular ES chains. Scale bar is 10 µm. **B:** Cells expressing the ES marker treated with MAO-2_{etp7} followed FtsZ staining by IFA are shown. Merge 1 shows the alignment of mScarlet for ETP1 and IFA signal for FtsZ. Merge 2 shows the alignment of Hoechst 33342, ETP1, and FtsZ. Merge 3 shows the alignment of DNA, ETP1, FtsZ, and DNA. White arrowhead indicates a tubular chain of the ES. Scale bar is 5 µm. Abbreviation: S, symbiont.

2.2.3. Reduced ETP1 dosage results in morphological change in the ES

To explore the cellular function of ETP1 (aim II), a heterozygous *etp1* deletion mutant was previously generated by Sofia Kokkori (Kokkori, 2018, PhD thesis). During my PhD work, I performed fluorescence *in situ* hybridization (FISH) using the 16S rRNA-specific Eub338 probe (Amann et al., 1990 and Fuchs et al., 2007) to stain the ES. I observed that in many mutant cells, the ES appeared roundish or small peanut-shaped (Fig. 2.5 A, middle image and Fig. 2.5 C, highlighted by yellow arrowheads on the right image) or lost (Fig. 2.5 A, right image and Fig. 2.5 C, highlighted by black arrowhead on the right image) compared to the regular peanut-shaped ES in Wt cells (Fig. 2.5 A, left image and Fig. 2.5 C, highlighted by green arrowhead on the left image). Furthermore, to understand the severity of *etp1* deletion, I performed a quantification of phenotypes and found out that the heterozygous *etp1* mutant cell line showed less cells in normal stage (~ 72%, cells with a single bacterium) compared to Wt cells (~ 90%) (Fig. 2.5 B). Interestingly, I observed that ~ 20% of the mutant cells lost the ES compared to 0.8% in Wt cells. Lastly, I also observed a slower growth rate of mutant cells than Wt cells (data not shown). The data indicates that ETP1 might be required for maintenance of normal ES morphology by regulating the PG synthesis in *A. deanei*.

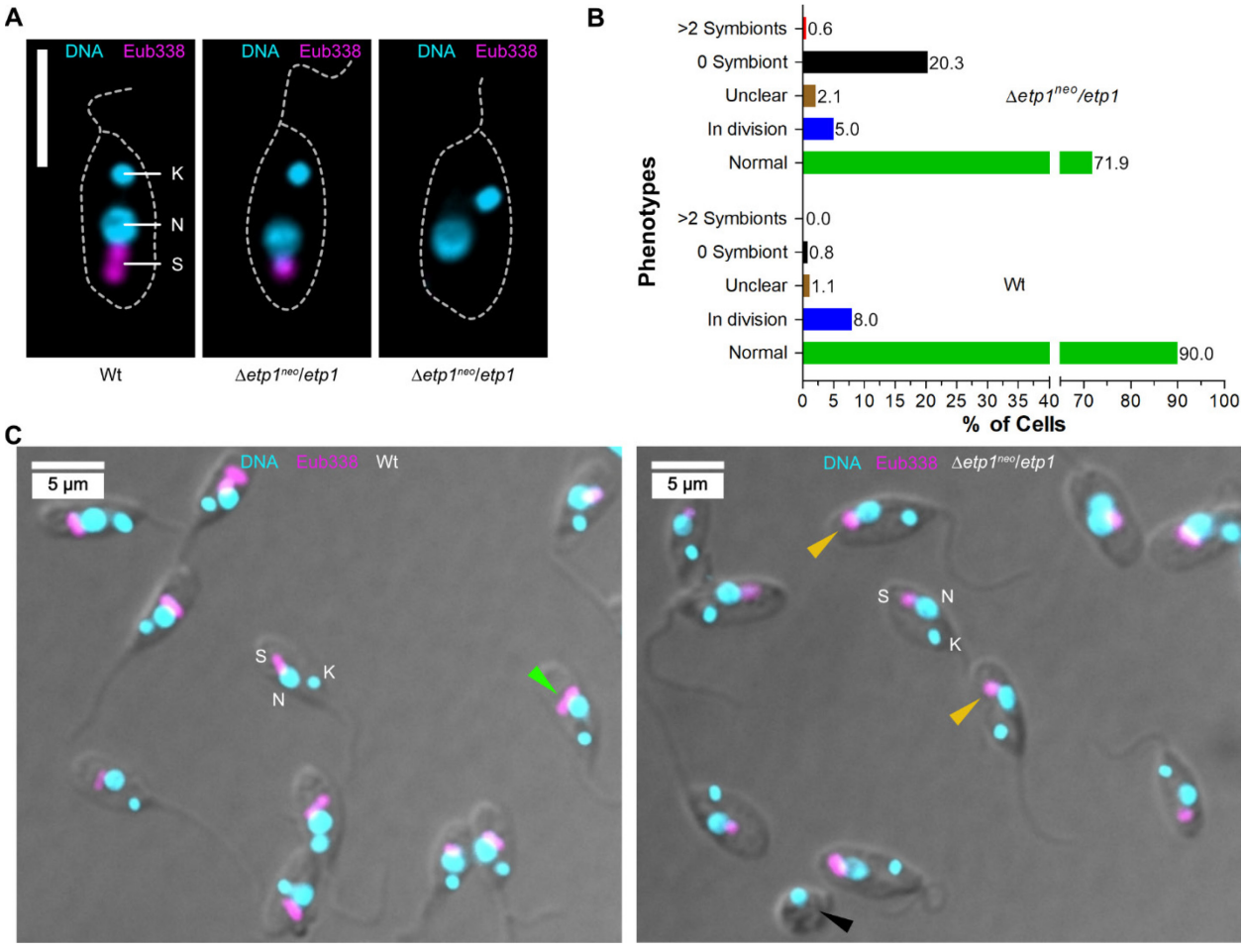

Figure 2.5: Heterozygous *etp1* deletion mutant cells shows round-shaped ES.

A: The Wt cell showing a regular peanut-shaped ES (left image) and heterozygous *etp1* mutant showing a roundish ES (middle image) or loss of the ES (right image). **B:** Quantification of phenotypes from heterozygous *etp1* mutant cells compared to Wt cells in around 500 cells in the mid-log phase following FISH and Hoechst 33342 staining, and epifluorescence microscopy. **C:** An overview image of the Wt (on the left) and the heterozygous *etp1* mutant (on the right) showing ES shapes in many cells. Abbreviations: K, kinetoplast; S, symbiont and N, nucleus. Green, yellow, and black arrow heads show regular peanut-shaped, round, and loss of the ES, respectively. Cyan, DNA staining with Hoechst 33342. Magenta, the ES staining using 16S rRNA-specific Eub338 bacterial probe by FISH. Scale bar: 5 µm for both, single cell and overview images.

2.2.4. ETP5 likely controls ES division and segregation of host cellular structures

ETP5 (an ortholog of KMP11) is conserved across trypanosomatids. To investigate if the subcellular localization of ETP5 orthologs from closely related non-symbiont harboring trypanosomatids, such as *T. brucei* and *L. donovani* is same as *Ad*ETP5 when heterologously expressed in *A. deanei*, I generated *A. deanei* cell lines expressing the recombinant protein *Tb*ETP5-eGFP (*δ-ama*$^{tbetp5\text{-}egfp}$/*δ-ama*) and *Ld*ETP5-eGFP (*δ-ama*$^{ldetp5\text{-}egfp}$/*δ-ama*) in the background of the ES marker mScarlet-ETP1 (*γ-ama*$^{mScarlet\text{-}etp1}$/*γ-ama*). Both recombinant proteins showed similar subcellular localization to *Ad*ETP5-eGFP (*δ-ama*$^{adetp5\text{-}egfp}$/*δ-ama*) in *A. deanei* (Fig. 2.6 A). They localized at the anterior part of the cell with a dot-like structure next to the kinetoplast (shown by a white arrowhead), which was previously shown to be the BB for *Ad*ETP5 (Morales et al., 2023, Fig. S2 C). Additionally, they were associated with the kinetoplast and nucleus. Interestingly, both orthologs were also localized to the ES envelope suggesting the conserved nature of this protein in trypanosomatids (Fig. 2.6 A).

Next, to study the cellular function of ETP5 in *A. deanei* (aim II), deletion mutants were generated. ETP5 has four copies of its gene on each of the two chromosome sets (on Chromosome 7), referred here as *etp5* locus 1 and locus 2. Previously, a heterozygous *etp5* mutant was generated by replacing all four copies of *etp5* on locus 1 with a hygromycin resistance marker by Jan Wieneke. Further, I generated two knockouts where I replaced the first two copies and the last two copies independently by a neomycin resistance marker on locus 2 (Fig. 2.7 B and D; Fig. 5.1 A), leaving two copies (termed here as 'partial homozygous mutants'). All strains were verified by touch down PCR as well as Southern blot analysis (Fig. 2.7 A and C). The heterozygous and both partial homozygous *etp5* mutants grew slower than the Wt strain (Fig. 2.6 B). Further observation of these mutant cells with microscopy upon FISH revealed that ES division and segregation of host cellular structures including the ES appears to be impaired. The ES formed an elongated chain especially in the partial homozygous *etp5* mutant cells (Fig. 2.6 C). In addition, some mutant cells also lost the ES. Lastly, to understand the severity of the *etp5* deletion, I quantified division phenotypes in around 500 cells. Subsequently, I observed that mutant cells showed lesser number of cells in normal stage (1K1N1S), more cells in division (1K1N2S, 2K1N2S, and 2K2N2S) and more cells with loss of the ES (1K1S0S) compared to Wt cells. Importantly, some mutant cells (~ 1-3%) also appeared in tubular chains that were not detected in the Wt strain. These cells with division phenotypes were more abundant in the partial homozygous mutants than in the heterozygous *etp5* mutant (Fig. 2.6 D).

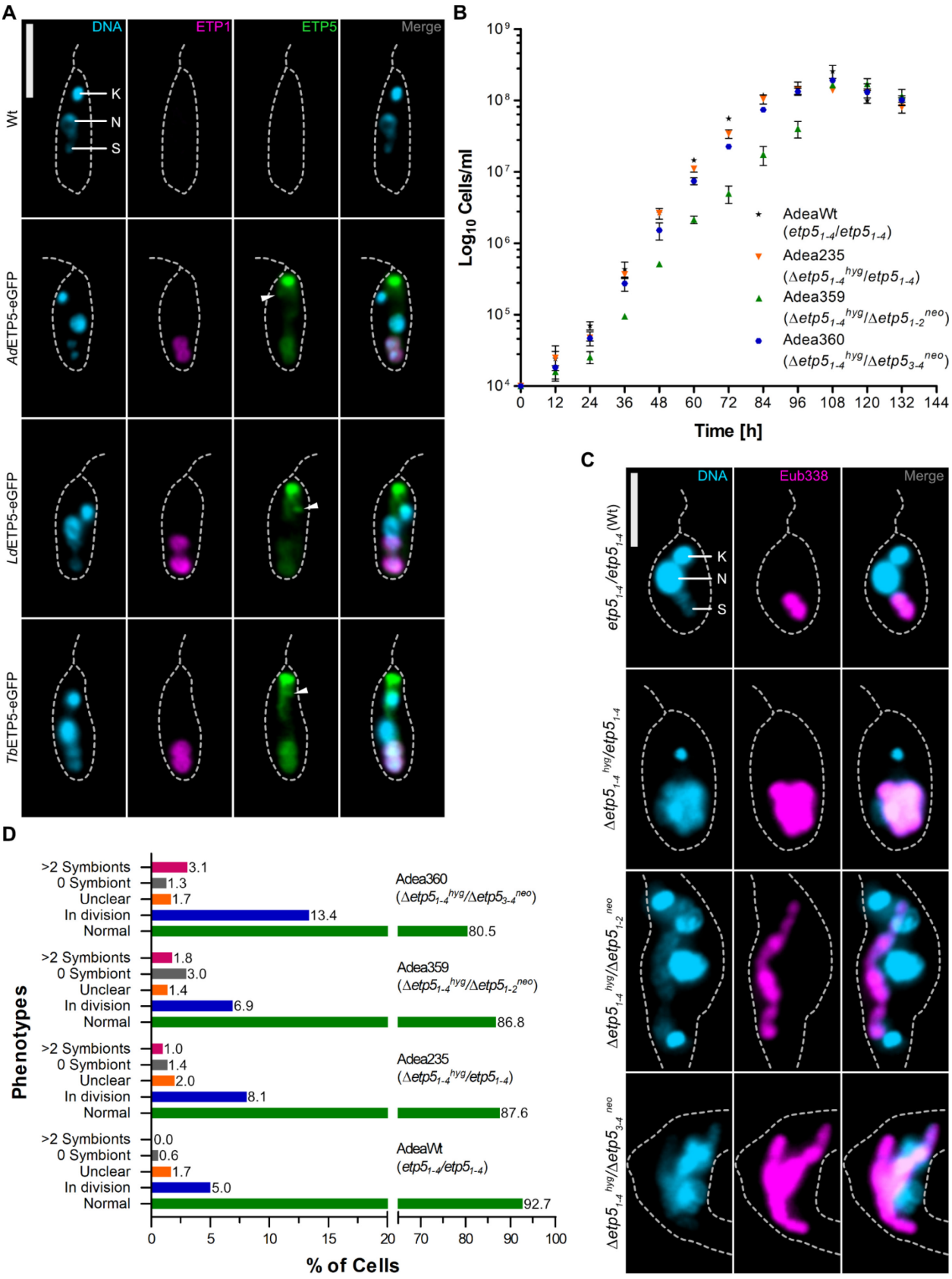
A
DNA
ETP1
ETP5
Merge
Wt
K
N
S
AdETP5-eGFP
LdETP5-eGFP
TbETP5-eGFP
B
Log10 Cells/ml
Time [h]
AdeaWt
(etp5 1-4/etp5 1-4)
Adea235
(Δetp5 1-4 hyg/etp5 1-4)
Adea359
(Δetp5 1-4 hyg/Δetp5 1-2 neo)
Adea360
(Δetp5 1-4 hyg/Δetp5 3-4 neo)
C
DNA
Eub338
Merge
etp5 1-4/etp5 1-4 (Wt)
Δetp5 1-4 hyg/etp5 1-4
Δetp5 1-4 hyg/Δetp5 1-2 neo
Δetp5 1-4 hyg/Δetp5 3-4 neo
D
Phenotypes
>2 Symbionts
0 Symbiont
Unclear
In division
Normal
Adea360
(Δetp5 1-4 hyg/Δetp5 3-4 neo)
Adea359
(Δetp5 1-4 hyg/Δetp5 1-2 neo)
Adea235
(Δetp5 1-4 hyg/etp5 1-4)
AdeaWt
(etp5 1-4/etp5 1-4)
% of Cells

Figure 2.6: Subcellular localization of *etp5* and characterization of *etp5* knockouts in *A. deanei*.

A: Subcellular localization studies of the recombinant *Ld*ETP5, *Tb*ETP5, and *Ad*ETP5 by epifluorescence microscopy. Merge image shows the alignment of the Hoechst 33342, mScarlet, and eGFP channels. **B:** Measurements of growth rate of *etp5* knockout cells recorded over a period of 132 h plotted logarithmically. The bars show mean and standard deviation from three biological replicates. **C:** Representative images of *etp5* knockout cells acquired by epifluorescence microscopy following FISH staining using the 16S rRNA-specific probe Eub338. **D:** Quantification of cell phenotypes of *etp5* mutant cells in around 500 cells (images from Fig. C). The merged image shows the alignment of the Hoechst 33342 and Cy3 channels. $etp5_{1\text{-}4}$ indicates presence of all four copies of *etp5* on each of the two loci. $etp5_{1\text{-}4}^{hyg}$ shows replacement of all four copies of *etp5* on locus 1 by a hygromycin resistance marker. $etp5_{1\text{-}2}{}^{neo}$ or $etp5_{3\text{-}4}{}^{neo}$ indicate replacement of the first two or the last two copies of *etp5* on locus 2 by a neomycin resistance marker, respectively. Abbreviations: K, kinetoplast; N, nucleus and S, endosymbiont. The Hoechst 33342-stained DNA is shown in cyan, eGFP in green, and mScarlet or Cy3 in magenta. Broken grey line indicates cell border. Scale bar: 5 µm.

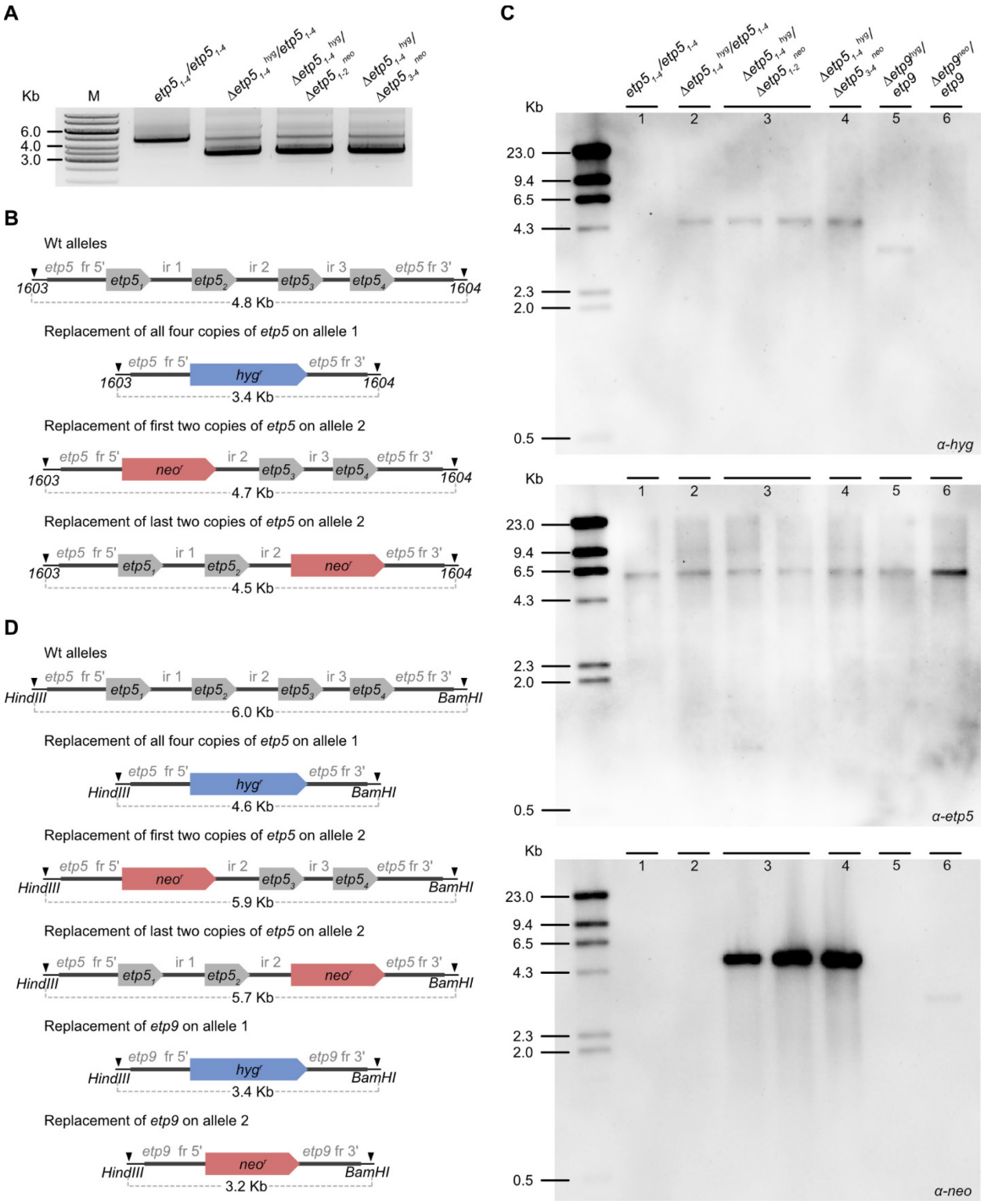

Figure 2.7: Generation and verification of *etp5* knockout cells in *A. deanei*.

A: Agarose gel showing verification of *etp5* mutant cells by touch down PCR. **B:** Maps of the recombinant *etp5* locus used for PCR verification. Primers used for PCR verifications were 1603 and 1604 that bind in

the genomic region (outside the inserted cassette). **C:** Verification of *etp5* knockout cells by Southern blot using *α-neo*, *α-hyg*, and *α-etp5* probes. **D:** Maps of the recombinant *etp5* locus digested using restriction enzymes for verification. Abbreviations: fr, flanking region; ir, intergenic region, M, DIG-labelled DNA marker; *hyg/hyg*^{r}, *hygromycin* resistance marker and *neo/neo*^{r}, *neomycin* resistance marker. *etp5*$_{1-4}$ indicates presence of all four copies of *etp5* on each of the two loci. *etp5*$_{1-4}^{hyg}$ shows replacement of all four copies of *etp5* on locus 1 by a hygromycin resistance marker. *etp5*$_{1-2}$ ^{neo} or *etp5*$_{3-4}$ ^{neo} indicate replacement of the first two or the last two copies of *etp5* on locus 2 by a neomycin resistance marker, respectively. Black arrowhead indicates the primer binding site/cutting site for restriction enzyme(s). The grey dotted line indicates the expected band size of the PCR/digested fragment. As positive control, *etp9* mutant strains were used for Southern blot analysis.

2.2.5. Host-encoded SNAREs localize on the vesicle in the close vicinity of the ES

SNARE proteins are mainly involved in mediating vesicle fusion to specific target membranes. Interestingly, in our previous mass spectrometry studies (Morales et al., 2023), we found three nucleus-encoded proteins in the ES fraction. The first protein CAD2221024.1 harbors a regulated-SNARE-like domain as per its annotation and was termed here ‘SNARE1’. The second and third candidates CAD2220808.1 and CAD2219450.1 were both annotated as vesicle transport SNARE proteins (v-SNARE) and named as ‘SNARE2’ and ‘SNARE3’, respectively (see Table 2.1).

Table 2.1: Annotation of host-encoded ES-associated SNARE proteins.

Protein ID	Annotation
CAD2221024.1 (SNARE1)	Regulated-SNARE-like domain/Synaptobrevin, putative [*Angomonas deanei*]
CAD2220808.1 (SNARE2)	Vesicle transport v-SNARE protein N-terminus/Snare region anchored in the vesicle membrane C-terminus, putative [*Angomonas deanei*]
CAD2219450.1 (SNARE3)	Vesicle transport v-SNARE protein N-terminus/Snare region anchored in the vesicle membrane C-terminus/Sec20, putative [*Angomonas deanei*]

To investigate their subcellular localization in *A. deanei* (related to aim III), Lindsay Dittmann (ITiM student, 2022) and I generated mScarlet fusions of SNARE proteins. The mScarlet fusion was made at the N-terminal end of the protein as the C-terminal end has been reported to harbor a transmembrane helix (TMH) (Criado et al., 1999; Sieber et al., 2006 and Han et al., 2017). The mScarlet-SNARE1 showed a very weak cytosolic fluorescence signal compared to Wt cells. However, SNARE2 and SNARE3 fusions showed a strong mScarlet signal at the anterior part of the cell, probably at the flagellar pocket, (i.e. the region where endocytosis and exocytosis takes place in trypanosomatids (Field & Carrington, 2009 and Demmel et al., 2014). Additionally, both proteins also showed in some cells weak dot-like structures mainly near the peanut-shaped ES that was stained with Hoechst 33342 (marked by white arrowheads in Fig. 2.8 A).

Next, to better visualize the localization of SNARE2 and SNARE3 with respect to the ES, I further generated cell lines expressing eGFP-ETP1 (the ES marker) in the background of mScarlet-SNARE2 or mScarlet-SNARE3. Subsequently, I observed that both recombinant proteins sometimes showed a sharp signal, likely representing a SNARE protein-containing vesicle, in the close vicinity of the ES or possibly fusing with the ES envelope, marked by white arrowheads. In

addition, both fusion proteins show a strong fluorescence signal at the anterior part of the cell (Fig. 2.8 B).

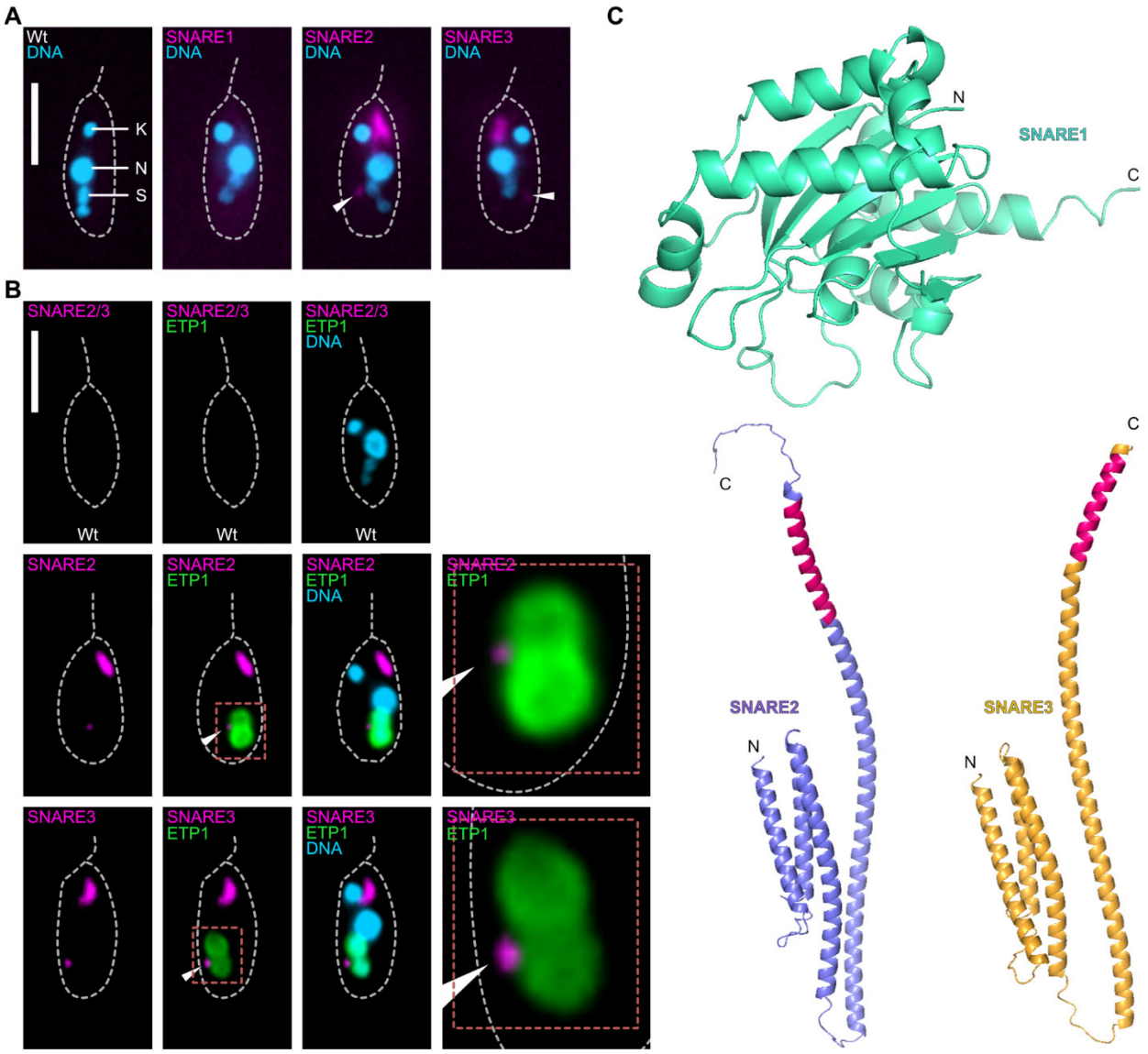

Figure 2.8: Subcellular localization of host-encoded SNARE proteins and their structural analysis.

A: Subcellular localization of SNARE1, SNARE2, and SNARE3 in the background of Hoechst 33342-stained DNA. Each image shows the merge of Hoechst 33342 and mScarlet channels. The white arrowhead emphasizes a dot-like structure near the ES DNA signal. **B:** Subcellular localization of SNARE2 and SNARE3 in the background of eGFP-ETP1 marking the ES envelope. For each set of images of SNARE/Wt, the image on the left shows the mScarlet channel, the image in the middle shows the merge of mScarlet and eGFP channels (for these images, a closeup is shown on the far right, with brown dotted box), and the image on the right shows the merge of mScarlet, eGFP, and Hoechst 33342 channels. The white arrowhead highlights a dot-like structure near the peanut-shaped ES, which is marked by eGFP-ETP1. **C:** Structural analysis of SNARE1, SNARE2, and SNARE3 showing the presence or absence of a predicted TMH (magenta). The N and C in the predicted structures indicate protein termini. Abbreviations: K, kinetoplast;

N, nucleus and S, endosymbiont. Hoechst 33342-stained DNA is shown in cyan, eGFP in green, and mScarlet in magenta. Broken grey lines indicate cell border. Scale bar: 5 µm.

Finally, to test for the presence of signal peptides or TMHs and their position in different SNARE proteins, I performed TMH and signal peptide prediction using TMHMM 2.0 and TargetP 2.0, respectively, as well as structure prediction using ColabFold. SNARE1 harbors no signal peptide or TMH (data not shown) and showed a different predicted structure (contains α-helices and β-sheets) than SNARE2 and SNARE3 (Fig. 2.8 C). In comparison, SNARE2 and SNARE3 both possess a TMH (in magenta) at the C-terminal end of the protein but no signal peptide (data not shown) and showed a similar predicted structure (contain α-helices only) to each other (Fig. 2.8 C) and importantly to other SNARE proteins (Adnan et al., 2019 and Stein et al., 2009) that are known to carry out vesicle fusions.

2.2.6. Potential ES/organellar proteins showed distinct subcellular localization

In a collaborative study with Prof. Dr. Yurchenko Vyacheslav (University of Ostrava, Czech Republic) and Prof. Dr. Julius Lukeš (Czech Academy of Sciences, Czech Republic), whose labs generated proteome data using localization of organelle proteins by isotope tagging (LOPIT) analysis of *A. deanei*, we identified a plethora of potential candidate proteins for several cellular compartments including the ES, Golgi apparatus, glycosomes, mitochondria, ER, and others. In our lab, we tested the subcellular localization of these potential candidates in *A. deanei* ATCC PRA 265. For this purpose, we generated eGFP fusions at the N- and or C-terminus of each candidate with a linker (GS_5) between the protein of interest (POI) and eGFP (Fig. 5.1 A). I contributed to the study by analyzing the subcellular localization of potential cytosol-, ES-, and Golgi apparatus-localized candidates (manuscript in preparation).

Firstly, to study the subcellular localization of three potential cytosol candidates, eGFP fusion was made at the C-terminus of each protein. The recombinant protein CAD2221863.1-GS_5-eGFP showed a weak cytosolic fluorescence signal (based on a cut-off file generated using Wt cells) (Fig. 2.9 A, upper image). CAD2220061.1-GS_5-eGFP showed no fluorescence signal at all (Fig. 2.9 A, middle image). Lastly, the recombinant protein for the cytosol marker (used as a positive control for the cytosol candidates in the LOPIT analysis) CAD2222212.1-GS_5-eGFP showed a stronger cytosolic signal (Fig. 2.9 A, lower image) compared to CAD2221863.1. As expected, all three candidates showed no organelle-targeting signal peptide or TMH (data not shown).

Secondly, to study the subcellular localization of three potential ES candidates, eGFP fusions were made at both the C- and N-termini of each protein. The recombinant protein CAD2219020.1-GS_5-eGFP showed a dot-like signal co-localizing at the kinetoplast and a stripes-like signal throughout the cell, typical for mitochondrion-localized protein (Fig. 2.9 B, upper left and see Morales et al. 2016). However, eGFP-GS_5-CAD2219020.1 showed a weak dot-like signal at one pole of the kinetoplast and in the cytosol in some cells (Fig. 2.9 B, upper right). CAD2214939.1-GS_5-eGFP showed no fluorescence signal at all (Fig. 2.9 B, middle left), however, interestingly, eGFP-GS_5-CAD2214939.1 appeared to localize at the ES envelope (Fig. 2.9 B, middle right). Lastly, CAD2218596.1-GS_5-eGFP and eGFP-GS_5-CAD2218596.1, both resulted in a lack of fluorescence signal anywhere in the cell (Fig. 2.9 B, lower left and right, respectively). In line with above data, *in silico* studies revealed that CAD2219020.1 harbors a mitochondrial-targeting signal

at its N-terminus with a TMH in the middle of the protein. However, the remaining two candidates, CAD2214939.1 and CAD2218596.1, showed no organelle-targeting signal peptide or TMH.

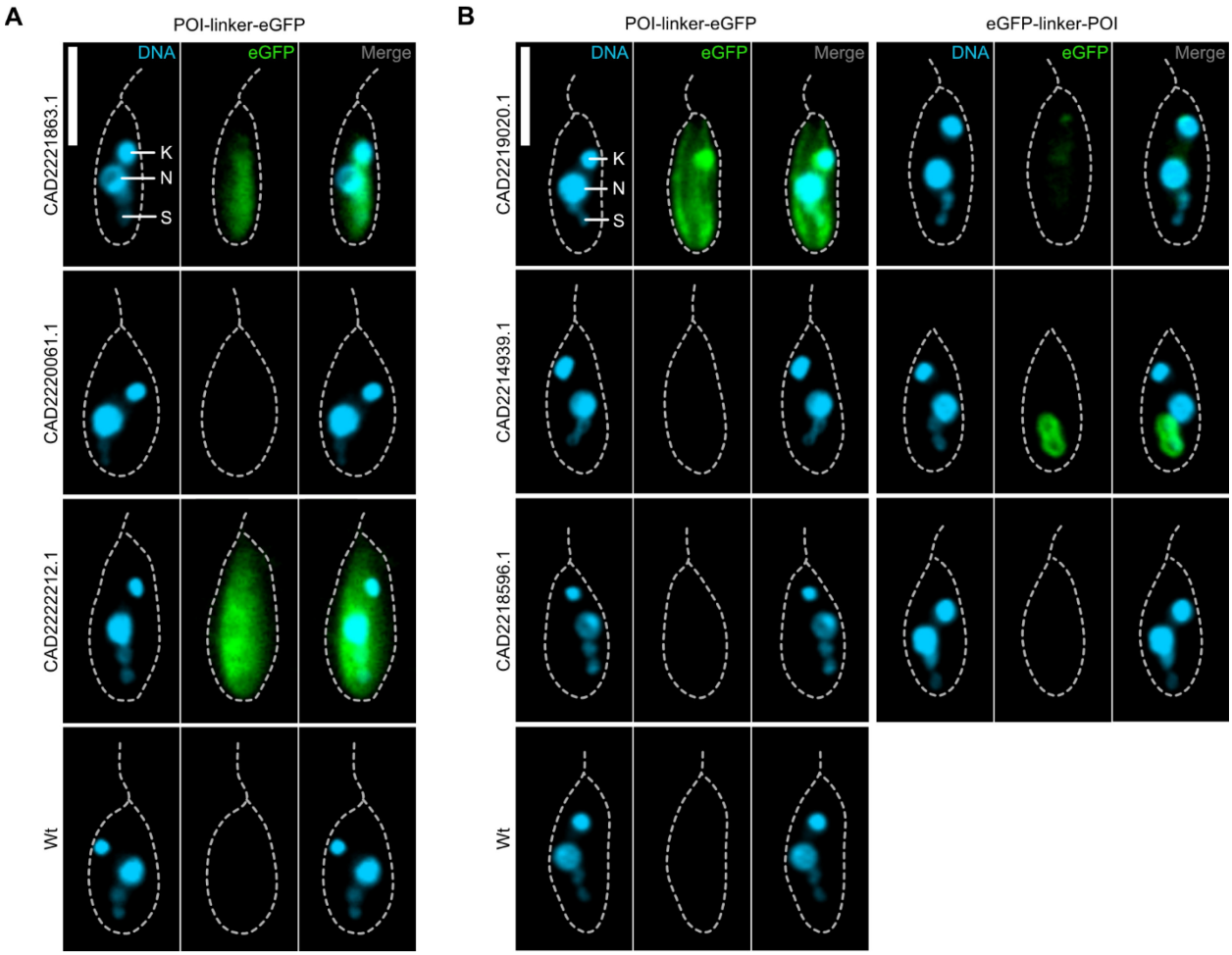

Figure 2.9: Localization of potential cytosol and ES candidates from LOPIT analysis.

A: Subcellular localization of potential cytosol candidates in *A. deanei*. **B:** Subcellular localization of potential ES-targeted candidates. Abbreviations: K, kinetoplast; N, nucleus; S, endosymbiont and POI, protein of interest. Hoechst 33342-stained DNA is shown in cyan and eGFP in green. Merge shows the alignment of eGFP and Hoechst 33342 channels. Broken grey lines indicate cell borders. Scale bar: 5 µm.

Finally, to study the subcellular localization of three potential Golgi candidates, eGFP fusions were made at the C- and/or N-termini of each protein. Subsequently, I observed that the recombinant protein CAD2219791.1-GS_5-eGFP showed a dot-like fluorescence signal next to the nucleus (Fig. 2.10 A, upper left). However, eGFP-GS_5-CAD2219791.1 showed no signal in the cell (Fig. 2.10 A, upper middle). The recombinant Golgi marker protein (used as a positive control for the Golgi candidates in the LOPIT analysis), CAD2212931.1-GS_5-eGFP showed no fluorescence signal (Fig. 2.10 A, lower left), however, eGFP-GS_5-CAD2212931.1 showed a strong signal next to the nucleus (Fig. 2.10 A, lower middle). Lastly, for the recombinant protein CAD2221326.1-GS_5-eGFP, no fluorescence signal was detected (Fig. 2.10 A, upper right).

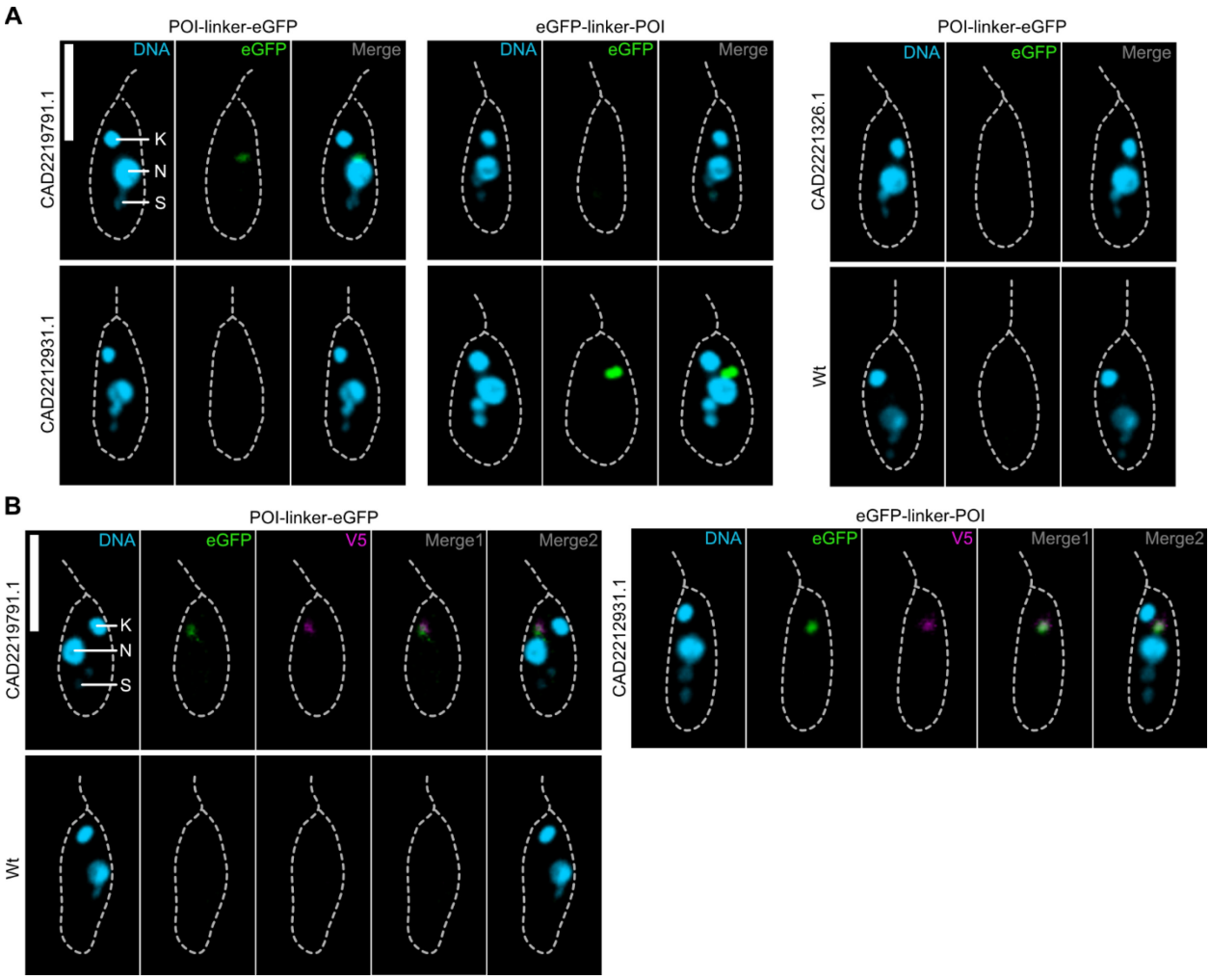

Figure 2.10: Localization of potential Golgi apparatus candidates from LOPIT analysis and their co-localization with trans-Golgi marker ARL1.

A: Subcellular localization of potential Golgi apparatus-targeted candidates in *A. deanei*. **B:** Co-localization of Golgi apparatus candidates with trans-Golgi marker ARL1-V5. Hoechst 33342-stained DNA is shown in cyan, eGFP in green, and V5 in magenta. Merge 1 shows the alignment of eGFP and V5, and merge 2 of eGFP, V5, and Hoechst 33342 channels. Broken grey lines indicate cell borders. Scale bar: 5 µm.

Next, to test if the subcellular localization observed for CAD2219791.1 and CAD2212931.1 is corresponding to a Golgi localization, I performed a co-localization study by IFA using the previously established trans-Golgi marker ARL1 in *A. deanei* (Morales et al., 2023). Recombinant proteins of both potential Golgi candidates CAD2219791.1 and CAD2212931.1 (Fig. 2.10 B, upper left and upper right, respectively) showed a partial co-localization with the recombinant ARL1-V5. Furthermore, *in silico* studies revealed that CAD2219791.1 possesses a TMH at the N-terminus and a signal peptide (with a low prediction score), CAD2212931.1 showed a TMH at the C-terminus with no signal peptide, and CAD2221326.1 showed no TMH or signal peptide.

3. Discussion

In eukaryotic cells, organelles such as mitochondria and plastids must be structurally and functionally maintained. This includes that the cells must have means to divide their organelles at a suitable timepoint and segregate them into daughter cells. Failure to do so would result in cell death. Interestingly, this level of control has not only been reached for mitochondria and plastids that evolved over 1.5 billion years ago but is also observed in cells with newly acquired organelles such as *P. chromatophora* with their two photosynthetic chromatophores and *B. bigelowii* with its nitrogen-fixing organelle 'nitroplast' (Singer et al., 2017 and Coale et al., 2024). Additionally, eukaryotic cells harboring tightly integrated endosymbionts must ensure correct vertical transmission to daughter cells upon division to maintain the growth, physiology, and integrity of the host cell. During my doctoral research, I unveiled that various host-encoded ETPs play distinct roles related to ES division and segregation in *A. deanei* as discussed below.

3.1. Host-encoded proteins form a division machinery controlling ES division

In free-living bacteria, FtsZ is an essential component of the bacterial cell division machinery. In eukaryotes with mitochondria and chloroplast, the presence of FtsZ varies. FtsZ is maintained by the chloroplast of most organisms such as the chrysophyte *Mallomonas,* red and green algae, and land plants (TerBush et al. 2018). However, FtsZ in the chloroplast is encoded by the nuclear genome and its presence alone does not appear to initiate chloroplast division (Arimura, & Tsutsumi, 2002). In comparison, it is lost from the mitochondria of animals, higher plants, fungi, and Apicomplexa members such as *Plasmodium* sp., however, is still retained by many organisms, for instance, *Dictyostelium* spp. and *Chlamydomonas reinhardtii* (Gilson et al., 2003 and Leger et al. 2015). The loss of FtsZ from mitochondria of many organisms suggests that at some point during evolution, its role became dispensable, and its function was taken over by nuclear-encoded DRPs and other effector proteins (Margolin, 2005).

Of the eukaryotic origin, the most important host-encoded proteins involved herein are the members of DSPs such as dynamins, mainly involved in endocytosis and cytokinesis, and DRPs involved in division of mitochondria and plastids. Though DSPs have a range of functions across organisms, their conserved motifs such as G domain and HBs are suggestive of similar mechanisms for their assembly and functions. A common mode of action includes GTP binding followed by its hydrolysis leading to a change in the protein conformation and lastly the vesicle or organelle fission.

In *A. deanei* ATCC PRA-265 (the strain under study), FtsZ is present and still encoded by the ES, and localized at the ESDS (Maurya et al., 2025). However, it was earlier reported to be diffused in the ES cytosol in another *A. deanei* strain (Motta et al., 2004). Due to the essential nature of the ES in *A. deanei* ATCC PRA-265 and unavailability of genetic tools to modify the ES, it remains difficult to delete *ftsZ* gene and study its effect. Furthermore, other essential division genes were observed to be lost from the ES of *A. deanei* and other members of the subfamily Strigomonadinae (Motta et al., 2013 and Maurya et al., 2025) suggesting that the ES cannot divide on its own and must involve nucleus-encoded effectors such as the dynamin-like protein ETP9, ETP2 (a mostly intrinsically disordered protein), and ETP7 (annotated as 'Phage tail lysozyme').

Importantly, I found by IFA that all three nucleus-encoded proteins (ETP9, ETP2, and ETP7) exhibit cell cycle-dependent localization together with the ES-encoded FtsZ. Furthermore, in the overexpression cell line, the recombinant ETP2 appears to be the first protein to reach the ESDS followed by FtsZ (detected by IFA). However, the endogenously tagged ETP2 seems to appear at the ESDS at the same time point with FtsZ (Maurya et al., under review). This sequentially leads to the arrival of the recombinant ETP9, both the overexpressed and endogenously expressed versions (Maurya et al., 2025). Interestingly, the recombinant ETP7 (overexpression cell line) seems to be always detectable over the ES cytosol, however, it enriches at the ESDS during the bacterial elongation.

Interestingly, the generation of heterozygous *etp9* mutants resulted in abnormal division phenotypes, for instance, some mutant cells with the elongated ES and many cells with the loss of the ES in the symbiotic, but not in the aposymbiotic strain (Maurya et al., 2025). These phenotypes might result from, for example, improper division and subsequent segregation of the ES in parental cell where one giant/distorted host cell with a chain of endosymbionts can give rise to multiple cells with loss of the ES sequentially. Further, symbiotic heterozygous *etp9* mutant cells also showed fewer cells in the 'normal' stage (1K1N1S) and more in division stages (1K1N2S, 2K1N2S, and 2K2N2S) compared to the Wt cells. This might be due to slower growth of the mutant cells where cells are specifically affected by division impairment of the ES leading to more cells in division stages as the cell cycle is tightly synchronized and the ES is the first one to divide. Importantly, the generation of homozygous *etp9* mutants was apparently lethal in the symbiotic but not in the aposymbiotic strain. Remarkably, knockdown using two independent MAOs clearly showed that most of the MAO-treated cells (in both MAO treatments) contain long tubular ES in completely distorted host cells only in the symbiotic strain demonstrating that ETP9 is indispensable for ES division in *A. deanei*.

Like ETP9, another novel nucleus-encoded protein, ETP2, also localized at the ESDS (Morales et al., 2023), was found to be important for ES division and segregation (Maurya et al., under review). Interestingly, both heterozygous and homozygous *etp2* mutant cell lines can be generated in the symbiotic strain. Though heterozygous mutant cells did not show any noticeable division phenotypes, homozygous mutant cells were severely affected, for instance, many homozygous *etp2* mutant cells showed long tubular ES or with the loss of the ES suggesting its role in ES division and segregation. Like ETP9, knockdown using MAO against *etp2* also resulted in similar phenotypes in symbiotic cells suggesting its important role in ES division.

Like ETP9 and ETP2, the third nucleus-encoded protein ETP7, annotated as a 'Phage tail lysozyme' (sequence identity, 24%), was also localized at the ESDS (Morales et al., 2023). Comparison of the predicted structure of ETP7 resulted in ~ 93% similarity between the C-terminal part of ETP7 and the N-terminal domain of a cell wall degrading enzyme (gp13) from the bacteriophage ϕ 29 (Xiang et al., 2008 and Morales et al., 2023). This suggests that ETP7 might be involved in the PG hydrolysis.

Based on the annotation, structure, and localization of ETP7 at the ESDS and periphery of the ES especially in elongated ES (Fig. 2.2 A-B, ETP7 stage 1-2), it appears that it has a dual function, a role in ES division and the bacterial elongation. For the latter, PG hydrolases such as CwlO and

LytE endopeptidases have been shown to break PG cross-links and support cell growth and elongation in *B. subtilis* (Hashimoto et al., 2012).

To explore the cellular function(s) of ETP7, in our previous studies, heterozygous *etp7* mutant cell lines could easily be generated, and cells did not show any noticeable phenotypes. However, all efforts to generate homozygous mutant cell lines proved unsuccessful (Morales et al., 2023). In this case, replacement of both *etp7* alleles relied on the same approach, the use of upstream and downstream flanking regions of the gene for homologous recombination. This method might not succeed (especially for important or essential genes) in replacing the second *etp7* allele and rather could result in replacing the first inserted cassette. In future, it would be worth trying another approach, for example, the one described for *etp2* (Maurya et al., under review).

Due to the time limits and difficulty in the generation of homozygous *etp7* mutant cells to study its functional role in *A. deanei*, I used two non-overlapping MAOs, the first one mainly binding at the start of *etp7* gene (MAO-1_{etp7}) and the second one in the 5' UTR of *etp7* (MAO-2_{etp7}) (Fig. 2.3). The knockdown of ETP7 by MAO-2_{etp7} resulted in the formation of tubular chains of the bacterial endosymbionts in some distorted host cells suggestive of its contribution to ES division (Fig. 2.3 and Fig. 2.4). The effect of ETP9 knockdown appeared to be the strongest followed by ETP2, and ETP7 under the tested laboratory conditions. Similar to ETP7, DipM (a nucleus-encoded PG hydrolase) has been shown to hydrolyze the PG layer during chloroplast division in Glaucophytes and some Viridiplantae (Miyagishima et al., 2014). However, cells treated with MAO-1_{etp7} did not result in any obvious phenotypes. One possible explanation could be the effectiveness of translation inhibition by MAO-1_{etp7}. It has been reported that MAOs binding (on the mRNA) near the start codon or immediately upstream are more effective than the ones binding far upstream, in the coding sequence or far downstream the start codon (Moulton, 2017). Unfortunately, due to a short length of 5' UTR of *etp7*, designing more non-overlapping MAOs was difficult. Together, the data in hand suggests that ETP7 contributes to ES division in *A. deanei*, however, further investigations of its functionality is needed.

In sum, it appears that three nucleus-encoded proteins ETP9, ETP2, and ETP7 form a host-derived ES division machinery that might have evolved specifically in *A. deanei* and other members of the subfamily Strigomonadinae. The division machinery likely involves additional components both originating from the ES and its host making it of dual genetic origin.

3.2. ETP1 likely plays a role in the structural maintenance of the ES

RodZ is a morphogenic protein that is conserved in most bacteria and plays a universal role in cell morphogenesis (Daniel & Errington, 2003; Alyahya et al., 2009 and Philippe et al., 2014). In rod-shaped bacteria, RodZ has a dispensable role in the maintenance of cell morphology together with MreB which is essential for cell shape maintenance (Bendezú & de Boer, 2008). MreB is conserved only in rod-shaped bacteria but not in cocci-shaped bacteria where RodZ has been shown to act as scaffold protein (Lamanna et al., 2022). Interestingly, all endosymbionts of symbiont-harboring trypanosomatids in the subfamily Strigomonadinae (including *A. deanei*) lack the *rodZ* gene but harbor *mreB* (Maurya et al., 2025). It has earlier been shown that deletion of *rodZ* in rod-shaped bacteria such as *E. coli*, *C. crescentus*, *B. subtilis*, and *D. grandis* results in round to small rod-shaped bacteria (Shiomi et al., 2008; Alyahya et al., 2009; Bendezú et al.,

2009; Muchová et al., 2013 and Morita et al., 2019). Furthermore, it was found that overproduction of RodZ results in elongated or swollen *E. coli* cells (Bendezú et al., 2009). Lastly, cells lacking RodZ have also been shown to grow slower than the Wt strain (Shiomi et al., 2013).

Interestingly, host-encoded ETP1 has been shown previously to localize at the envelope of the ES in *A. deanei* (Morales et al., 2023). Like RodZ in rod-shaped bacteria, *etp1* mutant showed round to small peanut-shaped bacteria (Fig. 2.5 A and C) with cells growing slower than Wt cells (data not shown). Together, the data suggests that ETP1 likely plays a role in cell shape maintenance of the ES in *A. deanei* likely by regulation the PG synthesis, in the absence of RodZ. It will be important to investigate the exact localization of ETP1 in the ES envelope and gain further evidence of its functionality.

3.3. ETP5 likely supports ES division and controls segregation of cellular structures

Segregation of organelles in different organisms is regulated by a number of components. In eukaryotes, segregation of the spindle pole body/BB/centrosome is mediated by Centrins, that are also involved in cell division (Salisbury et al., 1988; Spang et al., 1993; Errabolu et al., 1994; Satisbury, 1995 and Wolfrum & Salisbury,1998). Similarly, *Tb*Cen1, *Tb*Cen2, and *Tb*Cen3 from *T. brucei* are involved in organelle segregation such as the kinetoplast, BB, nucleus, and the Golgi with an additional role in cytokinesis (Selvapandiyan et al., 2007; Lacomble et al., 2010 and Selvapandiyan et al., 2012). Furthermore, microtubules in trypanosomes control the positioning, segregation, and cytokinesis of organelles (Robinson et al., 1995). Lastly, KMP11 has been shown to be important for the BB segregation and cytokinesis in *T. brucei* (Li & Wang, 2008).

Interestingly, ETP5 (an ortholog of KMP11) has previously been shown to localize at the anterior part of the cell including the BB, associates with the kinetoplast and nucleus, envelope of the ES and weakly associates with cytoskeletal structures in *A. deanei* (Morales et al., 2023), Further, orthologs of ETP5 (*Ad*ETP5) from non-symbiont-harboring trypanosomatids such as *Ld*ETP5 from *L. donovani* and *Tb*ETP5 from *T. brucei* show similar subcellular localization as *Ad*ETP5 when expressed in *A. deanei* (Fig. 2.6 A) suggesting that ETP5 is indeed conserved in trypanosomatids and might play similar roles. Moreover, it suggests that the ability of ETP5 to interact with the ES did not evolve specifically in *A. deanei* but appears to depend on a preexisting property of the protein, likely its ability to bind to specific membranes (Lim et al., 2017). Importantly, knockouts of *etp5* resulted in slower growth of mutant cells with some cells showing a tubular ES formation in giant host cells whereas some cells had lost the ES (Fig. 2.6 B and C), like in ETP9. The data suggests that ETP5 appears to contribute to the ES division likely by interacting with microtubules. Moreover, in line with the above data and previous reports, for example, the depletion of KMP11 using RNAi led to the inhibition of segregation of the BB and cytokinesis (Li et al., 2008 and Li and Wang, 2008), ETP5 also seems to be involved in segregation of host cellular structures including the ES likely by interacting with organelle lipids (Lim et al., 2017), and perhaps in cytokinesis.

3.4. Host-encoded SNAREs might be involved in protein import to the ES

SNARE or SNARE-like proteins have been shown to mediate vesicle fusion across the tree of life including intracellular pathogens (Murungi et al., 2014; Flanagan et al., 2015; Venkatesh et al., 2017 and Chatterjee et al., 2024) suggesting the conservation of this process.

In *A. deanei*, to gain a tight control over the ES, host-encoded proteins are targeted to the ES. In our previous studies (Morales et al., 2023), we found two unique host-encoded proteins targeted to the ES, named ETP3 and ETP8, that -based on the confocal images- appear to cross the ES membranes (IM and OM) and reach the ES cytosol. In addition, these two proteins were found to localize also in the Golgi apparatus. In our lab, other colleagues are working on an experimental validation for protein import into the ES. However, my work focused on testing if host-derived ES-associated SNARE proteins identified in the previous study in ES fractions might play a role in the import of ETP3 and ETP8 into the ES.

Two of the nucleus-encoded recombinant SNARE proteins SNARE2 and SNARE3 (both annotated as v-SNAREs) showed the strongest fluorescence signal at the anterior part of the cell, probably at the flagellar pocket (Fig. 2.8 A-B). This region is well-known for endocytosis and exocytosis to occur in trypanosomatids (Field & Carrington, 2009 and Demmel et al., 2014). Similarly, other SNARE proteins have been reported to be present on the Golgi, ER, lysosomes, plasma membrane, vacuoles, and other vesicles in eukaryotes (Tao-Cheng et al., 2015 and Han et al., 2017). The prediction of 3D structures of SNARE2 and SNARE3 showed an extended α-helical structure and a TMH present at the C-terminus (Fig. 2.8 C). Similar α-helical structures of other SNAREs have been reported earlier with the presence of a TMH at the C-terminus, for example, Sec22 from different organisms (Stein et al., 2009 and Adnan et al., 2019). Based on this data, it appears that SNARE2 and SNARE3 mediate vesicle fusion in *A. deanei*.

Interestingly, the additional presence of weak dot-like fluorescent signals in the close proximity of the ES or apparently fusing to the ES envelope suggests that SNARE2 and SNARE3 might also be playing roles in fusion of host vesicles to the ES, and thus, possibly the import of ETP3 and ETP8. Importantly, the OM of the ES is derived from the bacterium and therefore, host vesicle fusion to the ES is unlikely. Interestingly, vesicle fusion to the ES/organelle in other systems have been reported such as in aphids and *P. chomatophora* (Nowack & Grossman, 2012; Shigenobu & Stern, 2013 and Nakabachi et al., 2014). However, in these systems, the OM of the ES/organelle is host-derived, making vesicle fusions more likely. Eukaryotic membranes are structurally (due to their membrane composition), functionally (harbor fusion proteins such as SNAREs), and evolutionarily adapted for vesicle fusion whereas bacterial membranes are structurally resistant, generally lack fusion proteins, and do not use vesicle-based compartmentalization internally. Nonetheless, possible events of host-derived vesicle fusions to the ES in the members of Strigomonadinae have previously been shown in TEM images (Chang, 1974). An ongoing project in our lab aims at testing by TEM if these vesicular structures, that might represent vesicle fusion events with the ES, are indeed SNARE2 or SNARE3-positive and studying if both proteins mediate import of ETP3 and ETP8 (aim III).

The third and last SNARE protein is SNARE1. Based on the observed subcellular localization (a very weak cytosolic fluorescence signal) an involvement in vesicle targeting to the ES is currently not supported (Table 2.1 and Fig. 2.8).

3.5. The identification of the subcellular localization of proteins by LOPIT method

LOPIT is a spatial proteomic approach used to determine the subcellular localization of proteins on a large scale. The method uses cell fractionation combined with quantitative mass spectrometry analysis and isotope labeling. Based on the comparison of protein abundance across subcellular fractions, a high-resolution map of protein distribution within the cell can be created. Using this approach, we identified potential organellar candidates and tagged them with the eGFP at N- and/or C-terminal ends to confirm their fluorescence-based subcellular localization in *A. deanei* (manuscript in preparation). For this, tagging vectors containing the eGFP were already established in our lab that helped cloning the gene easily and studying a large number of potential organellar candidates.

For the potential ES candidates, one of the recombinant proteins CAD2219020.1-GS_5-eGFP showed a similar fluorescence pattern (Fig. 2.9 B, upper left) as it was observed in *A. deanei* expressing the eGFP tagged with a mitochondrial signal peptide (Morales et al., 2016) suggesting for a mitochondrial localization of CAD2219020.1, in line with the predicted mitochondrial signal peptide. This would also explain the cytosolic localization of eGFP-GS_5-CAD2219020.1, in which the N-terminal mitochondrial targeting signal was blocked (Fig. 2.9 B, upper right). Interestingly, the localization of eGFP-GS_5-CAD2214939.1 (Fig. 2.9 B, middle right) is the same as observed for the established ES marker ETP1 in *A. deanei* (Morales et al., 2016) demonstrating that CAD2214939.1 is indeed an ES-localized protein that has been renamed ‘ETP10’. This newly discovered ETP by LOPIT is now being functionally characterized in the lab of our collaboration partner Julius Lukes.

Also of the potential Golgi candidates, two of the recombinant proteins (CAD2219791.1-GS_5-eGFP and eGFP-GS_5-CAD2212931.1) could be confirmed as Golgi-localized based on partial co-localization with the *A. deanei* trans-Golgi marker ARL1 (Fig. 2.10 B, upper left and upper right, respectively) (Morales et al., 2023). Additionally, the absence of fluorescence signal for the eGFP-GS_5-CAD2219791.1 and CAD2212931.1-GS_5-eGFP might be explained by the presence of a TMH at their N-terminal and C-terminal ends, respectively which can interfere with the proper localization of recombinant proteins to the Golgi apparatus. Subsequently, this can result in mis-localization of proteins, for example, to the cytosol which is difficult to detect for low abundance proteins. In conclusion, the data suggests that CAD2219791.1 and CAD2212931.1 are indeed Golgi candidates.

The absence of fluorescence signal for the remaining recombinant proteins of the potential cytosol, ES, and Golgi candidates, could be caused by several factors, for instance, low mRNA or protein stability, low expression combined with a dispersed distribution throughout the cell, low fluorescence signal in the organelle. The expression of the fusion protein could be further tested by Western blot analysis.

3.6. Conclusions

To sum up, the endosymbiotic theory states that an archaeal cell internalized a free-living α-proteobacterium which gave rise to mitochondrion. Later, some of the resulting eukaryotic cells also acquired a cyanobacterial ES which eventually evolved into the chloroplast (Bodył & Mackiewicz, 2013). Over time, many adaptations occurred in these bacterial endosymbionts that turned them into true organelles. These evolutionary changes in an organelle include extreme genome reduction, synchronized cell cycle between the host and the organelle, the EGT where bacterial genes were transferred to the nucleus, and, most importantly, massive protein import from the host to the organelle leading to extensive nuclear control over the organelle. Since these evolutionary events occurred more than 1.5 billion years ago, it is very difficult to reconstruct these environments in the lab to study them and answer some of the key questions. However, there are a few endosymbiotic associations or organellogenesis events known today that have recently occurred between eukaryotes and wide lineages of prokaryotes (Moya et al., 2008). Two good examples are *P. chromatophora* with two photosynthetic chromatophores and *B. begelowii* with a nitroplast (Singer et al., 2017 and Coale et al., 2024), however, there are some challenges with these systems such as slow growth rate and difficulty in genetic manipulations.

Therefore, I used another recent endosymbiotic system, the trypanosomatid *A. deanei* which harbors a single β-proteobacterial ES with a reduced genome size of 0.8 Mb. Importantly, the ES has lost most of the essential components of its divisome and, hence, the ability to divide autonomously (Motta et al., 2013 and Maurya et al., 2025). Interestingly, our previous research identified seven host-encoded proteins transported to the ES termed ETPs and one EGT-derived protein OCD (Morales et al., 2023). Previously, it has been shown that the cell cycles of the *A. deanei* and its ES are tightly synchronized (Motta et al., 2010). Further, I showed that the host effector dynamin-like protein ETP9 and the ES-encoded FtsZ show a cell cycle-dependent localization (Maurya et al., 2025). Importantly, in the absence of many essential ES division genes, ETP9 plays an indispensable role in ES division in the symbiotic strain. In addition, I (together with other researchers) could show that ETP2 also plays an important role in (Maurya et al., under review) and ETP7 contributes to ES division, and both show a cell cycle-dependent localization. Lastly, I could show that ETP1 might be important for structural maintenance of the ES, ETP5 for ES division and segregation of host cellular structures upon host cell division, and SNARE proteins might be involved in protein import into the ES via a vesicle fusion-based mechanism. Together, these results indicate that the ES of *A. deanei* evolved far beyond endosymbiosis and could now be termed as ‘an early-stage organelle’.

4. Outlook

This PhD thesis investigated the function of several newly identified ETPs especially ETP9, ETP2, and ETP7 that are localized at the ESDS using fluorescent reporter fusion, knockout, and knockdown approaches. The results obtained revealed that these proteins compensate for the loss of essential ES division genes in *A. deanei*.

In line with the above data, it would be of great interest to find additional components involved in ES division, the molecular mechanism behind the constriction and fission of the double membrane system surrounding the ES as well as the regulation of this process. To find possible interaction partners involved in ES division, proximity labeling (for transient or weak interactions), co-immunoprecipitation (for stable interactions) followed by mass spectrometry, pull down assay (for confirming direct interactions) or yeast-two-hybrid assay (for high throughput screening) can be performed. Interestingly, to investigate if ETP9, ETP2, and ETP7 interact with each other, I performed yeast-two-hybrid assay during my MOI IV lab rotation with Prof. Dr. Johannes Hegemann (HHU). The study resulted in unconclusive outcomes and will need further investigations using any of the above suggested approaches.

Further, it would be important to uncover the exact subcellular localization of the DS-localized proteins (ETP9, ETP2, and ETP7). Is ETP9 associated with the OM of the ES? Is ETP7 in the periplasm? Where does ETP2 localize? For this, high resolution microscopies such as an expansion microscopy protocol can be performed to better understand the mechanism controlling ES division. I performed an iterative ultrastructure expansion microscopy during my stay abroad studies at Institute Pasteur with Prof. Dr. Philippe Bastin. Subsequently, I observed that the ES as well as other host cellular structures can be isotropically expanded, however, the protocol needs further optimization to boost the fluorescence signals for studying recombinant ETPs in *A. deanei*.

Next, it would be crucial to further understand the functional role of ETP7. For this, an alternative approach to disrupt the second *etp7* allele as described for *etp9* and *etp2* (Maurya et al., 2025 and Maurya et al., under review) can be tried. In addition, the exploration of mutational studies on the catalytic amino acid residues of ETP7 (Morales et al., 2023) might help understand its role.

Moreover, for the newly identified ETP10 by LOPIT analysis and fluorescence microscopy, it would be nice to explore its functional role, for example, by generating knockout mutant cell lines. Similarly, to study the cellular function of the ES marker ETP1, heterozygous mutant cell line was previously generated, all efforts to generate homozygous *etp1* mutant remained futile. It is important to employ another approach such as disrupting the second allele of *etp1* in the background of heterozygous mutant cell line as described for the generation of homozygous *etp2* mutant (Maurya et al., under review).

In addition, other colleagues strive to understand if ETP3 and ETP8 are imported inside the ES. However, my work focused on testing if host-derived ES-associated SNARE proteins play a role in the import of both ETPs. Currently, our lab aims at testing by TEM if SNARE2 or SNARE3-positive vesicles close or fusing to the ES mediate import of ETP3 and ETP8.

Interestingly, to study endosymbiosis events, an alternative approach to natural endosymbiotic systems would be to use synthetic endosymbiotic systems, which have been generated in a number of cases (Cournoyer et al., 2022; Giger et al., 2024 and Hu et al., 2024). A good example is the induction of a novel endosymbiosis by introducing bacteria in fungi (Giger et al., 2024). It remains, however, difficult for the hosts to establish complex integration and maintain the artificially transformed bacteria as endosymbionts for longer duration. Therefore, naturally evolving recent endosymbiotic systems that can be genetically modified such as the members of Strigomonadinae (*Angomonas*, *Kentomonas*, and *Strigomonas* spp.) can be used. Another symbiont-harboring trypanosomatid that can be used is *N. esmeraldas*. However, it maintains a varying number of multiple endosymbionts per host cell with less genome reduction of the ES and, importantly, the ES cell cycle is not synchronized with the one of the host (Zakharova et al., 2021).

In comparison to trypanosomatids without endosymbionts such as *Trypanosoma* spp. and *Leishmania* spp., symbiont-harboring trypanosomatids have limited genetic tools established, for instance, no conditional gene expression systems yet fully operational. One of the reasons is the presence of an integrated ES in symbiont-harboring trypanosomatids which makes them less genetically tractable than model trypanosomatids. Interestingly, we found that all ETPs identified in *A. deanei* represented a combination of pre-existing trypanosomatid proteins (for example, ETP5) and evolved specifically in *A. deanei* or the members of Strigomonadinae (for example, ETP9). For the former candidates, investigating the functional role in the cell becomes easier.

Finally, I believe that *A. deanei* has become a magnificent model system to study endosymbiosis and organellogenesis due to the listed reasons. First, it is a non-pathogenic unicellular eukaryote with a single ES per host cell. Secondly, it grows in simple and inexpensive medium with a doubling time of ~ 6 h. Thirdly, the genome of the host and its ES has been sequenced. Additionally, genetic tools have been developed. Lastly, the ES has evolved with some organellar features such as massive genome reduction, cell cycle synchronization, protein import and EGT. I believe that the scientific advances made within this model system during this study help other researchers answer some of the key questions related to the organelle evolution.

5. Methods

Methods described below belong to unpublished data in this thesis.

5.1. Media, cultures, and growth conditions

All media, microbial strains, and growth conditions are described earlier (Maurya et al., 2025).

5.2. Construction of plasmids

For the construction of pAdea246, ir 2 fragment (used as *etp5* fr 3') was amplified from *A. deanei* Wt genomic DNA using a primer combination 1829/1830 (see Table 5.1) and the backbone (pUMA 1467, *etp5* fr 5', *neo*^{r}) from pAdea212 (see Fig. 5.1) using primers 1827/1828. Both fragments were assembled using the Gibson method as described earlier (Gibson et al., 2009 and Morales et al., 2023). Similarly, pAdea247 was generated by the amplification of ir 2 (used as *etp5* fr 5') from the genomic DNA using a primer combination 1833/1834 and the backbone (*neo*^{r}*, etp5* fr 3', pUMA 1467) from pAdea212 using primers 1831/1832, and assembled with the Gibson approach.

For the generation of pAdea367, pAdea366, and pAdea365, genes for CAD2221024.1, CAD2220808.1, and CAD2219450.1 were amplified from the genomic DNA using primer combinations 2545/2546, 2547/2548, and 2549/2550, respectively. The amplified gene fragments were cloned into tagging vector pAdea268 with the N-terminal mScarlet using previously described the Golden Gate approach (Engler et al., 2008 and Morales et al., 2023). For the generation of pAdea441 and pAdea442, genes for CAD2220808.1 and CAD2219450.1 were amplified from the genomic DNA using primer combinations 3228/3229 and 3230/3231, respectively and cloned into pAdea268 by the Golden Gate method.

For the generation of pAdea423, pAdea425, and pAdea429, genes for CAD2219020.1, CAD2214939.1, and CAD2218596.1 were amplified from *A. deanei* genomic DNA using primer combinations 3140/3141, 3134/3135, and 3207/3208, respectively. These gene inserts were cloned into a tagging vector pAdea235 with a C-terminal *egfp* (with respect to gene of interest to be cloned) using the Golden Gate approach. Similarly, for the generation of pAdea424 and 426, genes for CAD2219020.1 and CAD2214939.1 were amplified from the genomic DNA using primer pairs 3151/3152 and 3145/3146, respectively. These inserts were cloned into a tagging vector pAdea043 (see Fig. 5.1) with an N-terminal *egfp* (with respect to gene of interest) using the Golden Gate approach. For the construction of pAdea428, gene for CAD2218596.1 was amplified from the genomic DNA using primers 3149/3150 and backbone (pUMA 1467, *δ-ama* fr 5', *neo*^{r}*,* gapdh ir, *δ-ama* fr 3') from pAdea340 using a combination of primers 3147/3148. Both fragments were assembled using the Gibson assembly approach.

All plasmids were verified by sequencing (Microsynth AG, Balgach, Switzerland) using primers listed in Table 5.1. All verified plasmids were linearized by restriction enzyme(s) (see Fig. 5.1) for transfection in *A. deanei*.

5.3. Generation of transgenic cell lines of *A. deanei*

Transgenic *A. deanei* cell lines were generated as described earlier (Morales et al., 2023).

Table 5.1: All primers used in this study.

All primers used in this study for the plasmid generation, sequencing, PCR verification of transgenic cell lines, and probe synthesis for Southern blot analysis.

Internal primer no.	Primers used for the plasmid generation Primer sequence (5'-3')	DNA fragment amplified	Final plasmid generated
1829	TTCTTGACGAGTTCTTCTAAAGGGGAAACGATGATTGAAA	ir 2	pAdea246
1830	GATCCGATATCTAGACCTGCGATGAATAGAGAAAAGGGTTTGG		
1827	AACCCTTTTCTCTATTCATCGCAGGTCTAGATATCGGATC	pUMA 1467, *etp5* fr 5', *neo*^{r}	
1828	TTTCAATCATCGTTTCCCCTTTAGAAGAACTCGTCAAGAAGG		
1833	GTGAATTCGAGCTCACCTGAAGGGGAAACGATGATTGAAA	ir 2	pAdea247
1834	AATCCATCTTGTTCAATCATGATGAATAGAGAAAAGGGTTTGG		
1831	AACCCTTTTCTCTATTCATCATGATTGAACAAGATGGATTGC	*neo*^{r}, *etp5* fr 3', pUMA 1467	
1832	TTTCAATCATCGTTTCCCCTTCAGGTGAGCTCGAATTCAC		
2545	GGTCTCACAAGATGAAATTATACGCGATTGTCATC	*CAD2221024.1* gene	pAdea367
2546	GGTCTCATTTATTACATGACAGAACAGCAACC		
2547	GGTCTCACAAGATGACAACACTCCTGCAAACCTACG	*CAD2220808.1* gene	pAdea366
2548	GGTCTCATTTATTACACCACGTCGGTGGGGG		
2549	GGTCTCACAAGATGTCTAGTCTATTCTCCGC	*CAD2219450.1* gene	pAdea365
2550	GGTCTCATTTATTACTTTAGCTTCACATAAATAATAAGC		
3140	GGTCTCACCAAATGATGCGTCGTGTGTTCTC	*CAD2219020.1* gene	pAdea423
3141	GGTCTCATCACTGATCCTGATCCTGATCCTGATCCTGATCCTAGA GGGATGTTACCGTGCTTC		
3151	GGTCTCACAAGGGATCAGGATCAGGATCAGGATCAGGATCAATG ATGCGTCGTGTGTTCTCT	*CAD2219020.1* gene	pAdea424
3152	GGTCTCATCTTTTATAGAGGGATGTTACCGTGCTTC		
3134	GGTCTCACCAAATGTCGATTGACACCGGTGT	*CAD2214939.1* gene	pAdea425
3135	GGTCTCATCACTGATCCTGATCCTGATCCTGATCCTGATCCCACG TATGCCATATAGTCACTTCC		
3145	GGTCTCACAAGGGATCAGGATCAGGATCAGGATCAGGATCAATG TCGATTGACACCGGTGT	*CAD2214939.1* gene	pAdea426
3146	GGTCTCATCTTTTACACGTATGCCATATAGTCACTTCC		
3149	GGATCAGGATCAGGATCAGGATCAGGATCAATGACAGAGGAGGA GAAACTCTCC	*CAD2218596.1* gene	pAdea428
3150	ACGTCTCTCTCCCCCCTCTTTTACAGAGAGAATGGGTTGTAGCC		
3147	ACAACCCATTCTCTCTGTAAAAGAGGGGGGAGAGAGACG	pUMA 1467, *δ-ama* fr 5', *neo*^{r}, gapdh ir, *δ-ama* fr 3'	
3148	TGATCCTGATCCTGATCCTGATCCTGATCCCTTGTACAGCTCGTC CATGC		
3207	GGTCTCACCAAATGACAGAGGAGGAGAAACTCT	*CAD2218596.1* gene	pAdea429
3208	GGTCTCATCACTGATCCTGATCCTGATCCTGATCCTGATCCCAGA GAGAATGGGTTGTAGCC		
3228	GGTCTCACACCATGACAACACTCCTGCAAACC	*CAD2220808.1* gene	pAdea441
3229	GGTCTCATTTATTACACCACGTCGGTGGG		
3230	GGTCTCACACCATGTCTAGTCTATTCTCCGCC	*CAD2219450.1* gene	pAdea442
3231	GGTCTCATTTATTACTTTAGCTTCACATAAATAATAAGCA		
Internal primer no.	**Primers used for the plasmid sequencing Primer sequence (5'-3')**	**Binding site**	**-**
131	AAGTGCTAGTGAGAGTTTGACT	gapdh ir	-
310	CGAAACATCGCATCGAGCG	*neo*^{r}	-

311	ATCGACAAGACCGGCTTCC	*neo*^{r}	-
571	CCTAGTCCTGATTTCTTTGCGC	*δ-ama* fr 5'	-
572	GAGGTTCTCCCCTCTTTATTTCCT	*δ-ama* fr 3'	-
876	TGTTACCCTATTTCGTCTGTT	*γ-ama* fr 3'	-
1440	CGCCGAGGTGAAGTTCGAGGGC	*egfp*	-
3154	GGATCAGGATCAGGATCAGGATCAGGATCAATGAGCTCCAACTG GGGAAATC	*CAD2221471.1* gene	-
3176	TTGAGGATTTCCGACAGTCC	*CAD2218596.1* gene	-
3177	AGCAACAGTCCGACTTTGAG	*CAD2218596.1* gene	-
3178	ATCCAGGAAGGTGTGGTGTC	*CAD2219020.1 gene*	-
1438	TGTAAAACGACGGCCAGT	pUMA 1467	-
1439	CAGGAAACAGCTATGACCAT	pUMA 1467	-
Internal primer no.	**Primers used for PCR verification of genomic integration of insertion cassette in *A. deanei* Primer sequence (5'-3')**	**Locus**	**-**
49	ACTCCTCCACCACTACCACC	*δ-amastin* (Bind outside insertion cassette, in the genome)	-
545	CTCCCTAAGCGCCAATATCA		
80	CTTTCTGCCATCTGCCTCAT	*γ-amastin* (Bind outside insertion cassette, in the genome)	-
81	CATCCTTACGATCTTCTTATTTTTTGG		
311	ATCGACAAGACCGGCTTCC	*neo*^{r}	-
1603	GTAGTGCGTGTGAGTGTATGTATGG	*etp5* (Bind outside insertion cassette, in the genome)	-
1604	ATGTGCTTCATGCGCGT		
Internal primer no.	**Primers used for probe synthesis for Southern blot (5'-3')**	**Binding site**	**-**
51	TTGTCAAGACCGACCTGTC	*neo*^{r}	-
52	CAAGAAGGCGATAGAAGGC		
55	ATCTTAGCCAGACGAGCG	*hyg*^{r}	-
56	CACTATCGGCGAGTACTTCTACA		
1643/ 1845	GGTCTCGATGGCCACCACCCTTGAGG/ ATGGCCACCACCCTTGAGG	*etp5*	-
1644/ 1846	GGTCTCAGAGTGCTCGTGCATCTTGTTG/ GAGTGCTCGTGCATCTTGTTG		

A: Plasmids used for this study

Plasmid	Map	Generated by
pAdea039	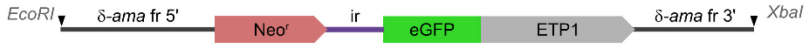	Sofia
pAdea043	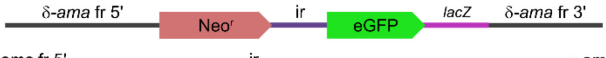	Morales et al., 2023
pAdea119	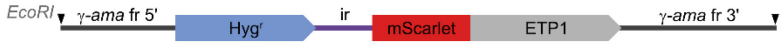	Morales et al., 2023
pAdea146	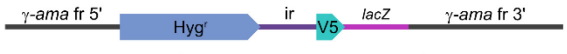	Eva
pAdea212		Jan
pAdea235	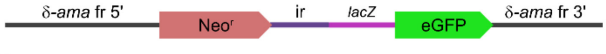	Morales et al., 2023
pAdea240		Jan
pAdea242		Jan
pAdea246		Anay
pAdea247	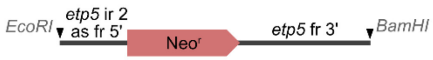	Anay
pAdea268	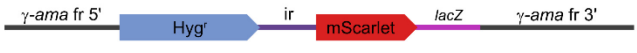	Lena
pAdea283		Morales et al., 2023
pAdea334		Slywia
pAdea340		Maurya et al., 2025
pAdea365	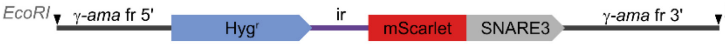	Lindsay/Anay
pAdea366		Lindsay/Anay
pAdea367	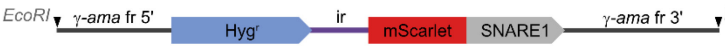	Lindsay/Anay
pAdea423		Anay
pAdea424		Anay
pAdea425	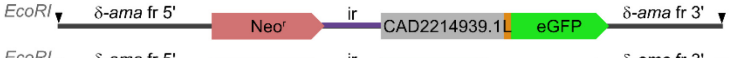	Anay
pAdea426		Anay
pAdea428		Anay
pAdea429		Anay
pAdea441		Anay
pAdea442		Anay
pAdea445		Lubomira
pAdea446		Lubomira
pAdea447		Lubomira
pAdea448		Lubomira
pAdea449		Lubomira
pAdea450		Lubomira
pAdea451		Lubomira
pAdea452	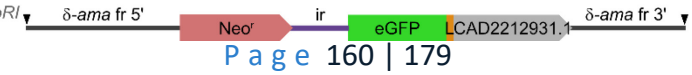	Lubomira

B: Adea strains used for this study generated by others

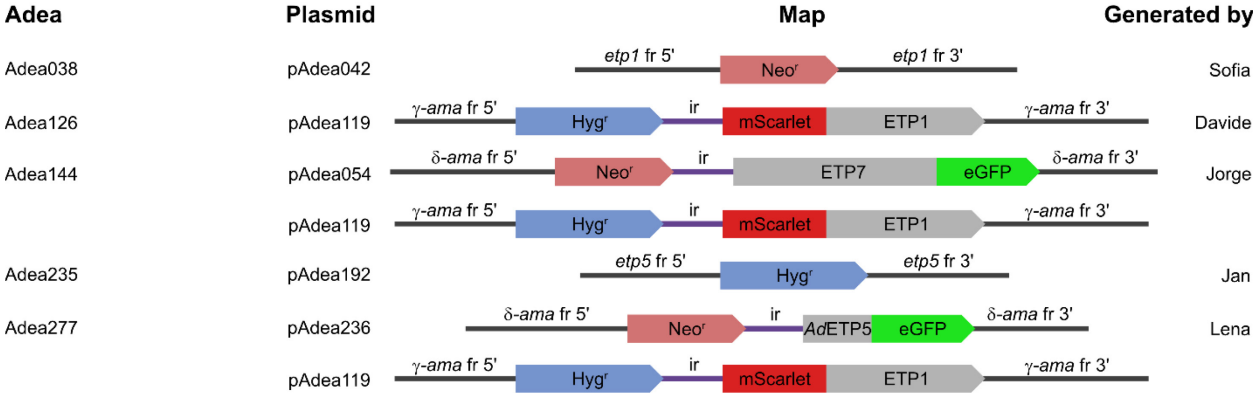

Figure 5.1: Description of all plasmids (pAdea) and *A. deanei* strains (Adea) used for this study.

A: pAdea043, pAdea146, pAdea235, and pAdea268 were used as tagging vectors to insert the gene of interests replacing *lacZ*. pAdea340 was used as a template for the generation of pAdea428. Restriction enzymes and their cutting positions were shown at the ends of plasmid maps that were digested/linearized before transfection. **B:** Details of Adea strains used in this study but generated by other researchers. Abbreviations: *γ/δ ama*/*etp* 5'/3' fr, *γ/δ amastin*/*etp* gene 5'/3' flanking regions used for homologous recombination; ir, intergenic region between *gapdh i* and *gapdh ii* genes; *etp5* ir 2 used as 5'/3' fr; *Ld*ETP5, *L. donovani* ETP5; *Tb*ETP5, *T. brucei* ETP5; *Ad*ETP5, *A. deanei* ETP5; *Ad*DLP, *A. deanei* dynamin-like protein; L, linker (GS_5); *Neo*^{r}, *Neomycin*/G418 resistance marker and *Hyg*^{r}, *Hygromycin* resistance marker.

5.4. Verification of clonal cell lines by PCR

Genomic DNA isolation and PCR verification of transgenic *A. deanei* cell lines were performed as described earlier (Maurya et al., 2025). All primers used for this purpose are listed in Table 5.1.

5.5. Southern blot verification

The verification of *etp5* knockouts was performed by Southern blot as described earlier (Morales et al., 2023 and Maurya et al., 2025). Specific probes against *etp5*, *neo*^{r}, and *hyg*^{r} were generated using digoxigenin-labelled dNTPs using primer combinations mentioned in Table 5.1. Hybridization of all probes to the target DNA was performed at 53 ˚C.

The membrane was stripped by washing once with water, two times with stripping buffer (0.2 M w/v NaOH and 0.1% w/v SDS) for 15 mins, and lastly, once with 2x SSC buffer (3 M w/v NaCl and 0.3 w/v trisodium citrate dihydrate) for 5 mins at 37 ˚C. The stripped membrane was further used to hybridize new probe as described above.

5.6. Autofluorescence microscopy

To detect the autofluorescence of fluorescent fusion proteins in *A. deanei*, fluorescence microscopy was performed as described before (Maurya et al., 2025).

5.7. Immunofluorescence assay

To detect ARL1-V5, anti-V5 primary antibody (mouse, monoclonal, IgG1κ, Chromotek) and anti-mouse secondary antibody (m-IgGk BP CFL 594, sc-516178, Santa Cruz Biotechnology) were used in an IFA experiment as described earlier (Maurya et al., 2025).

5.8. Fluorescence *in situ* hybridization

To detect and quantify the division phenotypes in *etp1* and *etp5* deletion mutants, FISH microscopy was performed as described before (Maurya et al., 2025).

5.9. Confocal microscopy

For visualizing cells with confocal microscopy, the slide was prepared as described before and imaged with default settings (Morales et al., 2023 and Maurya et al., 2025).

5.10. Knockdown assay with MAOs

ETP7 knockdown was performed as described earlier (Maurya et al., 2025) with 4 µl (200 µM, final concentration) of MAOs, MAO-1_{etp7} (5'-TGTCCCGTAAGGATTGCAGCATTCA-3'), MAO-2_{etp7} (5'-TGTTTGTCTTTTTCAGTGTGTATGT-3') or MAO_{tub} (5'-TGAATGCAGATAGCCTCACGCATGG-3') as a positive control synthesized by Gene Tools (LLC, Philomath, OR, USA).

5.11. Growth curve

Growth analysis of *etp5* knockouts was performed as described before (Maurya et al., 2025). For MAO treated cells, counting was performed at 6 h, 12 h, and 24 h in three technical triplicates.

5.12. Western blot analysis

Preparation of raw protein extracts, protein quantification, and Western blot analyses were done as described before (Maurya et al., 2025). The mScarlet was detected using α-RFP (1:2000, Chromotek, 5f8, rat) and α-rat-IgG HRP (1:5000, Invitrogen, PA1-28573) antibodies. The alpha-tubulin (as a loading control) was detected with α-alpha-tubulin (1:2000, Thermo Fisher, MA1-80017, rat) and α-rat-IgG HRP (1:10,000, Invitrogen, PA1-28573) antibodies.

5.13. *In silico* studies

The prediction of 3D structures of SNARE proteins was performed as described earlier (Maurya et al., 2025).

The presence of a mitochondrial signal peptide and/or a TMH was predicted by TargetP 2.0 and TMHMM 2.0, respectively in all the potential ES, Golgi, and cytosol candidates.

6. References

Adachi, Y., Itoh, K., Yamada, T., Cerveny, K.L., Suzuki, T.L., Macdonald, P., ... & Sesaki, H. (2016). Coincident phosphatidic acid interaction restrains Drp1 in mitochondrial division. *Molecular Cell*, *63*(6), 1034-1043.

Adnan, M., Islam, W., Zhang, J., Zheng, W., & Lu, G.D. (2019). Diverse role of SNARE protein Sec22 in vesicle trafficking, membrane fusion, and autophagy. *Cells*, *8* (4), 337.

Ago, R., & Shiomi, D. (2019). RodZ: a key-player in cell elongation and cell division in *Escherichia coli*. *AIMS Microbiology*, *5*(4), 358.

Alves, J.M., Klein, C.C., da Silva, F.M., Costa-Martins, A.G., Serrano, M.G., Buck, G.A., ... & Camargo, E.P. (2013a). Endosymbiosis in trypanosomatids: the genomic cooperation between bacterium and host in the synthesis of essential amino acids is heavily influenced by multiple horizontal gene transfers. *BMC Evolutionary Biology*, *13*, 1-20.

Alves, J.M., Serrano, M.G., Maia da Silva, F., Voegtly, L.J., Matveyev, A.V., Teixeira, M.M., ... & Buck, G.A. (2013b). Genome evolution and phylogenomic analysis of *Candidatus* Kinetoplastibacterium, the betaproteobacterial endosymbionts of *Strigomonas* and *Angomonas*. *Genome Biology and Evolution*, *5*(2), 338-350.

Alyahya, S.A., Alexander, R., Costa, T., Henriques, A.O., Emonet, T., & Jacobs-Wagner, C. (2009). RodZ, a component of the bacterial core morphogenic apparatus. *Proceedings of the National Academy of Sciences*, *106* (4), 1239-1244.

Amann, R.I., Krumholz, L., & Stahl, D.A. (1990). Fluorescent-oligonucleotide probing of whole cells for determinative, phylogenetic, and environmental studies in microbiology. *Journal of Bacteriology*, *172*(2), 762-770.

Arakaki, N., Nishihama, T., Owaki, H., Kuramoto, Y., Suenaga, M., Miyoshi, E., ... & Higuti, T. (2006). Dynamics of mitochondria during the cell cycle. *Biological and Pharmaceutical Bulletin*, *29*(9), 1962-1965.

Arimura, S.I., & Tsutsumi, N. (2002). A dynamin-like protein (ADL2b), rather than FtsZ, is involved in *Arabidopsis* mitochondrial division. *Proceedings of the National Academy of Sciences*, *99*(8), 5727-5731.

Attaibi, M., & den Blaauwen, T. (2022). An updated model of the divisome: regulation of the septal peptidoglycan synthesis machinery by the divisome. *International Journal of Molecular Sciences*, *23*(7), 3537.

Aussel, L., Barre, F.X., Aroyo, M., Stasiak, A., Stasiak, A.Z., & Sherratt, D. (2002). FtsK is a DNA motor protein that activates chromosome dimer resolution by switching the catalytic state of the XerC and XerD recombinases. *Cell*, *108*(2), 195-205.

Barrett, M.P., Burchmore, R.J., Stich, A., Lazzari, J.O., Frasch, A.C., Cazzulo, J.J., & Krishna, S. (2003). The trypanosomiases. *The Lancet*, *362*(9394), 1469-1480.

Bas, L., Papinski, D., Licheva, M., Torggler, R., Rohringer, S., Schuschnig, M., & Kraft, C. (2018). Reconstitution reveals Ykt6 as the autophagosomal SNARE in autophagosome–vacuole fusion. *Journal of Cell Biology*, *217*(10), 3656-3669.

References

Bendezú, F.O., & de Boer, P.A. (2008). Conditional lethality, division defects, membrane involution, and endocytosis in mre and mrd shape mutants of *Escherichia coli*. *Journal of Bacteriology*, *190*(5), 1792-1811.

Bendezú, F.O., Hale, C.A., Bernhardt, T.G., & De Boer, P.A. (2009). RodZ (YfgA) is required for proper assembly of the MreB actin cytoskeleton and cell shape in *E. coli*. *The EMBO Journal*, *28* (3), 193-204.

Berberich, C., Machado, G., Morales, G., Carrillo, G., Jiménez-Ruiz, A., & Alonso, C. (1998). The expression of the *Leishmania infantum* KMP-11 protein is developmentally regulated and stage specific. *Biochimica et Biophysica Acta (BBA)-Gene Structure and Expression*, *1442*(2-3), 230-237.

Berriman, M., Ghedin, E., Hertz-Fowler, C., Blandin, G., Renauld, H., Bartholomeu, D.C., ... & E.l.-Sayed, N.M. (2005). The genome of the African trypanosome *Trypanosoma brucei*. *Science*, *309* (5733), 416-422.

Bhattacharya, D., Yoon, H.S., & Hackett, J.D. (2004). Photosynthetic eukaryotes unite: endosymbiosis connects the dots. *Bioessays*, *26*(1), pp.50-60.

Bi, E., & Lutkenhaus, J. (1991). FtsZ ring structure associated with division in *Escherichia coli*. *Nature*, *354*(6349), 161-164.

Bleazard, W., McCaffery, J.M., King, E.J., Bale, S., Mozdy, A., Tieu, Q., ... & Shaw, J.M. (1999). The dynamin-related GTPase Dnm1 regulates mitochondrial fission in yeast. *Nature Cell Biology*, *1*(5), 298-304.

Bodył, A., & Mackiewicz, P. (2013). Endosymbiotic theory.

Borghesan, T.C., Campaner, M., Matsumoto, T.E., Espinosa, O.A., Razafindranaivo, V., Paiva, F., ... & Camargo, E.P. (2018). Genetic diversity and phylogenetic relationships of coevolving symbiont-harboring insect trypanosomatids, and their Neotropical dispersal by invader African blowflies (Calliphoridae). *Frontiers in Microbiology*, *9*, 131.

Bratton, B.P., Shaevitz, J.W., Gitai, Z., & Morgenstein, R.M. (2018). MreB polymers and curvature localization are enhanced by RodZ and predict *E. coli*'s cylindrical uniformity. *Nature Communications*, *9*(1), 2797.

Bruinsma, S., James, D.J., Serrano, M.Q., Esquibel, J., Woo, S.S., Kielar-Grevstad, E., ... & Martin, T.F. (2018). Small molecules that inhibit the late stage of Munc13-4–dependent secretory granule exocytosis in mast cells. *Journal of Biological Chemistry*, *293*(21), 8217-8229.

Bui, H.T., & Shaw, J.M. (2013). Dynamin assembly strategies and adaptor proteins in mitochondrial fission. *Current Biology*, *23*(19), R891-R899.

Busiek, K.K., Eraso, J.M., Wang, Y., & Margolin, W. (2012). The early divisome protein FtsA interacts directly through its 1c subdomain with the cytoplasmic domain of the late divisome protein FtsN. *Journal of Bacteriology*, *194*(8), 1989-2000.

Bustillo-Zabalbeitia, I., Montessuit, S., Raemy, E., Basañez, G., Terrones, O., & Martinou, J.C. (2014). Specific interaction with cardiolipin triggers functional activation of dynamin-related protein 1. *PloS One*, *9*(7), e102738.

Cameron, T.A., & Margolin, W. (2024). Insights into the assembly and regulation of the bacterial divisome. *Nature Reviews Microbiology*, *22*(1), 33-45.

References

Carrie, C., Giraud, E., & Whelan, J. (2009). Protein transport in organelles: dual targeting of proteins to mitochondria and chloroplasts. *The FEBS Journal*, *276*(5), 1187-1195.

Carvalho, A.L., & Deane, M.P. (1974). Trypanosomatidae isolated from *Zelus leucogrammus* (Perty, 1834) (Hemiptera, Reduviidae), with a discussion on flagellates of insectivorous bugs. *The Journal of Protozoology*, *21* (1), 5-8.

Chacinska, A., Koehler, C.M., Milenkovic, D., Lithgow, T., & Pfanner, N. (2009). Importing mitochondrial proteins: machineries and mechanisms. *Cell*, *138*(4), 628-644.

Chang, K.P. (1974). Ultrastructure of symbiotic bacteria in normal and antibiotic-treated *Blastocrithidia culicis* and *Crithidia oncopelti*. *The Journal of Protozoology*, *21*(5), 699-707.

Chappie, J.S., Acharya, S., Leonard, M., Schmid, S.L., & Dyda, F. (2010). G domain dimerization controls dynamin's assembly-stimulated GTPase activity. *Nature*, *465*(7297), 435-440.

Chatterjee, R., Setty, S.R.G., & Chakravortty, D. (2024). SNAREs: a double-edged sword for intravacuolar bacterial pathogens within host cells. *Trends in Microbiology*, *32*(5), 477-493.

Chen, Y.A., & Scheller, R.H. (2001). SNARE-mediated membrane fusion. *Nature Reviews Molecular Cell Biology*, *2*(2), 98-106.

Chiang, H.C., Shin, W., Zhao, W.D., Hamid, E., Sheng, J., Baydyuk, M., ... & Wu, L.G. (2014). Post-fusion structural changes and their roles in exocytosis and endocytosis of dense-core vesicles. *Nature Communications*, *5*(1), 3356.

Clinton, R.W., Francy, C.A., Ramachandran, R., Qi, X., & Mears, J.A. (2016). Dynamin-related protein 1 oligomerization in solution impairs functional interactions with membrane-anchored mitochondrial fission factor. *Journal of Biological Chemistry*, *291*(1), 478-492.

Coale, T.H., Loconte, V., Turk-Kubo, K.A., Vanslembrouck, B., Mak, W.K.E., Cheung, S., ... & Zehr, J.P. (2024). Nitrogen-fixing organelle in a marine alga. *Science*, *384*(6692), 217-222.

Cournoyer, J.E., Altman, S.D., Gao, Y.L., Wallace, C.L., Zhang, D., Lo, G.H., ... & Mehta, A.P. (2022). Engineering artificial photosynthetic life-forms through endosymbiosis. *Nature Communications*, *13*(1), 2254.

Cowling, B.S., Prokic, I., Tasfaout, H., Rabai, A., Humbert, F., Rinaldi, B., ... & Laporte, J. (2017). Amphiphysin (BIN1) negatively regulates dynamin 2 for normal muscle maturation. *The Journal of Clinical Investigation*, *127*(12), 4477-4487.

Criado, M., Gil, A., Viniegra, S., & GUTIErrez, L.M. (1999). A single amino acid near the C terminus of the synaptosome-associated protein of 25 kDa (SNAP-25) is essential for exocytosis in chromaffin cells. *Proceedings of the National Academy of Sciences*, *96*(13), 7256-7261.

Daniel, R.A., & Errington, J. (2003). Control of cell morphogenesis in bacteria: two distinct ways to make a rod-shaped cell. *Cell*, *113*(6), 767-776.

References

Davey, J.W., Catta-Preta, C.M., James, S., Forrester, S., Motta, M.C.M., Ashton, P.D., & Mottram, J.C. (2021). Chromosomal assembly of the nuclear genome of the endosymbiont-bearing trypanosomatid *Angomonas deanei*. *G3*, *11*(1), jkaa018.

De Gaudenzi, J.G., Noé, G., Campo, V.A., Frasch, A.C., & Cassola, A. (2011). Gene expression regulation in trypanosomatids. *Essays in Biochemistry*, *51*, 31-46.

Delaye, L., Valadez-Cano, C., & Pérez-Zamorano, B. (2016). How really ancient is *Paulinella chromatophora*?. *PLoS Currents*, *8*, ecurrents-tol.

Delevoye, C., Nilges, M., Dehoux, P., Paumet, F., Perrinet, S., Dautry-Varsat, A., & Subtil, A. (2008). SNARE protein mimicry by an intracellular bacterium. *PLoS Pathogens*, *4*(3), e1000022.

Demmel, L., Schmidt, K., Lucast, L., Havlicek, K., Zankel, A., Koestler, T., ... & Warren, G. (2014). The endocytic activity of the flagellar pocket in *Trypanosoma brucei* is regulated by an adjacent phosphatidylinositol phosphate kinase. *Journal of Cell Science*, *127* (10), 2351-2364.

Dollet, M. (1984). Plant diseases caused by flagellate protozoa (*Phytomonas*).

Du, S., Henke, W., Pichoff, S., & Lutkenhaus, J. (2019). How FtsEX localizes to the Z ring and interacts with FtsA to regulate cell division. *Molecular Microbiology*, *112*(3), 881-895.

Engler, C., Kandzia, R., & Marillonnet, S. (2008). A one pot, one step, precision cloning method with high throughput capability. *PLoS One,* 3, e3647. 10.1371/journal.pone.0003647.

Errabolu, R., Sanders, M.A., & Salisbury, J.L. (1994). Cloning of a cDNA encoding human centrin, an EF-hand protein of centrosomes and mitotic spindle poles. *Journal of Cell Science*, *107* (1), 9-16.

Evergren, E., Gad, H., Walther, K., Sundborger, A., Tomilin, N., & Shupliakov, O. (2007). Intersectin is a negative regulator of dynamin recruitment to the synaptic endocytic zone in the central synapse. *Journal of Neuroscience*, *27* (2), 379-390.

Faelber, K., Posor, Y., Gao, S., Held, M., Roske, Y., Schulze, D., ... & Daumke, O. (2011). Crystal structure of nucleotide-free dynamin. *Nature*, *477*(7366), 556-560.

Faktorová, D., Dobáková, E., Peña-Diaz, P., & Lukeš, J. (2016). From simple to supercomplex: mitochondrial genomes of euglenozoan protists. *F1000Research*, *5*, F1000-Faculty.

Fenton, A.K., & Gerdes, K. (2013). Direct interaction of FtsZ and MreB is required for septum synthesis and cell division in *Escherichia coli*. *The EMBO Journal*, *32* (13), 1953-1965.

Ferguson, K.M., Lemmon, M.A., Schlessinger, J., & Sigler, P.B. (1994). Crystal structure at 2.2 Å resolution of the pleckstrin homology domain from human dynamin. *Cell*, *79* (2), 199-209.

Field, M.C., & Carrington, M. (2009). The trypanosome flagellar pocket. *Nature Reviews Microbiology*, *7*(11), 775-786.

Flanagan, J.J., Mukherjee, I., & Barlowe, C. (2015). Examination of Sec22 homodimer formation and role in SNARE-dependent membrane fusion. *Journal of Biological Chemistry*, *290*(17), 10657-10666.

Ford, M.G., Jenni, S., & Nunnari, J. (2011). The crystal structure of dynamin. *Nature*, *477*(7366), 561-566.

References

Francy, C.A., Clinton, R.W., Fröhlich, C., Murphy, C., & Mears, J.A. (2017). Cryo-EM studies of Drp1 reveal cardiolipin interactions that activate the helical oligomer. *Scientific Reports*, *7*(1), 10744.

Fröhlich, C., Grabiger, S., Pelz, D., Faelber, K., Rosenbaum, E., Mears, J., ... & Daumke, O. (2013). Structural insights into oligomerization and mitochondrial remodeling of dynamin 1-like protein. *The EMBO Journal*, *32* (9), 1280-1292.

Fuchs, B.M., Pernthaler, J., & Amann, R. (2007). Single cell identification by fluorescence in situ hybridization. *Methods for General and Molecular Microbiology*, 886-896.

Gandre-Babbe, S., & van der Bliek, A.M. (2008). The novel tail-anchored membrane protein Mff controls mitochondrial and peroxisomal fission in mammalian cells. *Molecular Biology of the Cell*, *19*(6), 2402-2412.

Gao, H., Kadirjan-Kalbach, D., Froehlich, J.E., & Osteryoung, K.W. (2003). ARC5, a cytosolic dynamin-like protein from plants, is part of the chloroplast division machinery. *Proceedings of the National Academy of Sciences*, *100* (7), 4328-4333.

Gerding, M.A., Liu, B., Bendezú, F.O., Hale, C.A., Bernhardt, T.G., & de Boer, P.A. (2009). Self-enhanced accumulation of FtsN at division sites and roles for other proteins with a SPOR domain (DamX, DedD, and RlpA) in *Escherichia coli* cell constriction. *Journal of Bacteriology*, *191*(24), 7383-7401.

Gibbs, S. (1993). The evolution of algal chloroplasts. *Origin of Plastids.*, 107-121.

Gibson, D.G., Young, L., Chuang, R.Y., Venter, J.C., Hutchison III, C.A., & Smith, H.O. (2009). Enzymatic assembly of DNA molecules up to several hundred kilobases. *Nature Methods*, *6*(5), 343-345.

Giger, G.H., Ernst, C., Richter, I., Gassler, T., Field, C M., Sintsova, A., ... & Vorholt, J.A. (2024). Inducing novel endosymbioses by implanting bacteria in fungi. *Nature*, *635*(8038), 415-422.

Gilson, P.R., Yu, X.C., Hereld, D., Barth, C., Savage, A., Kiefel, B.R., ... & Beech, P.L. (2003). Two *Dictyostelium* orthologs of the prokaryotic cell division protein FtsZ localize to mitochondria and are required for the maintenance of normal mitochondrial morphology. *Eukaryotic Cell*, *2* (6), 1315-1326.

Glynn, J.M., Froehlich, J.E., & Osteryoung, K.W. (2008). *Arabidopsis* ARC6 coordinates the division machineries of the inner and outer chloroplast membranes through interaction with PDV2 in the intermembrane space. *The Plant Cell*, *20*(9), 2460-2470.

Glynn, J.M., Yang, Y., Vitha, S., Schmitz, A.J., Hemmes, M., Miyagishima, S.Y., & Osteryoung, K.W. (2009). PARC6, a novel chloroplast division factor, influences FtsZ assembly and is required for recruitment of PDV1 during chloroplast division in *Arabidopsis*. *The Plant Journal*, *59*(5), 700-711.

Griffin, E.E., Graumann, J., & Chan, D.C. (2005). The WD40 protein Caf4p is a component of the mitochondrial fission machinery and recruits Dnm1p to mitochondria. *The Journal of Cell Biology*, *170*(2), 237-248.

Hale, C.A., & de Boer, P.A. (1997). Direct binding of FtsZ to ZipA, an essential component of the septal ring structure that mediates cell division in *E. coli*. *Cell*, *88*(2), 175-185.

Han, J., Pluhackova, K., & Böckmann, R.A. (2017). The multifaceted role of SNARE proteins in membrane fusion. *Frontiers in Physiology*, *8*, 5.

References

Hanson, P.I., Heuser, J.E., & Jahn, R. (1997). Neurotransmitter release—four years of SNARE complexes. *Current Opinion in Neurobiology*, *7*(3), 310-315.

Hashimoto, M., Ooiwa, S., & Sekiguchi, J. (2012). Synthetic lethality of the lytE cwlO genotype in *Bacillus subtilis* is caused by lack of D, L-endopeptidase activity at the lateral cell wall. *Journal of Bacteriology*, *194*(4), 796-803.

He, C.Y., Pypaert, M., & Warren, G. (2005). Golgi duplication in *Trypanosoma brucei* requires Centrin2. *Science*, *310*(5751), 1196-1198.

Heidrich, C., Ursinus, A., Berger, J., Schwarz, H., & Höltje, J.V. (2002). Effects of multiple deletions of murein hydrolases on viability, septum cleavage, and sensitivity to large toxic molecules in *Escherichia coli*. *Journal of Bacteriology*, *184* (22), 6093-6099.

Hinshaw, J.E., & Schmid, S.L. (1995). Dynamin self-assembles into rings suggesting a mechanism for coated vesicle budding. *Nature*, *374* (6518), 190-192.

Hohendahl, A., Talledge, N., Galli, V., Shen, P.S., Humbert, F., De Camilli, P., ... & Roux, A. (2017). Structural inhibition of dynamin-mediated membrane fission by endophilin. *Elife*, *6*, e26856.

Hoogenraad, H.R. (1927). Rhizopoden and Heliozoë from the zoetwater of Netherlands. *Tijdschr. Nederl. Dierkund. Vereen, (2)*, *20*, 1-18.

Hu, G., Huang, J., & Fussenegger, M. (2024). Toward photosynthetic mammalian cells through artificial endosymbiosis. *Small*, *20*(31), 2310310.

Imoto, Y., Kuroiwa, H., Yoshida, Y., Ohnuma, M., Fujiwara, T., Yoshida, M., ... & Kuroiwa, T. (2013). Single-membrane–bounded peroxisome division revealed by isolation of dynamin-based machinery. *Proceedings of the National Academy of Sciences*, *110*(23), 9583-9588.

Ivens, A.C., Peacock, C.S., Worthey, E.A., Murphy, L., Aggarwal, G., Berriman, M., ... & Myler, P.J. (2005). The genome of the kinetoplastid parasite, *Leishmania* major. *Science*, *309* (5733), 436-442.

Jahn, R., & Scheller, R.H. (2006). SNAREs—engines for membrane fusion. *Nature Reviews Molecular Cell Biology*, *7*(9), 631-643.

Jahn, R., Cafiso, D.C., & Tamm, L.K. (2024). Mechanisms of SNARE proteins in membrane fusion. *Nature Reviews Molecular Cell Biology*, *25*(2), 101-118.

Jarvis, P. (2008). Targeting of nucleus-encoded proteins to chloroplasts in plants. *New phytologist*, *179*(2), 257-285.

Jimah, J.R., & Hinshaw, J.E. (2019). Structural insights into the mechanism of dynamin superfamily proteins. *Trends in Cell Biology*, *29*(3), 257-273.

Klein, C.C., Alves, J.M., Serrano, M.G., Buck, G.A., Vasconcelos, A.T.R., Sagot, M.F., ... & Motta, M.C.M. (2013). Biosynthesis of vitamins and cofactors in bacterium-harbouring trypanosomatids depends on the symbiotic association as revealed by genomic analyses. *PLoS One*, *8*(11), e79786.

Koch, A., Thiemann, M., Grabenbauer, M., Yoon, Y., McNiven, M.A., & Schrader, M. (2003). Dynamin-like protein 1 is involved in peroxisomal fission. *Journal of Biological Chemistry*, *278*(10), 8597-8605.

References

Koirala, S., Guo, Q., Kalia, R., Bui, H.T., Eckert, D.M., Frost, A., & Shaw, J.M. (2013). Interchangeable adaptors regulate mitochondrial dynamin assembly for membrane scission. *Proceedings of the National Academy of Sciences*, *110*(15), E1342-E1351.

Kokkori, S. (2018). Genetic tools for the trypanosomatid *Angomonas deanei* help to dissect host-endosymbiont interactions (Doctoral dissertation, Düsseldorf, Heinrich-Heine-Universität, 2018).

Kostygov, A.Y., Dobáková, E., Grybchuk-Ieremenko, A., Váhala, D., Maslov, D.A., Votýpka, J., ... & Yurchenko, V. (2016). Novel trypanosomatid-bacterium association: evolution of endosymbiosis in action. *MBio*, *7* (2), 10-1128.

Králová, J., Grybchuk-Ieremenko, A., Votýpka, J., Novotný, V., Kment, P., Lukeš, J., ... & Kostygov, A.Y. (2019). Insect trypanosomatids in Papua New Guinea: high endemism and diversity. *International Journal for Parasitology*, *49*(13-14), 1075-1086.

Kraus, F., Roy, K., Pucadyil, T.J., & Ryan, M.T. (2021). Function and regulation of the divisome for mitochondrial fission. *Nature*, *590*(7844), 57-66.

Kuravi, K., Nagotu, S., Krikken, A.M., Sjollema, K., Deckers, M., Erdmann, R., ... & Van Der Klei, I.J. (2006). Dynamin-related proteins Vps1p and Dnm1p control peroxisome abundance in *Saccharomyces cerevisiae*. *Journal of Cell Science*, *119* (19), 3994-4001.

Kuroiwa, T., Kuroiwa, H., Sakai, A., Takahashi, H., Toda, K., & Itoh, R. (1998). The division apparatus of plastids and mitochondria. *International Review of Cytology*, *181*, 1-41.

Kuroiwa, T., Nishida, K., Yoshida, Y., Fujiwara, T., Mori, T., Kuroiwa, H., & Misumi, O. (2006). Structure, function and evolution of the mitochondrial division apparatus. *Biochimica et Biophysica Acta (BBA)-Molecular Cell Research*, *1763* (5-6), 510-521.

Lacomble, S., Vaughan, S., Gadelha, C., Morphew, M.K., Shaw, M.K., McIntosh, J.R., & Gull, K. (2010). Basal body movements orchestrate membrane organelle division and cell morphogenesis in *Trypanosoma brucei*. *Journal of Cell Science*, *123*(17), 2884-2891.

Lamanna, M.M., Manzoor, I., Joseph, M., Ye, Z.A., Benedet, M., Zanardi, A., ... & Winkler, M.E. (2022). Roles of RodZ and class A PBP1b in the assembly and regulation of the peripheral peptidoglycan elongasome in ovoid-shaped cells of *Streptococcus pneumoniae* D39. *Molecular Microbiology*, *118* (4), 336-368.

Lauterborn, R. (1895). Protozoan studies II. *Paulinella chromatophora* nov. gen. nov. spec., a freshwater rhizopod with blue-green chromatophore-like inclusions. *Zeitschrift für Wiss Zoologische*, *59*, 537.

Leger, M.M., Petrů, M., Žárský, V., Eme, L., Vlček, Č., Harding, T., ... & Roger, A.J. (2015). An ancestral bacterial division system is widespread in eukaryotic mitochondria. *Proceedings of the National Academy of Sciences*, *112*(33), 10239-10246.

Lhee, D., Ha, J.S., Kim, S., Park, M.G., Bhattacharya, D., & Yoon, H.S. (2019). Evolutionary dynamics of the chromatophore genome in three photosynthetic *Paulinella* species. *Scientific Reports*, *9*(1), 2560.

Lhee, D., Lee, J., Ettahi, K., Cho, C.H., Ha, J.S., Chan, Y.F., ... & Yoon, H.S. (2021). Amoeba genome reveals dominant host contribution to plastid endosymbiosis. *Molecular Biology and Evolution*, *38* (2), 344-357.

Li, S., Xu, S., Roelofs, B.A., Boyman, L., Lederer, W.J., Sesaki, H., & Karbowski, M. (2015a). Transient assembly of F-actin on the outer mitochondrial membrane contributes to mitochondrial fission. *Journal of Cell Biology*, *208* (1), 109-123.

Li, X., & Gould, S.J. (2003). The dynamin-like GTPase DLP1 is essential for peroxisome division and is recruited to peroxisomes in part by PEX11. *Journal of Biological Chemistry*, *278*(19), 17012-17020.

Li, X., Wu, Y., Shen, C., Belenkaya, T.Y., Ray, L., & Lin, X. (2015b). *Drosophila* p24 and Sec22 regulate Wingless trafficking in the early secretory pathway. *Biochemical and Biophysical Research Communications*, *463*(4), 483-489.

Li, Z., & Wang, C.C. (2008). KMP-11, a basal body and flagellar protein, is required for cell division in *Trypanosoma brucei*. *Eukaryotic Cell*, *7*(11), 1941-1950.

Li, Z., Lee, J.H., Chu, F., Burlingame, A.L., Günzl, A., & Wang, C.C. (2008). Identification of a novel chromosomal passenger complex and its unique localization during cytokinesis in *Trypanosoma brucei*. *PLoS One*, *3* (6), e2354.

Lim, L.Z., Ee, S., Fu, J., Tan, Y., He, C.Y., & Song, J. (2017). Kinetoplastid membrane protein-11 adopts a four-helix bundle fold in DPC micelle. *FEBS Letters*, *591* (22), 3793-3804.

Liu, G., Draper, G.C., & Donachie, W.D. (1998). FtsK is a bifunctional protein involved in cell division and chromosome localization in *Escherichia coli*. *Molecular Microbiology*, *29*(3), 893-903.

Liu, X., Biboy, J., Consoli, E., Vollmer, W., & den Blaauwen, T. (2020). MreC and MreD balance the interaction between the elongasome proteins PBP2 and RodA. *PLoS Genetics*, *16*(12), e1009276.

Losón, O.C., Song, Z., Chen, H., & Chan, D.C. (2013). Fis1, Mff, MiD49, and MiD51 mediate Drp1 recruitment in mitochondrial fission. *Molecular Biology of the Cell*, *24*(5), 659-667.

Lu, B., Kennedy, B., Clinton, R.W., Wang, E.J., McHugh, D., Stepanyants, N., ... & Ramachandran, R. (2018). Steric interference from intrinsically disordered regions controls dynamin-related protein 1 self-assembly during mitochondrial fission. *Scientific Reports*, *8*(1), 10879.

Margolin, W. (2005). FtsZ and the division of prokaryotic cells and organelles. *Nature Reviews Molecular Cell Biology*, *6*(11), 862-871.

Margulis, L. (1993). Symbiosis in Cell Evolution. Microbial Communities in the Archaean and Proterozoic Eons (W. H. Freeman and Co., New York.

Marin, B., Nowack, E.C., & Melkonian, M. (2005). A plastid in the making: evidence for a second primary endosymbiosis. *Protist*, *156*(4), 425-432.

Marmont, L.S., & Bernhardt, T.G. (2020). A conserved subcomplex within the bacterial cytokinetic ring activates cell wall synthesis by the FtsW-FtsI synthase. *Proceedings of the National Academy of Sciences*, *117*(38), 23879-23885.

Maróti, G., & Kondorosi, É. (2014). Nitrogen-fixing *Rhizobium*-legume symbiosis: are polyploidy and host peptide-governed symbiont differentiation general principles of endosymbiosis?. *Frontiers in Microbiology*, *5*, 326.

References

Maslov, D.A., Opperdoes, F.R., Kostygov, A.Y., Hashimi, H., Lukeš, J., & Yurchenko, V. (2019). Recent advances in trypanosomatid research: genome organization, expression, metabolism, taxonomy and evolution. *Parasitology*, *146*(1), 1-27.

Maurya, A.K., Cadena, L.R., Ehret, G., Nowack, E.C.M. (2025). A novel host-encoded protein, ETP2, plays an important role in endosymbiont division in the trypanosomatid *Angomonas deanei*. (Under review).

Maurya, A.K., Kröninger, L., Ehret, G., Bäumers, M., Marson, M., Scheu, S., Nowack, E.C.M. (2025). A nucleus-encoded dynamin-like protein controls endosymbiont division in the trypanosomatid *Angomonas deanei*. *Science Advances*, 11(12), eadp8518.

Mears, J.A., Lackner, L.L., Fang, S., Ingerman, E., Nunnari, J., & Hinshaw, J.E. (2011). Conformational changes in Dnm1 support a contractile mechanism for mitochondrial fission. *Nature Structural & Molecular Biology*, *18*(1), 20-26.

Melkonian, M., & Mollenhauer, D. (2005). Robert Lauterborn (1869-1952) and his *Paulinella chromatophora*. *Protist*, *156*(2), 253-262.

Mirdita, M., Schütze, K., Moriwaki, Y., Heo, L., Ovchinnikov, S., & Steinegger, M. (2022). ColabFold: making protein folding accessible to all. *Nature Methods*, *19*(6), 679-682.

Miyagishima, S.Y., Itoh, R., Toda, K., Takahashi, H., Kuroiwa, H., & Kuroiwa, T. (1998). Identification of a triple ring structure involved in plastid division in the primitive red alga *Cyanidioschyzon merolae*. *Microscopy*, *47*(3), 269-272.

Miyagishima, S.Y., Kabeya, Y., Sugita, C., Sugita, M., & Fujiwara, T. (2014). DipM is required for peptidoglycan hydrolysis during chloroplast division. *BMC Plant Biology*, *14*, 1-15.

Miyagishima, S.Y., Nishida, K., Mori, T., Matsuzaki, M., Higashiyama, T., Kuroiwa, H., & Kuroiwa, T. (2003). A plant-specific dynamin-related protein forms a ring at the chloroplast division site. *The Plant Cell*, *15*(3), 655-665.

Möll, A., & Thanbichler, M. (2009). FtsN-like proteins are conserved components of the cell division machinery in proteobacteria. *Molecular Microbiology*, *72*(4), 1037-1053.

Morales, J., Ehret, G., Poschmann, G., Reinicke, T., Maurya, A.K., Kröninger, L., ... & Nowack, E.C. (2023). Host-symbiont interactions in *Angomonas deanei* include the evolution of a host-derived dynamin ring around the endosymbiont division site. *Current Biology*, *33*(1), 28-40.

Morales, J., Kokkori, S., Weidauer, D., Chapman, J., Goltsman, E., Rokhsar, D., ... & Nowack, E.C. (2016). Development of a toolbox to dissect host-endosymbiont interactions and protein trafficking in the trypanosomatid *Angomonas deanei*. *BMC Evolutionary Biology*, *16*, 1-12.

Moran, N.A., & Plague, G.R. (2004). Genomic changes following host restriction in bacteria. *Current Opinion in Genetics & Development*, *14*(6), 627-633.

Morita, Y., Okumura, M., Narumi, I., & Nishida, H. (2019). Sensitivity of *Deinococcus grandis* rodZ deletion mutant to calcium ions results in enhanced spheroplast size. *AIMS Microbiology*, *5*(2), 176.

References

Motta, M.C., Soares, M.J., Attias, M., Morgado, J., Lemos, A.D.P., Saad-Nehme, J., ... & De Souza, W. (1997). Ultrastructural and biochemical analysis of the relationship of *Crithidia deanei* with its endosymbiont. *European Journal of Cell Biology*, *72*(4), 370-377.

Motta, M.C.M., Catta-Preta, C.M.C., Schenkman, S., Martins, A.C.D.A., Miranda, K., de Souza, W., & Elias, M.C. (2010). The bacterium endosymbiont of *Crithidia deanei* undergoes coordinated division with the host cell nucleus. *PLoS One*, *5*(8), e12415.

Motta, M.C.M., Martins, A.C.D.A., de Souza, S.S.A., Catta-Preta, C.M.C., Silva, R., Klein, C.C., ... & de Vasconcelos, A.T.R. (2013). Predicting the proteins of *Angomonas deanei*, *Strigomonas culicis* and their respective endosymbionts reveals new aspects of the trypanosomatidae family. *PloS One*, *8*(4), e60209.

Motta, M.C.M., Picchi, G.F.A., Palmie-Pekoto, I.V., Rocha, M.R., de Carvalho, T.M.U., Morgado-Diaz, Jose, ... & Fragoso, S.P. (2004). The microtubule analog protein, FtsZ, in the endosymbiont of trypanosomatid protozoa. *Journal of Eukaryotic Microbiology*, *51* (4), 394-401.

Moulton, J.D. (2017). Using morpholinos to control gene expression. *Current Protocols in Nucleic Acid Chemistry*, *68*(1), 4-30.

Moya, A., Peretó, J., Gil, R., & Latorre, A. (2008). Learning how to live together: genomic insights into prokaryote–animal symbioses. *Nature Reviews Genetics*, *9*(3), 218-229.

Mozdy, A.D., McCaffery, J.M., & Shaw, J.M. (2000). Dnm1p GTPase-mediated mitochondrial fission is a multi-step process requiring the novel integral membrane component Fis1p. *The Journal of Cell Biology*, *151*(2), 367-380.

Muchová, K., Chromiková, Z., & Barák, I. (2013). Control of *Bacillus subtilis* cell shape by RodZ. *Environmental Microbiology*, *15* (12), 3259-3271.

Mundim, M.H., & Roitman, I. (1977). Extra nutritional requirements of artificially aposymbiotic *Crithidia deanei*. *The Journal of Protozoology*, *24*(2), 329-331.

Murungi, E., Barlow, L.D., Venkatesh, D., Adung'a, V.O., Dacks, J.B., Field, M.C., & Christoffels, A. (2014). A comparative analysis of trypanosomatid SNARE proteins. *Parasitology International*, *63*(2), 341-348.

Nagashima, S., Tábara, L.C., Tilokani, L., Paupe, V., Anand, H., Pogson, J.H., ... & Prudent, J. (2020). Golgi-derived PI (4) P-containing vesicles drive late steps of mitochondrial division. *Science*, *367* (6484), 1366-1371.

Nakabachi, A., Ishida, K., Hongoh, Y., Ohkuma, M., & Miyagishima, S.Y. (2014). Aphid gene of bacterial origin encodes a protein transported to an obligate endosymbiont. *Current Biology*, *24*(14), R640-R641.

Niemann, H.H., Knetsch, M.L., Scherer, A., Manstein, D.J., & Kull, F.J. (2001). Crystal structure of a dynamin GTPase domain in both nucleotide-free and GDP-bound forms. *The EMBO Journal*.

Nowack, E.C., & Grossman, A.R. (2012). Trafficking of protein into the recently established photosynthetic organelles of *Paulinella chromatophora*. *Proceedings of the National Academy of Sciences*, *109*(14), 5340-5345.

References

Nowack, E.C., Price, D.C., Bhattacharya, D., Singer, A., Melkonian, M., & Grossman, A.R. (2016). Gene transfers from diverse bacteria compensate for reductive genome evolution in the chromatophore of *Paulinella chromatophora*. *Proceedings of the National Academy of Sciences*, *113*(43), 12214-12219.

Otsuga, D., Keegan, B.R., Brisch, E., Thatcher, J.W., Hermann, G.J., Bleazard, W., & Shaw, J.M. (1998). The dynamin-related GTPase, Dnm1p, controls mitochondrial morphology in yeast. *The Journal of Cell Biology*, *143*(2), 333-349.

Palmer, C.S., Osellame, L.D., Laine, D., Koutsopoulos, O.S., Frazier, A.E., & Ryan, M.T. (2011). MiD49 and MiD51, new components of the mitochondrial fission machinery. *EMBO Reports*, *12* (6), 565-573.

Pan, R., & Hu, J. (2011). The conserved fission complex on peroxisomes and mitochondria. *Plant Signaling & Behavior*, *6*(6), 870-872.

Parsons, M. (2004). Glycosomes: parasites and the divergence of peroxisomal purpose. *Molecular Microbiology*, *53*(3), 717-724.

Paumet, F., Wesolowski, J., Garcia-Diaz, A., Delevoye, C., Aulner, N., Shuman, H.A., ... & Rothman, J.E. (2009). Intracellular bacteria encode inhibitory SNARE-like proteins. *PloS One*, *4* (10), e7375.

Pérez-Brocal, V., Gil, R., Ramos, S., Lamelas, A., Postigo, M., Michelena, J.M., ... & Latorre, A. (2006). A small microbial genome: the end of a long symbiotic relationship?. *Science*, *314* (5797), 312-313.

Philippe, J., Vernet, T., & Zapun, A. (2014). The elongation of ovococci. *Microbial Drug Resistance*, *20*(3), 215-221.

Pichoff, S., & Lutkenhaus, J. (2002). Unique and overlapping roles for ZipA and FtsA in septal ring assembly in *Escherichia coli*. *The EMBO Journal*.

Pichoff, S., & Lutkenhaus, J. (2005). Tethering the Z ring to the membrane through a conserved membrane targeting sequence in FtsA. *Molecular Microbiology*, *55* (6), 1722-1734.

Pichoff, S., Du, S., & Lutkenhaus, J. (2015). The bypass of ZipA by overexpression of FtsN requires a previously unknown conserved FtsN motif essential for FtsA–FtsN interaction supporting a model in which FtsA monomers recruit late cell division proteins to the Z ring. *Molecular Microbiology*, *95* (6), 971-987.

Plague, G.R., Dunbar, H.E., Tran, P.L., & Moran, N.A. (2008). Extensive proliferation of transposable elements in heritable bacterial symbionts. *Journal of Bacteriology*, *190*(2), 777-779.

Pyke, K. A. (1999). Plastid division and development. *The Plant Cell*, *11*(4), 549-556.

Ramachandran, R., & Schmid, S.L. (2018). The dynamin superfamily. *Current Biology*, *28*(8), R411-R416.

Rico, A.I., Krupka, M., & Vicente, M. (2013). In the beginning, *Escherichia coli* assembled the proto-ring: an initial phase of division. *Journal of Biological Chemistry*, *288*(29), 20830-20836.

Robinson, D.R., Sherwin, T., Ploubidou, A., Byard, E.H., & Gull, K. (1995). Microtubule polarity and dynamics in the control of organelle positioning, segregation, and cytokinesis in the trypanosome cell cycle. *The Journal of Cell Biology*, *128*(6), 1163-1172.

Rosati, G. (2004). Ectosymbiosis in ciliated protozoa. In *Symbiosis: mechanisms and model systems* (pp. 475-488). Dordrecht: Springer Netherlands.

References

Rothman, J.E. (2013). The Principle of Membrane Fusion in the Cell. *Prize Lecture*.

Salisbury, J.L., Baron, A.T., & Sanders, M.A. (1988). The centrin-based cytoskeleton of *Chlamydomonas reinhardtii*: distribution in interphase and mitotic cells. *The Journal of Cell Biology*, *107*(2), 635-641.

Satisbury, J.L. (1995). Centrin, centrosomes, and mitotic spindle poles. *Current Opinion in Cell Biology*, *7*(1), 39-45.

Selvapandiyan, A., Kumar, P., Morris, J.C., Salisbury, J.L., Wang, C.C., & Nakhasi, H.L. (2007). Centrin1 is required for organelle segregation and cytokinesis in *Trypanosoma brucei*. *Molecular Biology of the Cell*, *18*(9), 3290-3301.

Selvapandiyan, A., Kumar, P., Salisbury, J.L., Wang, C.C., & Nakhasi, H.L. (2012). Role of centrins 2 and 3 in organelle segregation and cytokinesis in *Trypanosoma brucei*.

Shi, X., Halder, P., Yavuz, H., Jahn, R., & Shuman, H.A. (2016). Direct targeting of membrane fusion by SNARE mimicry: Convergent evolution of *Legionella* effectors. *Proceedings of the National Academy of Sciences*, *113*(31), 8807-8812.

Shigenobu, S., & Stern, D.L. (2013). Aphids evolved novel secreted proteins for symbiosis with bacterial endosymbiont. *Proceedings of the Royal Society B: Biological Sciences*, *280*(1750), 20121952.

Shiomi, D., Sakai, M., & Niki, H. (2008). Determination of bacterial rod shape by a novel cytoskeletal membrane protein. *The EMBO Journal*, *27* (23), 3081-3091.

Shiomi, D., Toyoda, A., Aizu, T., Ejima, F., Fujiyama, A., Shini, T., ... & Niki, H. (2013). Mutations in cell elongation genes mreB, mrdA and mrdB suppress the shape defect of RodZ-deficient cells. *Molecular Microbiology*, *87* (5), 1029-1044.

Sieber, J.J., Willig, K.I., Heintzmann, R., Hell, S.W., & Lang, T. (2006). The SNARE motif is essential for the formation of syntaxin clusters in the plasma membrane. *Biophysical Journal*, *90* (8), 2843-2851.

Singer, A., Poschmann, G., Mühlich, C., Valadez-Cano, C., Hänsch, S., Hüren, V., ... & Nowack, E.C. (2017). Massive protein import into the early-evolutionary-stage photosynthetic organelle of the amoeba *Paulinella chromatophora*. *Current Biology*, *27*(18), 2763-2773.

Singh, P.K., Kapoor, A., Lomash, R.M., Kumar, K., Kamerkar, S.C., Pucadyil, T.J., & Mukhopadhyay, A. (2018). *Salmonella* SipA mimics a cognate SNARE for host Syntaxin8 to promote fusion with early endosomes. *Journal of Cell Biology*, *217*(12), 4199-4214.

Smirnova, E., Shurland, D.L., Ryazantsev, S.N., & van der Bliek, A.M. (1998). A human dynamin-related protein controls the distribution of mitochondria. *The Journal of Cell Biology*, *143*(2), 351-358.

Söllner, T., Bennett, M.K., Whiteheart, S.W., Scheller, R.H., & Rothman, J.E. (1993a). A protein assembly-disassembly pathway in vitro that may correspond to sequential steps of synaptic vesicle docking, activation, and fusion. *Cell*, *75*(3), 409-418.

Söllner, T., Whiteheart, S.W., Brunner, M., Erdjument-Bromage, H., Geromanos, S., Tempst, P., & Rothman, J.E. (1993b). SNAP receptors implicated in vesicle targeting and fusion. *Nature*, *362*(6418), 318-324.

References

Sørensen, M.E., Stiller, M.L., Kröninger, L., & Nowack, E.C. (2024). Protein import into bacterial endosymbionts and evolving organelles. *The FEBS Journal*.

Spang, A., Courtney, I., Fackler, U., Matzner, M., & Schiebel, E. (1993). The calcium-binding protein cell division cycle 31 of *Saccharomyces cerevisiae* is a component of the half bridge of the spindle pole body. *The Journal of Cell Biology*, *123* (2), 405-416.

Stebeck, C.E., Beecroft, R.P., Singh, B.N., Jardim, A., Olafson, R.W., Tuckey, C., ... & Pearson, T.W. (1995). Kinetoplastid membrane protein-11 (KMP-11) is differentially expressed during the life cycle of African trypanosomes and is found in a wide variety of kinetoplastid parasites. *Molecular and Biochemical Parasitology*, *71*(1), 1-13.

Stein, A., Weber, G., Wahl, M.C., & Jahn, R. (2009). Helical extension of the neuronal SNARE complex into the membrane. *Nature*, *460*(7254), 525-528.

Sun, Q., Cao, X., Liu, Z., An, C., Hu, J., Wang, Y., ... & Gao, H. (2023). Structural and functional insights into the chloroplast division site regulators PARC6 and PDV1 in the intermembrane space. *Proceedings of the National Academy of Sciences*, *120*(5), e2215575120.

Suzuki, S., Kawachi, M., Tsukakoshi, C., Nakamura, A., Hagino, K., Inouye, I., & Ishida, K.I. (2021). Unstable relationship between *Braarudosphaera bigelowii* (= *Chrysochromulina parkeae*) and its nitrogen-fixing endosymbiont. *Frontiers in Plant Science*, *12*, 749895.

Taguchi, A., Welsh, M.A., Marmont, L.S., Lee, W., Sjodt, M., Kruse, A.C., ... & Walker, S. (2019). FtsW is a peptidoglycan polymerase that is functional only in complex with its cognate penicillin-binding protein. *Nature Microbiology*, *4*(4), 587-594.

Tao-Cheng, J.H., Pham, A., Yang, Y., Winters, C.A., Gallant, P.E., & Reese, T.S. (2015). Syntaxin 4 is concentrated on plasma membrane of astrocytes. *Neuroscience*, *286*, 264-271.

TerBush, A.D., MacCready, J.S., Chen, C., Ducat, D.C., & Osteryoung, K.W. (2018). Conserved dynamics of chloroplast cytoskeletal FtsZ proteins across photosynthetic lineages. *Plant Physiology*, *176* (1), 295-306.

Tieu, Q., Okreglak, V., Naylor, K., & Nunnari, J. (2002). The WD repeat protein, Mdv1p, functions as a molecular adaptor by interacting with Dnm1p and Fis1p during mitochondrial fission. *The Journal of Cell Biology*, *158*(3), 445-452.

Timm, D., Salim, K., Gout, I., Guruprasad, L., Waterfield, M., & Blundell, T. (1994). Crystal structure of the pleckstrin homology domain from dynamin. *Nature Structural Biology*, *1* (11), 782-788.

Timmis, J.N., Ayliffe, M.A., Huang, C.Y., & Martin, W. (2004). Endosymbiotic gene transfer: organelle genomes forge eukaryotic chromosomes. *Nature Reviews Genetics*, *5*(2), 123-135.

Tripp, H.J., Bench, S.R., Turk, K.A., Foster, R.A., Desany, B.A., Niazi, F., ... & Zehr, J.P. (2010). Metabolic streamlining in an open-ocean nitrogen-fixing cyanobacterium. *Nature*, *464*(7285), 90-94.

Twig, G., Elorza, A., Molina, A.J., Mohamed, H., Wikstrom, J.D., Walzer, G., ... & Shirihai, O.S. (2008). Fission and selective fusion govern mitochondrial segregation and elimination by autophagy. *The EMBO Journal*, *27*(2), 433-446.

References

Van den Ent, F., & Löwe, J. (2000). Crystal structure of the cell division protein FtsA from *Thermotoga maritima*. *The EMBO Journal*.

Van den Ent, F., Amos, L.A., & Löwe, J. (2001). Prokaryotic origin of the actin cytoskeleton. *Nature*, *413*(6851), 39-44.

Van der Ploeg, R., Verheul, J., Vischer, N.O., Alexeeva, S., Hoogendoorn, E., Postma, M., ... & Den Blaauwen, T. (2013). Colocalization and interaction between elongasome and divisome during a preparative cell division phase in *Escherichia coli*. *Molecular Microbiology*, *87* (5), 1074-1087.

Venkatesh, D., Boehm, C., Barlow, L.D., Nankissoor, N.N., O'Reilly, A., Kelly, S., ... & Field, M.C. (2017). Evolution of the endomembrane systems of trypanosomatids–conservation and specialisation. *Journal of Cell Science*, *130*(8), 1421-1434.

Wang, W., Li, J., Sun, Q., Yu, X., Zhang, W., Jia, N., ... & Feng, Y. (2017). Structural insights into the coordination of plastid division by the ARC6–PDV2 complex. *Nature Plants*, *3*(3), 1-9.

Wernegreen, J.J. (2002). Genome evolution in bacterial endosymbionts of insects. *Nature Reviews Genetics*, *3*(11), 850-861.

Wissel, M.C., & Weiss, D.S. (2004). Genetic analysis of the cell division protein FtsI (PBP3): amino acid substitutions that impair septal localization of FtsI and recruitment of FtsN. *Journal of Bacteriology*, *186* (2), 490-502.

Wolfrum, U., & Salisbury, J.L. (1998). Expression of centrin isoforms in the mammalian retina. *Experimental Cell Research*, *242*(1), 10-17.

Wong, Y.C., Ysselstein, D., & Krainc, D. (2018). Mitochondria–lysosome contacts regulate mitochondrial fission via RAB7 GTP hydrolysis. *Nature*, *554*(7692), 382-386.

Xiang, Y., Morais, M.C., Cohen, D.N., Bowman, V.D., Anderson, D.L., & Rossmann, M.G. (2008). Crystal and cryoEM structural studies of a cell wall degrading enzyme in the bacteriophage φ29 tail. *Proceedings of the National Academy of Sciences*, *105*(28), 9552-9557.

Yoshida, Y. (2018). Insights into the mechanisms of chloroplast division. *International Journal of Molecular Sciences*, *19* (3), 733.

Yoshida, Y., Kuroiwa, H., Misumi, O., Yoshida, M., Ohnuma, M., Fujiwara, T., ... & Kuroiwa, T. (2010). Chloroplasts divide by contraction of a bundle of nanofilaments consisting of polyglucan. *Science*, *329* (5994), 949-953.

Yoshida, Y., Kuroiwa, H., Shimada, T., Yoshida, M., Ohnuma, M., Fujiwara, T., ... & Kuroiwa, T. (2017). Glycosyltransferase MDR1 assembles a dividing ring for mitochondrial proliferation comprising polyglucan nanofilaments. *Proceedings of the National Academy of Sciences*, *114* (50), 13284-13289.

Yoshida, Y., Miyagishima, S.Y., Kuroiwa, H., & Kuroiwa, T. (2012). The plastid-dividing machinery: formation, constriction and fission. *Current Opinion in Plant Biology*, *15* (6), 714-721.

Zakharova, A., Saura, A., Butenko, A., Podešvová, L., Warmusová, S., Kostygov, A.Y., ... & Yurchenko, V. (2021). A new model trypanosomatid, *Novymonas esmeraldas*: Genomic perception of its "*Candidatus* Pandoraea novymonadis" endosymbiont. *Mbio*, *12*(4), 10-1128.

References

Zehr, J.P., Bench, S.R., Carter, B.J., Hewson, I., Niazi, F., Shi, T., ... & Affourtit, J.P. (2008). Globally distributed uncultivated oceanic N2-fixing cyanobacteria lack oxygenic photosystem II. *Science*, *322*(5904), 1110-1112.

Zehr, J.P., Shilova, I.N., Farnelid, H.M., Muñoz-Marín, M.D.C., & Turk-Kubo, K.A. (2016). Unusual marine unicellular symbiosis with the nitrogen-fixing cyanobacterium UCYN-A. *Nature Microbiology*, *2*(1), 1-11.

Zhang, M., Chen, C., Froehlich, J.E., TerBush, A.D., & Osteryoung, K.W. (2016). Roles of *Arabidopsis* PARC6 in coordination of the chloroplast division complex and negative regulation of FtsZ assembly. *Plant Physiology*, *170* (1), 250-262.

Zhang, P., & Hinshaw, J.E. (2001). Three-dimensional reconstruction of dynamin in the constricted state. *Nature Cell Biology*, *3*(10), 922-926.

Zhao, J., Liu, T., Jin, S., Wang, X., Qu, M., Uhlén, P., ... & Nistér, M. (2011). Human MIEF1 recruits Drp1 to mitochondrial outer membranes and promotes mitochondrial fusion rather than fission. *The EMBO Journal*, *30* (14), 2762-2778.

Zhao, X., Yang, H., Liu, W., Duan, X., Shang, W., Xia, D., & Tong, C. (2015). Sec22 regulates endoplasmic reticulum morphology but not autophagy and is required for eye development in *Drosophila*. *Journal of Biological Chemistry*, *290*(12), 7943-7951.

Zimorski, V., Ku, C., Martin, W.F., & Gould, S.B. (2014). Endosymbiotic theory for organelle origins. *Current Opinion in Microbiology*, *22*, 38-48.

7. Acknowledgements

Firstly, I would like to extend my huge thanks to the Molecules of Infection IV (MOI IV), Manchot Graduate School at Heinrich Heine University (HHU) Düsseldorf for providing me a great opportunity to carry out my doctoral research. The school not only offered financial support via a scholarship throughout my studies but also gave freedom to visit other MOI IV labs, supported stay abroad research, conferences, and many other features made this journey invaluable and unforgettable. Additionally, thanks to the MOI IV coordinator Dr. Stephanie Spelberg for all the support throughout my study.

Secondly, it gives me immense pleasure to express my sincere and heartfelt thanks to Prof. Dr. Eva Nowack for providing me with a chance to work in her lab. Her enormous support on various scales made this journey feasible. I appreciate the freedom, motivation, and supervision that I was provided with. Thanks for finding out time for personal discussions and sharing a lot of suggestions leading to a nice improvement I have made today.

Thirdly, I would like to thank Prof. Dr. Johannes H. Hegemann for spending his precious time to investigate my work and providing valuable suggestions during the entire study.

Next, I would like to thank two most important pillars- Lena Kröninger and Georg Ehret whom I have started my lab journey with. Both lab mates have been wonderful supporters on different levels. They have not only been my co-authors and helped me in the lab in every up and down but also have supported during my personal obstacles as well.

I also extend my thanks to Nicole Brand, Victoria Klimenko, Tobias Reinicke, Linda Westhoff, Luis Macorano, Megan Sørensen, Mygg Stiller, Natascha Künzel, Lawrence Rudy Cadena, Taniya Mary Binny, Tobias Spiegl, and Linda Wiegand for all the technical, personal, emotional, and research related support they provided during the study.

I would also like to thank all my students- Lucie Hansen, Jil Thormann, Zio Kim, and Lindsay Viola Dittmann for supporting my work, being nice to me, and tolerating me as a supervisor during their studies. Additionally, I thank all alumni, students Laura Czwallina and Christian Stiebeling, and other people who have fortunately been part of my research journey.

I also thank the entire team at the Center for Advanced Imaging (CAi), HHU for their valuable support especially Prof. Dr. Stefanie Weidtkamp-Peters for providing opportunity, Sebastian Hänsch for fluorescence microscopy, and Miriam Baümers for TEM.

During my MOI IV lab rotations, I would like to express my heartfelt gratitude to Prof. Dr. Johannes H. Hegemann, Fabienne Kocher, Sarune Daunaraviciute for my first lab rotation, Dr. Daniel Degrandi and Gowshiga Sivalingam for second lab rotation, and Prof. Dr. Stefanie Scheu and Marcel Marson for my third and last MOI IV lab rotation.

Also, I would like to extend my thanks to Prof. Dr. Philippe Bastin and Christine Girard-Blanc for supporting my stay abroad studies at Institute Pasteur, Paris (France).

Last but not the least, a huge thanks to my parents, sisters, nieces, other family members, friends, and teachers for encouraging, supporting, having patience, and believing in me.

“Evolution does not produce something that is perfect, it just produces something that works.” (Tim Skern)